ESL-TR-92-79
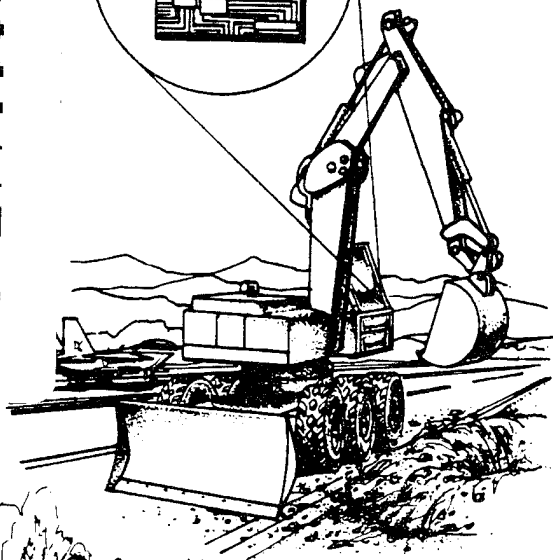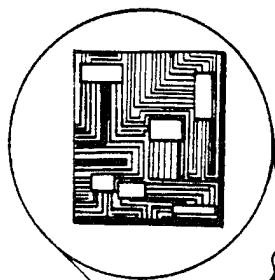
ANALYSIS AND INTERPRETATION OF SINAI TEST STRUCTURE DATA AND INVESTIGATION OF THE APPLICABILITY OF SELECTED DYNAMIC RESPONSE PROGRAMS TO SUCH STRUCTURES

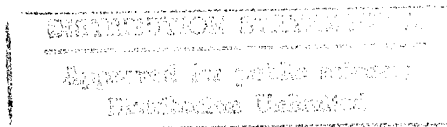S.L. PAUL, J.D. HALTIWANGER, J.R. HAYES, D. GROSSMAN, J.B. GAMBILL, C. HA

UNIVERSITY OF ILLINOIS AT URBANA-CHAMPAIGN
URBANA IL 61816

JULY 1995

FINAL REPORT

JUNE 1989 - JULY 1993

ENGINEERING RESEARCH DIVISION
Air Force Civil Engineering Support Agency
Civil Engineering Laboratory
Tyndall Air Force Base, Florida 32403

19960117 053

NOTICE

PLEASE DO NOT REQUEST COPIES OF THIS REPORT FROM HQ AFCESA/RA (AIR FORCE CIVIL ENGINEERING SUPPORT AGENCY). ADDITIONAL COPIES MAY BE PURCHASED FROM:

> NATIONAL TECHNICAL INFORMATION SERVICE
> 5285 PORT ROYAL ROAD
> SPRINGFIELD, VIRGINIA 22161

FEDERAL GOVERNMENT AGENCIES AND THEIR CONTRACTORS REGISTERED WITH DEFENSE TECHNICAL INFORMATION CENTER SHOULD DIRECT REQUESTS FOR COPIES OF THIS REPORT TO:

> DEFENSE TECHNICAL INFORMATION CENTER
> CAMERON STATION
> ALEXANDRIA, VIRGINIA 22314

REPORT DOCUMENTATION PAGE

Form Approved
OMB No. 0704-0188

1. AGENCY USE ONLY (Leave blank)	2. REPORT DATE July 1995	3. REPORT TYPE AND DATES COVERED Final, 26 Jun 89 - 14 Jul 93

4. TITLE AND SUBTITLE
Analysis and Interpretation of Sinai Test Structure Data and Investigation of the Applicability of Selected Dynamic Response Programs to Such Structures

5. FUNDING NUMBERS

6. AUTHOR(S)
S.L. Paul, J.D. Haltiwanger, J.R. Hayes, D. Grossman, J.B. Gambill, and C. Ha

7. PERFORMING ORGANIZATION NAME(S) AND ADDRESS(ES)
University of Illinois at Urbana-Champaign
Urbana, IL 61801

U.S. Army Construction Engineering Research Laboratories
Champaign, IL 61816

8. PERFORMING ORGANIZATION REPORT NUMBER

N/A

9. SPONSORING/MONITORING AGENCY NAME(S) AND ADDRESS(ES)
HQ Air Force Civil Engineering Support Agency
Tyndall AFB, FL 32403

10. SPONSORING/MONITORING AGENCY REPORT NUMBER

ESL-TR-92-79

11. SUPPLEMENTARY NOTES

N/A

12a. DISTRIBUTION/AVAILABILITY STATEMENT
Approved for Public Release
Distribution Unlimited

12b. DISTRIBUTION CODE

13. ABSTRACT (Maximum 200 words)

Data from a series of field weapons effects tests are analyzed for their applicability to protective structure design procedures. Microcomputer-based single-degree-of-freedom dynamic analysis models and a mainframe nonlinear finite element analysis model are used to analyze numerical models of the field test structures. The computer models are evaluated for their effectiveness and applicability to protective structure design.

14. SUBJECT TERMS

15. NUMBER OF PAGES
249

16. PRICE CODE

17. SECURITY CLASSIFICATION OF REPORT UNCLASSIFIED	18. SECURITY CLASSIFICATION OF THIS PAGE UNCLASSIFIED	19. SECURITY CLASSIFICATION OF ABSTRACT UNCLASSIFIED	20. LIMITATION OF ABSTRACT UL

NSN 7540-01-280-5500

i
(The reverse of this page is blank.)
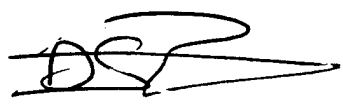
Standard Form 298 (Rev 2-89)

PREFACE

This report was prepared by the US Army Construction Engineering Research Laboratories (USACERL). Work was also performed under USACERL contracts DACA 88-88-D-0005 and DACA 88-90-D-0003, with the Department of Civil Engineering at the University of Illinois at Urbana-Champaign (UIUC); and under USACERL contract DACA 88-92-M-0625, with Southwest Research Institute. The project was co-sponsored by the Air Force Civil Engineering Support Agency (AFCESA), Civil Engineering Laboratory, Tyndall Air Force Base, Florida, and the Israeli Air Force (IAF) Civil Engineering Division Headquarters, Tel Aviv, Israel.

This report summarizes work accomplished between 26 June 1989 and 14 July 1993. Majors Jacob Gheriani and Dan Shenbach, IAF, and Captain Diane Miller, USAF, were the HQ AFCESA/RACS project officers during the effort.
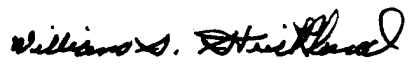
The microcomputer model SDOF, and associated modeling techniques, were exercised by Dr. John Haltiwanger, Professor Emeritus, UIUC. Questions concerning its derivation may be directed to Dr. Haltiwanger. The microcomputer model SASDE was developed by Dr. Theodor Krauthammer, who was partly supported by the US Air Force to develop the model. SASDE is not a commercial code at this time; qualified government-related engineers may contact Dr. Krauthammer at Pennsylvania State University concerning its use.

This report has been reviewed by the AFCESA Public Affairs Office and is releasable to the National Technical Information Service (NTIS). At NTIS, it will be available to the public, including foreign nationals.

This report has been reviewed and is approved for publication

Dan Shenbach, Major, IAF
Project Officer

Edgar F. Alexander
Chief, Air Base Systems Branch

William S. Strickland
Chief, Airbase Survivability Section

Accession For		
NTIS GRA&I	☑	
DTIC TAB	☐	
Unannounced	☐	
Justification		
By		
Distribution/		
Availability Codes		
Dist	Avail and/or Special	
A-1		

iii
(The reverse of this page is blank)

Executive Summary

A. OBJECTIVE

This report documents a research effort undertaken by the Airbase Survivability Branch, Engineering Research Division Air Force Civil Engineering Support Agency (AFCESA/RACS). Project objectives were twofold. First, the project engineers evaluated the quality of field test data obtained in high explosives tests of protective structures by the Israeli Defense Forces (IDF). Second, the project engineers applied those data, and data collected by the US Air Force in other tests, to evaluate the applicability of available micro-computer structural analysis programs to protective structures design procedures. The applicability of a complex mainframe nonlinear dynamic finite analysis computer program was also evaluated.

B. BACKGROUND

The IDF conducted a series of high explosives (HE) tests in which both bare explosives charges and actual weapons were detonated in close proximity to airbase protective structures. Later, the US Air Force (USAF) conducted a series of similar high-explosives tests using cased charges and a test structure. The IDF and USAF then undertook a cooperative research project to reduce the IDF field test data and use the data to validate techniques currently being used to predict the responses of above-ground protective walls to the effects of conventional weapons.

In parallel but unrelated efforts, a number of single-degree-of-freedom (SDOF) dynamic analysis codes were developed for use on IBM-compatible microcomputers. Some of these codes were developed commercially, while others were developed by government agencies. In addition, a number of nonlinear dynamic finite element analysis codes were developed for use on mainframe computer systems.

USAF project officers wished to use the IDF and USAF field-test data as means of evaluating a representative sampling of the available computer codes for their accuracy and ease of use in protective structure design. Using the measured airblast distributions on the test structure walls, the measured responses of those walls would be compared to responses predicted by the computer codes.

C. SCOPE

This report first describes the IDF test program and examines the data collected by the IDF. Next, the report briefly describes the USAF tests. No attempt is made to analyze the USAF data, as such analyses have already been reported. The report then summarizes the exercising of four microcomputer codes and assesses their viability for use in design. The exercising of a nonlinear dynamic finite element analysis is also discussed. Overall conclusions from the data reduction and computer modeling are presented. Two appendices are included:

the first presents representative samples of the IDF test data, and the second summarizes the approaches used by the authors to model the airblast pressure-time histories for use in the various computer programs.

D.   RESULTS

1.   IDF Test Data

The first general objective for the project was to analyze the IDF test data. Two structures were tested, called herein "Structure 1" and "Structure 2." Because very little instrumented response was observed in Structure 2, the authors concentrated their efforts on the Structure 1 data. Reflected and free field airblast, wall accelerations, and residual (posttest) wall centerline deflections were reported by the IDF. The airblast data were generally consistent with established theoretical values for larger charge standoff distances, but the airblast data for close-in detonations were very inconsistent, probably due to the many difficulties associated with measuring high pressure spikes. Attempts to compare impulses based on the measured airblast data with those obtained from theoretical calculations were largely unsuccessful. Measured residual displacements for tests on two supposedly identical wall sections showed quite different results, making the use of residual displacement data difficult. Measured wall acceleration data also produced mixed results. Problems seemed to arise both from the digitizing rates chosen for recording the data and, in some cases, from the acceleration ranges chosen for the accelerometers used in the tests. The authors concluded after extensive analysis efforts that the data reported did not offer significant advances to the current technology base of structural response information.

2.   Single-Degree-of-Freedom (SDOF) Microcomputer Models

Four microcomputer models were exercised and evaluated: "UofI," a simple undamped SDOF model developed at the University of Illinois at Urbana-Champaign; "SASDE," a model developed by Dr. Theodor Krauthammer; "BIGGS," a model developed by Wilfred Baker Engineering; and "BLAST," a model developed for the U.S. Department of State. All four models are based on the same general analytical approach. They differ largely in the level of detail provided in the analysis, and in their "user-friendliness."

UofI is general-purpose in nature and can be used for any system for which basic SDOF structural and load properties can be calculated by the analyst. It considers only flexural response, and its output is largely limited to the time-history of the SDOF system response, up to time of maximum response. UofI is not commercially available.

SASDE provides many more options to the analyst than UofI. It is unique in considering both shear and flexural response. SASDE can compute most basic structural and load properties based on user inputs for predefined structural configurations; it will also accept externally calculated values for most of those properties. SASDE also considers equivalent viscous damping of any

magnitude. Output is available in tabulated or graphical form. The program was not initially developed for commercial application. Its user's manual and required data input formats are not clear, and considerable experience in its use is needed before analyses are straightforward. With additional refinement, SASDE has significant potential.

BIGGS has been developed for commercial application and is thus more user-friendly than either UofI or SASDE. BIGGS resembles both UofI and SASDE in key areas. Like UofI, loading and resistance functions must be computed externally. Like SASDE, BIGGS considers both shear and flexure, and it includes viscous damping.

BLAST was apparently based on a different philosophy than the other programs evaluated herein. While it is essentially the same numerical model as the other programs, it is a much-simplified model that provides basic information on wall vulnerabilities to high-explosive charge detonations.

3. GENERAL PURPOSE FINITE ELEMENT PROGRAM

The nonlinear dynamic analysis program "ADINA" was selected for the evaluation effort. A key reason for its selection was its incorporation of a complex concrete material model, a feature not found frequently. Models of the IDF and USAF walls were developed and exercised; the models utilized two- and three-dimensional solid "brick" elements to represent concrete and truss elements to represent reinforcing bars. ADINA was exercised to examine the effects of different load representations, element mesh densities, end condition representations, material properties (e.g., concrete tensile strength), in-plane force effects (caused by restraints), and various unique reinforcement details. ADINA may be run two-dimensionally or three-dimensionally. Both configurations were exercised, but the three-dimensional representation was found to be far more computationally expensive, without a corresponding increase in accuracy of results. In general, the authors found that ADINA could be used to perform detailed parametric studies that assess design options, as the analyses showed reasonable correlation with test results. However, its use comes at a cost. ADINA is a highly specialized program and requires extensive user experience before it can be exercised with predictable accuracy. The combination of the use of nonlinear material models and a large number very short time steps leads to extremely long computation times, even for very capable minicomputers or mainframe computers (both were used in this study). The extremely high pressures associated with the airblast loads, when combined with the material strength parameters used in the ADINA material models, also frequently lead to computational instabilities, causing program termination. Again, user practice is needed to provide the intuition needed to resolve such instabilities. Note that the authors used an academic version of ADINA that did not permit access to its source code. Commercial versions of ADINA commonly include source code access. Such access would permit material model modifications that were not possible in this study.

E.   CONCLUSIONS

Each microcomputer program exercised by the authors showed reasonable capabilities and could be applied by analysts or designers. Except for the BLAST program, which was meant for simplified analyses by designers, all of the microcomputer programs require understanding of the fundamentals of structural dynamics, nonlinear material behavior, and blast loadings.

ADINA showed its potential for use in performing detailed parametric studies during design or research projects. The analysts who use it must be thoroughly familiar with structural dynamics, nonlinear material behavior, blast loading, and finite element analysis. In addition, analysts must become thoroughly familiar with the ADINA program. ADINA analyses in the nonlinear region involve long computer run times, incurring whatever costs are associated with computer use.

In general, the finite element analysis approach would seem to be best employed in research; design of large, complex structures; or in design of "definitive," or prototype, structures for a large number of site-adaptation designs. With refined use, the microcomputer models can provide good estimates of overall structural behavior; such estimates can be combined with the testing experience reported in the literature to perform adequate design of typical protective structures.

F.   RECOMMENDATIONS

The primary purpose of the study covered by this report was to assess the usefulness of specific field test data to improving protective structure design procedures and the effectiveness of several computer modeling techniques. Future research directions were not of primary importance. However, an area of potentially major impact illustrated in this project is that of a combined simplified/detailed analysis platform. In such a platform, simple, easy-to-use SDOF models would be used for general parameter studies, and detailed finite element models would be used for refined calculations. The development of such an integrated software package would be of immeasurable use to the protective design community.

TABLE OF CONTENTS

TABLE OF CONTENTS
(Continued)

FIGURES

TABLES

SECTION I

INTRODUCTION

A. OBJECTIVES OF THE STUDY

The primary objectives of this study were to:

(1) Evaluate the data obtained in high explosives tests of protective structures that were conducted by the Israeli Defense Forces (IDF); reduce the data to a suitable form for defining the loadings to which the test structures were subjected; and analyze the responses of the structures to those loads.

(2) Use the loading and response data, as well as the data from tests conducted by the US Air Force at Tyndall AFB, to evaluate the suitability and potential usefulness of several currently available, single-degree-of-freedom (SDOF), dynamic structural response microcomputer programs. These programs generate analyses of walls subjected to blast loadings from conventional weapons. It was expected that these computer program evaluations would include assessments of their ease of use, the assumptions implicit in their formulation, the corresponding constraints on their applicability, and the extent to which the responses as predicted by these programs agreed with the observed responses of the test structures.

(3) Use the IDF and Tyndall test data to assess the applicability of a comprehensive finite element computer program to the analysis of the behavior of structural elements when subjected to blast pressure loadings produced by conventional weapons. Automated Dynamic Incremental Nonlinear Analysis (ADINA), a program developed by ADINA R&D, Inc., of Watertown, MA, was selected because of its current use at several U.S. Army and Air Force research and design facilities, and because of its ability to model nonlinear, reinforced concrete and steel structural behavior. These analyses were also expected to provide a comparison between the SDOF and finite element computer programs, considering their ease of use, the accuracy of their predictions, and their suitability for design calculations.

Despite how reasonable these objectives were, the IDF structures used in this study were not designed and constructed as research structures; neither the properties of the materials used in them, nor the details of their actual construction, were as carefully documented as they would have been in a structure that was designed and built for research purposes. The control of material properties and the care used in the construction process for these structures were consistent with normal construction practices rather than with the practices of a research laboratory. Consequently, the uncertainty concerning the actual resistances of the IDF test structures was more than it would have been in a carefully designed and executed research exercise. Hence, the validity of comparisons between measured responses and the responses computed by such resistances is properly subject to some question.

1

B.   BACKGROUND

The IDF conducted a series of high explosive (HE) tests in which both bare explosive charges and actual weapons were detonated in close proximity to protective structures. The IDF and the U.S. Air Force (USAF) later undertook a cooperative research project to reduce the IDF field test data and use it to validate techniques currently being used to predict the structural response of above-ground walls to the effects of conventional weapons. The IDF field test data were supplemented by data obtained from similar HEs effects tests that were conducted by the USAF at Tyndall AFB, Florida. The Tyndall tests involved loadings that produced significant shear responses in the walls of the test structures rather than the flexure-dominated responses that were observed in the IDF tests; they also explored a much more severe dynamic loading environment.

C.   SCOPE OF STUDY

This study involved the analysis of data acquired in 15 HE tests conducted by the IDF on the walls of two structures (Reference 1) and in two similar tests that were conducted at Tyndall AFB on NATO-type structures (Reference 2).

One of the IDF structures was tested four times on one wall and five times on its opposite wall. Bare HE charges were detonated at different distances from the walls, and the pressure loadings and wall responses were measured. Those data were then analyzed and interpreted in the studies reported here. The first wall of this structure received only minor flexural damage, as did the second wall for its first four tests. But in the fifth test on the second wall, in which the charge was placed closest to the wall, the wall experienced severe, localized, shear damage near its base.

The second IDF structure was tested six times using cased charges; primary damage resulted from fragment penetration. Because no wall blast pressure loading data and only limited and uncertain deflection data were recorded in these tests, no confirming analytical studies of the wall responses to the blasts were attempted in this study.

The Tyndall tests that were studied here were identified as Tests 6 and 10 in the series that was reported in Reference 2. In those tests, two similar walls of different thicknesses and reinforcement amounts were subjected to the cased HE charges detonated on the ground surface near the walls. Wall pressure loading and response measurements, which were taken during those tests, were used in this study, in the same manner as the IDF tests data were used, to evaluate the applicability of several currently available computer programs for the prediction of the blast damage to walls in cases typified by these tests.

Among the analytical models examined in this project were four micro-computer programs based on a SDOF approach, which are identified as follows:

(1)   UofI, which was developed at the University of Illinois.

(2)   SASDE, Structural Analysis for Severe Dynamic Environments, which was developed by Dr. Theodor Krauthammer, of the University of Minnesota (now at Pennsylvania State University).

(3)   BLAST, which was developed for the U.S. Department of State.

2

(4)   BIGGS, which was developed by Wilfred Baker Engineering, Inc., of
       San Antonio, TX.

The first of these SDOF programs, UofI, performs a numerical integration of the equations of motion, with multilinear resistance functions and loading functions that are generated by the analyst outside of the program, by data that define the geometry of the structure and the properties of the materials of which it is made, and loading data that are obtained either from measurements or from theoretical calculations. In this program, the resistance and loading functions are expressed by unit area pressures applied uniformly over the entire wall surface. Only flexural behavior of the wall is considered, and the effects of damping are neglected.

SASDE differs from the UofI program primarily in that it computes the resistance function internally in the program using the slab geometry, support conditions, and material properties that are input into the program. The loading function can be input directly as a multilinear pressure-time function, or it can be generated internally by the program using given charge sizes and locations. Additionally, SASDE includes the effects of damping, and considers both flexural and shear responses of the slab.

BLAST was intended by its developers to be a screening device for assessing the vulnerabilities of walls to blast loadings when not much is known about the strength of the walls, and/or when the analyst is not familiar with the computational procedures for analyzing protective structures. Consequently, except for the general wall type and its dimensions, the program includes default values for all of the parameters that are needed to generate a resistance function. However, if more detailed information about those parameters is available, the default values are easily replaced from those better data, and the resistance function is then generated by the program from those data and predefined slab support conditions that cannot be changed by the analyst. The loading function is generated internally by the program from an input charge size and location with respect to the wall being studied.

BIGGS is a microcomputer implementation of the SDOF representation of beams and slabs as described by Dr. John M. Biggs in his book, <u>Introduction to Structural Dynamics</u> (Reference 3). It is similar to UofI in that the loading and resistance functions must be computed externally by the analyst and input directly into the program, and in that only flexural behavior of the slab is considered. However, it differs from UofI in that damping is considered, and it assumes that the maximum resistance, once reached, is maintained at all greater deflections, in contrast to UofI, for which the resistance function is not so constrained.

Another analytical technique used in this study is a mainframe finite element code. Several commercially available programs could have been used, but ADINA was selected for these studies because of its existing use in government laboratories, its ability to perform dynamic analyses, and its inclusion of a

model for the behavior of concrete to failure. Part of the work with this program was performed on workstations, and longer runs were made on a CRAY super-computer at the University of Illinois, which was available to the investigators.

SECTION II

DESCRIPTION OF ISRAELI DEFENSE FORCES TESTS

A.   DESCRIPTION OF TEST STRUCTURES

Two full-scale reinforced concrete structures were tested and were designated as Structure 1 and Structure 2. The first structure was subjected to nine bare charge detonations, and the second one to six detonations of cased explosives. The two structures were quite similar in geometry and construction; however, Structure 2 was loaded by cased charge detonations that caused localized fragment damage on the walls and doors but very little added overall structural response. In addition, wall pressures were not recorded for Structure 2, so correlations with computed responses were not possible for that structure.

Structure 1 had internal dimensions of 22 x 23 x 9.8 feet with exterior wall and roof thicknesses of 15.7 inches. Figure 1 shows a plan view and Figure 2 shows a cross section of this structure. Protected doorways are shown on the left and right of the drawing; there is also an opening in the roof. The test walls are those at the top and bottom of the plan view, designated walls A and B. The clear horizontal span of the walls is 23.0 feet, and the clear vertical height is 9.8 feet.

The test walls were cast integrally with the roof and sidewalls. However, the walls are not attached to the floor, but continue 31.5 inches below the top
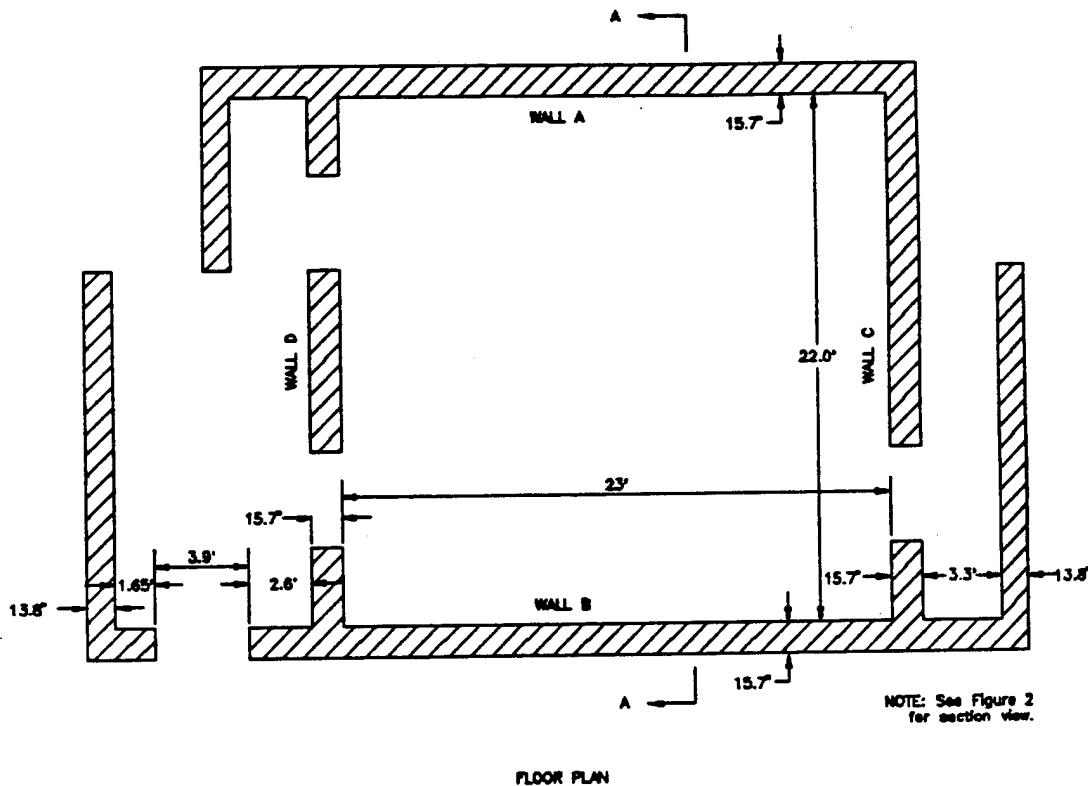
Figure 1.   Plan View of IDF Structure 1.

5
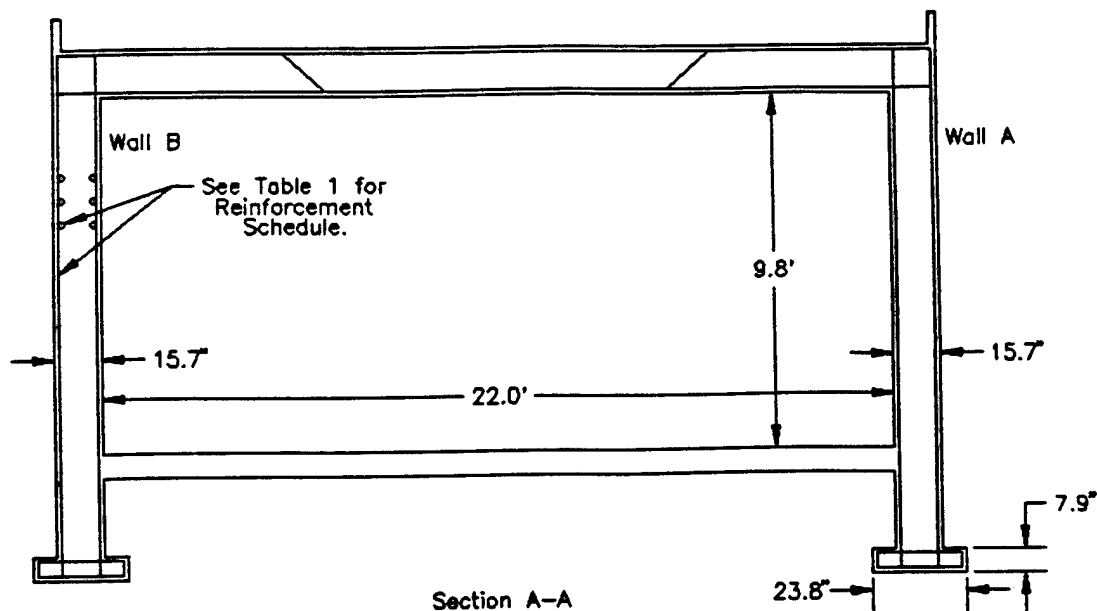
Figure 2. Cross Section of IDF Structure 1.

of the floor to a continuous wall footing that is approximately 23.6 inches wide x 7.9 inches deep, as shown in Figure 2. Thus, the boundary condition to be modeled at the floor lies between fixed and pinned. The reinforcement for test walls A and B is summarized in Table 1.

Vertical reinforcement on the outside surface is more dense in the top 39.4 inches, as shown in Table 1. Cover on the reinforcement was 0.59 inch on both faces for the vertical bars, so the effective depth of the slab section was 15.2 inches for positive and negative bending for the vertical span. The horizontal bars are inside the vertical bars, and therefore the effective depth is slightly smaller.

TABLE 1. REINFORCEMENT OF TEST WALLS OF IDF STRUCTURE 1.

Reinforcement location	Bar diameter/spacing (mm/cm)		Area/foot (in^2)	
Walls A and B	Vertical	Horizontal	Vertical	Horizontal
Outside top 1m and	12mm/20cm 16mm/20cm	8mm/20cm	0.73	0.11
Outside bottom	12mm/20cm	8mm/20cm	0.26	0.11
Inside	12mm/10cm	8mm/10cm	0.53	0.23

The concrete was designed for a minimum unconfined compressive strength of 300 kg/cm² based on tests of 12 cm cubes, which would be equivalent to a 6 x 12 inch cylinder strength, f_c', of 3220 psi. This conversion accounts for the different size and configuration of the specimen (Reference 4). The assumed elastic modulus for the grade of concrete used is $E_c = 300,000$ kg/cm² (4,270,000 psi), using procedures specified by the IDF (this differs from prevailing US practice).

The reinforcing steel had a specified minimum yield strength of 2200 kg/cm² (31,200 psi) and a minimum ultimate strength of 3700 kg/cm² (52,600 psi). The minimum required ultimate strain for this steel is 18 percent, and the Young's modulus was taken as 2.1 x 10⁶ kg/cm² (29,800 ksi).

Evaluations of the resistance of the structure were based on these nominal material properties. Samples of the actual materials used were not tested, so the actual strengths may have differed from the specified values.

The plan view of Structure 2 is shown in Figure 3 and cross sections in two directions are shown in Figure 4. Also, the reinforcement for the test walls is shown in Table 2. This structure was not analyzed, nor were its responses compared, as is discussed in Section II-C; however, fragment damage is discussed in Section II-D.
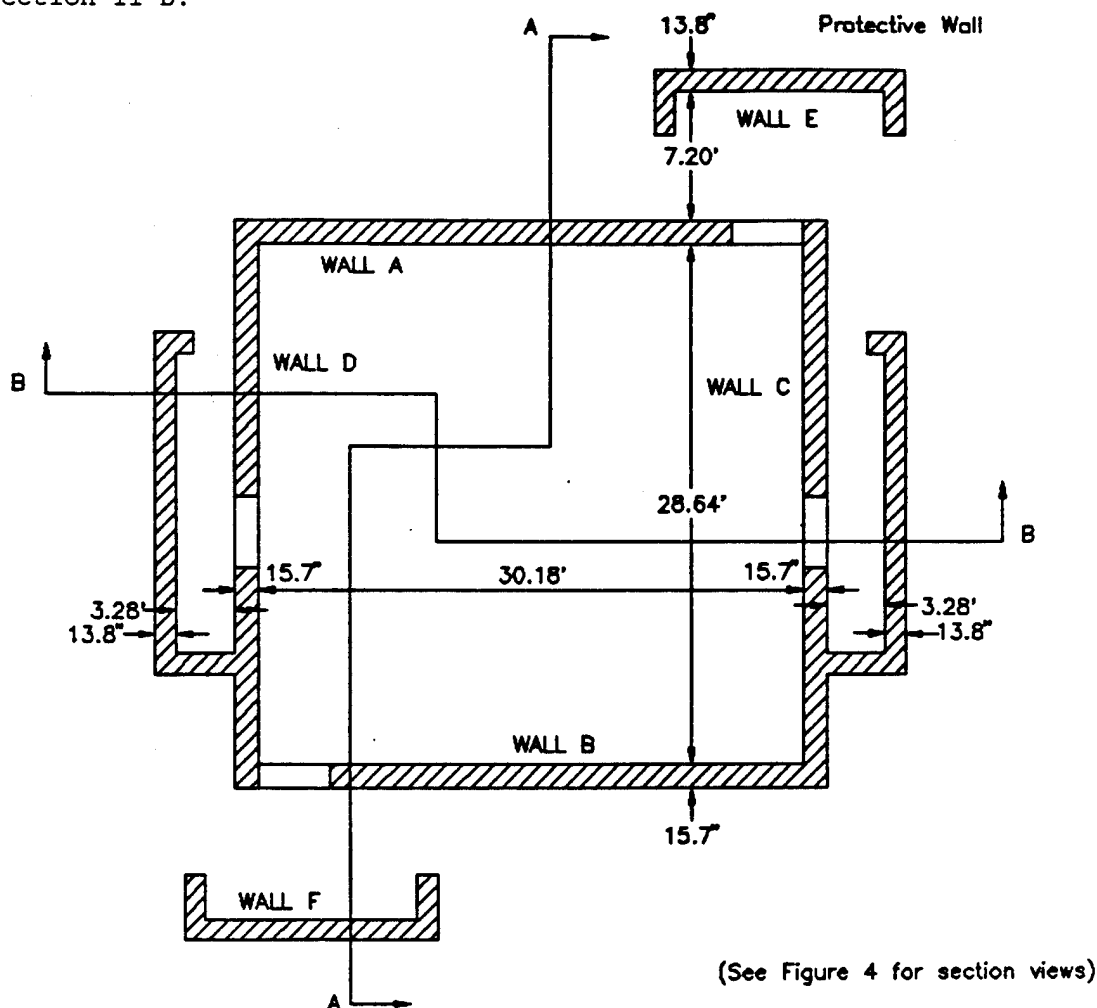
Figure 3. Plan View of IDF Structure 2.

Section A-A
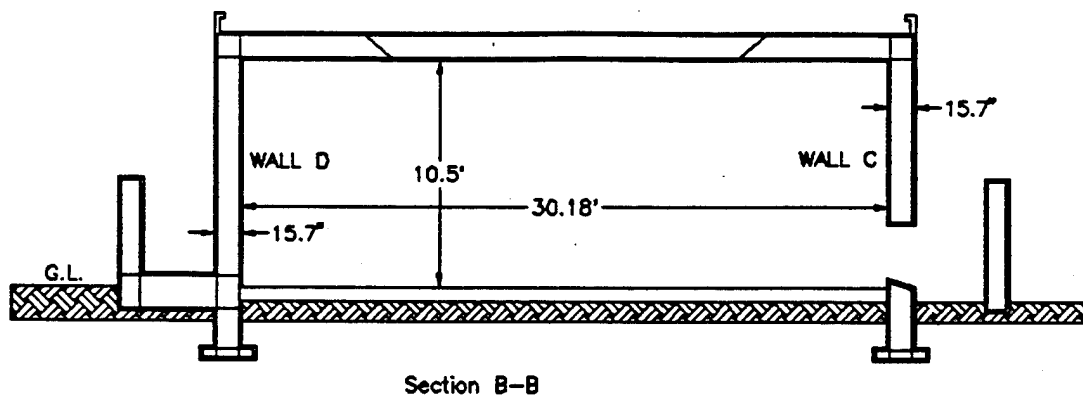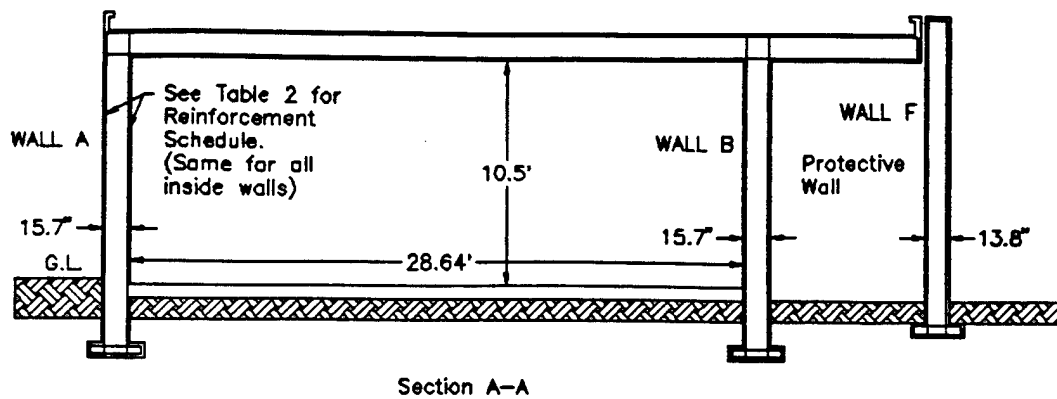
Section B-B

Figure 4. Cross Section of IDF Structure 2.

TABLE 2. REINFORCEMENT OF TEST WALLS OF IDF STRUCTURE 2.

Reinforcement location	Bar diameter/spacing (mm/cm)		Area/foot (in²)	
	Vertical	Horizontal	Vertical	Horizontal
Walls A and B				
Outside top 1m	14mm/20cm	8mm/20cm	0.36	0.11
Outside bottom	14mm/20cm	8mm/20cm	0.36	0.11
Inside	14mm/10cm	8mm/10cm	0.73	0.23
Walls C and D				
Outside	8mm/30cm	8mm/30cm	0.08	0.08
Inside	8mm/15cm	10mm/15cm	0.16	0.25
Walls E and F				
Outside	8mm/30cm	8mm/30cm	0.08	0.08
Inside	12mm/15cm	8mm/15cm	0.36	0.16

8

B. INSTRUMENTATION OF TEST STRUCTURES

Four pressure records and from three to five accelerometer records were obtained for each test. Pressures were measured outside the test structure with four gages. Three PCB Piezotronics 113-A gages were used on each wall to measure reflected pressure, and one Calesco LC-13 gage was placed beside the structure in the plane of the wall, to measure the free field pressure. The locations of the gages on each wall are shown in Figures 5 and 6. The reflected pressure gages were at the center of the wall at midheight, at the center of the wall at ground level, and at the center of the left half of the wall. The free field gage was at the same elevation as the midheight of the wall. In addition, two pressure gages were placed inside the structure.

Accelerometers were attached to the inside surfaces of the test walls, the ceiling, and the floor. The expected acceleration measurements were fairly uncertain in both magnitude and frequency; therefore, most of the measurements were duplicated with two or three sampling frequencies and voltage ranges.

Both pressure and acceleration were recorded with an analog-to-digital converter that used a 6-bit word. This word provides a maximum of 64 digital steps between the extreme positive and negative values of the signal, provided the range is set to match that of the measured signal. In some cases, the range was set larger than the expected signal to ensure that it was adequate, resulting in fewer than 64 steps actually being used within the pressure range. In all cases, this precision gave a measured signal in which distinct steps were visible.

C. LOADINGS OF TEST STRUCTURES

Nine tests, designated as Tests 1-9, were performed on Structure 1 using bare charges of Composite-B explosive. Four charges of 82 kg (181 pounds) were
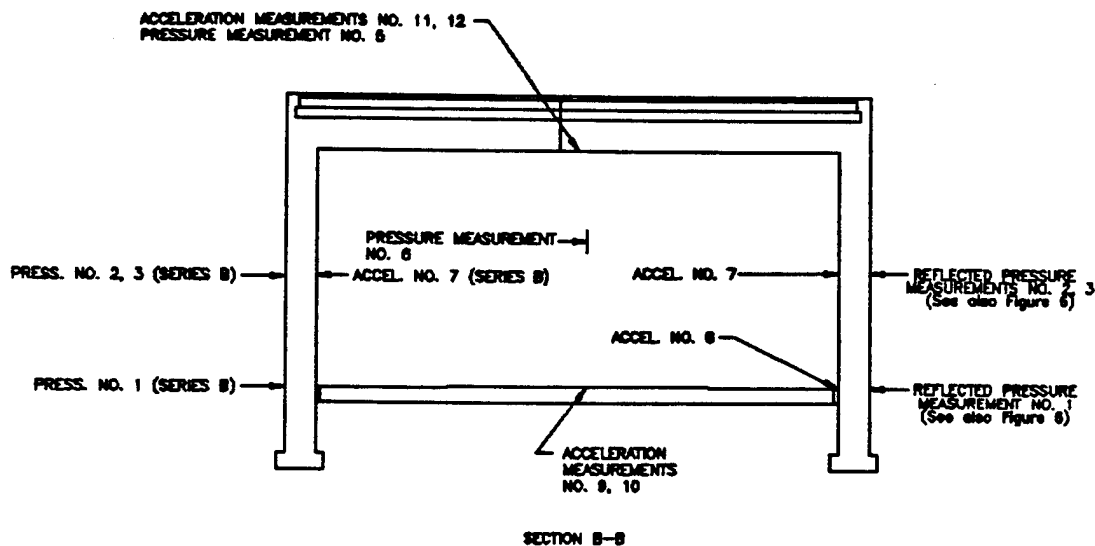
Figure 5. Locations of Pressure and Acceleration Measurements on IDF Structure 1.
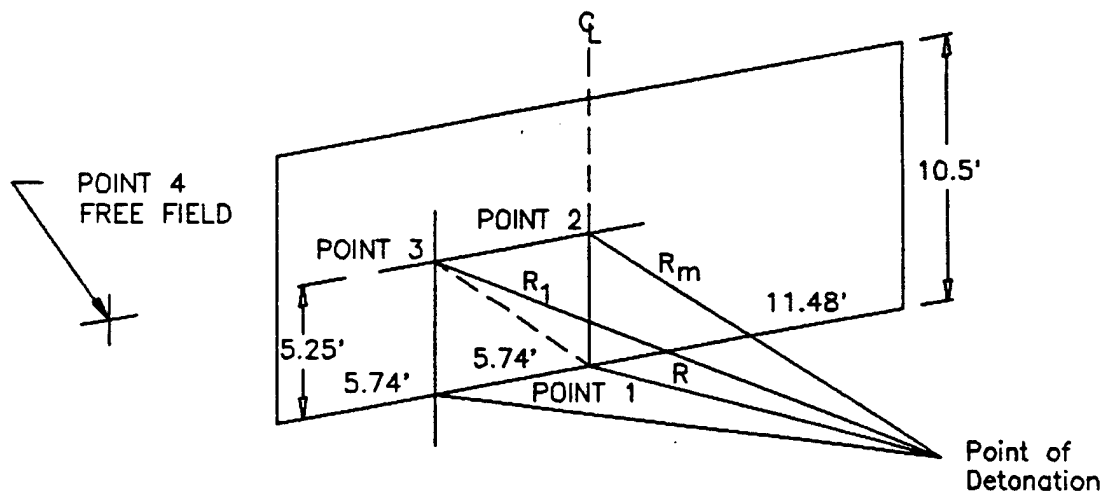
Figure 6.   Locations of Pressure Measurement and Detonation Points Relative
to Test Walls for IDF Structure 1.

detonated at various distances from test wall A, and five charges of 255 kg (562
pounds) were detonated at various distances from wall B. All the charges were
cylinders with a height-to-diameter ratio of 1:1, oriented with the axis of the
cylinder vertical and placed on the ground at the level of the bottom of the
wall.

Six tests, using cased charges, were performed on Structure 2 and were
designated as Tests 10-15. Three tests on walls A and C were made using MK-82
(500 pound) bombs, and three tests on walls A and B were made using 500 kg (1100
pound) bombs. In all tests the bombs were detonated on the ground at the bottom
of the wall, with their longitudinal axis horizontal and parallel to the wall.
This produced a significantly different loading distribution on the walls from
that of the vertically-oriented charges.

The locations of the charges relative to the test walls for Structure 1 are
shown in Figure 6, and the distances from the wall for each shot are summarized
in Tables 3 and 4. The first test in each series was performed with the
explosive farthest from the wall, and for each subsequent test, the charge was
detonated closer to the wall.

D.   TEST RESULTS

The data furnished by IDF consisted of visual descriptions of damage,
photographs, and pressure and acceleration records. The digital records were
evaluated by the U.S. Army Construction Engineering Research Laboratories
(USACERL) at Champaign, Illinois.

1.   Damage Observations

After each test of Structure 1 (Tests 1-9) the walls were examined and
visual damage was recorded by IDF personnel. This damage included shear and

10

TABLE 3. FIELD OBSERVATIONS FOR TESTS OF IDF STRUCTURE 1.

Test No.	R[a] (ft)	W[b] (lbs)	Center Displ.[c] (in.)	General Description of Damage
Series A - surface burst, bare charge				
1	49.2	181	none	No cracking, no influence
2	32.8	181	0.2	No cracking
3	23.0	181	0.3	Wall: Very small cracks of 0.04 inches Ceiling: Cracks, same width, parallel to wall Floor: Cracks perpendicular to wall, 0.08 inches
4	16.4	181	0.6	Wall: Internal cracks up to 0.04 inches, Diagonal cracks in corners up to same. Shear cracks along perimeter wall widened (probable the horizontal cracks).
Series B - Surface burst, bare charges				
5	65.6	562	none	No cracking, no influence
6	49.2	562	none	Beginning of internal cracks
7	32.8	562	0.6	Internal and external cracks Inside: Horiz. cracks near center of wall of 0.08-0.12 inches. Diagonal cracks up to 0.04 inches.
8	23.0	562	1.0	Light interior scabbing. Pieces of 0.8-inch wide by 2.4-inch length thrown 4.6 feet. Interior cracks of 0.8 inches near center of wall
9	16.4	562	15.7 lower level of wall	Failure of wall due to shear at ground level. Displacement at ground level 15.7 inches. Heavy scabbing. Pieces thrown to opposite wall 20.4 feet

[a] R = Range of detonation from the wall
[b] W = Weight of the charge
[c] Accumulated residual center deflection of the test wall after each test.

flexural cracking and some minor scabbing on the inside surface. In addition, a straightedge was held vertically against the middle of the wall and the deformation from this straightedge at the midheight was measured relative to the ends. This damage is summarized in Table 3.

Figure 7 shows the cracking that had occurred on the outside surface of Wall 1 of Structure 1 after Test 4, and represents the cumulative effects of Tests 1-4. This cracking is typical of a yield line pattern that would occur in a slab that is uniformly loaded and fixed on the edges. The permanent deflection

TABLE 4.   FIELD OBSERVATIONS FOR TESTS OF IDF STRUCTURE 2.

Test	R[a] (ft)	W[b] (lbs)	Struct. /wall	General description of damage
Series C Surface burst, cased charges (MK-82)				
10	32.8	181	2/A	Outside: Depth of fragment penetration up to 8.7 inches. Inside: Scabbing (concrete cover) up to 1.2-2.4 inch depth. Pieces thrown up to 9.8 feet. Ordinary plaster on inside surface thrown. No influence on special plaster with adhesive agent
11	49.2	181	2/A	Very similar
12	32.8	181	1/C	Outside: Depth of fragment penetration up to 6.3 inches. Inside: No scabbing. No internal cracks. Concrete seems to be better in this structure.
Series D Surface burst, cased charges (GP/Is./500 kg)				
13	49.2	1100	2/B	Inside: Light scabbing in a small area. Outside: Fragment penetration to 8.7 inches. Ordinary plaster failed, no influence on special plaster. Roof parapet failed along 3.65 feet (not well detailed). Crater in ground 16.8 feet dia. and 3.65 feet deep.
14	32.8	1100	2/B	Outside: Fragmentation same as before. Inside: Heavy scabbing; pieces all over floor and signs of hitting opposite wall. Reinforcing bars bent 1.97 inches.
15	49.2	1100	1/A	Inside: No influence, no separation of concrete or more cracking. Outside: Craters in concrete up to 4.72 inches. Concrete in this structure looks better.

[a] R = Range of detonation from the wall
[b] W = Weight of the charge

measured after this test was 0.6 inch. The description in Table 3 indicates that some shear cracking had started to form. Cumulative spalling for successsive tests on the inside of Wall 1 of this structure is clearly shown in Figure 8.

Figure 9 shows the damage on the outside surface of Wall 2 of Structure 1 after Test 9, reflecting the cumulative effects of Tests 5-9. The damage was much more severe for this wall, because the pressure was much greater. Yield lines have occurred around the upper edges and sides of the wall, as would be expected from a slab fixed at the edges, but along the bottom complete failure has occurred. This failure would be characterized as a localized shear failure, and occurred where the reflected pressure was the greatest. The wall has deformed inward at the bottom approximately 16 inches.
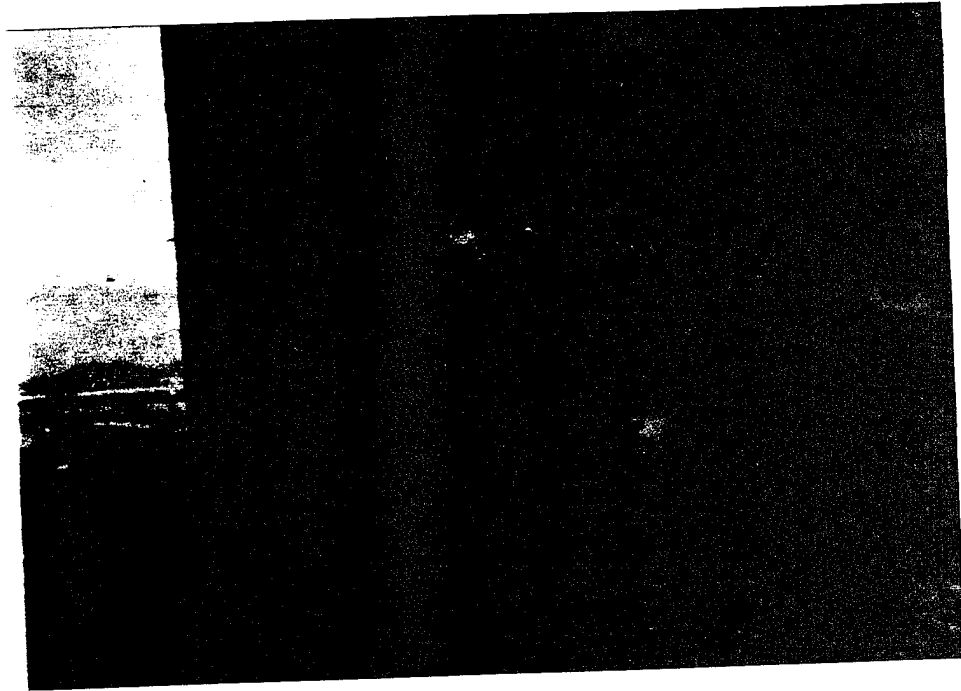
Figure 7. Cumulative Cracking of Wall 1 of IDF Structure 1 After Tests 1-4.
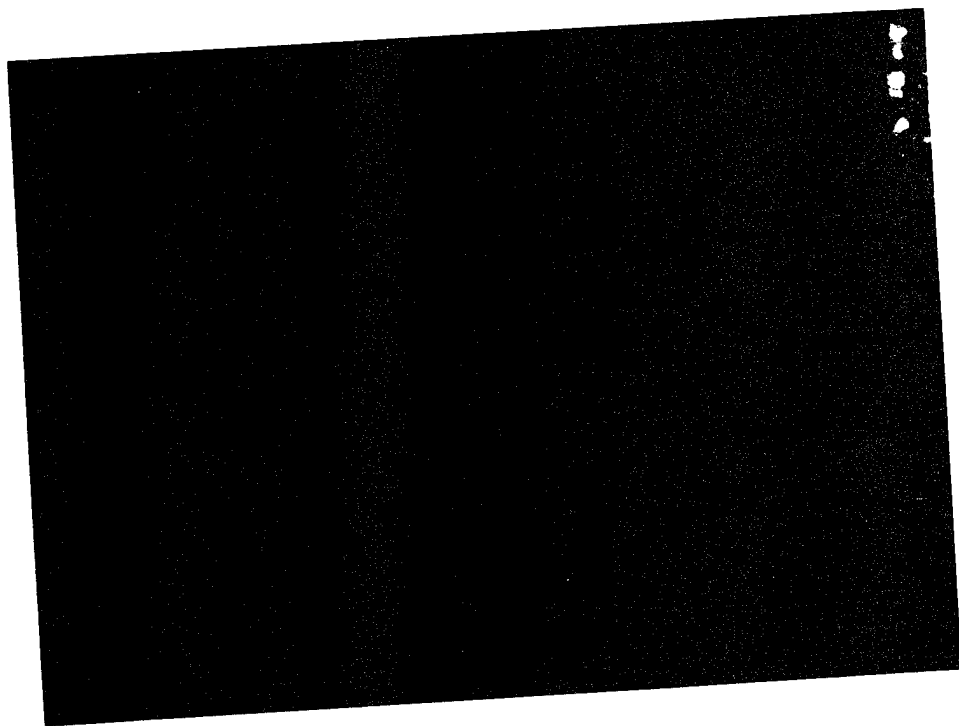
Figure 8. Cumulative Spalling of the Inside Surface of Wall 1 of IDF Structure 1 After Tests 1-4.
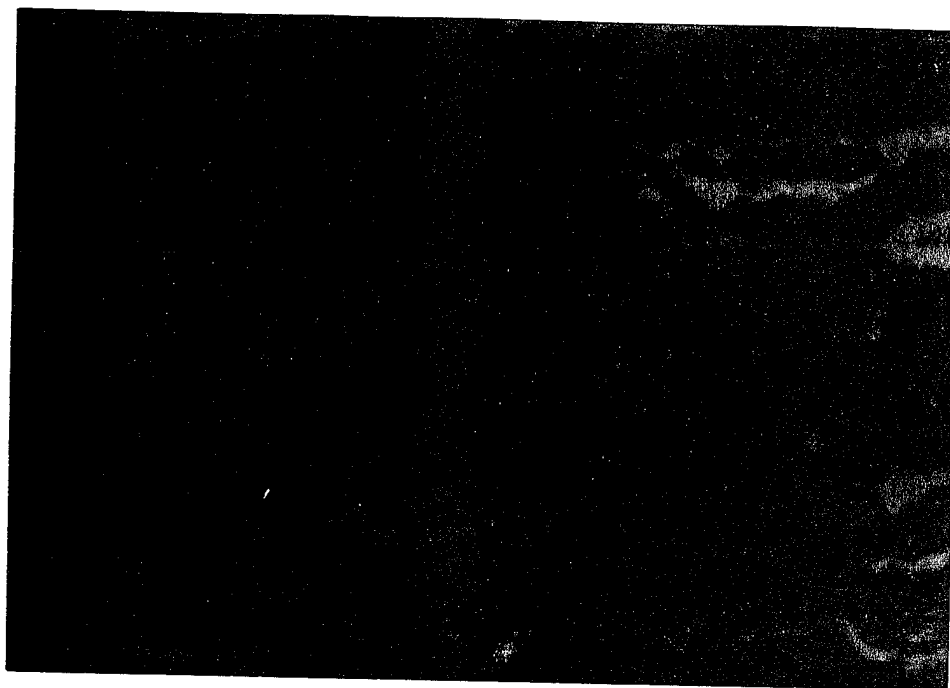
Figure 9. Cumulative Damage of Wall 2 of IDF Structure 1 after Tests 5-9.

The center deflections of the walls are the primary measurements that can be compared with analyses. There are two important points when comparing these measurements that must be remembered. First, they are cumulative measurements, so the damage that occurred in each shot was the difference between the deflection after the shot and what had accumulated before the shot. The wall suffered some damage in each test, so the resistance function was probably degraded as testing continued. Thus, in looking at successive shots, the pressure was increasing and the resistance was probably decreasing. Secondly, the measured deflections were residual values, and not maximum values that occurred. During the response, the wall deflects under the load, vibrates back and forth, and then comes to rest in a deformed position. Therefore, the analysis that is used must allow for inelastic behavior.

After each test of Structure 2 (Tests 10-15), the wall was examined for cracking and fragment penetration. In some tests "ordinary" and "special" plaster were placed on the inside surface of the wall, and the separation of the plaster from the wall was observed. Spalling of concrete on the inside surface was also observed. Flexural deflections of the walls were not recorded in these tests. The observations that were made are summarized in Table 4.

The most important information drawn from these tests is the extent of penetration of bomb casing fragments in the outer surfaces of the walls. Fragment penetration is a function of both the fragment size and the velocity with which it hits the wall, which is somewhat random. The sizes of the pieces that the casing happens to break into is variable, and the size that happens to

14

hit the wall is random. The crater size in the wall, as reported by IDF personnel, appears to be the deepest that occurred, rather than an average, or cumulative, quantity. Consequently, correlation of the crater size with wall properties and weapon properties is uncertain. Figures 10-12 show the extensive damage to the walls of Structure 2 that occurred from fragment penetration.

2.   Pressure Data

Four pressure measurements were made for each test as described in Section II.B, but some of the measurements were not usable. Three of the measurements were reflected pressures on the wall surface and the fourth was free field pressure beside the structure. These measurements are summarized in Table 5, and the corresponding plotted data are shown in Appendix A. The data had been reduced by the IDF personnel, and the arrival times, peak pressures, impulses, and durations of positive phases as reported by them, are also shown in Table 5.

To evaluate the accuracy of the data, the measurements were compared with theoretical values computed for the same charges at the same ranges. Calculations of peak-reflected pressures on the wall and of impulses under the reflected pressure curves were performed in three ways. First, the values were obtained from the computerized version of the plots in Reference 5. Secondly, they were obtained from a computer program called WALLPLOT that is distributed by the Omaha District of the U.S. Army Corps of Engineers (Reference 6). Finally, a third computer program, BLAST (Reference 7), distributed by the U.S.
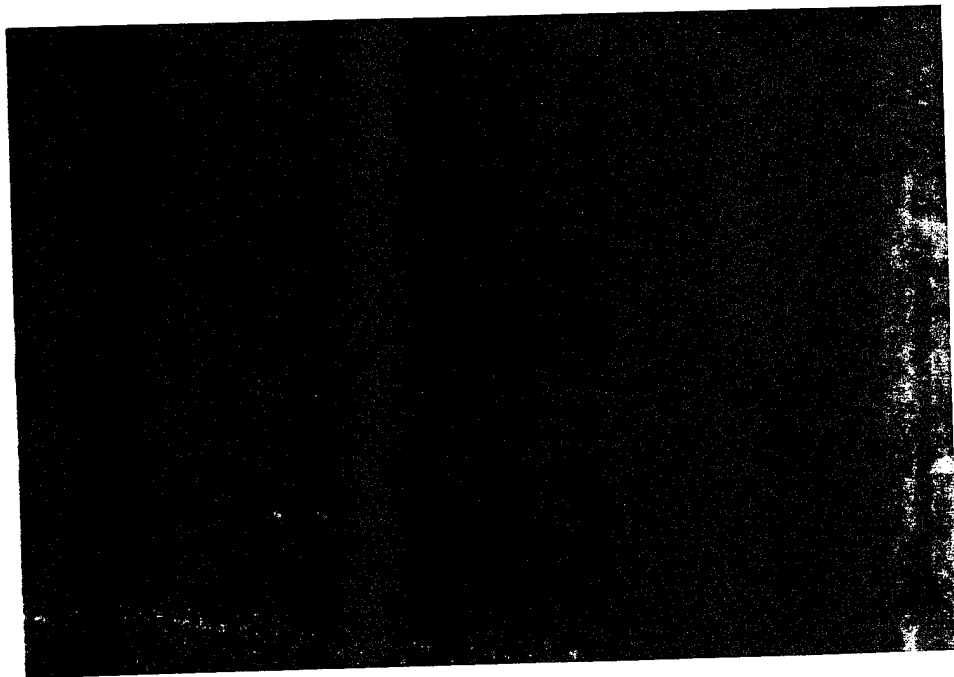
Figure 10.   Fragment Damage to Wall of IDF Structure 2.

15
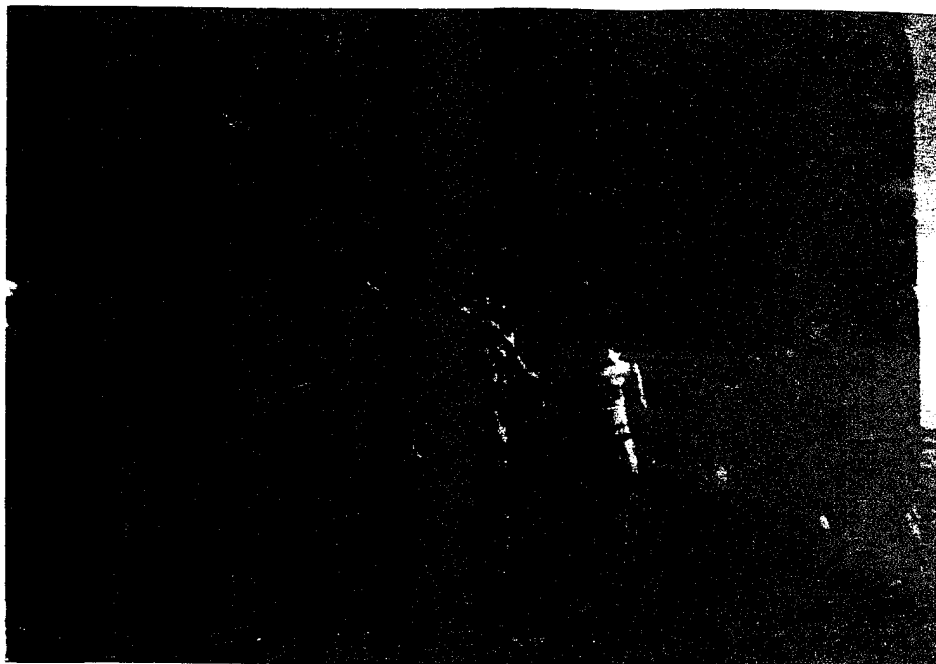
Figure 11. Fragment Damage to Wall of IDF Structure 2.

Figure 12. Fragment Damage to Wall of IDF Structure 2.

TABLE 5. PRESSURE MEASUREMENT DATA FOR IDF STRUCTURE 1.

Test	Range (ft)	Charge (lbs)	Gage[a] point	Arrival time(ms)	Pressure (psi)	Impulse (psi-ms)	Duration + phase(ms)
1	49.2	181	1	16.1	36.1	153.4	9.8
			2	16.6	31.4	108.2	8.6
			3	17.0	32.2	88.2	7.2
			4	16.6	19.7	50.1	7.45
2	32.8	181	1	7.29	197.3	217.2	4.8
			2	8.04	142.0	146.2	3.9
			3	8.33	125.0	128.2	3.9
			4	7.94	61.8	120.0	6.6
3	23.0	181	1	12.5	69.0	391.9	1.61
			2	13.4	282.6	210.6	2.65
			3	13.7	370.6	224.3	2.22
			4	13.2	152.0	224.3	8.0
4	16.4	181	1	2.36	2037	--	--
			2	3.0	393.0	88.8	0.81
			3	3.2	443.0	225.8	1.4
			4	--	--	--	--
5	65.6	562	1	18.5	44.0	149.1	11.5
			2	18.8	40.9	161.9	9.8
			3	20.1	41.9	163.3	11.2
			4	20.2	19.17	87.6	10.9
6	49.2	562	1	11.1	164.7	272.6	5.8
			2	11.5	160.5	264.1	5.6
			3	11.7	132.9	244.2	4.9
			4	11.2	53.25	145.0	6.75
7	32.8	562	1	4.8	705.7	573.7	2.75
			2	5.3	438.8	444.4	3.2
			3	5.4	322.3	316.6	3.0
			4	10.7	63.9	193.1	12.4
8	23.0	562	1	--	--	--	--
			2	--	--	--	--
			3	--	--	--	--
			4	7.5	107.2	369.2	13.3
9	16.4	562	1	--	--	--	--
			2	2.54	941.5	53.25	0.13
			3	2.36	1124.6	600.6	1.78
			4	6.2	144.8	305.3	9.5

[a] See Figure 5 for gage locations

Department of State, was used. Comparisons of reflected pressures and impulses as given by these several sources are shown in Figures 13-16.

Figure 13 shows the measured peak reflected pressures compared with the computed values for Tests 1-4. The computed values from the three sources agree quite well, and the measured values agree with the computed values at all ranges except the smallest. The lack of agreement at the closest range is quite large, and suggests that the measuring system may not be picking up the peak pressure accurately when it becomes very great. It is noteworthy that the computation procedures all assume spherical or hemispherical charge shapes, not cylindrical. This difference would likely result in discrepancies between measured and

17
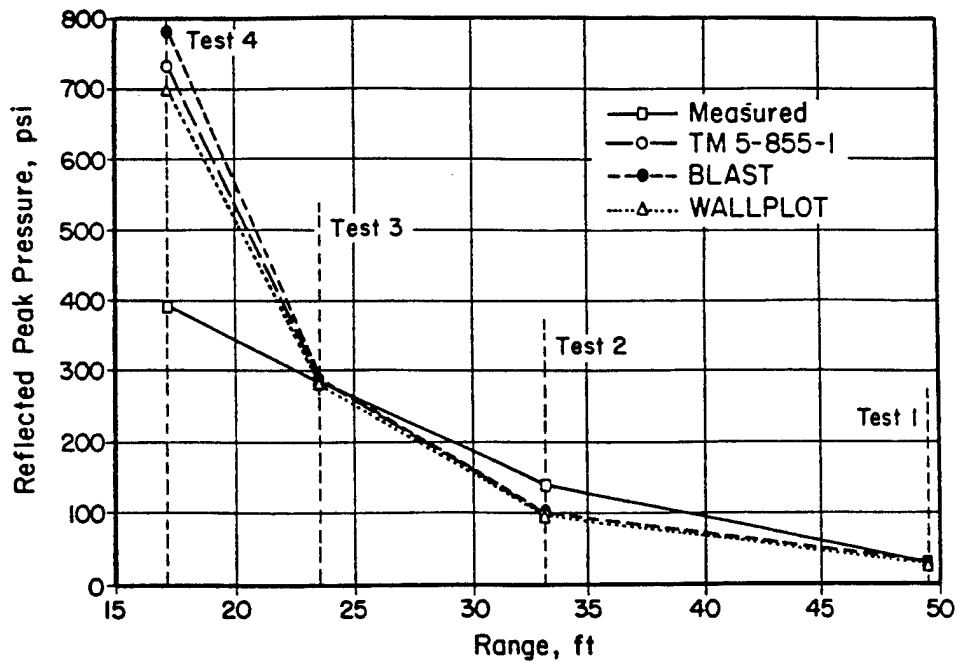
Figure 13.   Comparison of Peak Pressures at Center of Wall 1, IDF Structure 1, Tests 1-4.
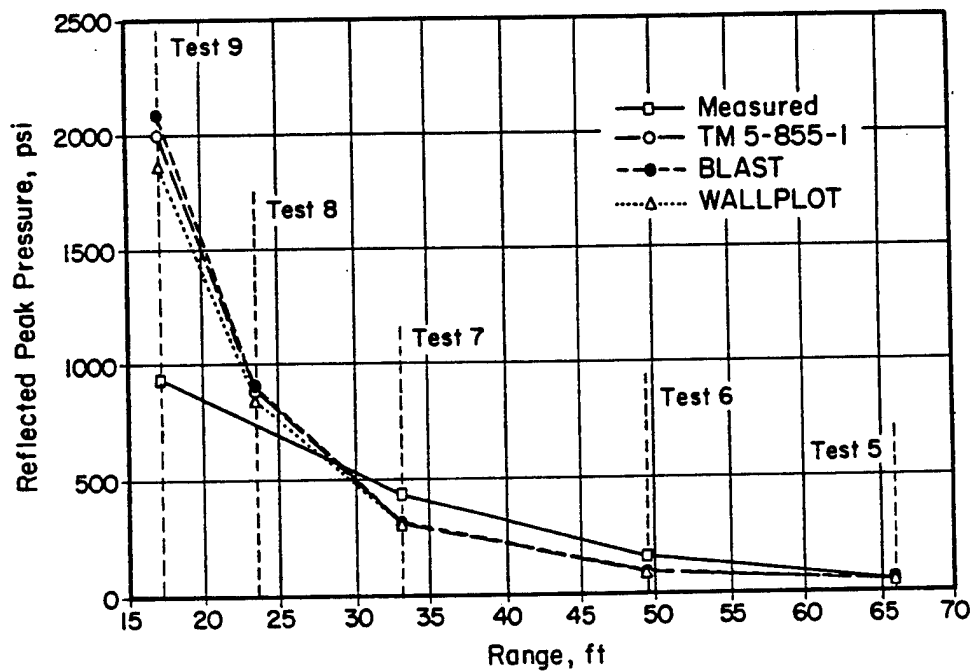
Figure 14.   Comparison of Peak Pressures at Center of Wall 1, IDF Structure 1, Tests 5-9.
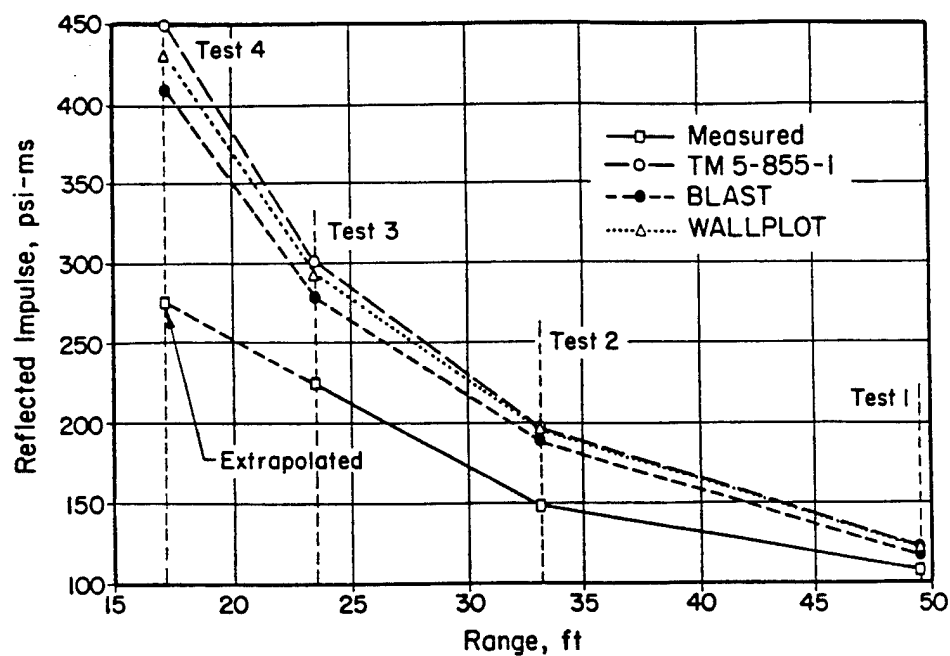
Figure 15. Comparison of Peak Impulses at Center of Wall 1, IDF Structure 1, Tests 1-4.
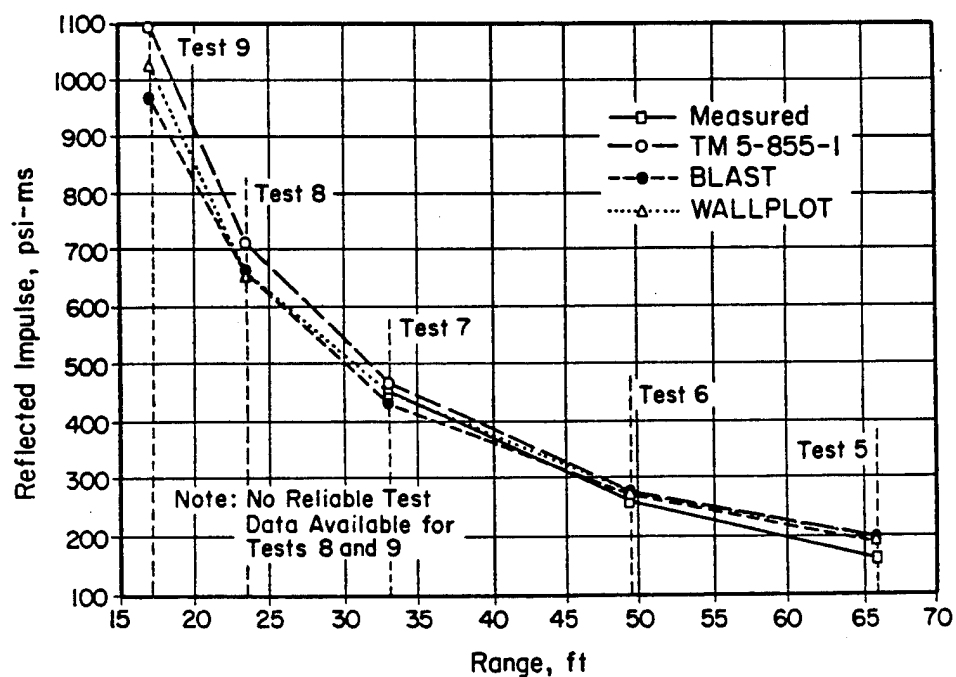
Figure 16. Comparison of Peak Impulses, Wall 1, IDF Structure 1, Tests 5-9.

19

calculated pressures; the discrepancies would be larger with decreased range. The same comparison for Tests 5-9 is shown in Figure 14, and appears to lead to a similar conclusion. The agreement is quite reasonable for all ranges except the closest. There were no usable pressure records for Test 8 at a range of 23 feet.

Figure 15 shows the measured impulse under the reflected pressure curves compared with the calculated positive phase impulse for Tests 1-4. The measured impulse is low relative to the calculated values throughout the range. For these tests the peak pressures were in agreement except for the closest range, so the source of this lack of agreement is not clear, but must depend on the shape of the pressure curve. It may result from the charge shape, which was actually cylindrical although it was assumed to be hemispherical in the calculations. Figure 16 shows the same comparison of impulse for Tests 5-9, and indicates good agreement for Tests 5-7, but the impulse for Test 9 is too low to be reliable, and impulse data for Test 8 are unavailable.

3. Acceleration Data

a. Data Quality and Issues in Data Reduction

The analytical procedures applied to Tests 1-9 deal with the displacement response of the walls to blast pressure. Consequently, the use of the acceleration data was limited to its use in determining the actual response of the test walls for comparison. This was done by integrating the acceleration records twice to obtain the displacement-time histories. The acceleration measurements are summarized in Table 6. The quality of the records varied greatly from fairly good to unusable. After discarding the obviously unusable records, various methods were investigated for processing those remaining for eventual comparison to the analyses performed in the remainder of the project. This section will discuss data quality, data processing, and the final records used for the analytical procedures.

During each test conducted on Structure 1, acceleration was measured at the center of the wall nearest the blast and at the base of the same wall. Acceleration measurements at ground level tend to show the effects of direct ground shock to a much greater extent than measurements made on the wall above the ground. This was found to be the case with these measurements. Consequently, only the measurements at the center of the wall were investigated for direct comparison with the observed results. Nine tests were conducted on the first structure, resulting in nine acceleration measurements for the center wall response.

The variance of the quality of acceleration records depended on a number of factors. The problems with the unusable records were caused by malfunctions in the measurement or recording equipment chain, or were due to false triggering of the recording channel, which caused the record to be taken at the wrong time. Of the nine records mentioned above, the record for Test 1 was unusable. There was no record for Test 9, because the accelerometer was removed from the wall and placed on a door.

20

TABLE 6. ACCELERATION MEASUREMENT DATA FOR IDF STRUCTURE 1.

Test	Range (ft)	ID of channel	Location on wall[a]	Sample rates (ms)	Frequency (Hz)	Gage cdlibration (pc/g)	Voltage range, +/- (Vol)
1	49.2	0107B3	7	20	50	1.0	0.5
		0107B4	7	50	20	1.0	1.0
		0108B5	8	50	20	20.6	0.5
2	32.8	0207B3	7	10	100	1.0	0.5
		0207B4	7	20	50	1.0	0.5
		0208A5	8	20	50	20.6	0.5
		0208B5	8	50	20	20.6	0.5
3	23.0	0307B3	7	5	200	1.0	2.0
		0307B4	7	10	100	1.0	2.0
		0308A5	8	20	50	20.6	2.0
		0308B5	8	5	200	20.6	2.0
4	16.4	0407B3	7	10	100	1.0	2.0
		0407B4	7	5	200	1.0	2.0
		0408A5	8	20	50	20.6	0.5
		0408B5	8	5	200	20.6	0.5
5	65.6	0507B3	7	20	50	1.0	0.2
		0507B4	7	5	200	1.0	0.5
		0508A5	8	20	50	20.6	1.0
		0508B5	8	5	200	20.6	1.0
6	49.2	0607B3	7	20	50	1.0	0.5
		0607B4	7	5	200	1.0	1.0
		0607D5	7	50	20	9.86	0.5
		0608A5	8	20	50	20.6	2.0
		0608B5	8	5	200	20.6	5.0
7	32.8	0707B3	7	20	50	1.0	0.2
		0707B4	7	5	200	1.0	0.5
		0707D5	7	50	20	9.86	0.1
		0708A5	8	20	50	20.6	0.5
		0708B5	8	5	200	20.6	2.0
8	23.0	0807B3	7	10	100	1.0	0.5
		0807B4	7	5	200	1.0	1.0
		0807D5	7	50	20	1.0	2.0
		0808A5	8	5	200	20.6	1.0
9	16.4	0907B3	7	5	200	1.0	2.0
		0907B4	7	2	500	1.0	2.0
		0907D5	7	10	100	1.0	2.0

[a]see Figure 5 for gage locations

For the remaining test records, the quality of the data varied depending on the sampling rate of the digitizing process and the maximum value of the recorded data compared to the full-scale setting of the digitizing equipment. The sampling rate determines the total time length of the resulting record, so if the sampling rate was set too high, the recording time was too short to represent all of the desired response motion; if the sampling rate was set too low, the data samples would not have enough resolution to resolve the high frequency peaks in the blast-induced motions. The ratio of the actual measured

maximum acceleration value to the full-scale setting of the digitizer determines the number of digital steps which are available to represent the data.

The data were digitized using 6-bit analog-to-digital (A/D) converters which provide 64 digital steps from plus full scale to minus full scale, or 32 steps from zero to either maximum; if the maximum value of the recorded data falls below the full-scale range, there will be proportionally fewer digital step values to represent the data. For example, if the maximum value of the recorded data is 50 percent of the full-scale setting of the digitizer, the number of steps available to resolve the data is only 32, so if the instrumentation setup is not optimum for each channel, the quality of the data drops rapidly. Also, if the maximum value of the data falls above the range, then the maximum data is cut off. In blast loading tests, much engineering judgment is required when setting up test instrumentation to determine the optimum settings for sampling rate and range, because there is only one chance to acquire the data for each test and blast test response is not easily predicted. These settings are most often based on previous experience and best estimates of the expected response values.

Figure 17, recorded in Test 5, is typical of the better quality acceleration records. The time length is sufficient to show the apparent free vibration response of the wall. Also, the maximum amplitude of the data is a large percentage of the full-scale setting of the digitizer (i.e., 400 g peak-to-peak). In this case, the digital steps are noticeable, but are still small compared to the maximum value of the data.
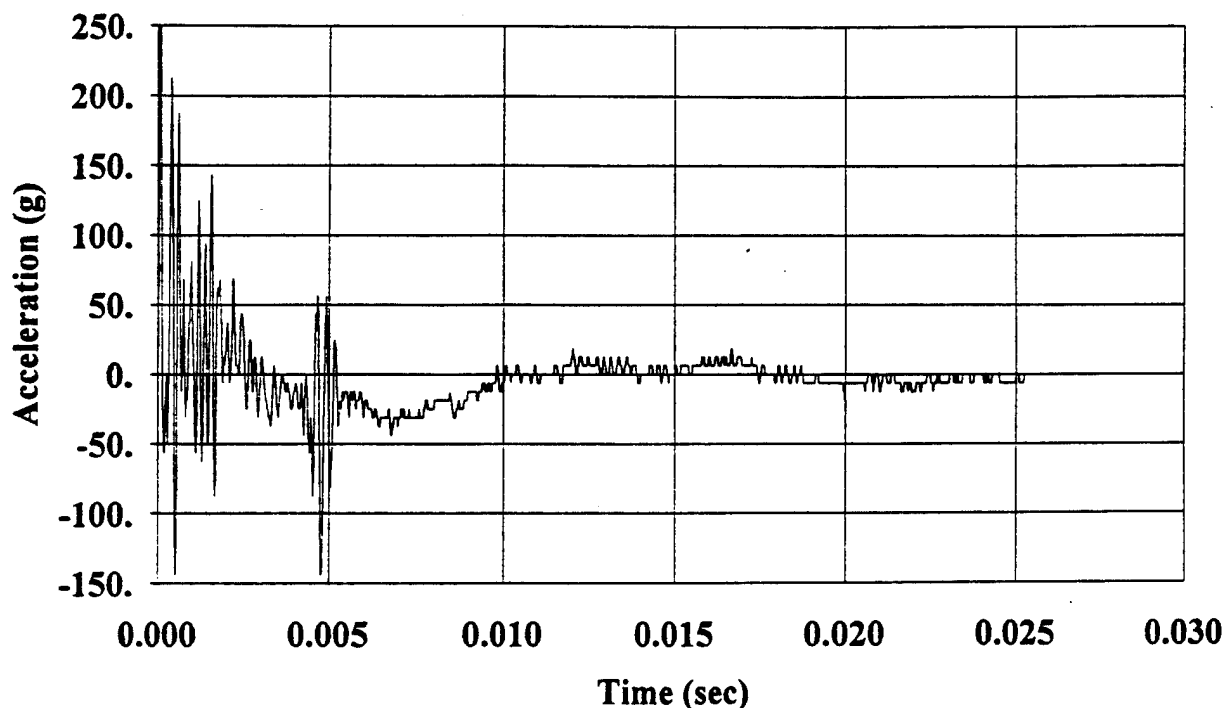
Figure 17. Typical Better Quality Acceleration Record, IDF Structure 1, Test 5.

22

Figure 18, from Test 3, is typical of the poorer quality records. The total time length of the record is short, approximately 0.007 seconds, which is not long enough to show the apparent free vibration response. The full-scale setting of the digitizer was 4000 g, but the maximum value of the recorded data was less than 1000 g. As a result, the digital steps are much more noticeable and are a much larger percentage of the maximum value of the data. This record was still considered to have sufficient quality to warrant further processing.

Figure 19, recorded in Test 1, is typical of the unusable records. The maximum value of the data is very small, compared to the full-scale setting of the digitizer (i.e., 2000 g peak-to-peak), so the digital step size is approximately 50 percent of the maximum value of the data.

b.   Comparison of Data Reduction and Filtering Methods

The basic objective in analyzing the acceleration records was to double-integrate them to produce displacement records for comparison with the calculated and measured displacements. Numerical integration routines are very sensitive to small errors in the original data, so the procedures employed to process the acceleration data had to be evaluated carefully to prevent the processing from introducing errors which would obscure the actual deflections of the structure. This section discusses filtering, baseline correction, baseline shifting, and the procedures finally chosen to process all the acceleration records.

The first procedure investigated was low-pass filtering. A digital filter was designed with a cutoff frequency set at 10 percent of the sampling frequency. The effect of this filter is to remove information from the data above the cutoff frequency. For example, if the data were sampled at 50,000 hz, the filter would remove information above 5000 hz. The objective was to remove high frequency noise from the data and to smooth the effects of the digital steps. Figures 20 and 21, from Tests 2 and 5, illustrate the effects of low-pass filtering. In each figure, the plots on the left show the unfiltered data and the plots on the right show the filtered data. The top plots are the acceleration traces and the remaining plots are the integrated velocities and displacements. The plots clearly show that the filtering had no significant effect on the integrated results, so filtering was dropped from consideration to reduce data processing time and to remove the possibility of filtering out some real response from the data.

Acceleration records normally have to be corrected somehow before they can be integrated. This is necessary to correct for any small initial offset or long period drift that may have occurred in the original recording process. Even though these effects are normally small in the original data, they can have a significant impact on the integrated result. Two correction methods were investigated. The first was baseline correction, or rotation, in which a linear regression is performed to determine any long period trend in the data which is then subtracted from the original data. This has the effect of rotating the data record about the point where the regression line crosses the zero baseline. This tends to force the initial and final acceleration, velocity, and displacement

23
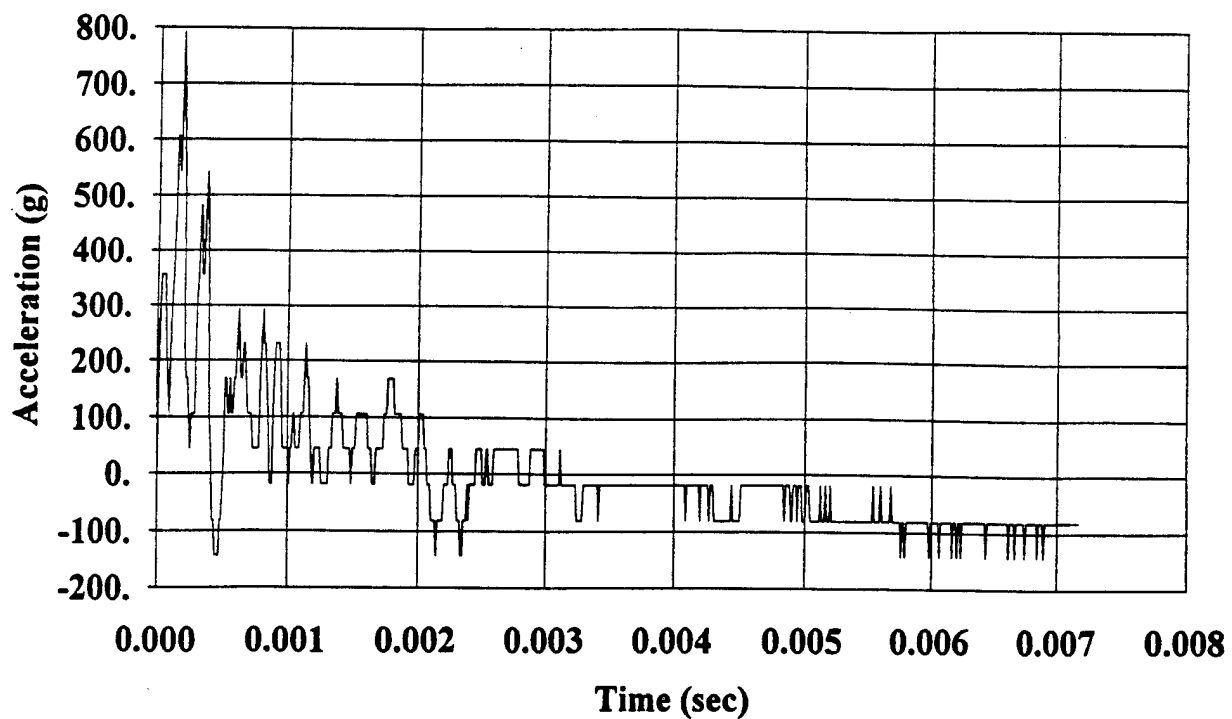
Figure 18.   Typical Poor Quality Acceleration Record, IDF Structure 1, Test 3.
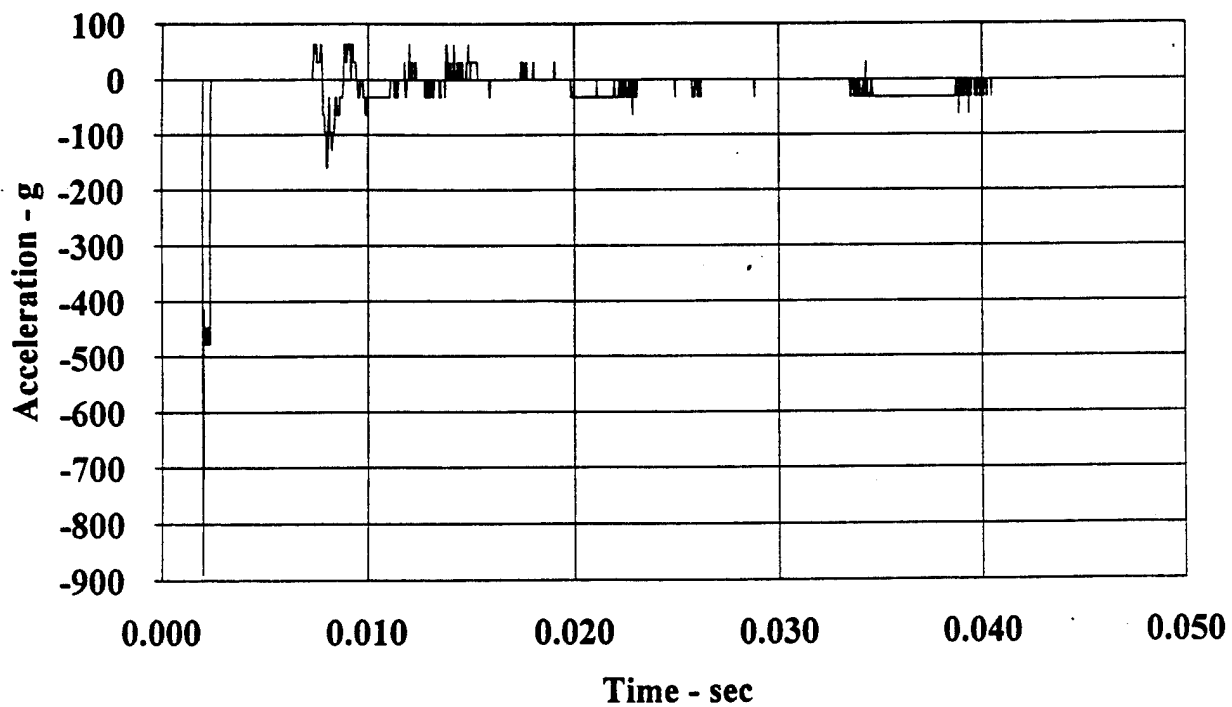
Figure 19.   Typical Unusable Acceleration Record, IDF Structure 1, Test 1.

24
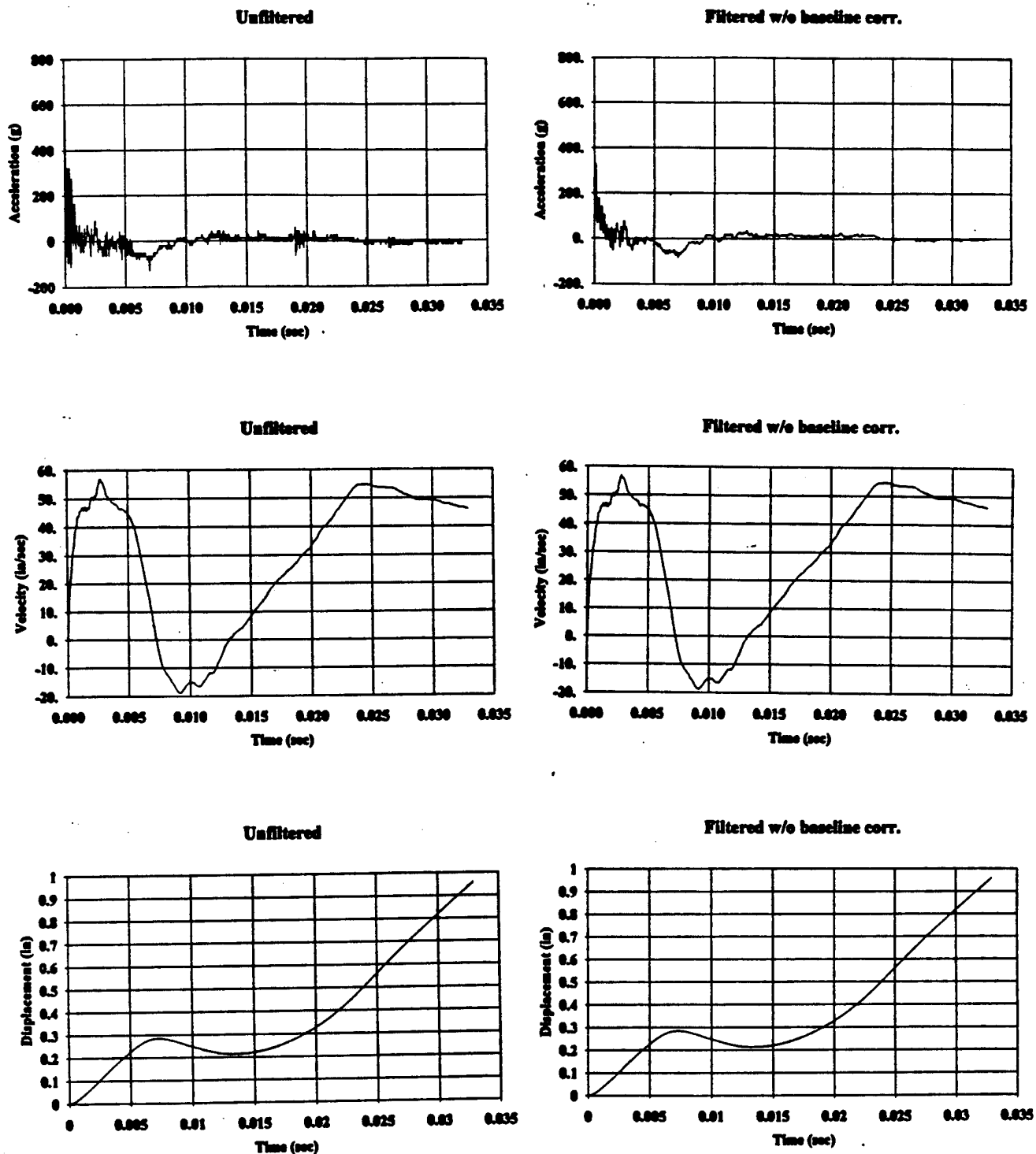
Figure 20.   Effects of Low-Pass Filtering, Test 2, IDF Structure 1.

25
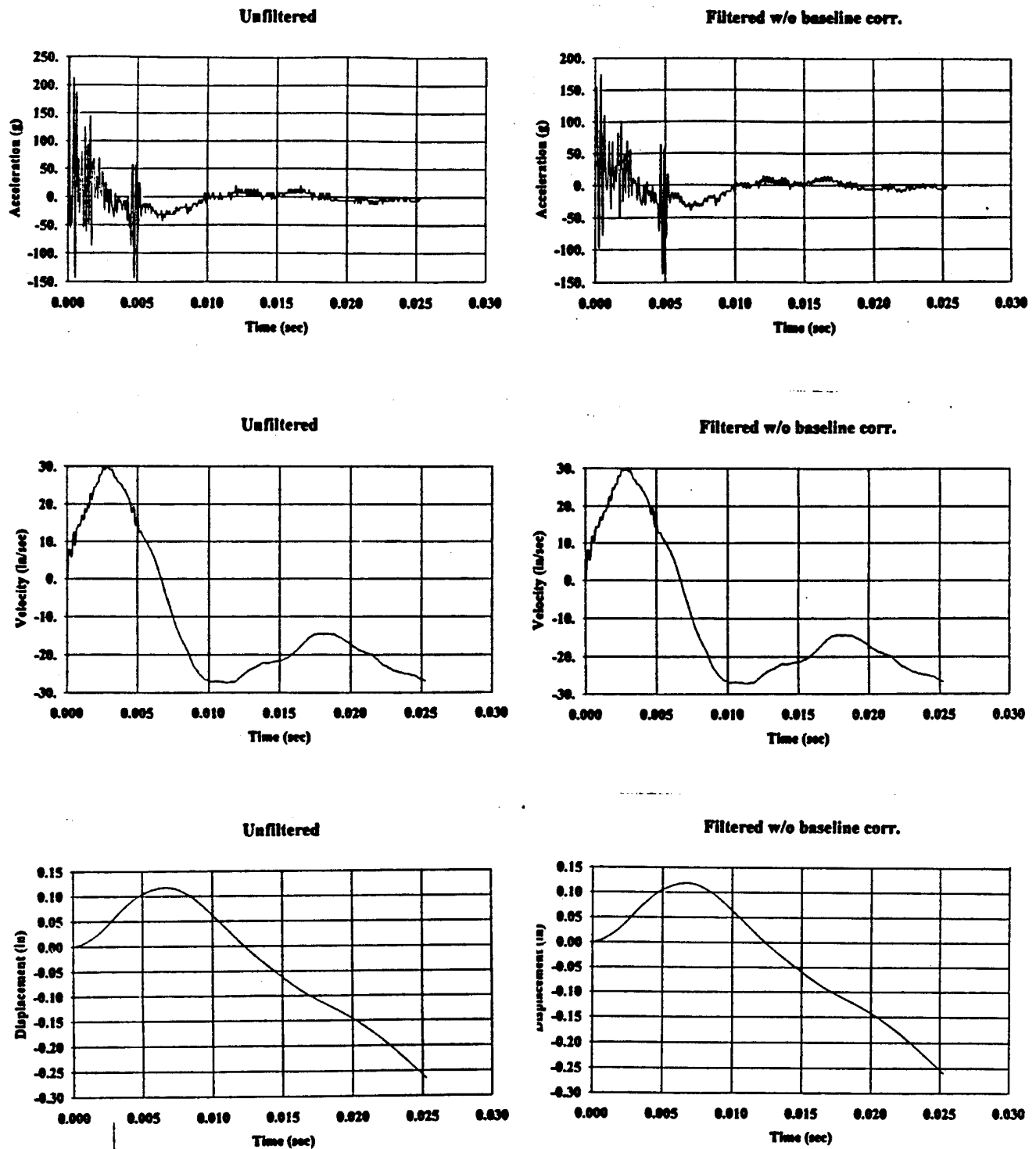
Figure 21. Effects of Low-Pass Filtering, Test 5, IDF Structure 1.

toward zero. This method is commonly used in seismic analysis, where the accelerations normally start and end at zero and are usually symmetrical about the zero baseline. But this is hard to justify for blast-induced acceleration where there is normally an instantaneous acceleration at the time the blast wave impacts the structure and the data are not normally symmetrical about the zero baseline. If there is a permanent deformation in the actual structure, baseline correction will tend to obscure this in the integrated displacement by tending to force the final displacement toward zero. Figures 22 and 23, from Tests 2 and 5, show the effects of baseline correction. In each figure, the left plots are the uncorrected data and the right plots are the corrected data. The downward and upward trend lines are evident in the left hand velocity and displacement plots and the trend removal is evident in the right hand plots, but the displacements are clearly being forced to zero at the end of the records.

Figures 24 and 25, also from Tests 2 and 5, illustrate the effect of baseline translation, the second correction method investigated. In this method, a constant is added to the record to shift it up or down before being integrated. This method seems to produce more reasonable results and was the method chosen to process all of the final data records. The criterion used for the correction was that the final velocity be zero or at least tending toward zero if the record was not long enough to show the complete response. This criterion indicates that the structure will eventually come back to rest after the impact. A second criterion applied to the integrated data related to the timing of the peak deflection. For the tests in which the response was elastic or nearly so, the peak should be reached in approximately one-fourth of the lowest natural period of the wall section; this period should tend to increase after repeated tests, and the time to peak should increase when plastic deformations occurred. These figures show the same records used in the previous figures, with the left plots being the uncorrected data and the right plots being the corrected data. In Figure 24 the velocity and displacement both come back to zero, but for this test there was no observed permanent displacement in the wall. In Figure 25 the velocity comes back to zero, but the displacement shows a permanent displacement which corresponds approximately with the observed permanent displacement in the wall.

Figure 26 shows the effect of recording the same accelerometer at two different sampling rates for Test 2. The left plots are at the higher sampling rate. Both records give the same general result, except that the higher sampling rate gives a shorter time record which is not long enough to show the final zero velocity. Because they are very similar, the longer one was used to apply the baseline translation correction, because more information was available to justify the correction criteria.

Figure 27 shows the general consistency of the correction method when applied to the same accelerometer in two successive tests. Tests 6 and 7 are in the same test series at successively higher load levels. Test 6 is on the left and Test 7 on the right. The peak acceleration, velocity, and displacement increase as the load level increases.
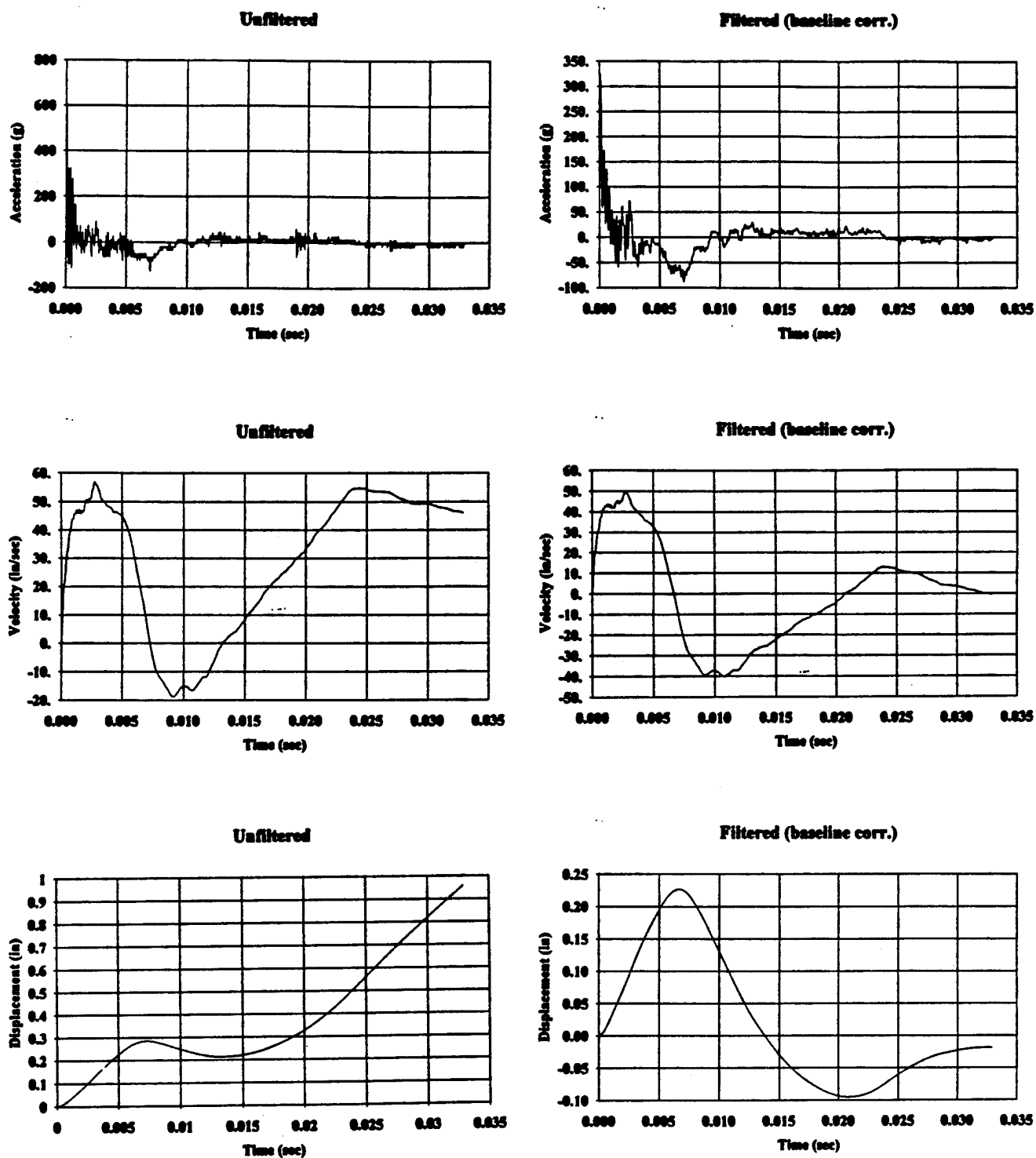
Figure 22.   Effects of Low-Pass Filtering and Baseline correction, Test 2, IDF
             Structure 1.

28
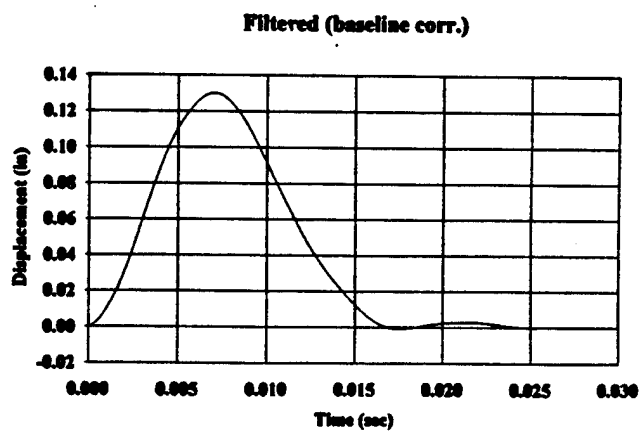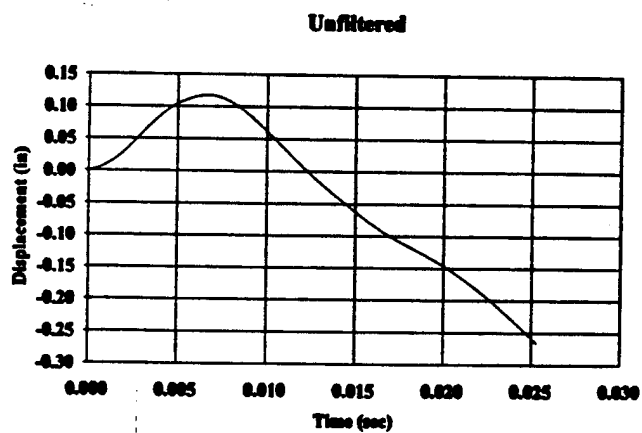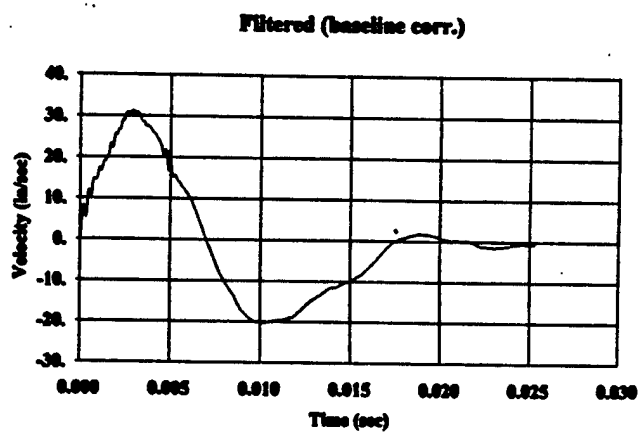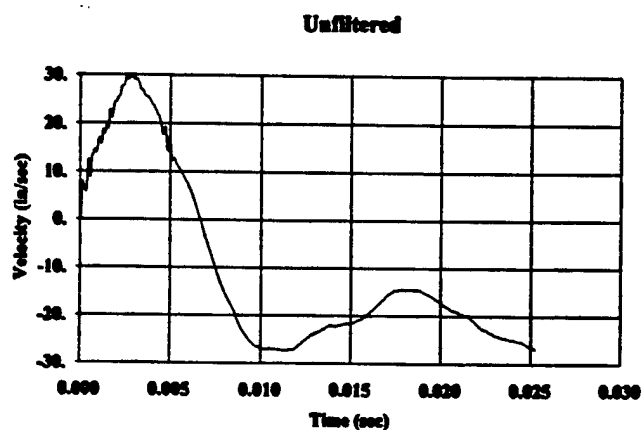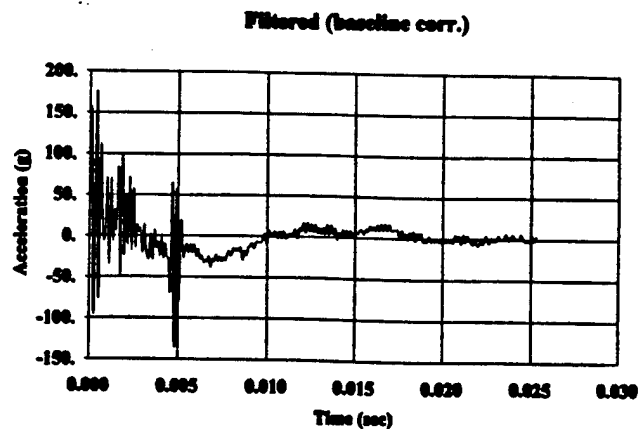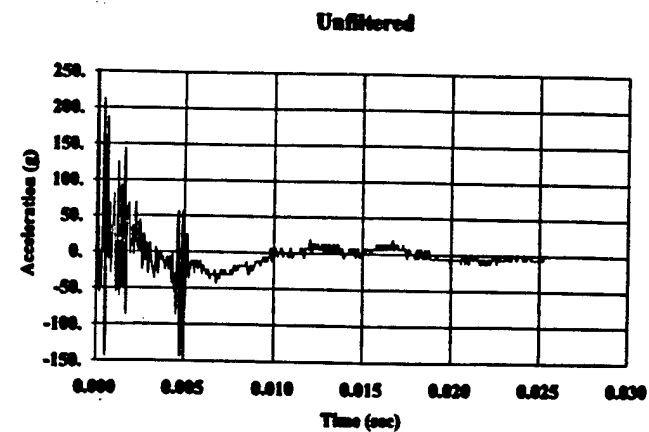
Figure 23.   Effects of Low-Pass Filtering and Baseline Correction, Test 5, IDF
Structure 1.
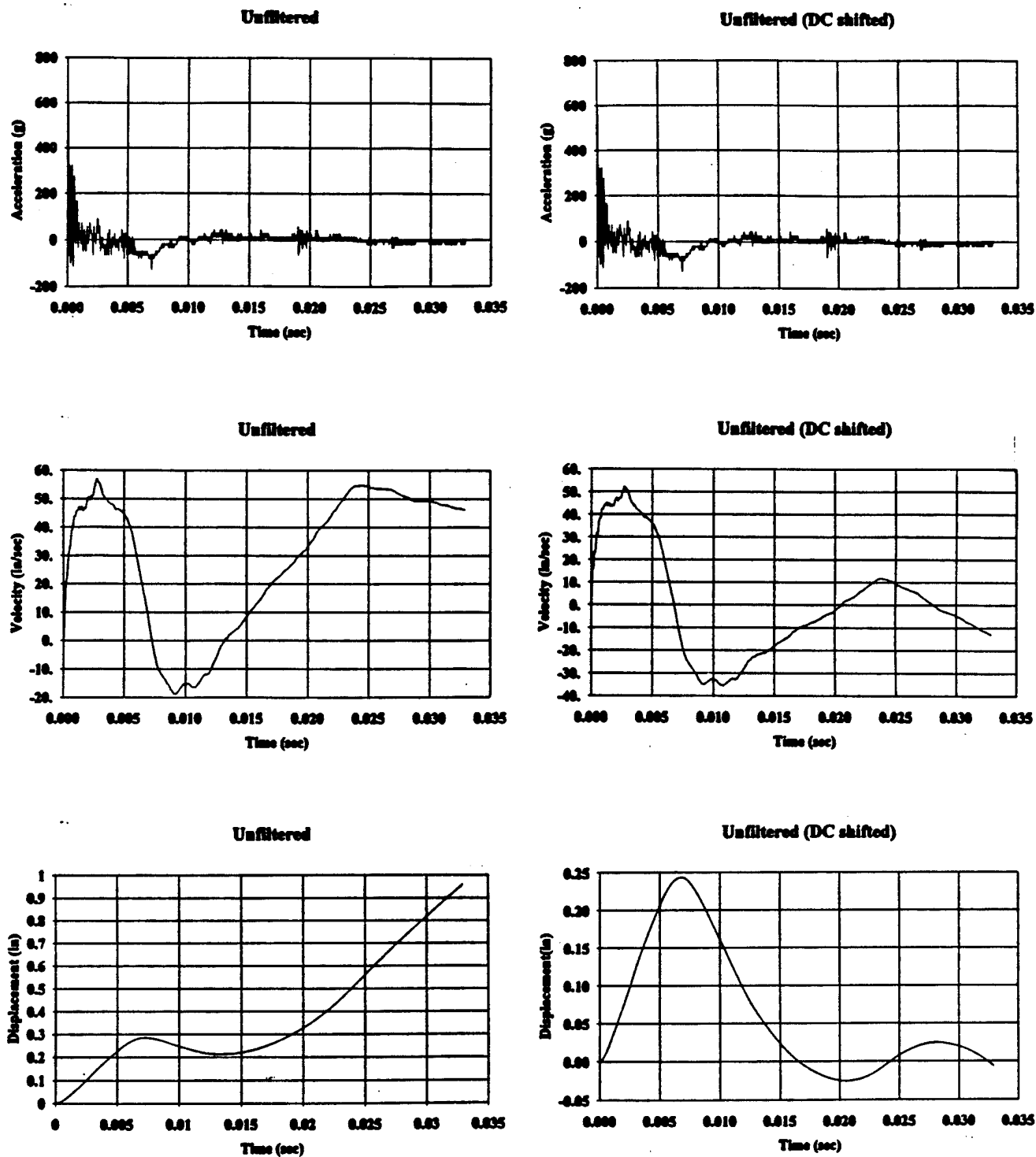
Figure 24. Effects of Baseline Correction, Test 2, IDF Structure 1.
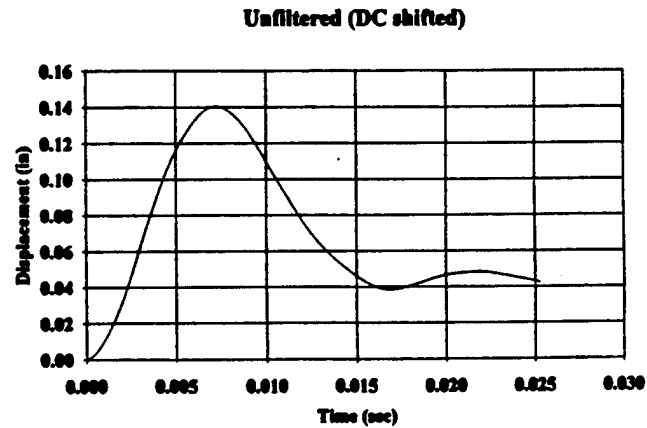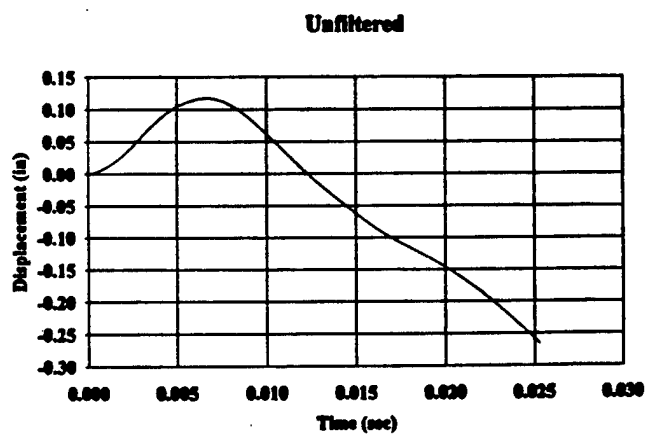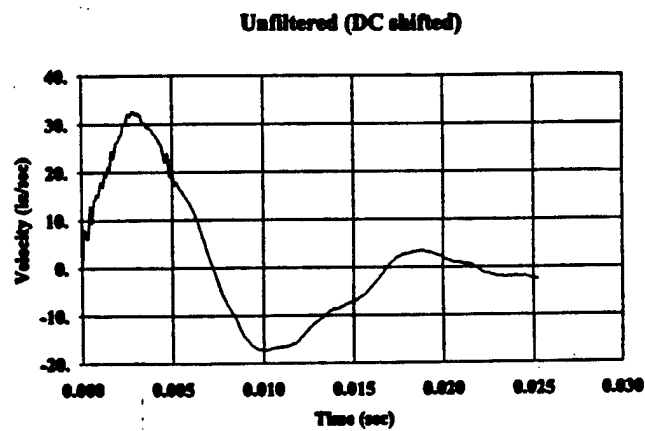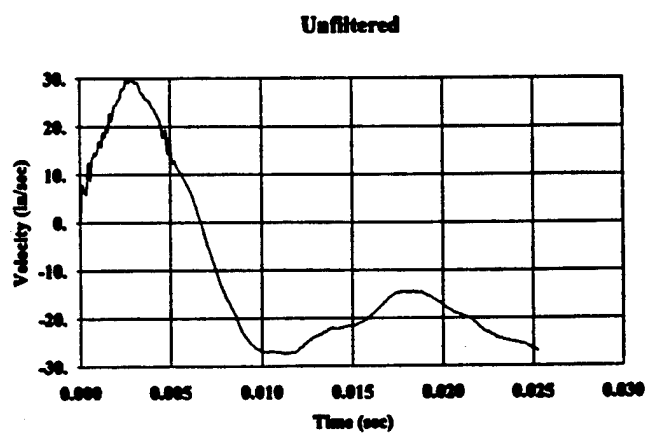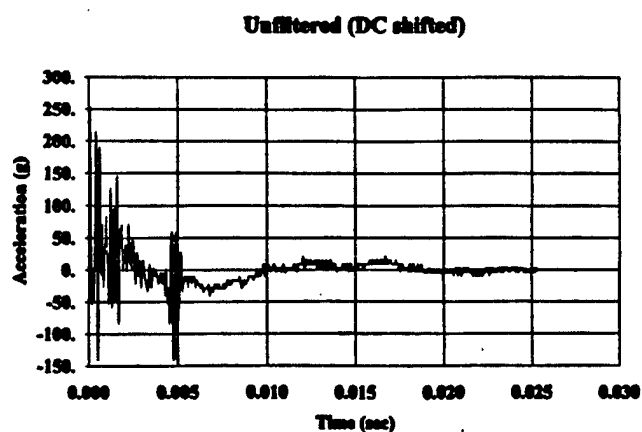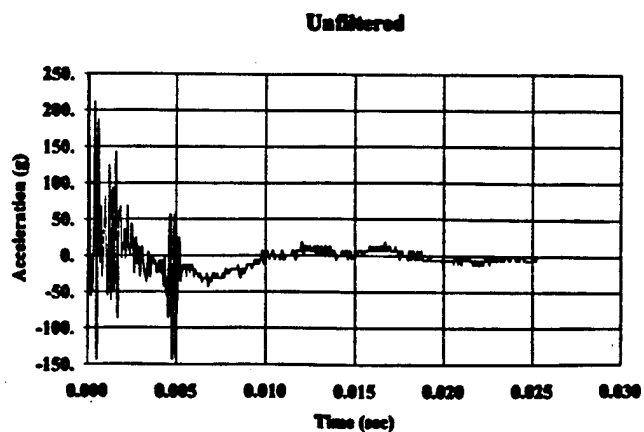
Figure 25. Effects of Baseline Correction, Test 5, IDF Structure 1.
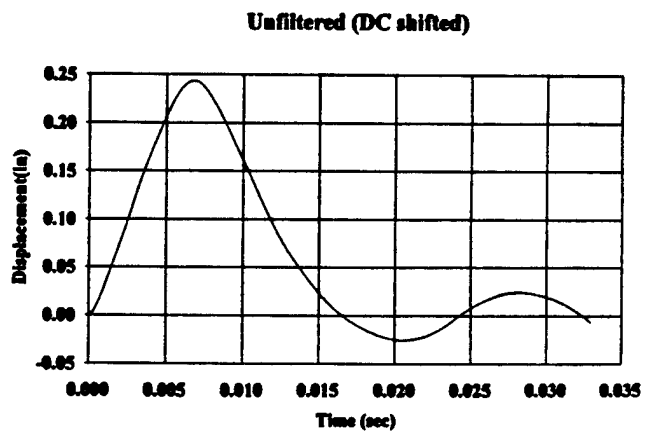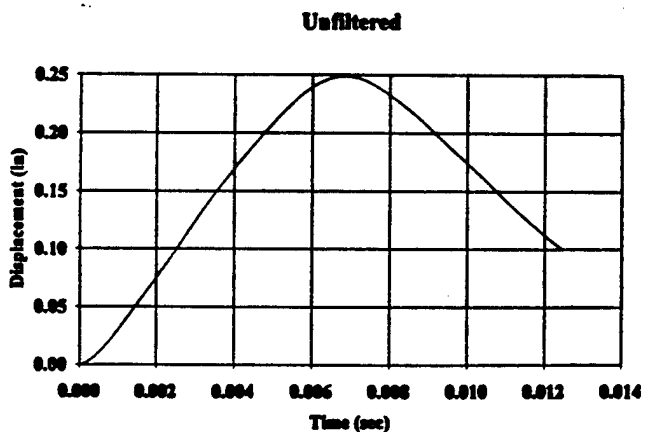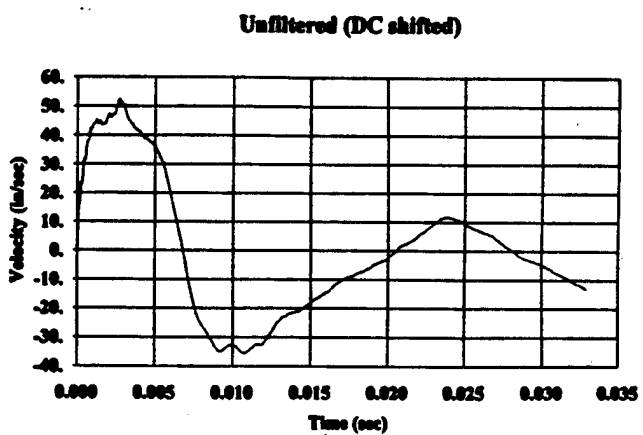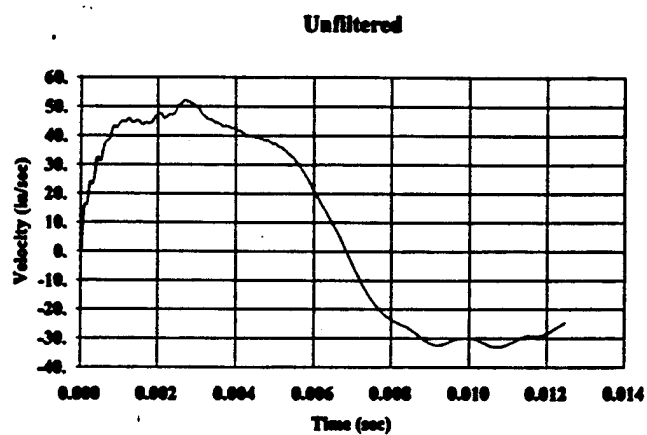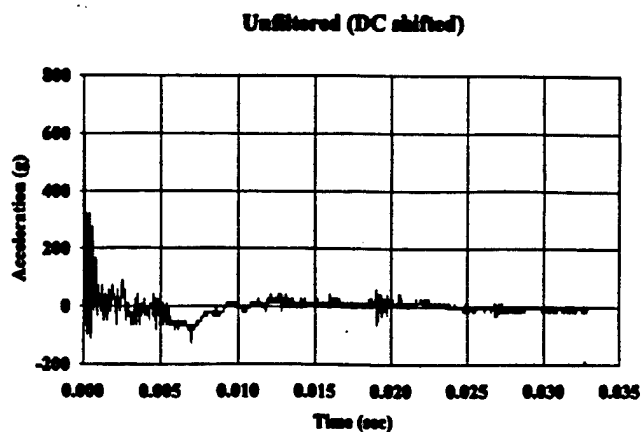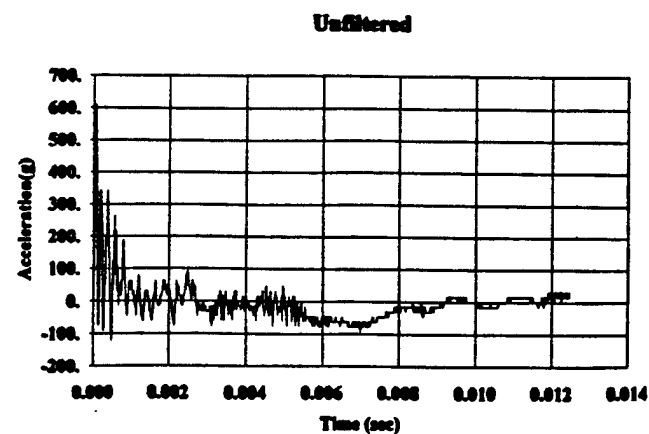
Figure 26.   Effects of Sampling Rate, Test 2, IDF Structure 1.
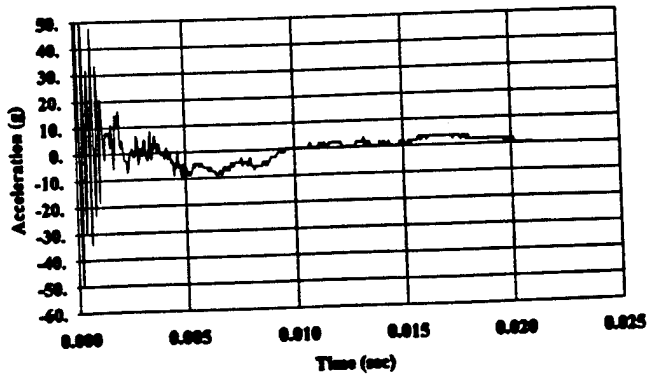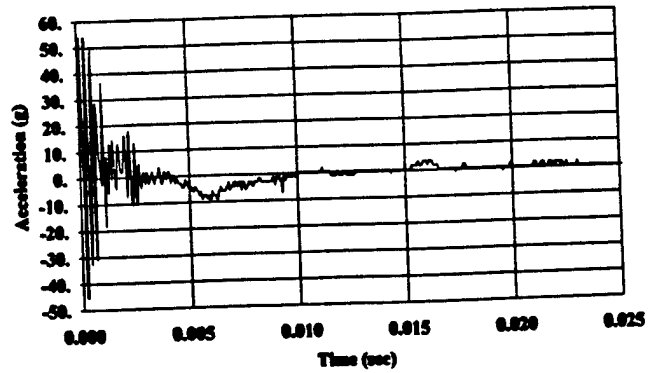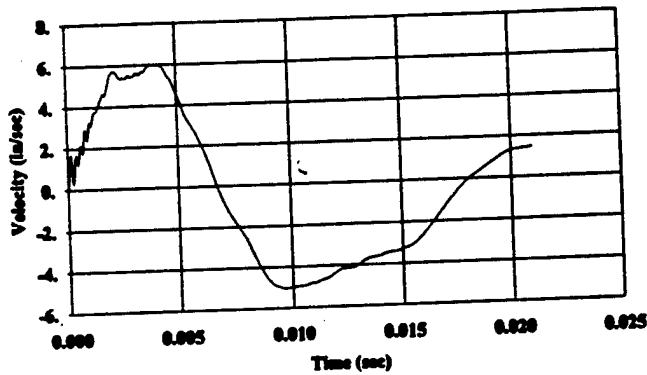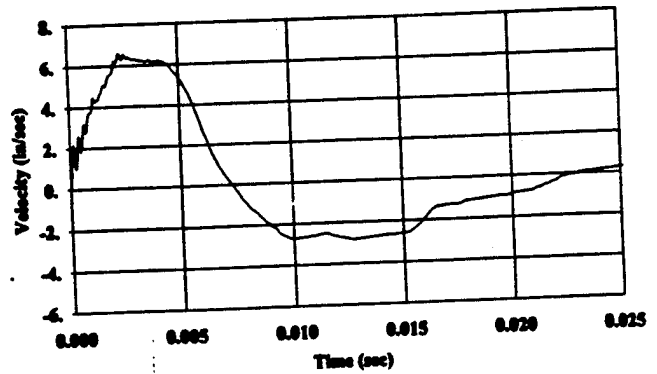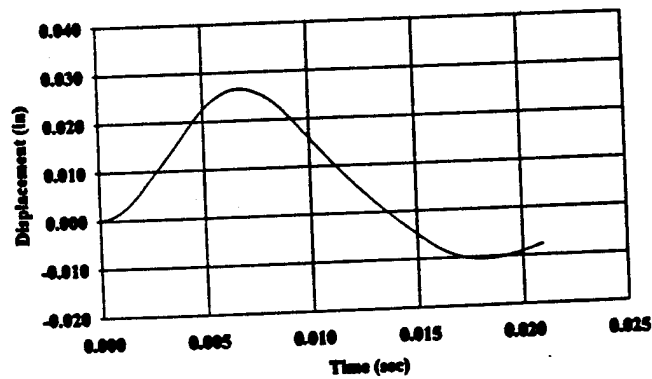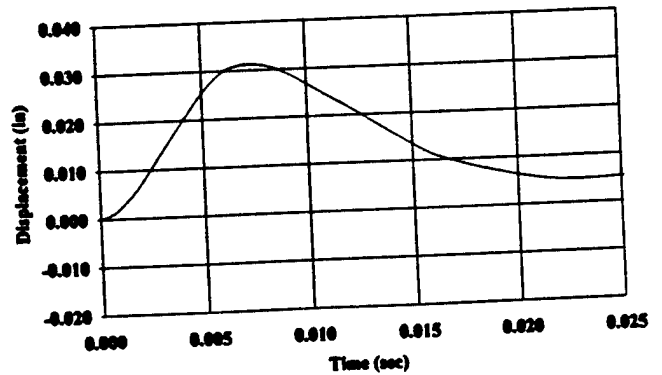
Figure 27. Consistency of Results for Two Successive Tests.

c.   Results of Integration of the Acceleration Records

Table 7 presents a summary of the baseline shifts and resulting peak deflections of the slab for all of the records investigated. The records were divided into three groups; for each group the same correction seemed appropriate. The correction used was a translation of the baseline. Selection of the baseline translation was based on a trial and error process in which the effect of translation on the final velocity, time to peak displacement, and value of peak displacement were observed. The main criterion was final velocity, but in some cases the record was not long enough to evaluate this criterion. Table 7 lists the groups in which the records were divided, the peak velocity and displacement values, and the time required to reach the peak displacement. Figures 28-34 show the corrected acceleration record, velocity-time history, and displacement-time history for each test that had usable records.

TABLE 7.   SUMMARY OF BASELINE CORRECTIONS FOR ACCELERATION RECORDS AND PEAK DISPLACEMENTS AFTER INTEGRATION.

Channel ID	Peak velocity (in./sec)	Peak displacement (in.)	Half period (ms)	Quarter period (ms)
Point B[a] (DC voltage shifts are constant at 24.3)				
0207B4	53	0.24	7	7
0307B4	100	0.62	7.5	5.5
0407B4	130	0.73	8	8
Point B[a] (DC voltage shifts vary from 22.6 to 23.7)				
0507B3	33	0.14	7.5	7.5
0607B3	68	0.33	7.5	7.5
0707B3	130	0.70	7.5	7.5
0807B3	275	---	8	---
Point D[a] (DC voltage shifts relatively high, around 30)				
0607D5	6	0.26	7	7
0707D5	6.3	0.32	7.5	7.5

[a]See Figure 5 for gage locations, Point B = location 7 and Point D = location 8

34
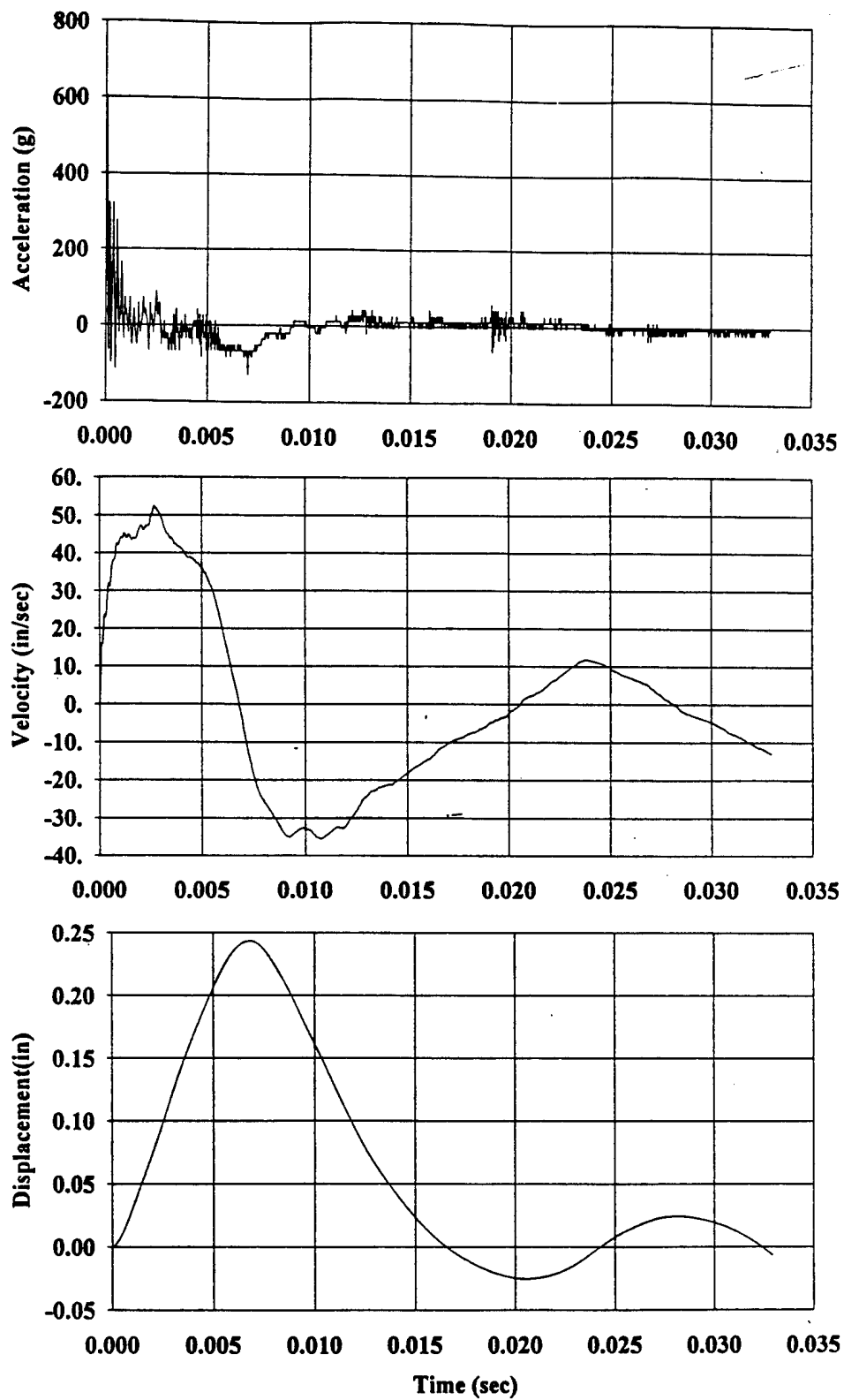
Figure 28. Double Integration of the Acceleration Record at Point 7 in Test 2
of the IDF Structures.
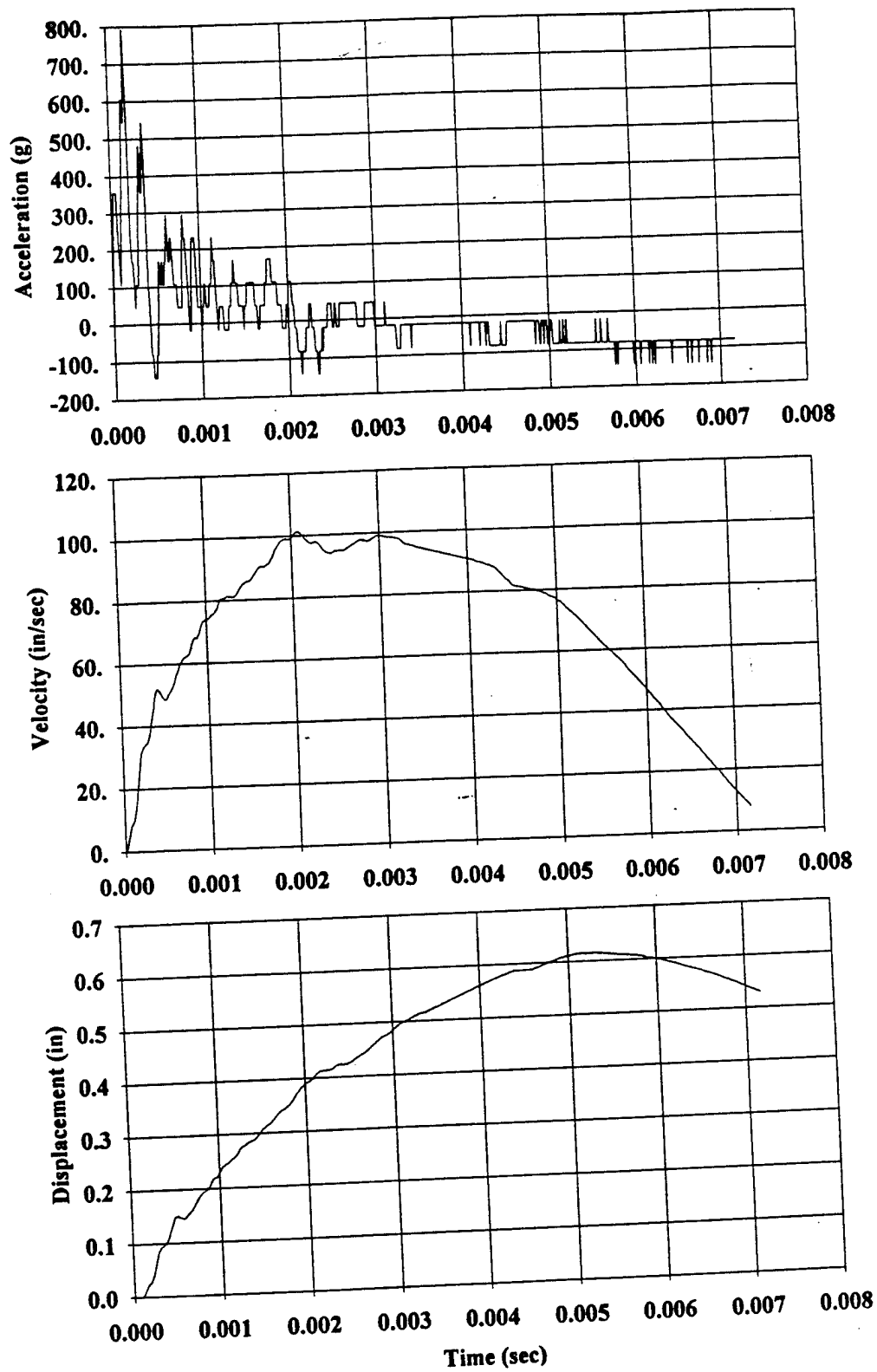
Figure 29. Double Integration of the Acceleration Record at Point 7 in Test 3
of the IDF Structures.
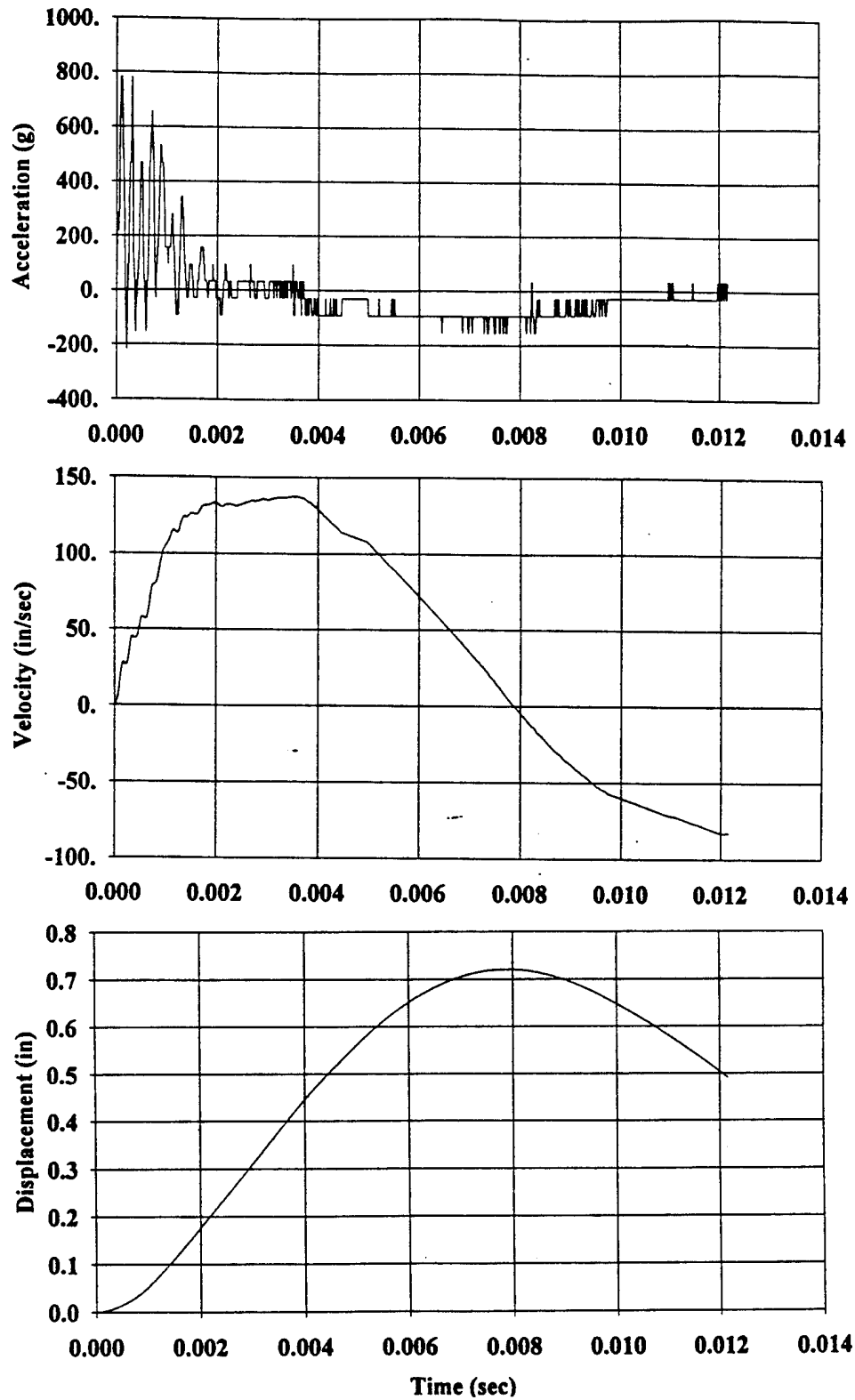
Figure 30. Double Integration of the Acceleration Record at Point 7 in Test 4 of the IDF Structures.
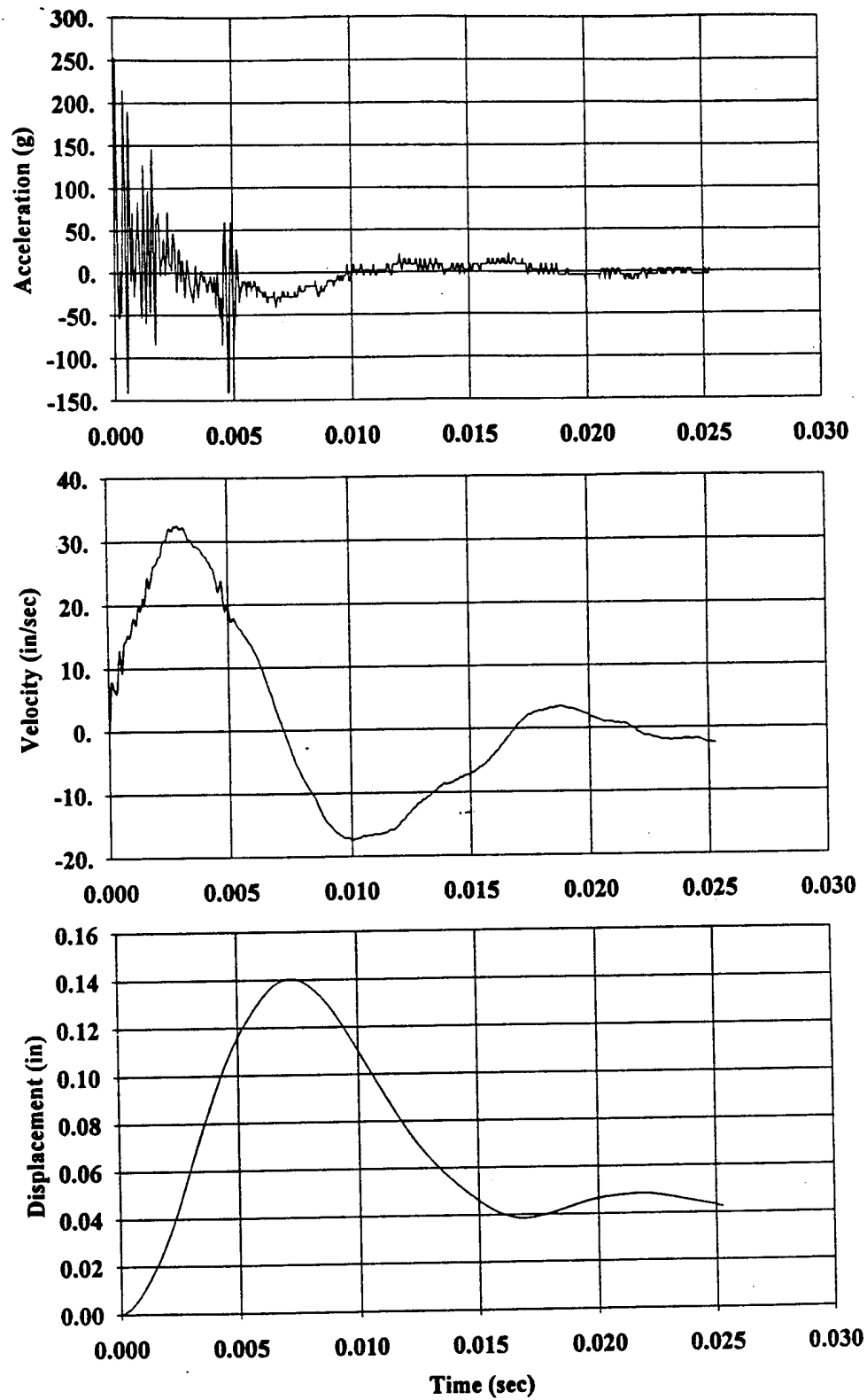
Figure 31. Double Integration of the Acceleration Record at Point 7 in Test 5 of the IDF Structures.
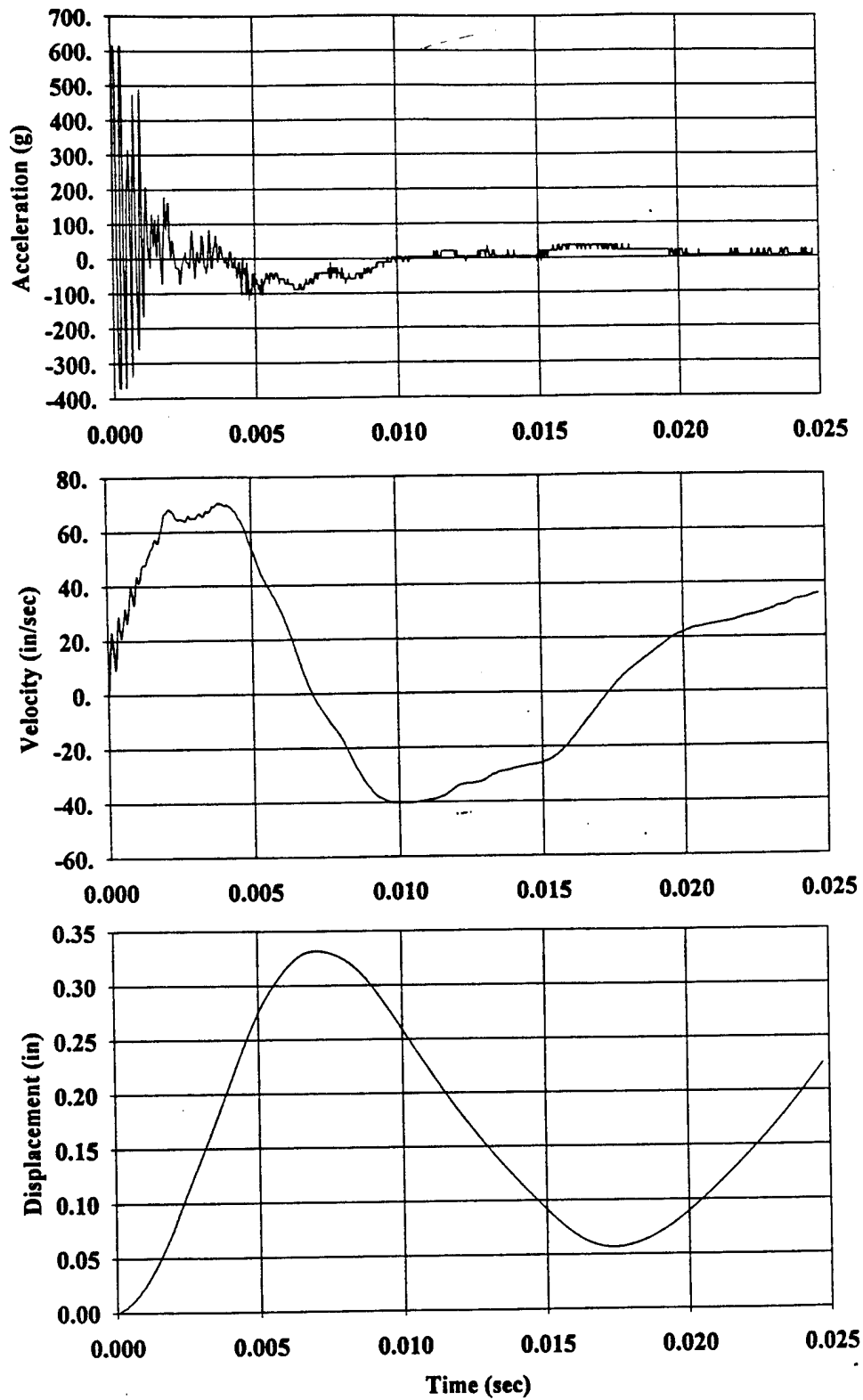
Figure 32. Double Integration of the Acceleration Record at Point 7 in Test 6 of the IDF Structures.
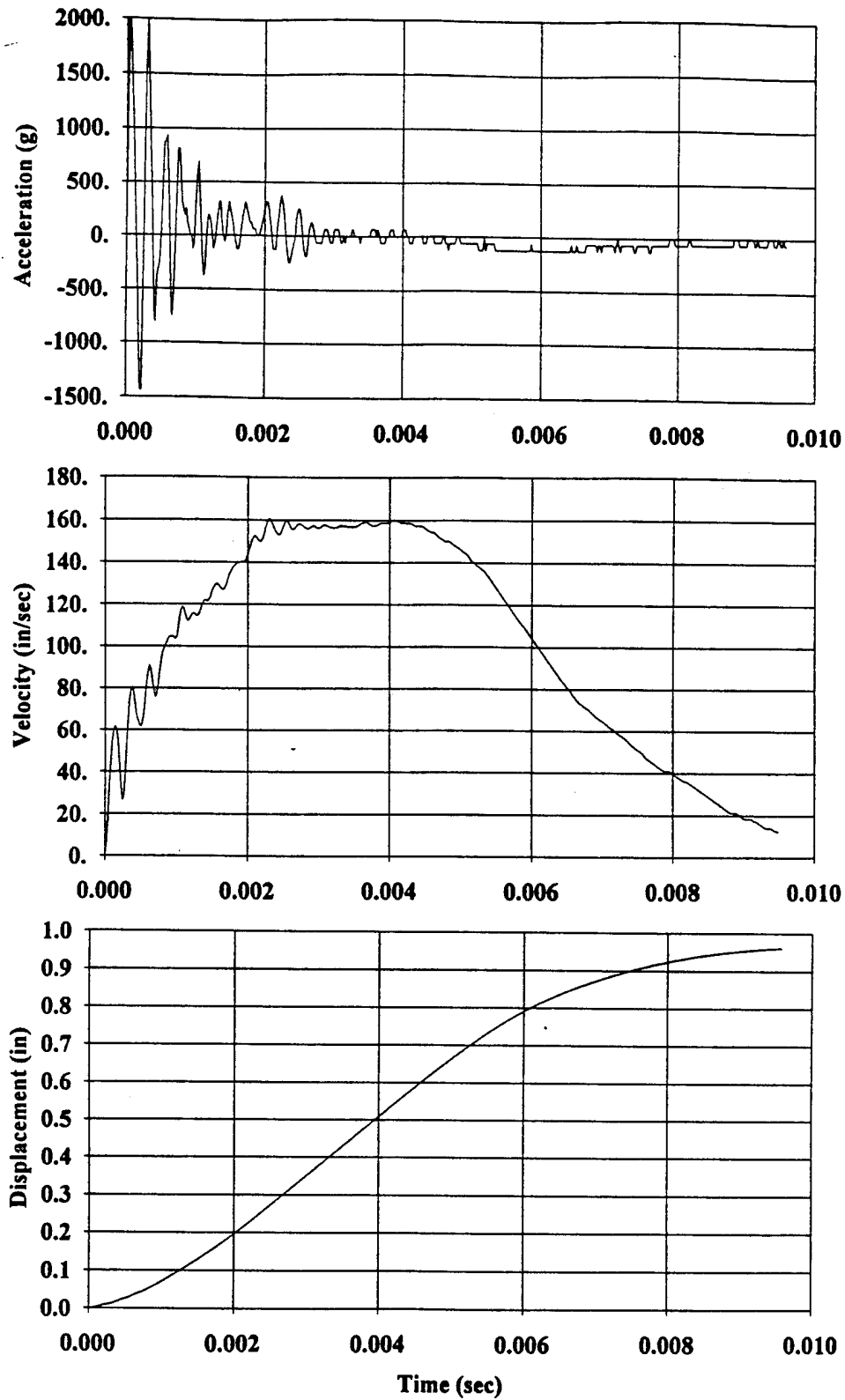
Figure 33. Double Integration of the Acceleration Record at Point 7 in Test 7
of the IDF Structures.
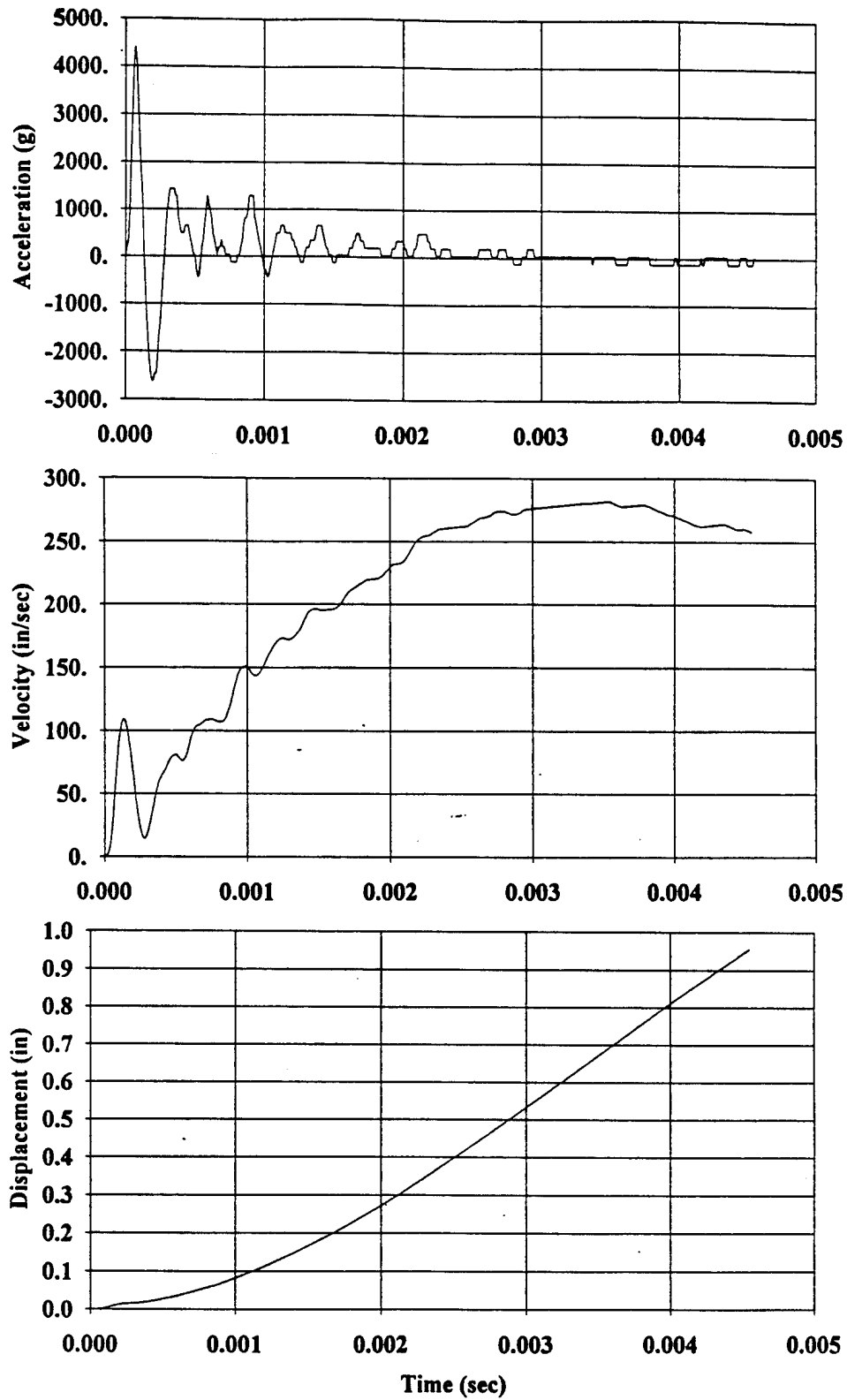
Figure 34. Double Integration of the Acceleration Record at Point 7 in Test 8 of the IDF Structures.

SECTION III
DESCRIPTION OF TYNDALL AIR FORCE BASE TESTS

A. DESCRIPTION OF TEST STRUCTURE

A series of tests was conducted at Tyndall Air Force Base to improve the criteria for the design of military structures that meet the NATO semihardened structure requirements for protection against conventional weapons effects. These full-scale tests were a continuation of a series of half-scale tests that was conducted earlier at Tyndall. It included 14 tests to study spall plates, blast valves, precast panels and revetments, and reinforced concrete walls. A summary report of these tests is contained in Reference 2, and detailed data reports of them are found in Reference 8.

Because they most nearly parallel the IDF tests that were described in Section II, Tests 6 and 10 of the Tyndall series were selected for inclusion in this study. These tests were conducted on the south and north walls, respectively, of the structure that is shown in plan view in Figure 35.

As will be observed from Figure 36, on which cross sections and reinforcement details for the walls are shown, the south wall is 25.5 inches thick while the north wall is 31.5 inches thick. The south wall was reinforced on each face with 0.25 percent steel vertically (#5 bars on 5.0-inch spacings) and 0.10 percent horizontally (#3 bars on 4.5-inch spacings), while the north wall was reinforced on each face with 0.16 percent steel (#5 bars on 6.0-inch spacings) both vertically and horizontally. Shear reinforcement of 0.12 percent was also provided over the full height in both walls. Both walls have concrete cover on the vertical steel of about 3.00 inches on the outside face and 0.75 inches on the inside face. Similarly, the cover on the horizontal bars is 3.6 inches on the outside face and 1.4 inches on the inside.

Both walls have well defined clear spans of 13 feet 2 inches in their vertical directions (see Figure 36). They are supported along their bottom edges by the basement walls and the floor slab of the first floor of the building, being integrally cast with both of these building elements. Along their upper edges, they are supported by the roof of the building, to which they are also rigidly connected.

The support conditions along the short sides of the walls are not as clearly defined. As will be observed from a study of Figure 35, doors exist at each end of these walls in such a way as to leave them unsupported on their short sides, for distances equal to the height of the doors (8 feet 0 inches), on spans of 43 feet 3.5 inches. But from the tops of the doors to the ceiling of the first floor, a distance of 5 feet 2 inches, they are supported on clear spans of 45 feet 9 inches by the walls into which they frame.

As will be seen in Section IV.B.1.a that follows, these walls were idealized for purposes of analysis with the SDOF procedures as two-way slabs that were fixed along their long edges, giving fixed-ended short spans of 158 inches, and simply supported along their short edges on spans of 519.5 inches. The appropriateness of this latter idealization is open to debate, but it seems
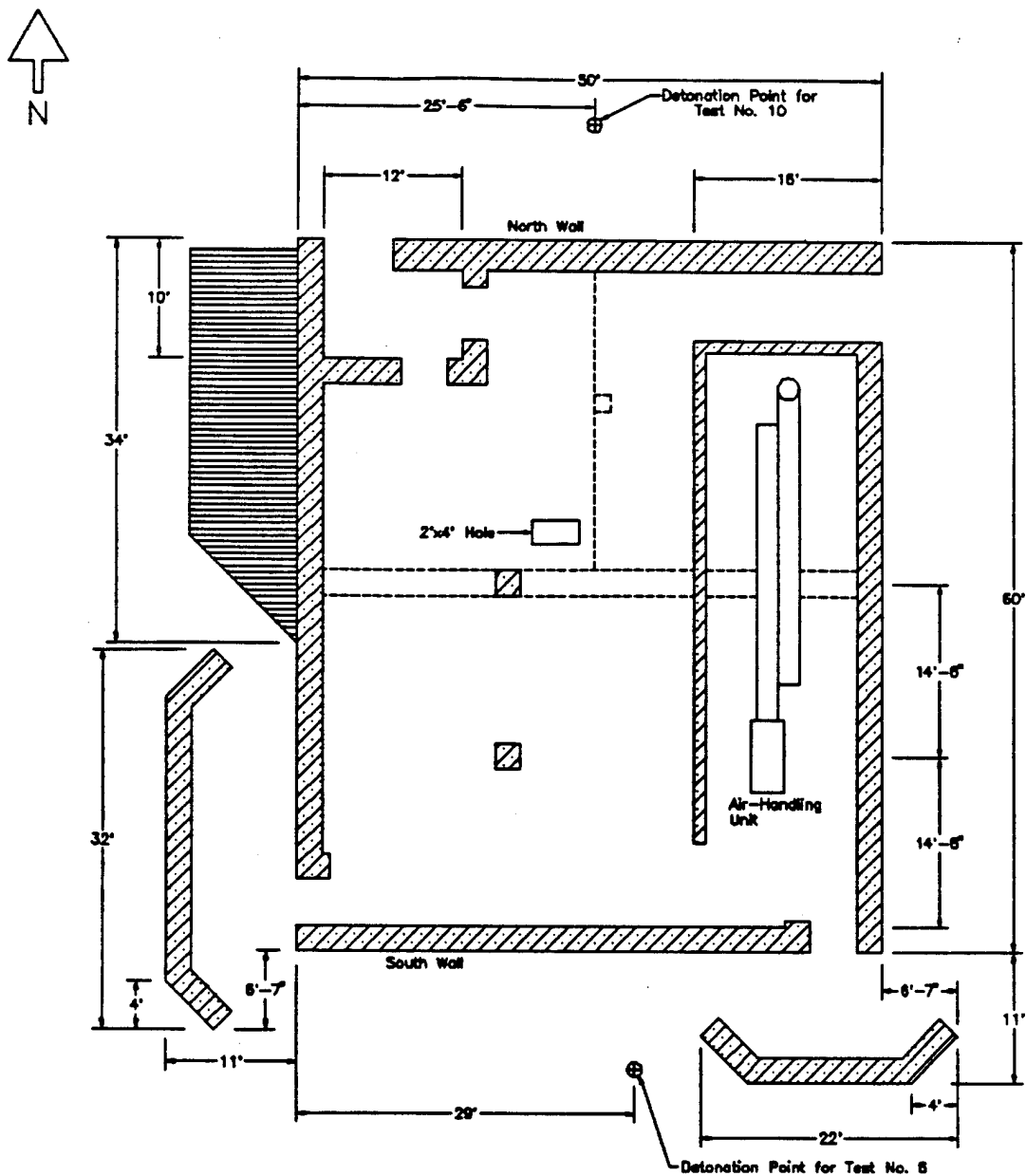
Figure 35. Plan View of Tyndall Test Structure, Ground Floor.

reasonable under the circumstances. Because the lower 8.0 feet of the walls were unsupported on spans of 519.5 inches and the upper 5 feet 2 inches of the walls were fixed-ended on spans of 549 inches, a simply supported span of 519.5 inches seemed like a reasonable intermediate position; because of the aspect ratio of the walls, the dominant response of the walls will be as one-way slabs in the short-span direction.

The walls were loaded by the detonation of cylindrical cased explosive charges that were located with respect to the walls as shown in Figure 35. The charges stood on end at fixed distances from the surfaces of the walls. It will
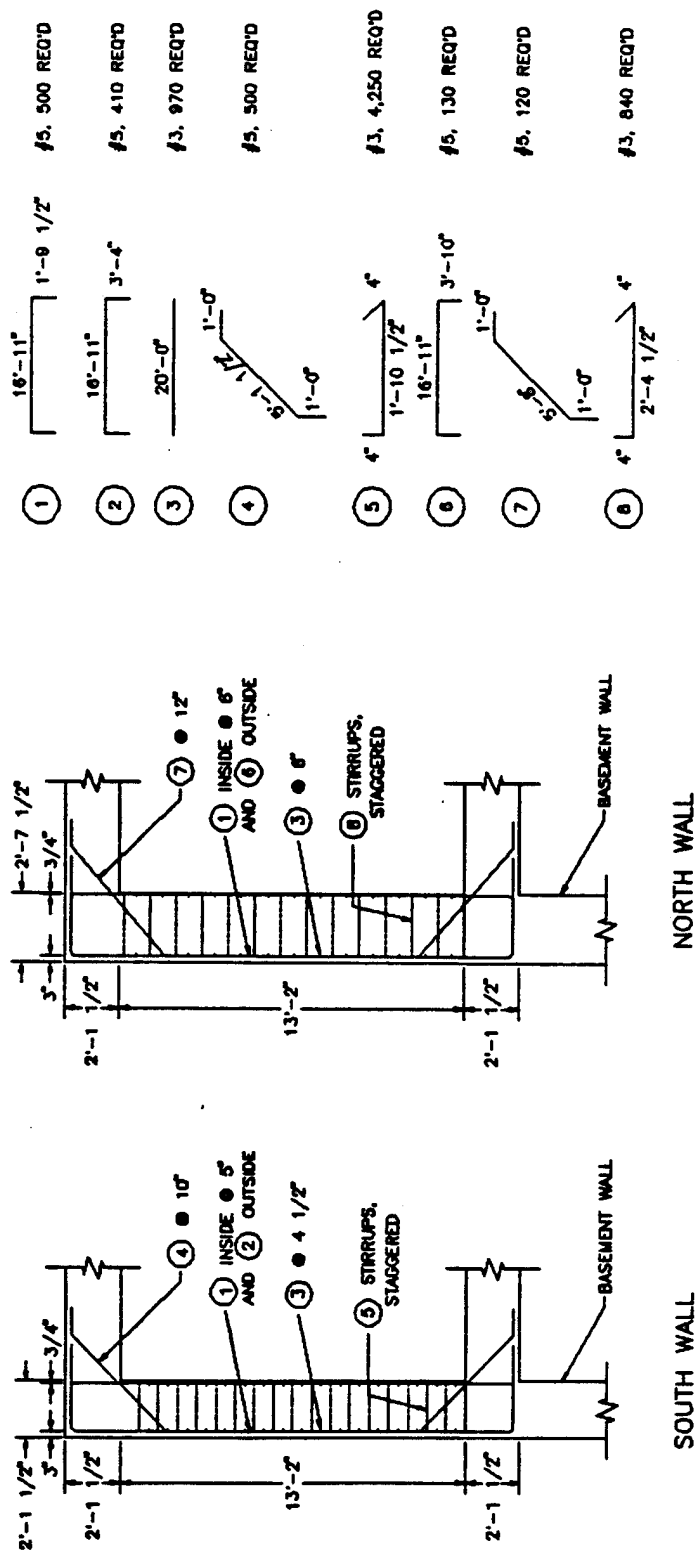
Figure 36. Tyndall Structure Test Wall Reinforcement Details.

44

be observed that the detonation point for Test 10 is very close to the center of the north wall, but the detonation point for Test 6 is displaced about 4.0 feet east of the center of the south wall, which should produce an unsymmetrical pressure loading of that wall. The existence of a protective wall about 6 feet from and parallel to the south wall near its southeast end, that is intended to protect the door in the wall that is located at that point (see Figure 35), may contribute to a further lack of symmetry of the blast pressure loading on that wall.

B.   INSTRUMENTATION AND MEASUREMENTS

The pressures produced on the test walls by the bomb detonations were recorded by pressure gages that were positioned flush with the exterior faces of the walls and were attached to gage mounts that were cast in the concrete. An array of 16 such gages was used on the south wall in Test 6 and an array of 12 gages was used on the north wall in Test 10, as shown in Figures 37(a) and (b), respectively. The pressure records taken by those gages are contained in the original data reports of Reference 8, and are summarized in the final report of that project, Reference 2. Because of its more detailed nature, the pressure data of Reference 8 were used to generate the spatially varying loading functions on the wall surfaces that were needed in the ADINA finite element analyses of this current study, while the summary data of Reference 2 were used to develop the loading functions that were employed in the four SDOF programs that were studied. The pressure data from both of these sources are summarized in Table 8.

Deflections of the walls were measured using active displacement gages that were mounted on the inside surfaces of the walls. These gages, which were supported on a steel frame that was anchored to the floor slab, were placed directly opposite the blast points. The displacement-time data taken by these gages were recorded on analog tape, which was later digitized. The measured peak deflection of the south wall in Test 6 was 2.46 inches while, for the north wall in Test 10, it was 1.94 inches.

For Test 6 on the south wall, the peak reflected pressures that were measured on the surface of the wall directly opposite the explosive charge ranged, as shown in Table 8, from a maximum of about 2830 (or 2890) psi near the center of the wall to a low of 400 psi at the top of the wall. The associated impulses under the reflected pressure curves were 1280 and 416 (or 400) psi-ms, respectively.

Significant damage was also produced by spalling of the concrete on the inside face of the wall. Spalling of the concrete cover on the reinforcement on the inside face of the wall took place over an area of about 75 square feet.

Beyond the region of severe spalling on the inside face, extensive cracking of the concrete in a random pattern was also evident, but no clearly defined flexural crack patterns could be seen. In view of the fact that the wall experienced a maximum deflection of almost 2.5 inches, flexural cracks should have been present near the center of the slab; it seems likely that such cracks existed, but were obscured by the more pervasive spall cracks. A negative moment
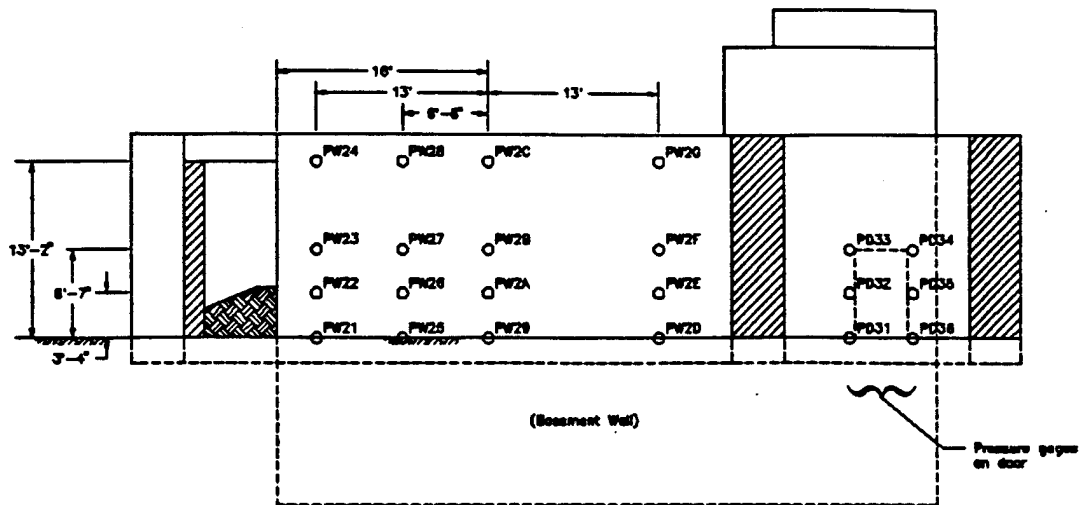
(a) South Wall
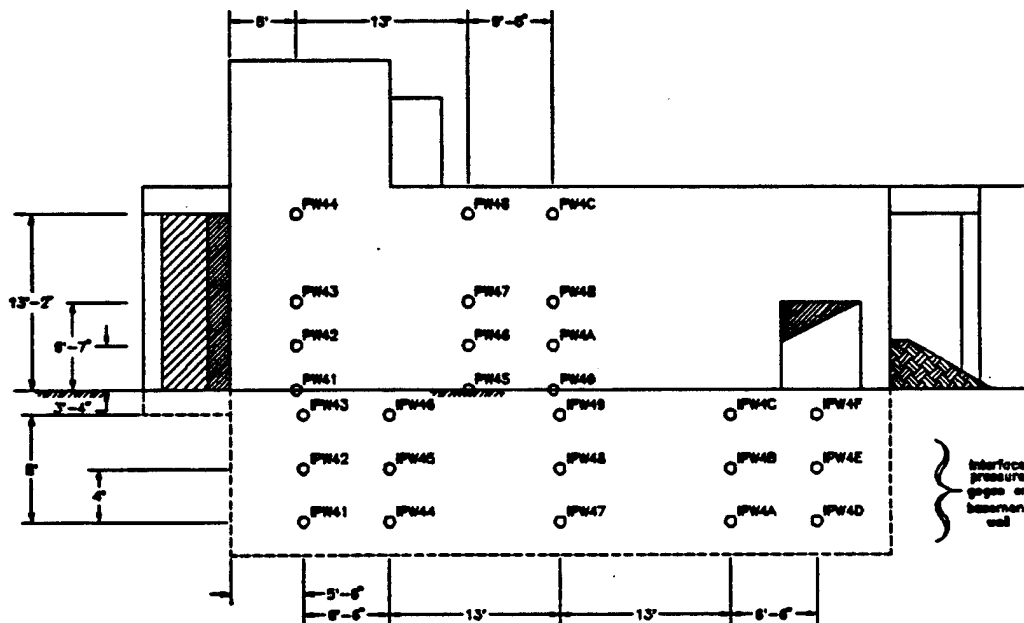
(b) North Wall

Figure 37. Airblast and Interface Pressure Gage Locations on Tyndall Test Walls.

46

TABLE 8.   SUMMARY OF AIRBLAST PRESSURE MEASUREMENTS ON THE TYNDALL
AFB TEST WALLS.

Gage number	As given by Reference 2		As given by Reference 8	
	Peak press. (psi)	Impulse (psi-ms)	Peak Press. (psi)	Impulse (psi-ms)
For south wall, Test 6				
PW-2D	1670+	125+	--	--
PW-2F	2830	1280	2890	1280
PW-2G	400	416	400	400
PW-22[a]	1400	--	1410	--
For north wall, Test 10				
PW-42	606	500	585	500
PW-43	623	139	630	330
PW-44	235	271	240	263
PW-45	3010	--	3050	220
PW-48	376	351	380	348
PW-4A	1720	920	1750	591[b]
PW-4B	2300	952	2360	940
PW-4C	443	331	450	330

[a]Data uncertain; may have been for gage PD-32, which was mounted on the door.
[b]Clearly in error as tabulated in Reference 8. The data trace in Reference 8 for this gage indicates a value of about 900 psi-ms.

flexural crack is clearly evident along the top of the wall on the outside face. If a similar crack existed along the bottom of the wall, as should have been the case, it was obscured by the damage done to that surface by the explosive casing fragments.

The damage to the north wall in Test 10 was very similar to that of the south wall. As noted in Table 8, the maximum reflected pressures measured on the wall directly opposite the explosive charge ranged from a maximum of 2300 (or 2360) psi near the center of the wall to a minimum of 443 (or 450) psi at the top of the wall, with corresponding impulses of 952 (or 940) and 331 (or 330) psi-ms, respectively, which agree quite well with the values measured at comparable points on the south wall in Test 6. It also experienced significant spall damage on the inside wall face, but the extent of this damage, which covered only about

35 square feet, was substantially less than was the extent of the similar damage to the south wall.

This test series is reported in detail elsewhere. This summary is provided only as an introduction to the structural analyses that follow.

SECTION IV

PREDICTION OF BEHAVIOR OF TEST STRUCTURES USING A UNIVERSITY OF ILLINOIS SDOF RESPONSE PROGRAM

A. BRIEF DESCRIPTION OF THE PROGRAM

An initial evaluation of the general quality of the data taken in the IDF field tests was made by using a simple, locally available SDOF program, with which the authors were thoroughly familiar and which could be used with confidence.

The program is a computerization of the Modified Beta Method of dynamic structural analysis. The Beta Method (Reference 9) was developed by N. M. Newmark as an iterative solution of the standard equations of motion of a SDOF system. A modification of that method, which permits a more direct solution, is described in Reference 10. It requires that the resistance of the responding system be input as a multilinear force-displacement function. The excitation may be entered either as a multilinear acceleration-time function applied to the base of the system or as a multilinear force-time function that is applied to the responding mass. In the application being considered here, the resistance function is computed as the relationship between a uniformly applied pressure on the surface of the wall of the test structure and the corresponding deflection at the center of the wall. The loading, too, is determined as the average uniformly distributed pressure produced on that wall, as a function of time, by explosive charges.

Additionally, the program requires that the natural period of vibration of the responding system be input, and that the nature of the variation of the acceleration during each integration time step be specified by appropriate selection of an input constant, Beta. Although several options were available for the case being studied, beta was selected to represent a linear variation o the acceleration of the responding mass, as a function of time, during eac integration time step.

B. APPLICATION OF THE PROGRAM TO THE IDF STRUCTURES

1. Idealization of Wall for Analysis

For purposes of dynamic analysis, the test walls were idealized as systems whose dynamic properties were those of two-way slabs that respond their fundamental flexural modes. The resistance functions and the ne periods of vibrations were estimated as described below, using the proc recommended in Reference 11 and/or 12. The geometry of the wall, a reinforcement patterns and amounts, are shown in Figure 38, which are ir ment with the data given earlier in Table 1.

a. Flexural Resistance Function

The flexural resistance-displacement curve is approximated as a plastic function which is shown as a solid line in Figure 39, and who:
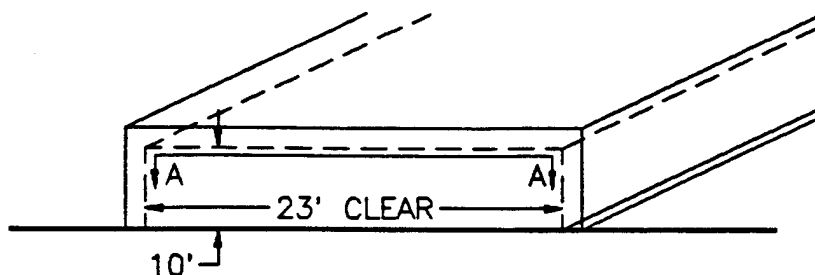
Note: Test wall is continuous with sidewalls and roof, but nature of rotational restraint at the base is intermediate between simply supported and continuous.
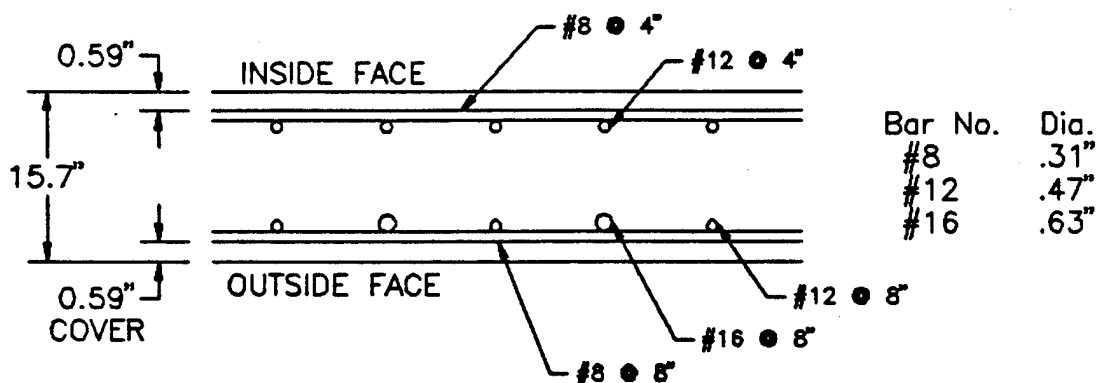
Note: In the outer face, #16 @ 8", the reinforcement is extended only down to 1/3 of the wall height from the top of the wall.

Figure 38. Geometry and Reinforcement of IDF Structure 1 Test Wall.

or ultimate capacity is given approximately by the following equation (References 11 and 12):

$$r_u = \frac{12\,(M_{es1} + 2M_{cs} + M_{es2})}{3L_s^2 - \dfrac{L_s^3}{L_L}} + \frac{12\,(M_{eL1} + 2M_{cL} + M_{eL2})}{3L_sL_L - L_s^2} \tag{1}$$

in which r_u = ultimate capacity of the slab, psi

M_{es1} = M'_u at one end in the short span direction, in.-lb/in.

M_{es2} = M'_u at the other end in the short span direction, in.-lb/in.

M_{cs} = M'_u at the center in the short span direction, in.-lb/in.

50
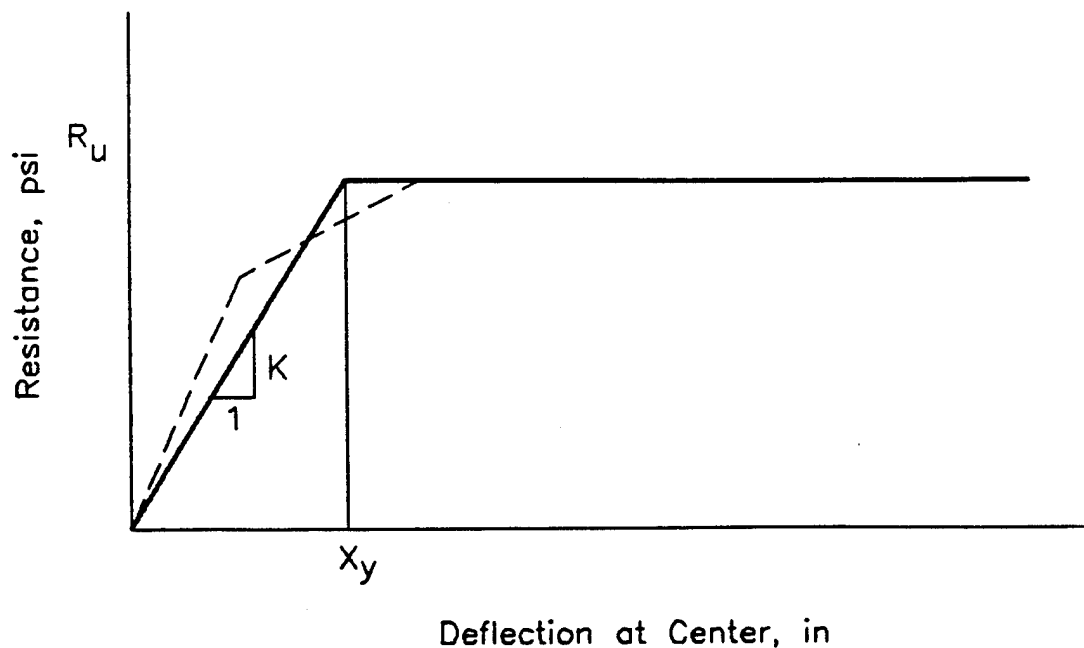
Figure 39. Idealized Flexural Resistance Function of IDF Structure 1 Test Walls.

M_{eL1} = M'_u at one end in the long span direction, in.-lb/in.

M_{eL2} = M'_u at the other end in the long span direction, in.-lb/in.

M_{cL} = M'_u at the center in the long span direction, in.-lb/in.

L_s = clear span in the short direction, in inches

L_L = clear span in the long direction, in inches

and M'_u = ultimate moment capacity per unit width on the section of interest, which is computed from Equation (2), which follows.

$$M'_u = [\rho(d - 0.5d_c) + \rho'(0.5d_c - d')](df_{dy})$$
$$+ (0.425\beta_1 K_u df_{dc})(dc - \beta_1 K_u d), in.-lb/in. \qquad (2)$$

in which d = effective depth of the slab, inches

d_c = total thickness of slab, inches

d' = distance from the compression face to the center of the compression steel, inches

ρ = positive moment reinforcement ratio

ρ' = negative moment reinforcement ratio

51

$$\beta' \quad = 0.85 \text{ for } f'_c \leq 4000 \text{ psi}$$

$$= 0.85 - 0.00005 \ (f'_c - 4000) \text{ for } f'_c > 4000 \text{ psi}$$

(taken as 0.85 for this study)

f'_{dc} = dynamic crushing strength of concrete, psi

f_{dy} = dynamic yield strength of the reinforcement, psi

and

$$K_u = \frac{N + (\rho - \rho') f_{dy} d}{0.85 \beta_1 f'_{dc} d} \tag{3}$$

in which N is the in-plane force, per unit width of slab, and the other quantities are as previously defined.

The resistance level computed in this manner is the uniformly distributed pressure that would have to be applied to the outside surface of the wall to develop the flexural yield line pattern of Figure 40. The actual yield line pattern, which is a function of the reinforcement amount and distribution, would differ somewhat from the idealized pattern of Figure 40, but the difference in the resistance levels of the actual and this idealized pattern will be relatively small. In view of the very substantial uncertainties that are present in the definition of the slab's material properties, an attempt at a more refined analysis is not typically deemed justified.

In the implementation of the procedures outlined above to evaluate the several ultimate unit moment capacities of the slab, the following assumptions were made:

(1) The static yield strength of the steel, which was given as 31,290 psi, was increased by approximately 30 percent to account for
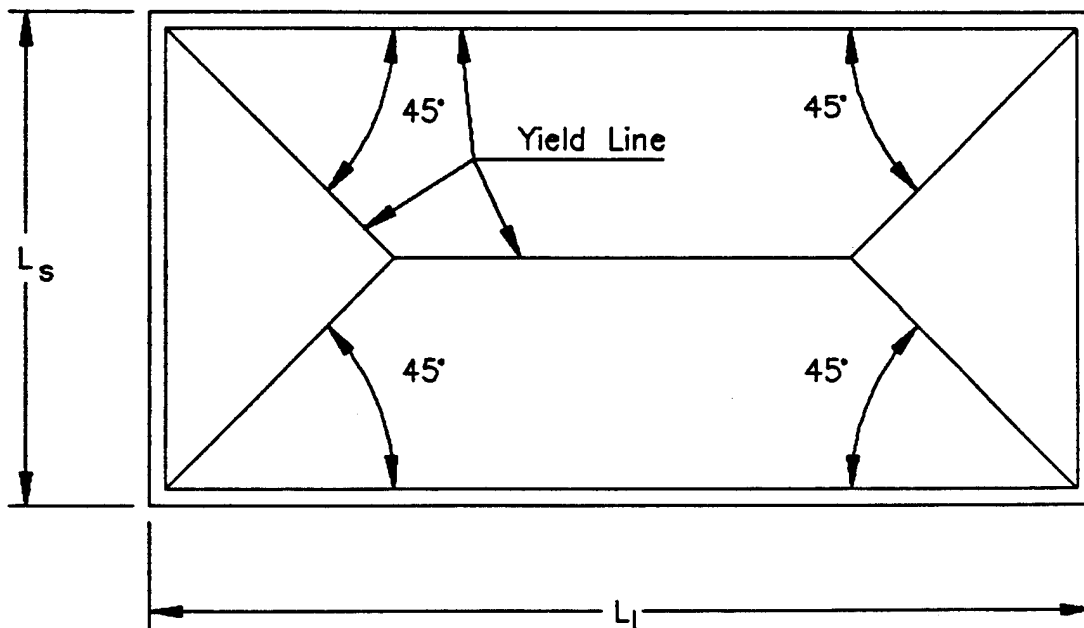
Figure 40. Idealized Yield Line Pattern for Two-Way Slab With Fixed Supports.

52

dynamic strain rate effects. Hence, f'_{dy} was taken as 41,000 psi in these analyses.

(2) For purposes of this analysis, the 28-day static crushing strength of concrete, which was given as 3220 psi, was increased in an attempt to recognize strength enhancement due both to age and to dynamic strain rate effects. As a consequence of the age of the structure at the time of the test (approximately 4 years), the static crushing strength was estimated to have increased to about 4000 psi, and this stress level was increased further by approximately 30 percent to account for dynamic strain rate effects. Consequently, for these analyses, f'_{dc} was taken as 5200 psi.

(3) The in-plane force, N, was assumed to be zero. As the pressure pulse engulfs the structure, the pressures on the roof and sidewalls induce in-plane forces in the wall being analyzed. To neglect these in-plane forces is to neglect also their effects on the ultimate moment capacities of sections through the slab. At moderate levels, in-plane forces increase the bending moment capacities and, hence, also increase the ultimate strength of the slab. In the case being studied here, the in-plane forces induced in the front wall were estimated to be so small as to have negligible effect on the resistance of that wall.

Using these assumptions and the reinforcement patterns shown in Figure 38 and Table 1, the several ultimate moments that are required for use in Equation (1) were evaluated as follows:

m_{es1} = ultimate moment at top of the wall
    = 34,472 in.-lb/in.

m_{es2} = ultimate moment at bottom of the wall. Depending on the nature of the support, it may vary between zero and 12,043 in.-lb/in.

m_{cs} = ultimate moment at center of slab, vertical direction = 25,008 in.-lb/in.

m_{eL1} = ultimate moment at one end of the wall
    = 5,309 in.-lb/in.

m_{eL2} = ultimate moment at the other end of the wall
    = m_{eL1} = 5,309 in.-lb/in.

m_{cL} = ultimate moment at the center, horizontal direction = 10,974 in.-lb/in.

Then, substituting into Equation (1), if the ultimate moment at the bottom of the wall is taken as zero, the ultimate resistance of the slab, r_u, is found to be 31.3 psi. Similarly, if the moment at the bottom of the wall is assumed to be 12,043 in.-lb/in., the slab resistance is found to be 35.2 psi. On these bases, then, the ultimate capacity of the wall was taken as the average of these two values, or 33.3 psi.

b.   Natural Period of Vibration

The natural period of vibration of a two-way slab is reasonably approximated by the following expression:

$$\frac{1}{T_2} = \frac{1}{T_{1L}} + \frac{1}{T_{1s}}$$ (4)

in which T_2 is the period of the two-way slab, T_{1s} is the period of vibration of a one-way slab spanning in the short direction, and T_{1L} is the period of vibration of a one-way slab spanning in the long direction.

The period of vibration of a continuous one-way slab is given approximately by the following equation:

$$T_1 = \frac{L^2}{2950d \sqrt{1.5\,(\rho_{e1} + \rho_{e2}) + \rho_c}}$$ (5)

in which L is the span length in feet, d is the effective depth in inches, ρ_{e1} and ρ_{e2} are the negative moment steel reinforcement ratios at the two ends, and ρ_c is the positive moment steel reinforcement ratio at the center of the span. For the slab being studied, as indicated in Figure 38, the short and long spans are, respectively, 10 and 23 feet, and the corresponding effective depths in the vertical and horizontal directions are 14.57 and 14.95 inches, respectively.

The reinforcement ratios, as defined by the reinforcement patterns given in Table 1, are as follows: In the vertical direction, ρ_c = .0030, ρ_{e1} (at top) = .0041, and ρ_{e2} (at bottom) varies between zero and .0015, depending on the extent to which the slab is restrained against rotation at that end. In a like manner, in the horizontal direction, ρ_{e1} = ρ_{e2} = .00061, and ρ_c = .00123.

Using these values, T_{1s}, the one-way period in the vertical direction, is computed to vary between 0.0216 and 0.0241 seconds, with an average value of about 0.023 seconds, and T_{1L}, the one-way period in the horizontal direction, is computed to be about 0.217 seconds. Then, from Equation (4), the period of vibration of the wall slab under study was taken to be about 0.020 seconds.

c.   Elastic Stiffness

The slope of the linearly elastic part of the idealized elasto-plastic resistance function as illustrated in Figure 39 is reasonably predicted by Equation (6) as follows:

$$K = \frac{4\pi^2 K_{LM}\, M}{T^2}$$ (6)

in which   M = mass of the wall per square inch of surface area
                = 0.0035 lb-sec^2/in.^{3}

$$T \; = \; \text{natural period of vibration}$$
$$= \; 0.020 \; \text{seconds}$$
$$K_{LM} \; = \; \text{Load-Mass factor}$$
$$= \; 0.61, \; \text{as evaluated by the equations of Reference 12}$$

Using these values, the idealized elastic stiffness of the slab is found to be 218 psi/in. Correspondingly, the yield deflection, x_y, computed as the ultimate resistance of 33.3 psi divided by the elastic stiffness of 218 psi/in., was estimated to be about 0.153 inch. The reasonableness of this value was supported by an independent calculation in which the yield hinges at the top and bottom of the slab were estimated to develop at a center deflection of about 0.06 inch and yield hinges at the center of the slab were predicted to form at a center deflection of about 0.16 inch. Hence a yield deflection of 0.153 inch would appear to be reasonable for the idealized linear rise of the resistance function.

d.   Loading Function

The loadings of interest are those that were produced on the wall by the airblast pressures generated by the nearby HE detonations. Generally, such loadings can be approximated by a pressure pulse of the form shown in Figure 41, in which the pressure decays from an initial maximum value equal to the peak reflected pressure on the wall surface to a value equal to the sum of the incident overpressure, $p_s(t)$, and the drag pressure, $C_d P_d(t)$, in a time of $3S/U$, where S is the smaller of half the width of the structure or the height of the structure and U is the incident shock front velocity. But defined as such for the cases being studied here, the total area under the loading curve (its total impulse) is greater than the actual total reflected impulse. Consequently, the total reflected impulse controls in these cases and a typical loading function used in these analyses is as illustrated in Figure 42 which is, simply, a plot of $P_r(t)$.

The dominant response of the wall is as a one-way slab with a 10-foot span in the vertical direction. Because the explosive charges are detonated on the ground surface at selected distances normal to the wall, the pressures induced on the wall by the impinging airblast wave vary from a maximum at the bottom to a smaller value at the top. It seems, then, not unreasonable to select the pressure at the center of the wall as an average of the loading function to be used in these SDOF analyses. This, in effect, assumed that the pressure-time function that existed at the center of the wall was applied uniformly, in both space and time, to the entire surface of the wall. Clearly, this loading function is an approximation that entails at least some error, thought to be small, especially in comparison with other uncertainties that exist in these analyses. However, this loading is studied further in Section VIII where the uniform and transient loadings are compared.

Copies of the pressure-time histories as recorded on the walls of the test structure are shown in Appendix A. Shown also are the smoothly decaying idealizations of these functions that were used in the computation of the
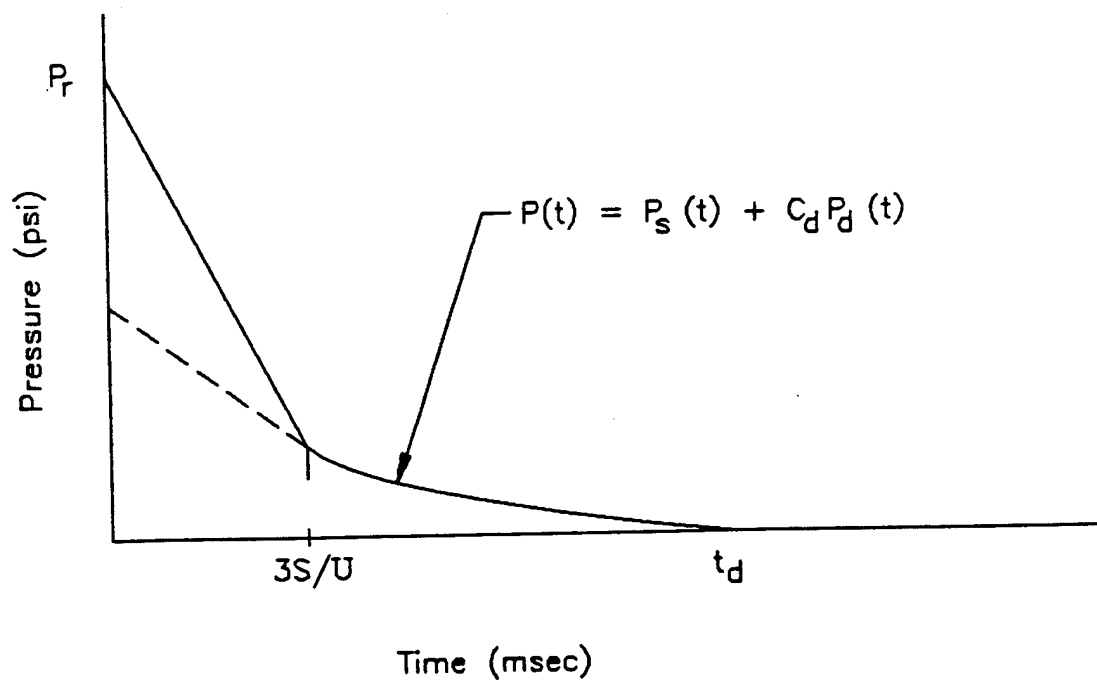
Figure 41. Generalized Wall Loading Function.
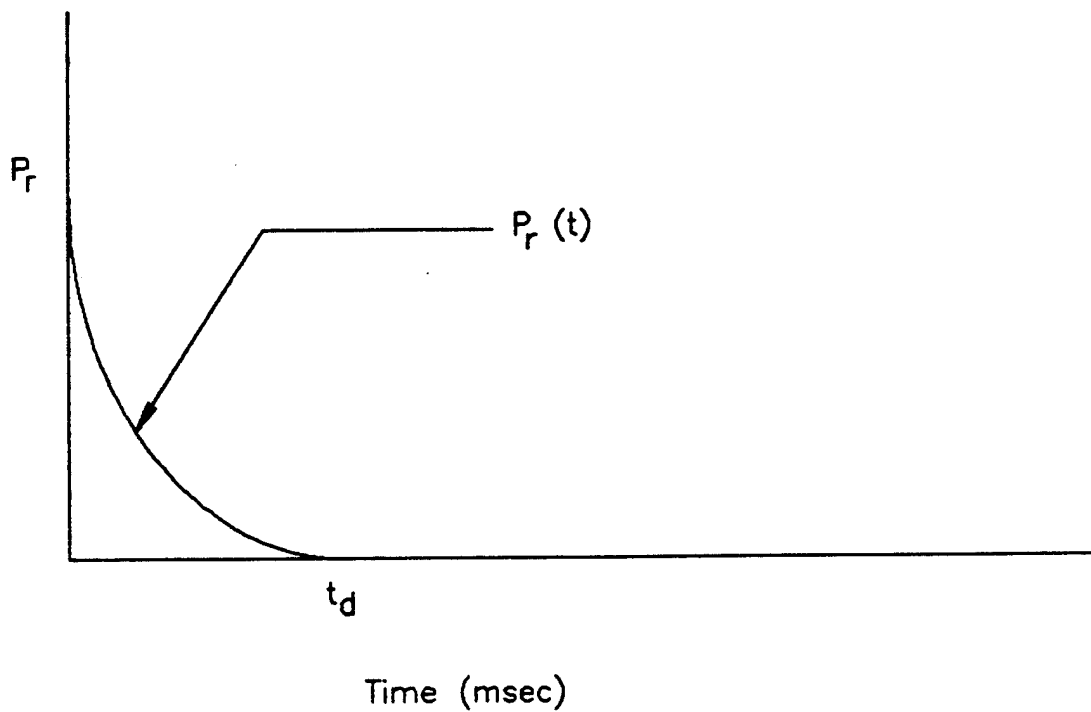
Figure 42. Typical Reflected Pressure Pulse on Wall.

56

responses of the wall to these pressures. When available, as they were in all tests except Tests 4, 8, and 9, the pressure records at point 2 (the center of the wall) were idealized for this purpose. In Tests 4 and 9, in the absence of data at point 2, the records at point 3 were used, and for Test 8, no usable pressure records were retrieved.

As reported earlier in Section II, Tests 1-4 were conducted on Wall A of Structure 1, using a 181-pound, 1:1, cylindrical charge of Composition B. Similarly, Tests 5-9 were conducted on Wall B of the same building (designed to be identical to Wall A), using a 561-pound, 1:1, cylindrical charge of the same material.

For convenient comparative purposes, the data shown on the above referenced figures of Appendix A are summarized in Table 9, together with loading data (peak reflected pressures and total reflected impulses) that would be computed at corresponding points on the wall using the predictive equations of Reference 5. While acknowledging the substantial differences that exist between the measured and computed pressure data in some cases, the agreement, especially in the lower pressure tests, is generally quite good.

The measured and computed pressure data are also compared, for both peak pressures and total positive phase impulses, in Figures 43 and 44. The relatively good agreement between the measured and computed data, especially in the lower pressure cases, is also evident in those plots.

2.   Analytical Results

The loading functions described in the preceding section were applied to the SDOF model, which was also defined in that section, to compute the maximum deflections that might have been expected at the center of the wall in each of the tests.   Such deflections were computed for both the measured and the theoretical loadings, and are tabulated in Table 9.   For convenient visual reference, these deflection data are also shown in Figures 45 and 46.

A study of these data plots provides both limited confirmation of the validity of the overall analytical procedure and some inconsistencies in its use. The confirmations are seen in a comparison, on Figure 45, of the measured residual displacements and the maximum responses of the wall in Tests 1-4 that were computed using the measured pressure data.   It will be observed in this comparison that if the computed maximum deflections are reduced by 0.15 inch, the computed yield deflection of the wall, the computed residual deflections will agree quite well with the measured residual deflections.   Actually, the comparison between the measured and the computed response is not quite as good as the description just given would suggest.   More correctly, the measured residual deflections should be compared with residual deflections that were estimated as the computed maximum deflection for a particular test plus the measured residual deflection of the previous test, minus the yield deflection of the wall.   But even on this more defensible comparative basis, the agreement between the measured and computed responses of the wall is not unreasonable, in view of the uncertainties that are involved, especially if we acknowledge the

57

TABLE 9.   COMPARISON OF MEASURED AND COMPUTED LOADING AND RESPONSE DATA
FOR IDF STRUCTURE 1.

Test	Point on wall[a]	Dist. (ft)	Measured data			Computed data			
			P_m (psi)	I (psi-ms)	Def (in.)	P_m (psi)	I (psi-ms)	X_1[b] (in.)	X_2[c] (in.)
1	1	49.2	36	153		35	124		
	2	49.5	31	106	0	34	123	0.135	0.128
	3	49.8	32	88		34	122		
2	1	32.8	197	217		106	200		
	2	33.1	142	149	0.2	102	197	0.293	0.217
	3	33.7	125	128		98	194		
3	1	23.0	?	392		308	310		
	2	23.5	284	215	0.3	288	301	0.674	0.377
	3	24.2	371	224		264	290		
4	1	16.4	2037	?		836	479		?
	2	17.2	393	?	0.6	730	450	1.519	0.461
	3	18.1	443	240		630	421		
5	1	65.6	44	149		44	201		
	2	65.8	41	148	0	43	200	0.204	0.168
	3	66.0	42	148		43	199		
6	1	49.2	165	273		97	282		
	2	49.5	161	275	0	95	280	0.448	0.522
	3	49.8	133	144		94	278		
7	1	32.8	706	574		329	464		
	2	33.1	439	451	0.6	317	457	1.368	1.392
	3	33.7	322	317		303	449		
8	1	23.0	?	?		932	735		
	2	23.5	?	?	1.0	878	715	3.524	?
	3	24.2	?	?		808	687		
9	1	16.4	?	?		2241	1166		
	2	17.2	942	?	15.7	1997	1091	8.086	?
	3	18.1	1125	667		1760	1017		3.027

[a]See Figure 5 for gage locations
[b]X_1 = Computed from theoretical impulses
[c]X_2 = Computed from measured impulses

progressive "softening" of the wall with each succeeding test, the effect of
which would be to increase the period of vibration and, thereby, to reduce the
computed maximum deflection that would be produced by any specified loading. No
attempt was made to reflect such softening in these computations.

However, the inconsistences are far more extensive than are these
agreements between measured and computed results.   There are significant
differences between the measured and the computed reflected pressure data for
Tests 1-4, with the disparity between the computed and the measured quantities
increasing quite dramatically as the distance from the point of detonation
decreases. Because of the previously noted agreement between measured residual
deflections and those deflections predicted computationally using the measured
pressure data as input, one is tempted to call the theoretical pressure data

58
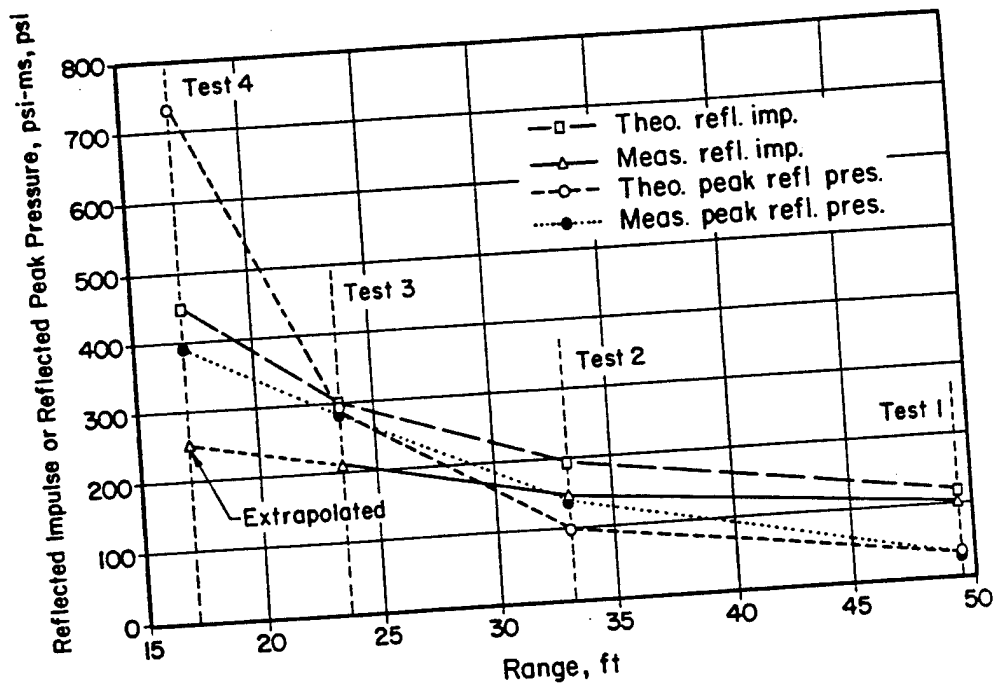
Figure 43. Loading Data for IDF Tests 1-4.
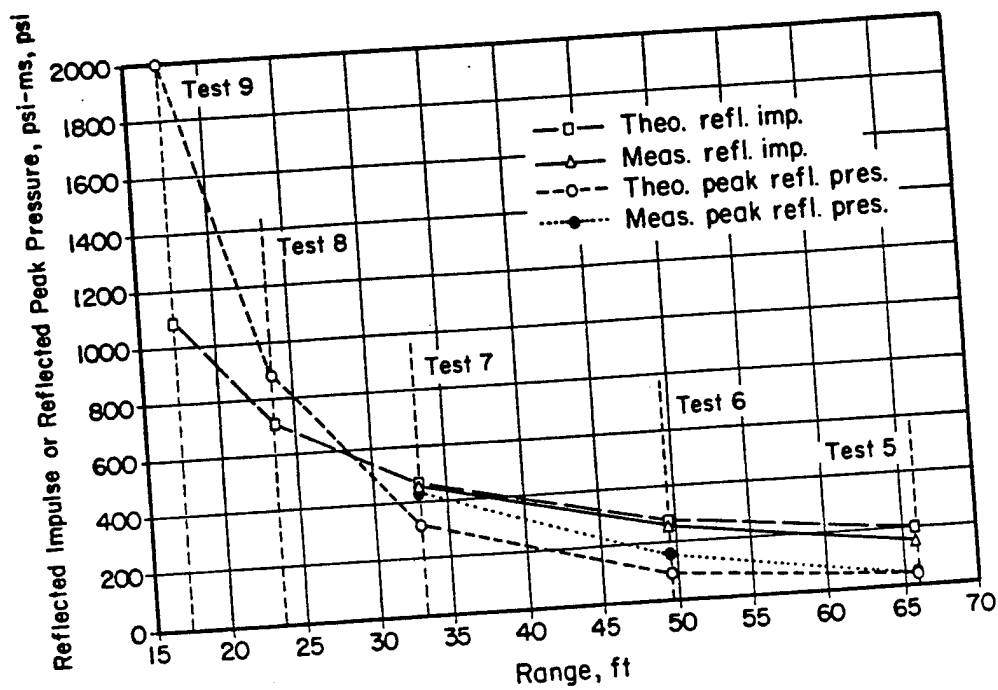
Figure 44. Loading Data for IDF Tests 5-9.

59
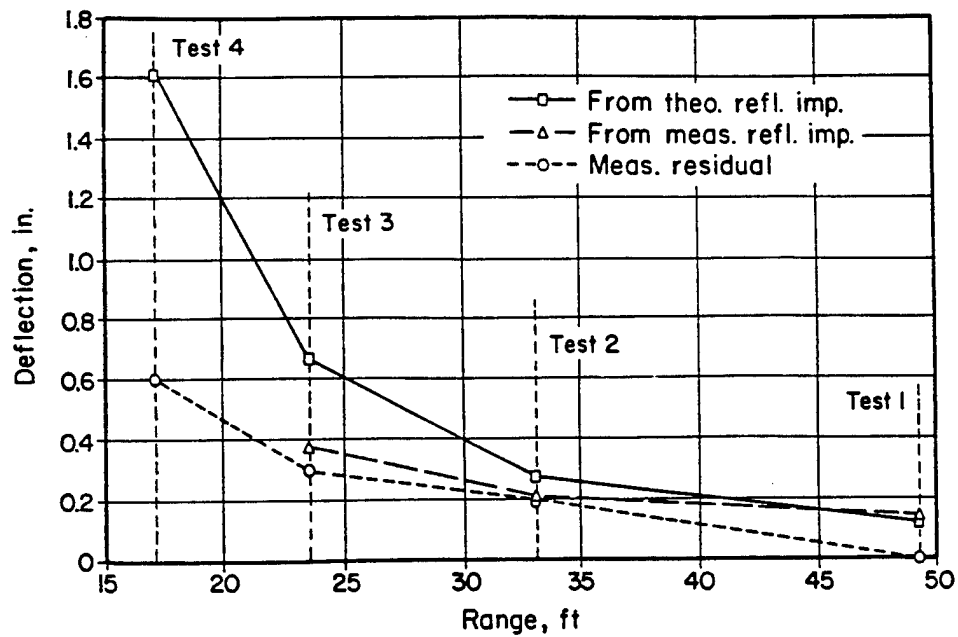
Figure 45.   Response Data for IDF Tests 1-4.
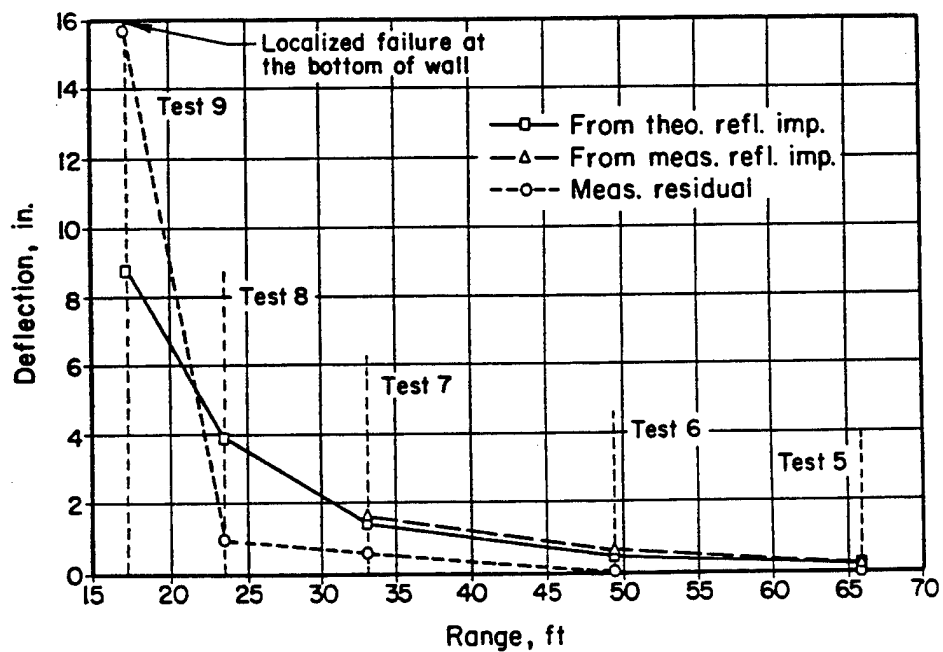
Figure 46.   Response Data for IDF Tests 5-9.

suspect, but this seems unlikely in view of the extent to which the applicability of the prediction equations used here have been previously confirmed. The effects of the charge shape are probably very influential.

Inspection of the data from Tests 5-9 reveals other inconsistencies. In contrast to the situation that prevailed in Tests 1-4, for Tests 5, 6, and 7 (which are the only tests of the second series for which we have measured pressure data at the midpoint of the wall) the computed and the measured impulse data are in quite good agreement. But the computed deformations for these tests do not agree with the measured residual deflections nearly as well as they did for the first series of tests. Additionally, measured residual displacements of zero are reported for Tests 5 and 6, despite the fact that blast-induced impulses applied to the wall in these two tests were significantly larger than were the impulsive loads that were generated in Tests 2 and 3 for which residual deflections of 0.2 and 0.3 inch, respectively, were reported. This inconsistency is further illustrated by observing that residual deflections of 0.6 inch are reported for Tests 4 and 7, but the measured loading impulse for Test 4 is given as only 275 psi-ms while the corresponding impulse for Test 7 is reported to be 574 psi-ms.

Clearly, a discrepancy exists. Either the wall for the second series of tests was decidedly stronger than was the wall of the first series, which seems unlikely, or some of the measured data are incorrect, which is a distinct possibility. This illustrates the danger of trying to draw too many conclusions from too little data, at least some of which is clearly questionable.

For example, because there is no pretest confirmation to the contrary, and the test structures were not originally designed and built as research structures, it is entirely possible that the test wall surfaces were out of plane by as much as one-tenth of an inch, or possibly more, before the tests. If such were the case, then the measured residual deflections of zero, or only a few tenths of an inch, under the lower pressure loadings have little meaning, and differences of a few tenths of an inch between computed and measured deflections are probably no cause for concern.

3.   Comparison of Measured and Predicted Pressure Data

Because the period of vibration of the responding wall is so much greater than the effective durations of the pressure pulses that were applied as loads on the wall, the actual shapes of these time-dependent forcing functions are of little or no consequence. As far as the wall is concerned, the load is effectively an impulse and the wall responds accordingly. In light of this, when comparisons between measured and computed data are made, the more significant basis for the comparison should be the total impulse under the pressure-time curve. Comparisons can also be made between measured and computed peak pressures, but the difficulty of precisely measuring initial peak pressures, especially when those pressures are very high, makes the absence of favorable comparisons of peak values at high pressure levels understandable.

61

However, we should be concerned about the disparity between the measured and predicted reflected pressure impulse data for the first test series. In the second series, the measured and predicted impulse data agree very well for the three tests for which measured pressure data were available. Why was there not similar agreement for the tests of the first series?

4.   Effects of Variations in Range and Angle of Incidence on Pressures on Wall Surface

For each of the nine tests, the HE charge was detonated at a point on the ground surface that was on a line normal to the base of the wall at its midpoint. Consequently, the pressure-time function that would be generated by the advancing shock wave as it impinged on the wall surface should vary from point to point on the wall for two reasons. First, because the radial distance from the point of detonation to points on the wall vary, the free-field incident pressure on the wall should vary, this pressure being maximum at the center of the base of the wall and minimum at the top corners of the wall. Secondly, because the angle of incidence with which the blast wave impinges on the wall varies from point to point on the wall surface, the magnitude of the reflection factor by which the incident pressure should be multiplied to produce the reflected pressure intensity also varies across the wall from a maximum at the midpoint of the bottom of the wall to a minimum at the top corners of the wall.

The significance of the first of these two factors can be seen in the data shown in Table 9 which were computed using the computerized version of TM 5-855-1 (Reference 5). Because the slab was rectangular (an aspect ratio of about 2.3 to 1.0), as well as the heavier reinforcement in the vertical direction, both the resistance and the behavior of the slab are dominated by the short span direction. Consequently, of primary concern in these analyses are the loading variations on the center section through the wall. These variations are seen in the data tabulations for points 1, 2, and 3 in Table 9. Note that the variations in the reflected impulses at these points are quite small, except perhaps for Tests 4, 8, and 9 for which the incident pressures were quite large. But even for these latter three tests, the impulse at point 2 should be a reasonable estimate of the effective "average" impulse that might be assumed to act over the entire wall surface. It was this midpoint impulse that was used as the "theoretical" load in the response calculations previously reported.

As is evident from the data of Table 9, the peak reflected pressure varies slightly more radically from point to point on the wall surface than does the reflected impulse. But, as noted earlier, this is of little consequence because the wall responds to the total impulse rather than to the peak pressure.

Clearly, the angle of incidence between the advancing shock front and the wall varies from point to point across the wall. Fortunately, however, this effect appears to be negligible in this case. A review of this question showed that, even under the most severe loading (Test 9), the reflection factor should, theoretically, vary by no more than about 10 percent from bottom to top of the wall at its midsection.

62

5.   Comparison of the Applicability of "Applicable" Manuals

Two manuals, <u>Fundamentals of Protective Design for Conventional Weapons</u>,
TM5-855-1 and <u>Protective Construction Design Manual</u>, AFESC ESL-TR-87-57
(References 5 and 13) were reviewed to assess their applicability to the test
data being analyzed in this study. Comparisons of the recommendations of each
of these manuals are summarized briefly below.

a.   Wall Loadings

For the conditions studied here, the loading recommendations are
essentially the same for both manuals. For very close-in blasts, the
recommendations of TM 5-855-1 are somewhat less rigorous, and less clearly
defined, than are those of the other manual.

b.   Resistance Functions

For flexure, both manuals give essentially the same recommendations -
standard yield-line theory. The two manuals give slightly different approximate
expressions for the ultimate moment capacities of the slab, should the user
choose to use them.

For shear, the two manuals define the resistance of the slab differently.
The Air Force manual relates the shear resistance of a two-way slab to that of
a one-way slab spanning in the short direction, while the Army manual uses the
ACI recommendations as modified by Gamble. However, both manuals appear to give
estimates of the ultimate shear capacity of a slab for design that are, usually,
substantially below its actual capacity.

c.   Methods of Analysis

Both manuals recommend the same SDOF response analysis procedures.

C.   APPLICATION OF THE PROGRAM TO THE TYNDALL STRUCTURES

1.   Idealization of the Walls for Analysis

The walls under study are the south and north walls of the Tyndall test
structure as described in Section III. Of particular interest is the behavior
of the south wall under Test 6 and the behavior of the north wall under Test 10
of the test program that was reported in Reference 2. Of the several tests that
were included in that program, Tests 6 and 10 most nearly paralleled those that
were conducted on the IDF structures, which were analyzed as described in the
preceding paragraphs.

a.   Geometry and Support Conditions

The two walls of interest are shown in a simplified outline in Figures 47
and 48, respectively. As described in Section III, they are two-way slabs, but
their edge support conditions are not easily modeled. Along their top and bottom
edges, they are continuous with other elements of the structure and may be
assumed, for purposes of analysis, to be fixed along these edges, with a clear
span of 158 inches. But their side supports are not so cleanly defined. Because

of the doors that exist both in the test walls and in the supporting sidewalls, the test walls are essentially unsupported over the lower halves of their sides, on spans of 519.5 inches, while the upper portions of these edges are continuous with the side walls, with clear spans of 549 inches.

Because the horizontal dimensions of the walls are more than three times their vertical dimensions, their dominant behavior will be as one-way slabs in the vertical direction, and the exact nature of their supports in the horizontal, or long, direction becomes relatively unimportant, insofar as their structural resistance and dynamic behavior properties are concerned. However, for consistency with the IDF structural analyses, both of the walls were idealized for this analysis as two-way slabs that were fixed in the short direction on spans of 158 inches and simply supported in the long direction on spans of 519.5 inches. The slab dimensions and reinforcement details, which were presented in Section III, are summarized for convenient reference here in Tables 10 and 11.
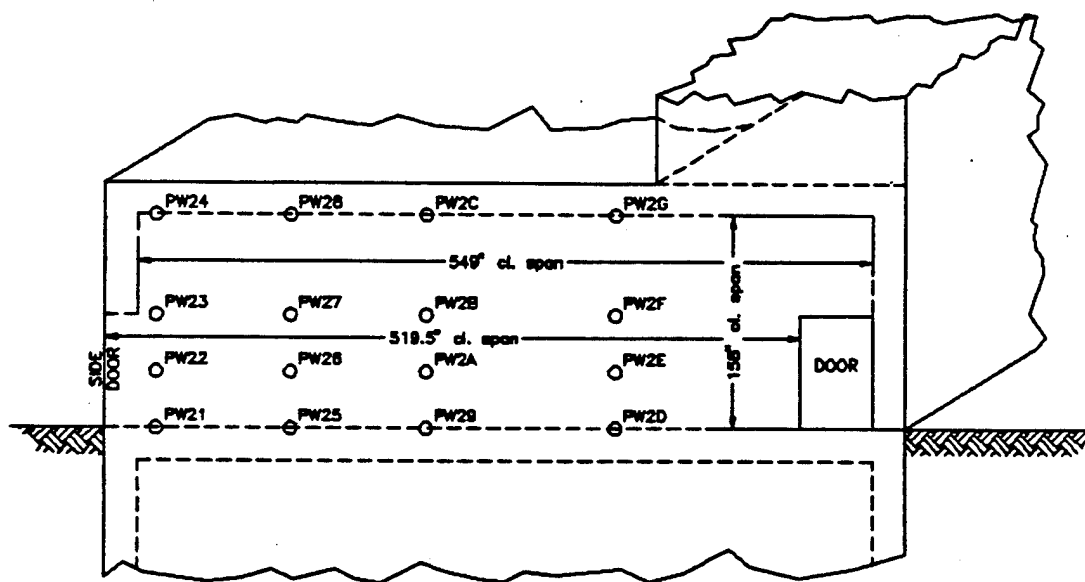
Summary of Measured Pressure Data

Gage	Peak Pressure (psi)	Pos. Phase Impulse (psi-ms)
PW22	1410*	—
PW2D	1670+	125+
PW2F	2830	1280
PW2G	400	416

* Data uncertain; may have been from Gage PD32, which was mounted on the door.

Figure 47. Wall Pressure Gage Locations and Measured Pressure Data for Test 6 on South Wall of Tyndall Structure.
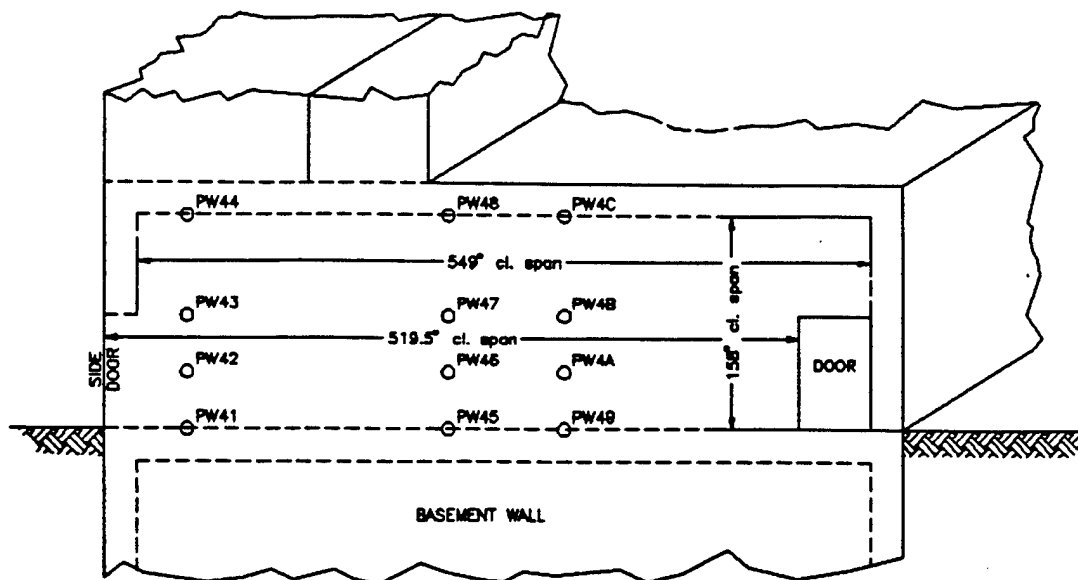
Summary of Measured Pressure Data

Gage	Peak Pressure (psi)	Pos. Phase Impulse (psi-ms)
PW42	606	500
PW43	623	139
PW44	235	271
PW45	3010	—
PW48	376	351
PW4A	1720	920
PW4B	2300	952
PW4C	443	331

Figure 48.   Wall Pressure Gage Locations and Measured Pressure Data for Test 10 on North Wall for Tyndall Structure.

b.   Resistance Functions and Dynamic Properties

Although not reported in Reference 2, an unpublished log (Reference 14) of the properties of the materials used in these test structures indicates that the average 28-day compressive strength of the concrete used was 4275 psi, and that, in the absence of other data, it could be assumed that the reinforcing steel was of Grade 60, with a static yield strength of 60,000 psi. For these analyses, it was assumed that, as a consequence of age, the static compressive strength of the concrete in the test walls had increased by about 25 percent at the time of the tests. Additionally, it was assumed that because of the very high strain rates that were experienced by the wall in these tests, the yield strengths of both the concrete and the steel would be increased by about 30 percent. Consequently, in

TABLE 10. PHYSICAL CHARACTERISTICS OF SOUTH WALL OF TYNDALL AFB TEST STRUCTURE.

Parameter	Short span direction	Long span direction
Clear span, in.	158.0	519.5
Total thickness, in.	25.5	25.5

For positive moment:
    Depth to tension steel, in.
    Depth to compression steel, in.
    Tension steel ratio
    Compression steel ratio
	24.44
	3.31
	0.0025
	0.0025
		23.94
		3.81
		0.0010
		0.0010

For negative moment:
    Depth to tension steel, in.
    Depth to compression steel, in.
    Tension steel ratio
    Compression steel ratio
	22.19
	1.06
	0.0025
	0.0025
		21.69
		1.56
		0.0010
		0.0010

TABLE 11. PHYSICAL CHARACTERISTICS OF NORTH WALL OF TYNDALL AFB TEST STRUCTURE.

Parameter	Short span direction	Long span direction
Clear span, in.	158.0	519.5
Total thickness, in.	31.5	31.5

For positive moment:
    Depth to tension steel, in.
    Depth to compression steel, in.
    Tension steel ratio
    Compression steel ratio
	30.44
	3.31
	0.0016
	0.0016
		29.81
		3.94
		0.0016
		0.0016

For negative moment:
    Depth to tension steel, in.
    Depth to compression steel, in.
    Tension steel ratio
    Compression steel ratio
	28.19
	1.06
	0.0016
	0.0016
		27.56
		1.69
		0.0016
		0.0016

these analyses, the dynamic compressive strength of the concrete was taken as 4275 x 1.25 x 1.3, or 6947 psi. Similarly, the dynamic yield strength of the reinforcing steel was taken to be 60,000 x 1.3, or 78,000 psi.

Using the material properties identified above, the slab dimensions and reinforcement percentages as given in Table 10, and the same computational methods that were outlined in Section IV.B.1 for the IDF structures, the yield resistance, yield deflection, elastic stiffness, and natural period of vibration of the south wall of the Tyndall structure were estimated to be about 72.7 psi, 0.25 inch, 288.6 psi, and 22.7 ms, respectively. Similarly, with the slab dimensions and reinforcement percentages as given in Table 11, the corresponding quantities for the north wall were estimated to be about 81.2 psi, 0.22 inch, 376.7 psi, and 22.1 ms. These resistance functions, natural periods, and elastic stiffnesses are shown on Figure 49.

c. Loading Functions

The loading functions applied to these test walls are uncertain and vaguely defined. The test data, as reported in Reference 2, are summarized in Figures 47 and 48. It will be observed from Figure 47 that useful data were obtained from only 2 of the 16 pressure gages that were installed on the south wall, one of which was near the center of the wall and the other of which was near the top center. Similarly, as will be observed from Figure 48, 7 of the 12 available gages on the north wall appear to have provided useful results. Because both walls were loaded in essentially the same way (the same explosive size, oriented in the same way with respect to the wall, and detonated at the same distance from the wall), the pressures produced on the walls should have been about the same. The only significant difference between the two loadings was the placement of the charges relative to the centers of the walls, the charge for Test 6 being about 4 feet off center. With only two data points available for the south wall, loading equality on the two walls cannot be confirmed. By comparing the data that were obtained from gages 2F and 2G on the south wall with the data from gages 4A, 4B, and 4C on the north wall, both sets of gages being directly opposite the detonation points, it could be concluded that the loading on the south wall was significantly greater (as measured by the impulses under the measured pressure-time curves) than was the loading on the north wall. The pressure gages represent only the forces applied to the walls by the airblast pressure, neglecting the energy of the casing fragments that impinge on them; however, the total energy applied to the walls may be comparable.

While the blast pressure loadings on the walls are ill-defined, the measured data are sufficient to confirm the wide variation in blast pressure loading that would be expected from the detonation of an explosive charge at close range from a wall that was 13 feet high and 45 feet long. To study the load variations that might reasonably be expected on the walls in these tests, theoretical peak pressures and positive phase impulses, both incident and reflected, were computed for a TNT charge of approximately the explosive equivalent of the charges used in the tests placed on the ground at the same

72.7 psi

Natural Period = 22.7 ms

K = 288.6 psi

0

0   0.25

Deflection, in
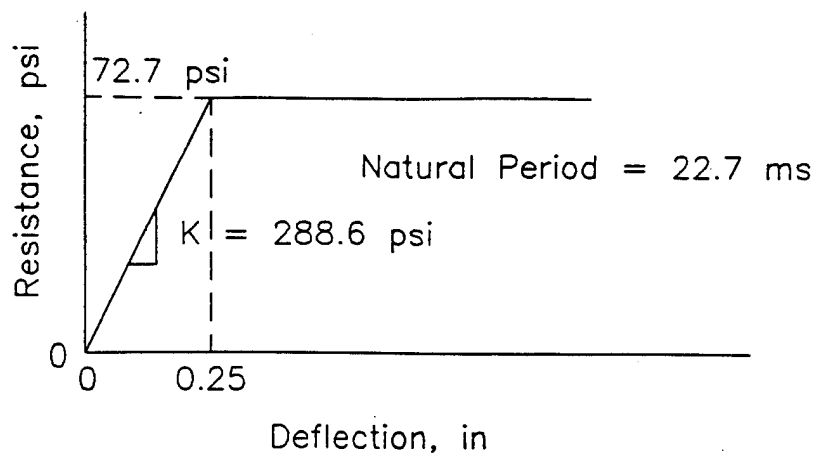
(a) Resistance of South Wall

81.2 psi

Natural Period = 22.1 ms

K = 376.7 psi

0

0   0.22

Deflection, in
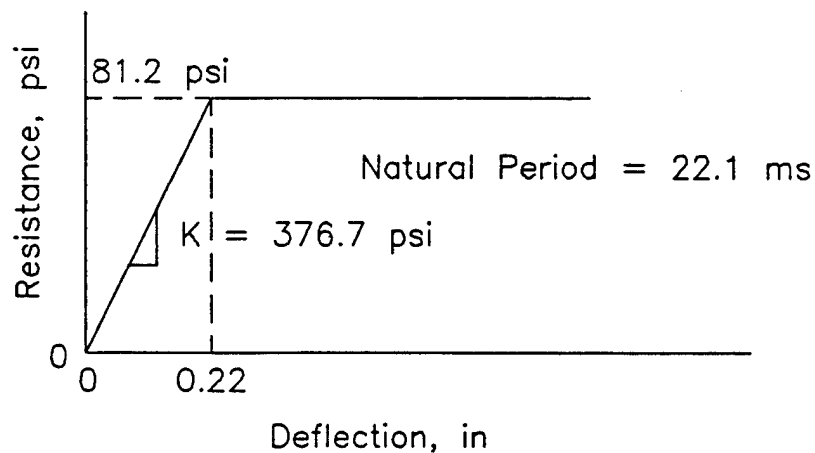
(b) Resistance of North Wall

Figure 49. Idealized Resistance Functions of Tyndall Structure Walls for use in UofI Program.

distance from the center of the wall as the actual charge location. These theoretical pressures and impulses, which were determined for a spherical charge using the CONWEP program that accompanied Reference 5, are as shown in Figure 50, and confirm the expected wide variation in pressure loading on the walls. But the pressure data shown on Figure 50 undoubtedly overestimate the airblast pressure loads that were actually produced on the walls because those data presumed a bare, hemispherical charge of TNT instead of a cylindrical cased explosive charge.

Because it was not possible to generate accurate equivalent SDOF loading functions from the test data for these walls, it was decided to analyze the walls using several loadings that would clearly bracket the pressure loadings actually felt by the walls, and compare the responses of the walls computed for those loadings with the corresponding measured maximum deflections. Those loadings are as shown in Figures 51 and 52. Loading (a) of Figure 51 is the measured loading

68
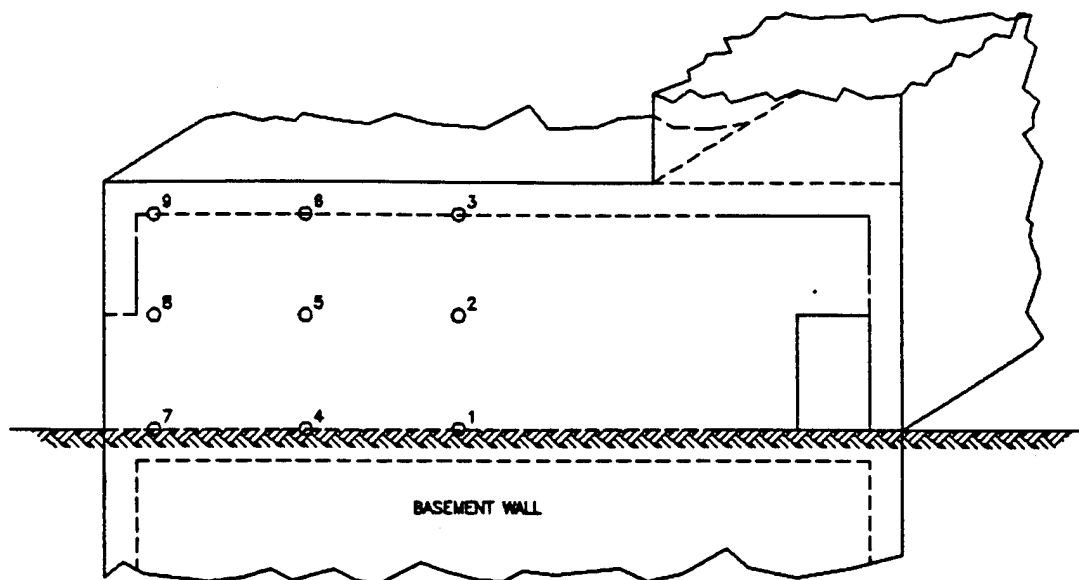
| Point on Wall | Theoretical Values | | | | |
| | Incident | | Normally Reflected | | |
	Peak Press. (psi)	Pos. Imp. (psi–ms)	Peak Press. (psi)	Pos. Imp. (psi–ms)	Angle of Incidence
1	726	147	5910	2150	0°
2	536	150	4096	1631	34°
3	294	182	1959	1024	53°
4	347	170	2407	1154	49°
5	293	182	1954	1022	53°
6	196	205	1178	781	61°
7	122	182	638	585	67°
8	113	177	578	560	68°
9	92	164	444	499	70°

Figure 50.   Theoretical Wall Pressures Produced by 500-Pound TNT Hemispherical Charge on the Ground Surface for the Tyndall Test Walls.

by gage PW2F, which is near the center of the south wall. Similarly, loading (a) of Figure 52 is the measured loading by gage PW4B, which is near the center of the north wall. Loadings (b) and (c) are identical for both walls because they represent theoretical values, which should be the same for both walls. Loading (b) is the full reflected pressure pulse as computed at the center of the wall (See point 2 on Figure 50), which is clearly an upper limit on the loadings for the walls.
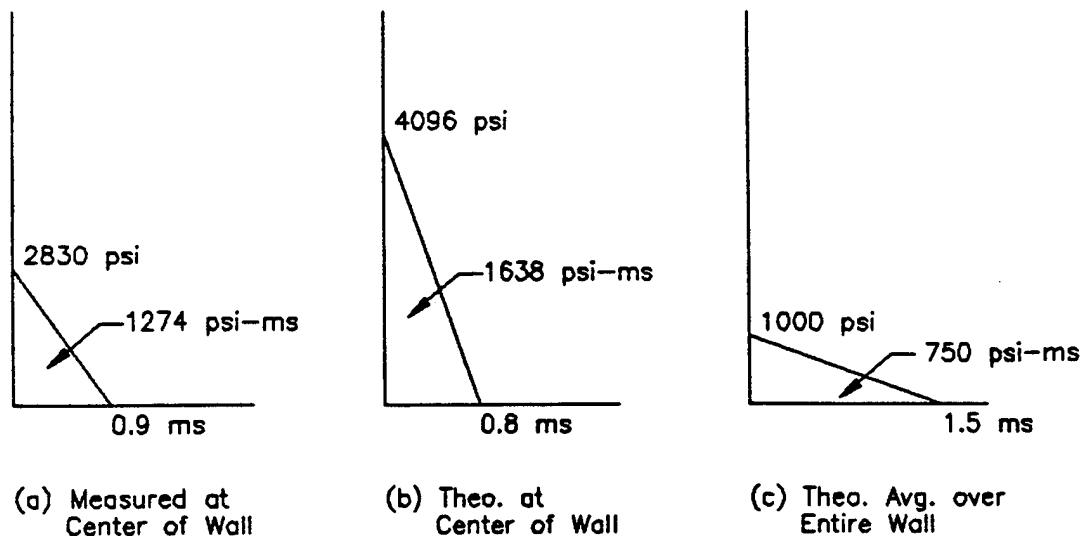
Figure 51.   Pressure Pulses Used in the Analysis of the Tyndall Structure, South
Wall, Test 6.
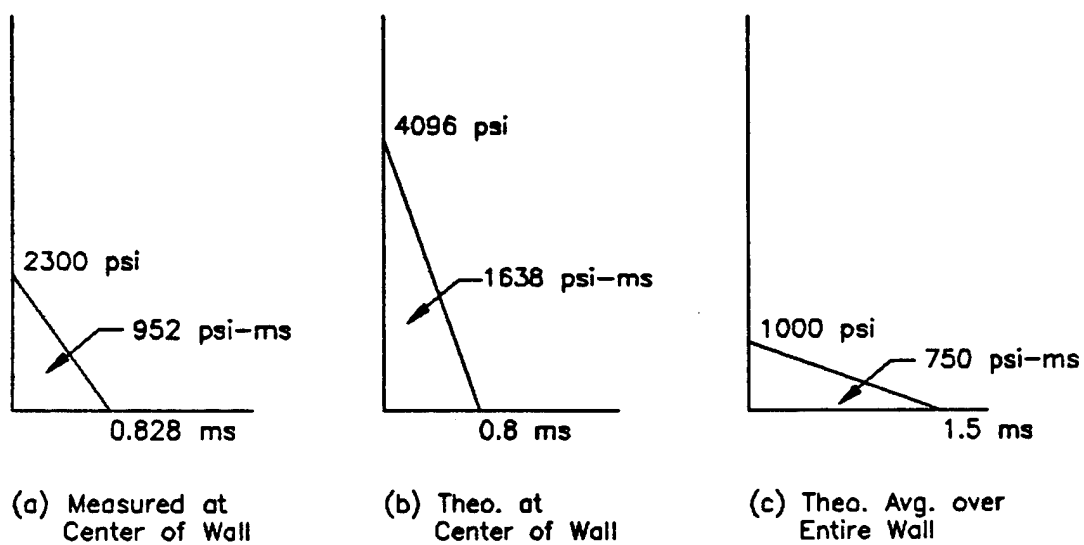
Figure 52.   Pressure Pulses Used in the Analysis of the Tyndall Structure, North
Wall, Test 10.

Loading (c) is an estimate of the average of the reflected impulses at the nine points identified on Figure 50, taking into account the angles of incidence with which the advancing pressure pulses impinged on the walls at those points. These reflected impulses were estimated using Figure 4.1 (Reference 11) in which it will be observed that, for angles of incidence less than about 40 degrees, the reflection factor for pressure is essentially unchanged; and that, for angles of incidence greater than about 40 degrees, that reflection factor decreases rapidly, approaching a value of 1.0 at an angle of incidence of 90 degrees. Assuming that the reflection factors for impulse vary as a function of angle of incidence in about the same way as do the reflection factors for peak pressure, it was estimated that the average reflected impulse on the wall was about 750 psi-ms, which, using an arbitrarily selected peak pressure of 1000 psi, produced the loading pulse of Figures 51(c) and 52(c). Because the pressure pulse generated in this way gives equal weight to the pressures as applied to all points on the wall surface, it diminishes the relative significance of the higher loadings over the central part of the wall whose contributions to the response of the wall are greater than are the contributions of the lower pressures near the edges of the wall. Consequently, this loading pulse is thought to be a reasonable lower bound on the actual pressure loadings to which the walls were subjected.

It will be noted that all of the loading pulses are depicted as triangles. No attempt was made to reflect the real nonlinear pressure decay because, in all cases, the effective load durations were sufficiently short relative to the periods of vibration of the walls that the loads could be treated as impulses, the actual shape of the pulse having little or no influence on the response of the wall.

2.   Response Computation Results

The maximum deflections of the two walls as computed by the UofI Program, using the idealized resistance functions, dynamic properties, and loading functions described above, are tabulated in Table 12, along with the corresponding measured maximum deflections as recorded in the tests. It will be noted from a review of those data, that the computed maximum deflections relate to the measured maximums about as expected, based on the loading pulses that were used in the computations.

Care should be taken not to conclude more from these results than is justified, but they do demonstrate the applicability of the UofI program to the study of the responses of these walls to airblast pressures produced by the detonation of conventional bombs, provided reasonable estimates of the blast pressure loadings felt by the walls can be determined.

TABLE 12. COMPARISON OF MEASURED AND COMPUTED RESPONSES OF THE TYNDALL AFB
STRUCTURES USING THE UofI PROGRAM.

Wall	Measured maximum deflection (in.)	Computed maximum deflection (in.)		
		Loading A	Loading B	Loading C
South	2.46	3.07	5.00	1.14
North	1.94	1.30	3.64	0.84

SECTION V

PREDICTION OF THE BEHAVIOR OF THE TEST STRUCTURES USING SASDE

A. BRIEF DESCRIPTION OF THE PROGRAM

This program, which is microcomputer MS/PC DOS based, is identified as Structural Analysis for Severe Dynamic Environments (SASDE). It is described in detail in its user's manual (Reference 15), as well as in several published papers (References 16 and 17). Its primary features are summarized briefly in the following paragraphs.

The program was developed to compute the responses of reinforced concrete slabs and walls of closed boxes to dynamically applied forces. It uses SDOF idealizations to compute responses in both flexure and shear, employing two uncoupled equations of motion. As described by its developer, Dr. T. Krauthammer (Reference 16), "For each time step, the motions of the slab center are computed (Reference 17), from which it is possible to derive a distribution of inertia forces on the slab, and then combine such forces with the applied load for obtaining a shear force at the supports, as described by Biggs (Reference 3) and Keenan (Reference 18). That shear force is used to drive the second SDOF system which provides the shearing motions at the supports. The slab responses at the center and at the supports are compared to failure criteria, which include an ultimate tensile strain of reinforcing bars, a critical shear slip, delta max, at the supports, and also a central deflection that may limit the serviceability of the structure."

The time history responses are computed using the Newmark Beta Method, which was also employed in the program discussed in Section IV, and is described in Reference 9.

This program accepts the following as input data to describe the structure, its environment, and the nature of its loading.

(a) Identification of the structure as a slab or a closed box.

(b) Dimensions of the structure.

(c) Support and/or edge restraint conditions.

(d) Reinforcement amounts or percentages, depending on the type of structure.

(e) Physical properties of the materials and factors that enhance the strength parameters for strain rate effects.

(f) Constants that must be applied to the distributed masses and loads of the actual systems to obtain equivalent SDOF systems, mass factors (MF), computational parameters, and damping.

(g) A specified time-dependent loading function, or the type, size, and location of the explosive charge that will produce the loading.

(h) Depth of burial and properties of the surrounding soil, if the structure is buried.

Using these data, the program generates internally the loading and resistance functions of the idealized system, which is then analyzed to determine

73

the behavior of the structure, and its potential for failure in either flexure or shear.

It should be noted that this program differs in two respects from the program described in the preceding section. First, and perhaps most significantly, it evaluates the failure potential of the structure, or structural element, in both flexure and shear, while the program described earlier considers flexural behavior only. Secondly, it computes the equivalent SDOF resistance functions internally, from the given structural dimensions and material properties, and has the capability of computing the equivalent loading function from a given charge and detonation location if the time-dependent loading function is not input directly. For the program described in the preceding section, the loading must be input directly as a multilinear force-time function. In these studies, a pressure-time function was provided so this added capability of SASDE was not used. The dynamic response computational methodologies, both of which are direct applications of the Newmark Beta Method, are essentially identical.

As noted earlier, SASDE was developed to compute the structural response of reinforced concrete slab and closed box-type structures to the pressure effects of either conventional or nuclear explosions. The types of problems within these general categories that can be treated by the program are identified in Figure 53.

As originally developed, the program treated rather narrowly defined box-type (BOX) and slab-type (SLB) structures. Its capabilities were later expanded to permit greater flexibility in the specification of edge support and restraint conditions of the independent slabs, and of the wall, roof, or floor elements of the box being studied. These more recent structural types are identified in the program as "New Box" (NBX) and "New Slab" (NSL), and, as noted in Figure 53, permit the analysis of either fixed one-way slabs, or of two-way slabs with a variety of support conditions. Additionally, for both the original and the later formulations, the loading functions can be input explicitly as multilinear pressure-time functions, or they can be input as specified explosive charges, from which the time-dependent loading functions that are needed for the analyses are generated internally by the program. Further, as indicated in Figure 53, box-type structures can be analyzed when they are either above ground (UNB) or buried (BUR). In the latter case, soil properties must also be specified because the nature of the loading imparted to a buried box is strongly influenced by the nature of the soil in which it lies. In either the BUR or UNB cases, the loading that is calculated can be from a conventional weapon charge (CON) or from a nuclear weapon (NUC). In a similar manner, in both the original and later forms, the resistance functions required in the analyses are computed by the program from the structural geometry and material properties that are provided as program input.
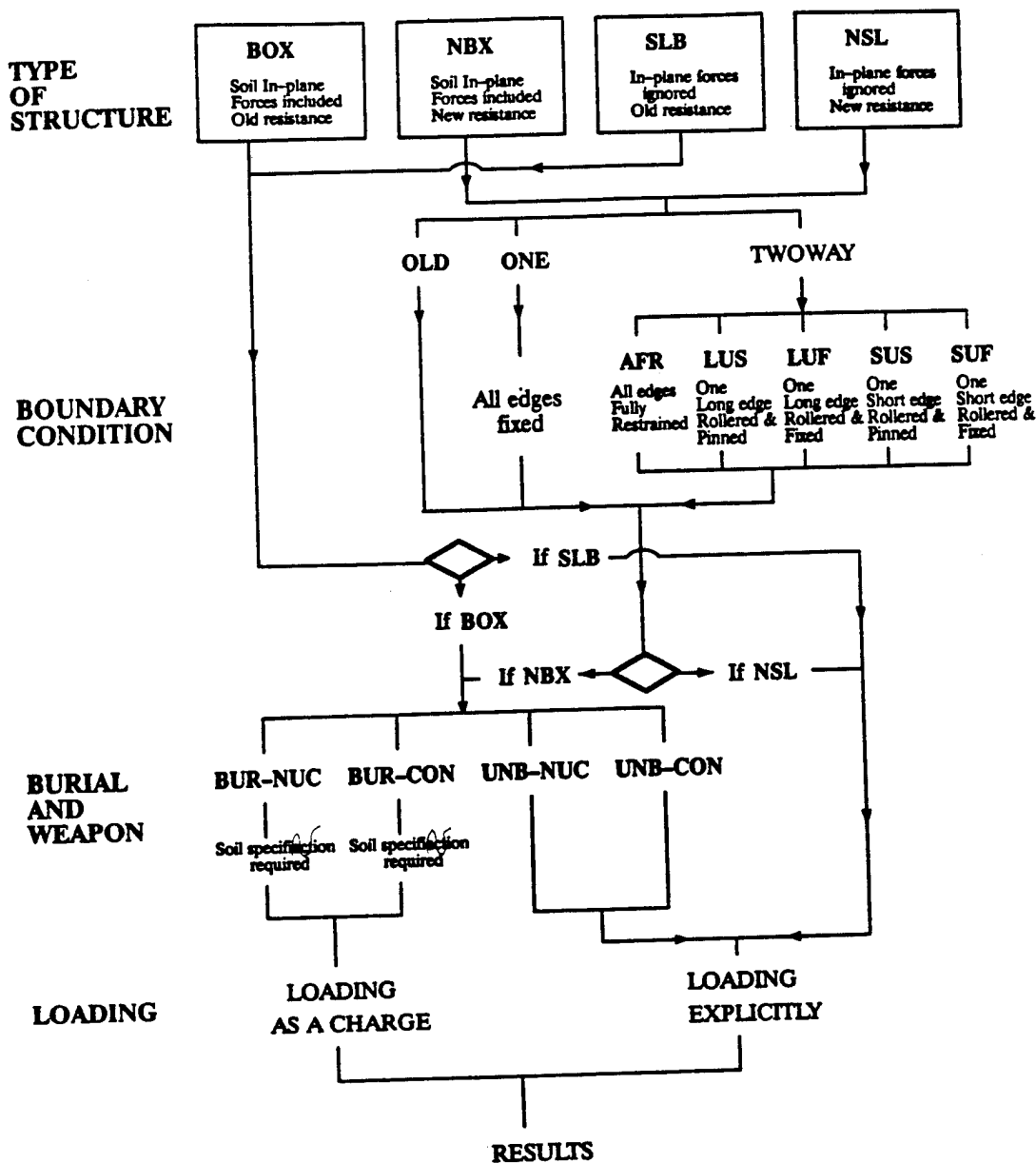
Figure 53. Problem Characterization Options Available in SASDE.

B. APPLICATION OF THE PROGRAM TO THE IDF STRUCTURES

1. Selection of Parameters

Because the resistance functions employed in this program are computed internally, a number of constraining or defining parameters must be input, in addition to the basic geometry of the slab or box, as well as the relevant physical properties of the concrete and reinforcing steel of which the structure being analyzed is constructed. These several constraining, or defining, parameters are identified and briefly discussed in the paragraphs that follow.

a. Resistance Function

As seen in Figure 53, *old resistance* is specified for the original programs, BOX and SLB, while *new resistance* is specified for the more recently developed programs, NBX and NSL. The old and new resistance functions for the flexural modes of response of the slabs, either as independent units or as elements of box-type structures, are described in References 16, 17, 19, and 20. The old functions are the conventional pressure versus displacement functions for reinforced concrete slabs that are completely unrestrained against in-plane motions at their supports.

In the new flexural model for slab behavior, the resistance function enhancement due to membrane effects in both compression and tension are included. Initially, the elastic flexural resistance gives the slope of the curve. At a deflection of approximately one-half the slab depth, the resistance is assumed to peak with the combination of flexural resistance and arch action resulting from in-plane compression at the supports. The resistance then falls off, and at a deflection of approximately twice the slab depth reaches a point in which the tension membrane action becomes the primary mechanism and the resistance increases again until failure of the reinforcement in tension.

The old resistance model for shear was based on a method proposed by Keenan (References 18 and 21). The revised or new model is based on direct interface shear resistance investigations by Mattock and Hawkins, as modified and documented by Murtha and Holland (Reference 22), followed by further modifications by Krauthammer et al. in Reference 16. The original resistance function was a nonlinear relationship between shear stress and shear slip at the shear interface. Krauthammer et al., (Reference 16) modified this original function to include the effects of load reversal by adding rules for slopes of the load-resistance paths when unloading occurs.

b. Mass Factor

The mass factor (MF) is the ratio of the equivalent SDOF mass to that of the total distributed mass of the original slab. The MF can be further defined as the integral of the distributed mass multiplied by the square of the displacement (in the mode under consideration), divided by the total distributed mass of the original slab. This implies that the MF will be different if the mode shape is different, which it will be if the deformation is elastic, or plastic, or somewhere in between these extreme cases. The values of MF given in Reference 3 for a fixed-fixed one-way slab are 0.41, 0.50, and 0.33 respectively, for the elastic, elastic-plastic, and plastic cases. For a fixed-fixed two-way slab with an aspect ratio of 2, the same reference gives values of 0.31, 0.41, and 0.25, respectively. Thus, the MF should change during the analysis as the shape of the responding slab changes, and depends also on the boundary conditions of the slab.

The test walls in this study (IDF structure) are cast monolithically with the roof and side walls, so the top and end edge conditions are probably closer to fixed than they are pinned. Within the edge support options permitted in this

program (see Figure 53), in the studies that follow these edges have been assumed to be fixed. The bottom edge continues below the floor to a footing, and therefore its support conditions lie between a fixed and a pinned condition, though where it is in this range is not clear. The program can allow this edge to be pinned or fixed if it is treated as a two-way slab, but if the one-way slab option is used, both ends are automatically assumed fixed. In the two-way slab problems, the bottom edge was assumed pinned, on the assumption that the real condition is probably closer to being pinned than fixed.

The MF selected for each test simulation in the IDF series was based on the maximum response of the test in question. If the response was primarily elastic, then the elastic MF was used, and if the maximum response was well into the plastic range, perhaps greater than three times the yield deflection, the plastic MF was used. When the response was in the plastic range less than about two times the elastic deflection, the elastic-plastic MF was used.

c. Load Factor

The load factor (the ratio of the force that must be applied to the equivalent mass of the idealized SDOF system to the total force that is applied to the surface of the slab of the real system) is computed to be of such a value that the total work done by the loads of the real and idealized systems are equal. The program does not require this factor as input, as it is programmed into the code. This can be done because the structure is assumed to be uniformly loaded, so the deflected shape and point of maximum deflection are assumed to be known for each case.

d. Material Strain Rate Effects

When concrete and steel are loaded rapidly, their strength characteristics are increased by strain rate effects; the amount of increase depends on the rate at which the structure responds to the loading. These effects are introduced into the program as constants by which the static properties of the materials are multiplied. In reality, this factor might be different each time the limit of the material strength is reached, but the factors are not known well enough to justify this level of detail in the solution.

The program requires the specification of strain rate enhancement factors for the yield strength of steel, for the crushing strength of concrete, and for the resistance. The first two of these enhancement factors are clearly understood, as observed in the preceding paragraph, but neither the justification for nor the significance of the *resistance enhancement factor* could be ascertained from the program description. However, limited parametric studies conducted as a part of the investigations reported here indicated that changes in that factor had no effect on the computed responses of the structures being studied. Consequently, then in these studies, all three of these enhancement factors were taken to be equal at a value of 1.30. This 30 percent enhancement factor is consistent with data contained in References 28 and 29 for strain rates

77

for steel and concrete comparable to those that should have been experienced in the IDF and Tyndall tests discussed here.

e.   Lateral Stiffness

In the early stages of flexural response of a slab, there is little tendency for in-plane dimension changes; however, as the deformation continues there will be a tendency for the edges to move outward at the bottom. This is particularly true if the slab is deep, and, if there is lateral resistance to this moment, it will lead to additional resistance from arch action in the slab. If the deformation continues, then eventually the arch action will be dissipated, the direction of the lateral forces at the supports will reverse, and a resistance will build up due to tensile membrane forces. The program includes each of these stages of behavior in the resistance function.

The SASDE program requires that the user provide, as input, the magnitude of the lateral stiffness, the resistance of the slab supports to outward motion parallel to the slab surface. In a given case, this quantity clearly depends on the manner in which the slab in question is framed into its supporting elements, which may be other walls, a roof, and/or floor slabs, and the flexibility of those elements. General guidelines for the estimation of this parameter are given in Reference 20, and additional data, for slabs with the smaller aspect ratios normally associated with protective structures, are provided in Reference 21. The test wall under study had a span to thickness ratio of 8, which is smaller than the reported tests in Reference 20, that were of the order of 20, but close to that of test W14-84 of Reference 21.

Theoretical studies indicate that the slab resistance would not be influenced significantly by in-plane forces until the flexural displacements of the slab reach one-quarter to one-half the thickness of the slab, depending on the lateral support stiffness. The residual displacements of the IDF test walls that responded in flexure were much smaller than this range; thus, it is not expected that the in-plane forces should influence the response of the test walls significantly. Furthermore, in this study the bottom of the wall in question is attached to a footing and the top is cast monolithically with a roof that spans completely across the top of the structure and is supported at its far end by another wall. Resistance to in-plane movement of the test wall comes from bending the roof and far wall. Using the procedure suggested in the program manual for its computation, this resistance is less than 100 lb-in./in.

f.   Loading

As observed earlier, the loading can be input directly as a multilinear pressure-time function that is applied to the slab surface, or an explosive charge and its location with respect to the wall being loaded can be specified, from which the program will compute the loading to be used in the analysis. To facilitate comparison of results, the same multilinear loading functions that were used in the analyses of Section IV were also used in the SASDE analyses. Hence, the loadings used in the SASDE studies were the pressure-time functions

that were measured at the center point of the walls, idealized and linearized as described in Section IV. These loading functions are summarized, as peak pressures and total impulses, in the data of Table 9, and are shown in Appendix A.

g. Time Step

The maximum number of time steps allowed by the program is 500. A time step of 0.0002 second was generally used. This was suitable for the numerical integration method employed, and provided a computed response time of 0.100 second, which was long enough to include the maximum and residual deflections of the wall.

h. Damping Ratio

The hysteretic process associated with plastic yielding of the structure is the most important mechanism by which energy is absorbed by the system. Damping is another mechanism for dissipating energy, and the amount dissipated depends on the damping ratio. This ratio is defined as the ratio of damping present to the critical damping. Values of 5 to 10 percent of critical are generally accepted as reasonable for reinforced concrete structures subjected to earthquake loading, and the same range is considered to be appropriate for the case being considered here. A value of 5 percent was used for the SASDE analyses.

For blast loading, it is generally agreed that damping is not of great importance if the initial response to maximum deformation is the prime consideration. However, if the full response, including the residual response after the vibration has stopped is of concern, damping becomes more important.

The significance of the damping effect on response depends on how large it is relative to the hysteretic effects. If the response is well into the plastic range, the energy loss due to hysteretic effects will be large, and the influence of damping will be relatively small. However, if the response remains in or near the elastic range, damping effects will be the more significant of the two effects. Further, with successive tests and cumulative damage, the damping will change for each test.

2. Comparison of Computations With Test Results

Efforts to use SASDE to analyze the IDF test structures as two-way slabs were, in general, unsuccessful. The resistance level computed for this case by the program was clearly incorrect, being over twice the strength of the wall as carefully determined by hand calculation. Consequently, deflections computed using this very high resistance were unrealistically low. No satisfactory explanation for the erroneous resistance level could be found. A possible explanation is that it is associated with an in-plane force amplification that is built into the program, but which is largely inapplicable to the present case.

Similarly, efforts to study the behavior of the test walls using the one-way slab model in SASDE achieved only limited success. The difficulty in using

79

the one-way slab program results, at least in part, from the fact that SASDE requires that both ends of the slab be fixed and that it be reinforced symmetrically, which was not the case that existed in the walls of the IDF structures. The reinforcement of the outside face was different from the inside face at the top and bottom of the wall. However, because the flexural resistance level of the slab was known from hand calculations to be approximately 33 psi, it was possible to select a set of symmetrical reinforcement percentages which would allow SASDE to compute a resistance level that agreed closely with this value.

However, the program would not run unless the level of lateral stiffness that was specified was greater than would have been realistic for the IDF structures; it appears that the minimum value allowed depended on the reinforcement ratio and MF specified. Nevertheless, an artificial set of reinforcement and lateral stiffness parameters was found that gave a realistic flexural resistance function, and to become more familiar with the program, it was exercised using those parameters. The reinforcement used was 0.0442 in.^{2}/in. for the inside face and 0.0408 in.^{2}/in. for the outside face. The lateral support stiffness required for a solution varied from 300 to 900 lb-in./in. The deflections are so low for the IDF structures that these lateral stiffnesses will not affect the results significantly. These values, when used in combination with actual geometry of the wall, static material yield strengths of 31,290 psi and 3220 psi for reinforcing steel and concrete, respectively, and a strain-rate multiplier of 1.30 for steel and concrete, resulted in the generation by SASDE of the resistance function shown on Figure 54. The corresponding shear resistance function is shown in Figure 55.

Before using these resistance functions to study directly the behavior of the walls in each of the several tests that were conducted on them, the flexural resistance of the one-way slab model was used in a series of runs to assess the extent to which the computed response of the walls might be influenced by variations in those parameters that possessed the greatest degree of uncertainty. The results of these parametric studies are shown in Figures 56-59, in which the effects of variations in strain-rate enhancement, damping, MF, and lateral stiffness, respectively, are shown. These parametric studies were run using the loading function that was developed for Test 3 from the measured pressure-time data at the center of the wall for that test. The peak pressure and the total impulse associated with that loading are summarized in Table 9, and the pressure-time pulse is shown in Appendix A.

The curves of Figure 56 show that only the strain rate enhancement factor for yield of the reinforcement had any significant effect on the response. This is reasonable because the yield plateau was reached by the reinforcement but not the ultimate region during the slab response, and the concrete strength does not affect the response a great deal in flexural computation.

To study the effect of damping on the residual response, a series of problems was run with damping ratios of 0, 3, 5, and 7 percent using the same one-way slab and loading for Test 3 described above, and holding the other

80
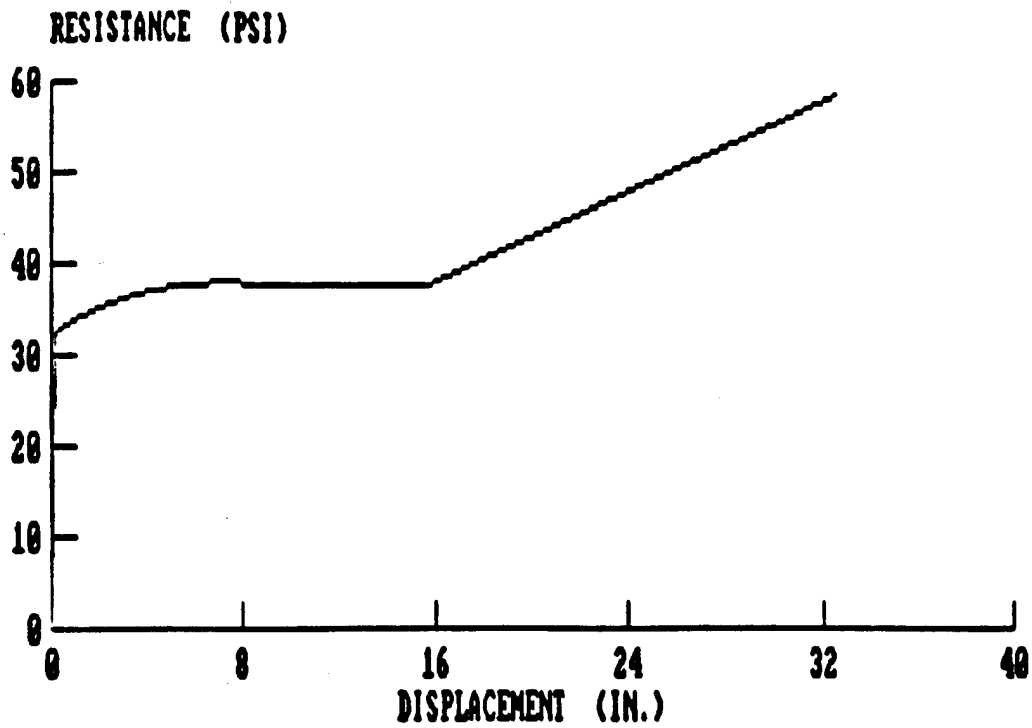
RESISTANCE (PSI)

Figure 54.   Static Resistance Function for Flexure and Membrane Action by SASDE
for IDF Test Walls.

SHEAR RESISTANCE
HAWKINS' MODEL
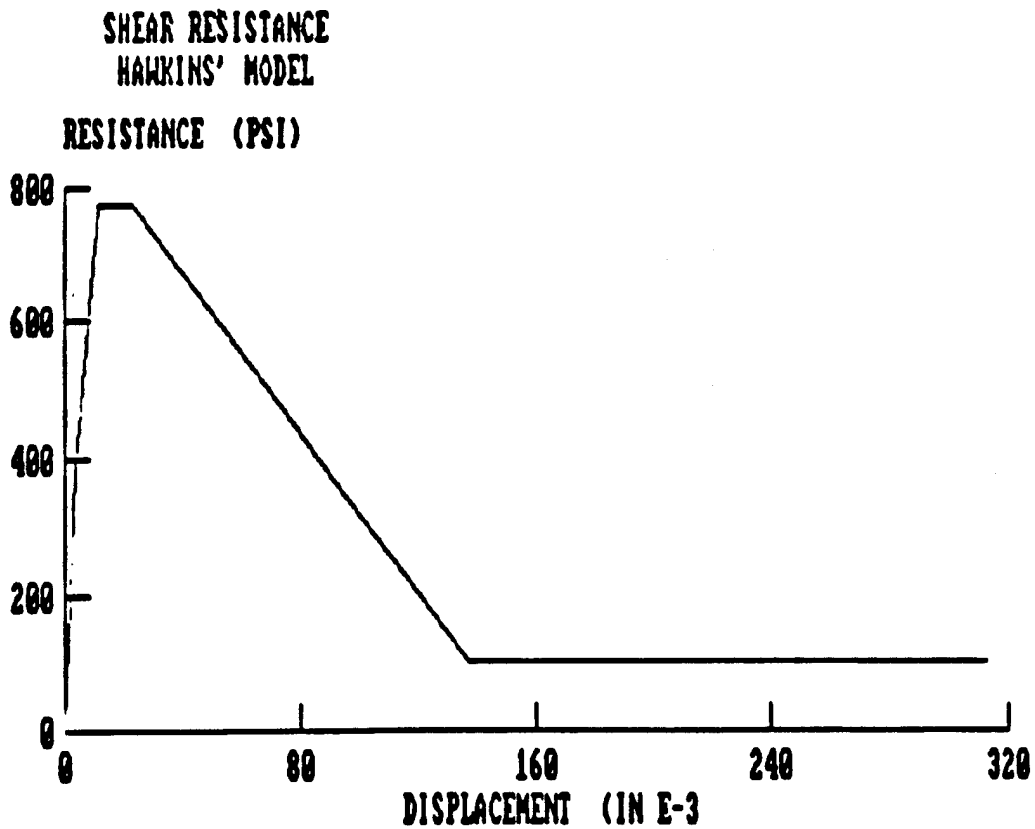
RESISTANCE (PSI)

Figure 55.   Static Resistance Function for Shear at the Support by SASDE for IDF
Test Walls.
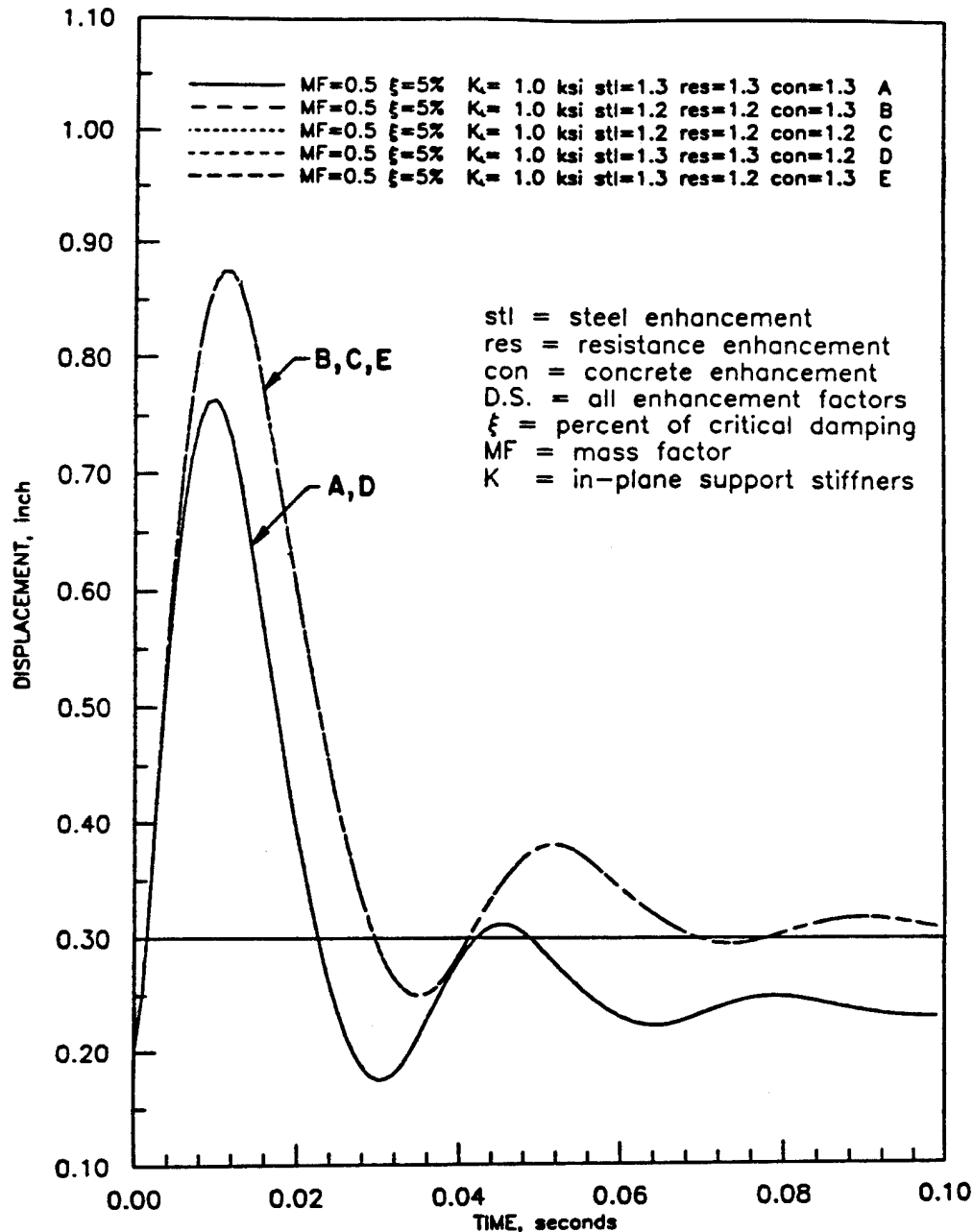
Figure 56.   Influence of Material Strain Rate Effects on the Wall Response
             Computed by SASDE.

parameters constant. The results are shown in Figure 57. The energy absorbed from yielding is enough to reduce the vibration significantly after the first peak. The influence of damping on the magnitude of the maximum deflection is modestly important, but its influence on the residual displacement is quite small.

Figure 58 demonstrates the effect on the displacement history for the one-way slab described above of using MF values of 0.41, 0.50, and 0.33. The effect on the residual displacement is almost proportional to the MF in this case, and

82
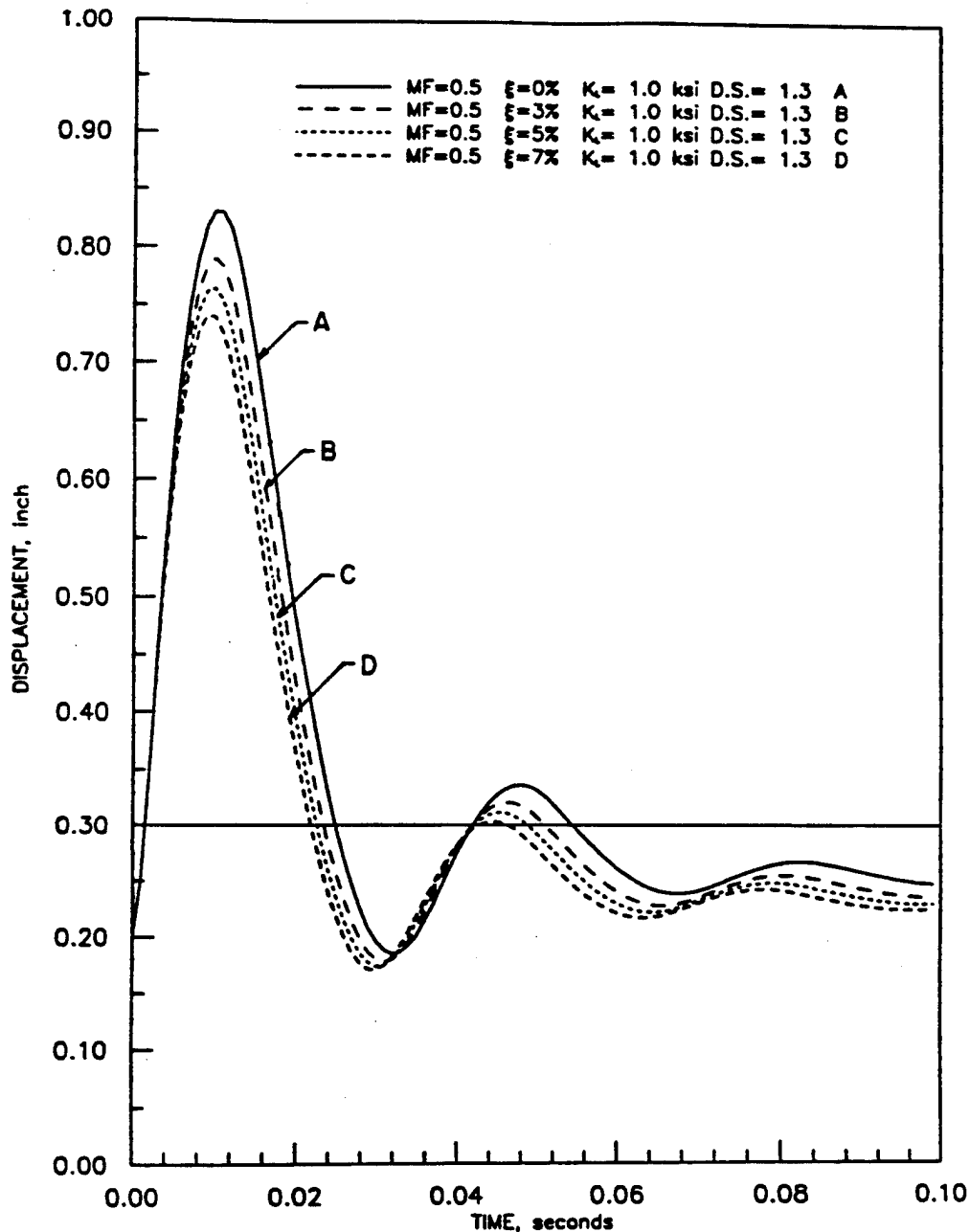
Figure 57. Influence of Damping Ratio on the Wall Response Computed by SASDE.

the effect on the peak displacements are somewhat larger than on the residual displacements. Thus, selection of the appropriate MF is important to the proper use of the program.

The SASDE model includes the effects of compression and tension membrane forces result from lateral restraint of the supports, on the flexural resistance of the slab. The variation of resistance with displacement as determined by SASDE, is shown in Figure 54 for the one-way slab described above. This figure shows a linear rise to yield of the reinforcement and then a region in which the
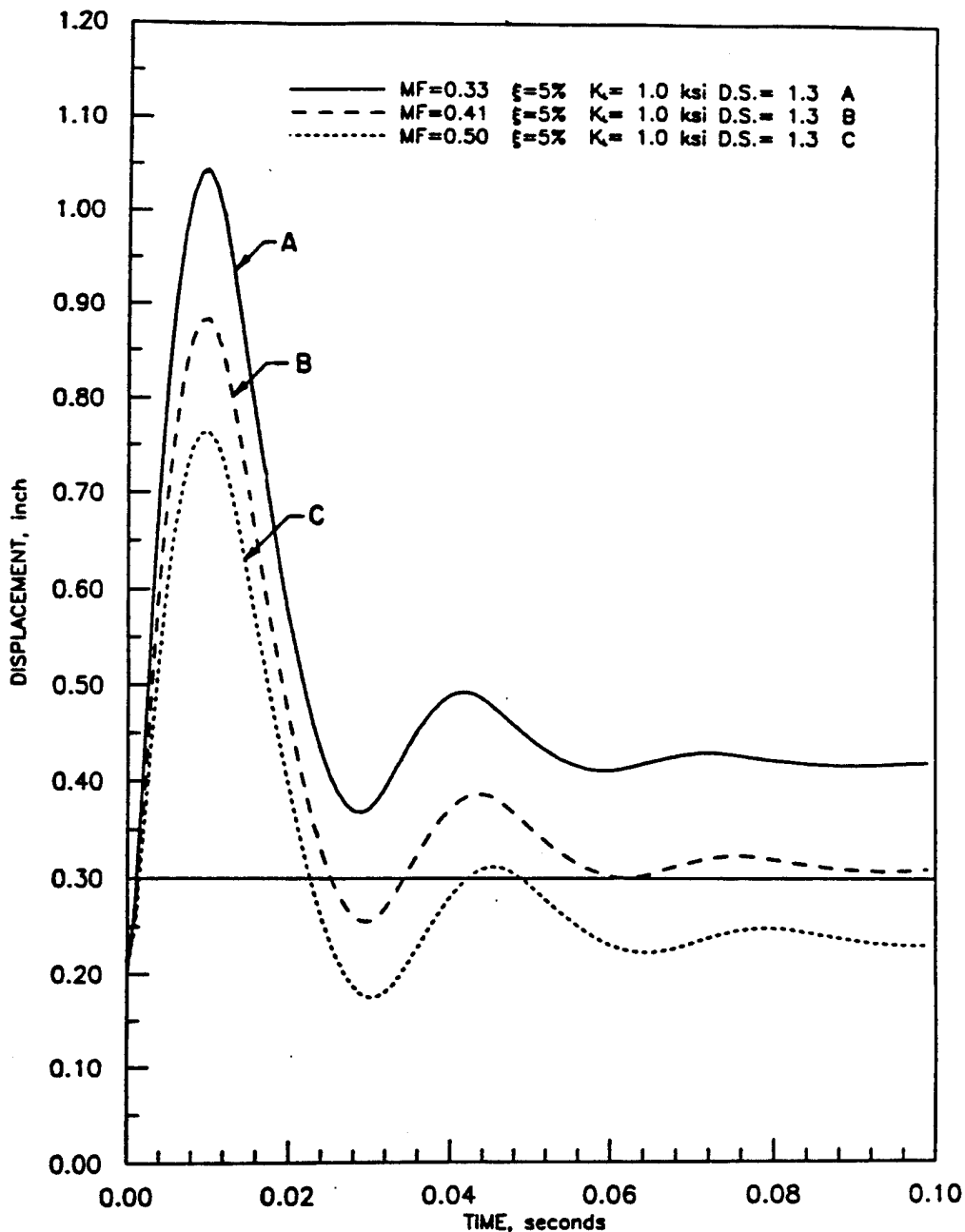
Figure 58. Influence of Mass Factor on the Wall Response Computed by SASDE.

resistance rises only slightly as the deflection continues. The slight rise is due to the small support lateral stiffness. At a deflection of about 9 inches the resistance begins to increase rapidly due to the tension membrane effect. The test slabs do not reach deflections large enough to get into this region.

The influence of lateral support stiffness on the test slabs subjected to the Test 3 loading is shown in Figure 59. The problem was run with lateral stiffnesses of 0.001, 1, 100, 1000, and 10,000 lb-in./in. There is no observable
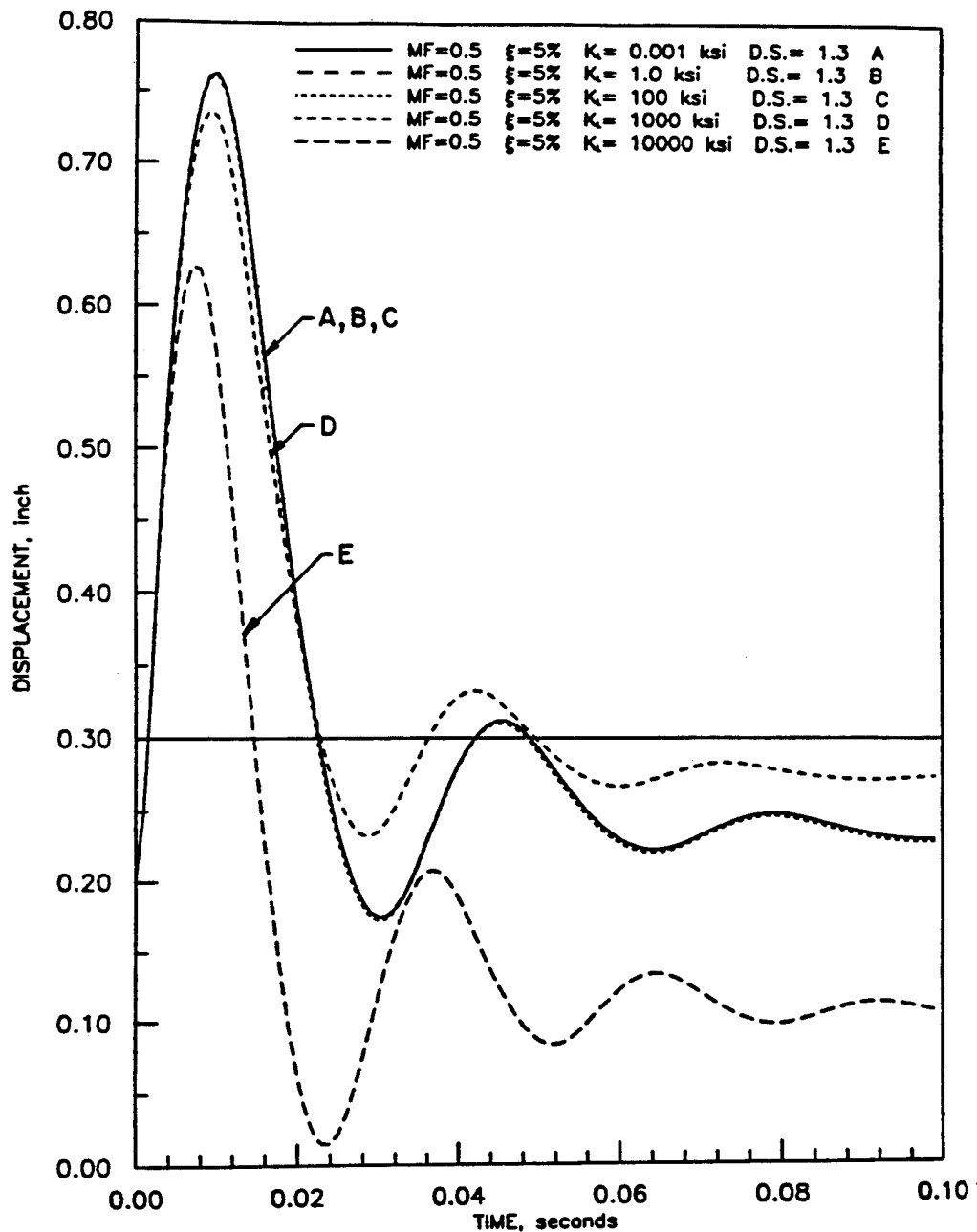
Figure 59. Influence of Support Lateral Stiffness on the Wall Response Computed by SASDE.

difference in the responses for the first three cases, but for lateral stiffness greater than 100 lb-in./in., the effects become significant.

The results of the SASDE analyses of the IDF test walls are summarized in Table 13. Shown in that table are not only the results of the calculations, but also the measured residual deflections with which the computed deflections should be compared. Included also are the lateral support stiffnesses that had to be used to get solutions, as well as the MFs that were employed for each of the

85

tests. It should also be noted that the calculations reported in that table employed the resistance functions of Figures 54 and 55, which, as discussed earlier, were somewhat contrived. Except as noted on the table, the loading functions that were used were the same measured functions that were used in the UofI program analyses that were reported in the previous section. All of the SASDE analyses assumed a damping factor of 5 percent of critical.

The deflection-time histories that were produced by SASDE for this test series, and which produced the data which are summarized in Table 13, are shown in Figures 60-70. As will be noticed in Table 13, the MFs were adjusted for each test to correspond to the ranges of response that were computed for each test. In Tests 8 and 9, the program was run using two different MFs to demonstrate the significance of that variable.

Because only the residual deflections were recorded in the tests, those results should be compared with computed residual deflections. To facilitate such a comparison, both calculated peak and residual deflections are shown in Table 13. Each calculation presumed the initial deflection to be zero, and the resulting peak deflections and residual deflections are shown in columns 4 and

TABLE 13.   COMPARISON OF MEASURED AND COMPUTED RESPONSES OF THE IDF STRUCTURES USING THE SASDE PROGRAM.

Test	MF[a]	Lateral stiffness (lb-in./in.)	Calc. peak defl. (in.)	Calc. resid. defl. (in.)	Calc. accum. resid. defl. (in.)	Meas. accum. resid. defl. (in.)
1	0.45	825	0.13	0	0	0
2	0.50	825	0.23	0	0	0.2
3	0.50	825	0.41	0.05	0.05	0.3
4	0.50	825	0.50	0.09	0.14	0.6
5	0.45	310	0.16	0	0	0
6	0.50	310	0.51	0.10	0.10	0
7	0.50	825	1.36[b]	0.65	0.75	0.6
8	0.33 / 0.50	310	5.0[bc] / 3.3[bc]	3.6 / 2.3	3.0	1.0
9	0.33 / 0.50	310	4.0[b] / 2.75[b]	2.8 / 1.5	4.5	~16 shear failure

[a] MF = Mass factor: Elastic = 0.45, Elastic-plastic = 0.50, Plastic = 0.33
[b] Shear failure was predicted by the program
[c] In the absence of measured pressure data, theoretical pressure data were used in the analysis for Test 8.

86

DISPLACEMENT (Inches)
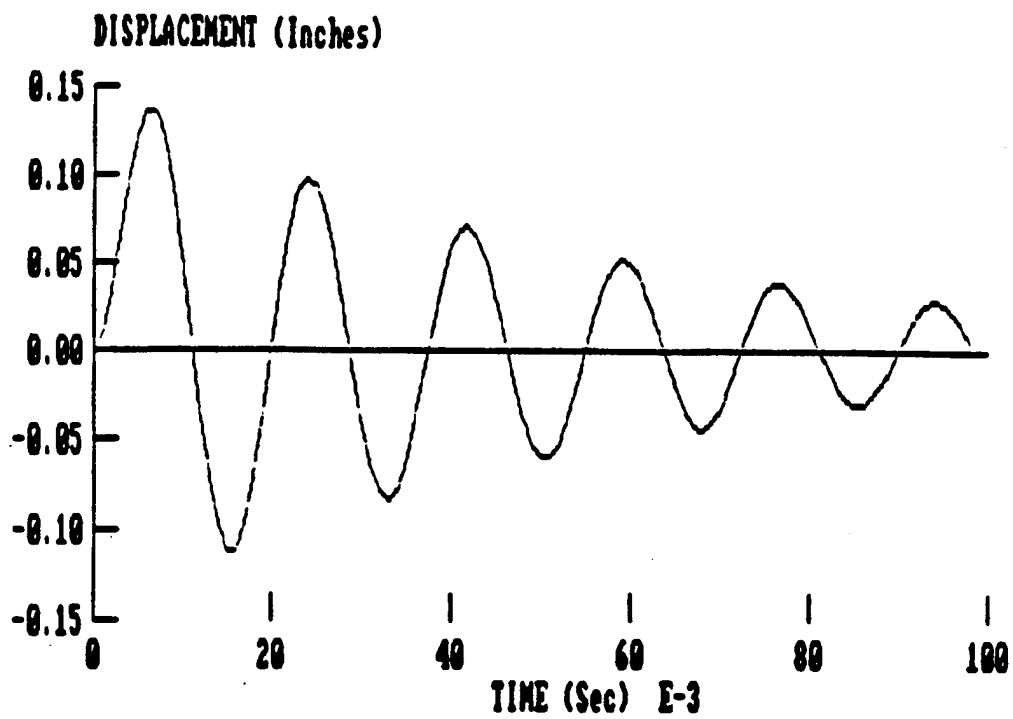
Figure 60. SASDE Analysis Results, IDF Test 1.

DISPLACEMENT (Inches)
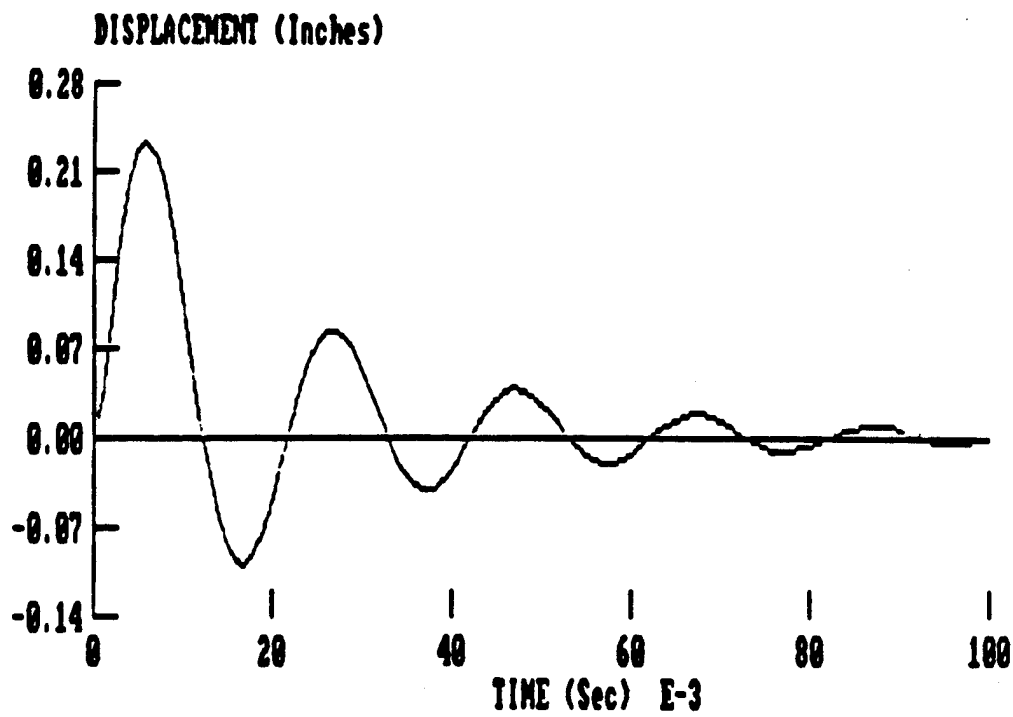
Figure 61. SASDE Analysis Results, IDF Test 2.

87
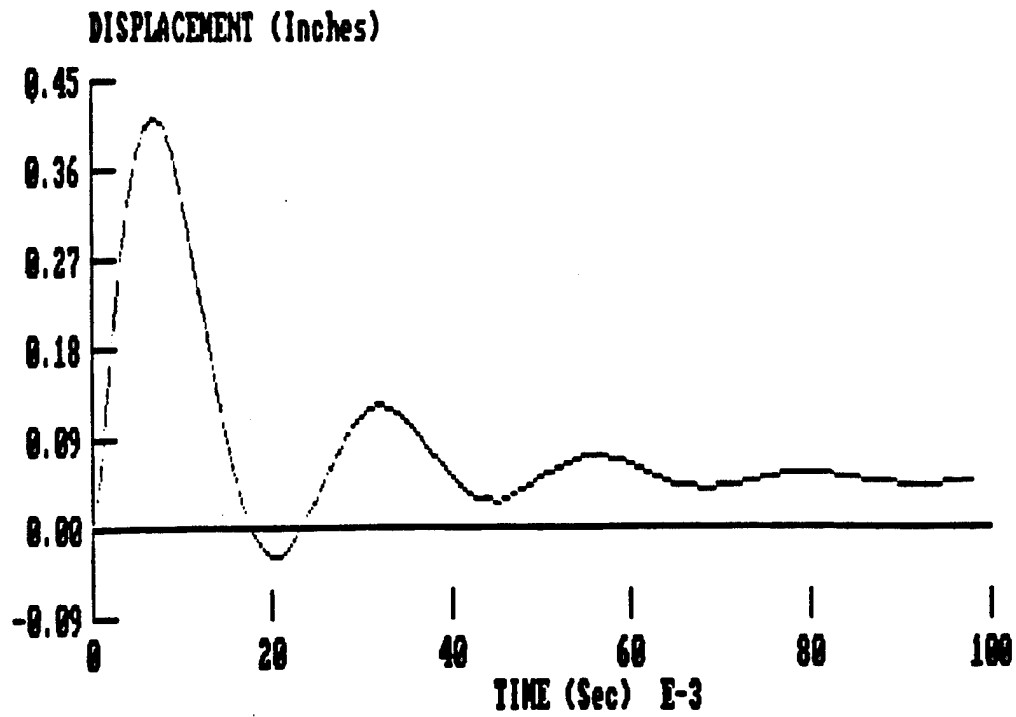
Figure 62. SASDE Analysis Results, IDF Test 3.
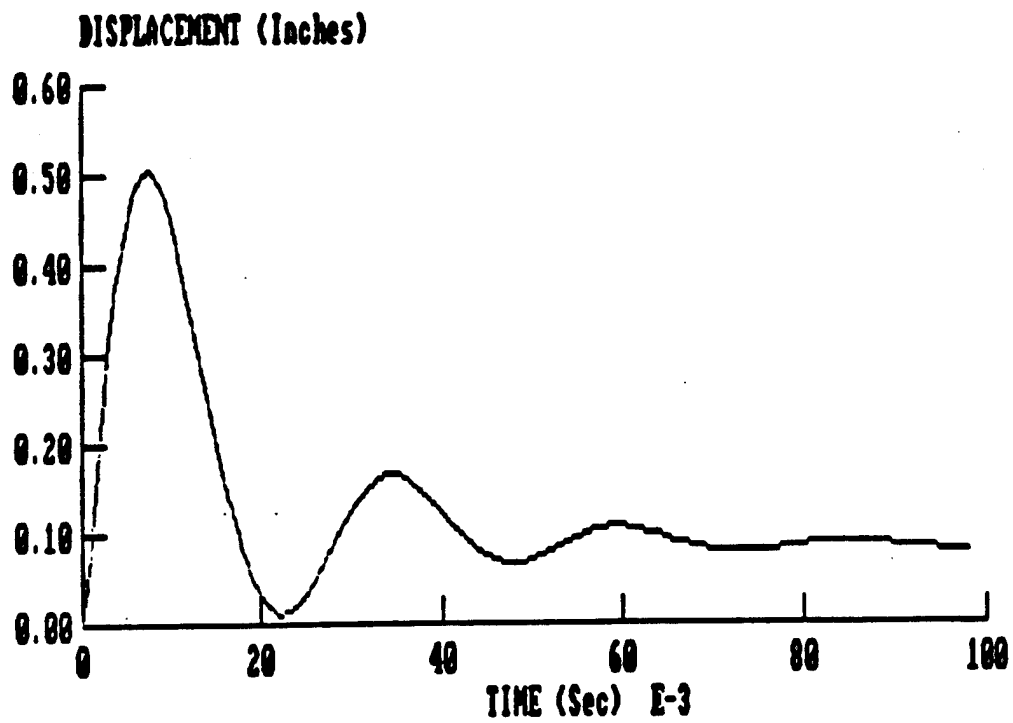
Figure 63. SASDE Analysis Results, IDF Test 4.

DISPLACEMENT (Inches)
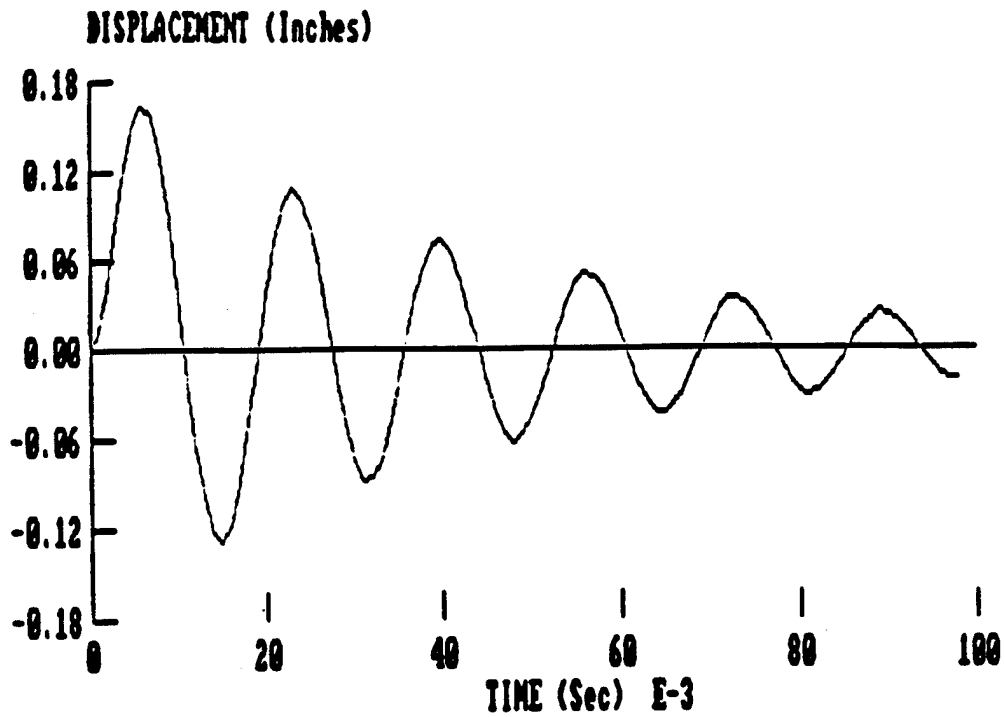
Figure 64.   SASDE Analysis Results, IDF Test 5.

DISPLACEMENT (Inches)
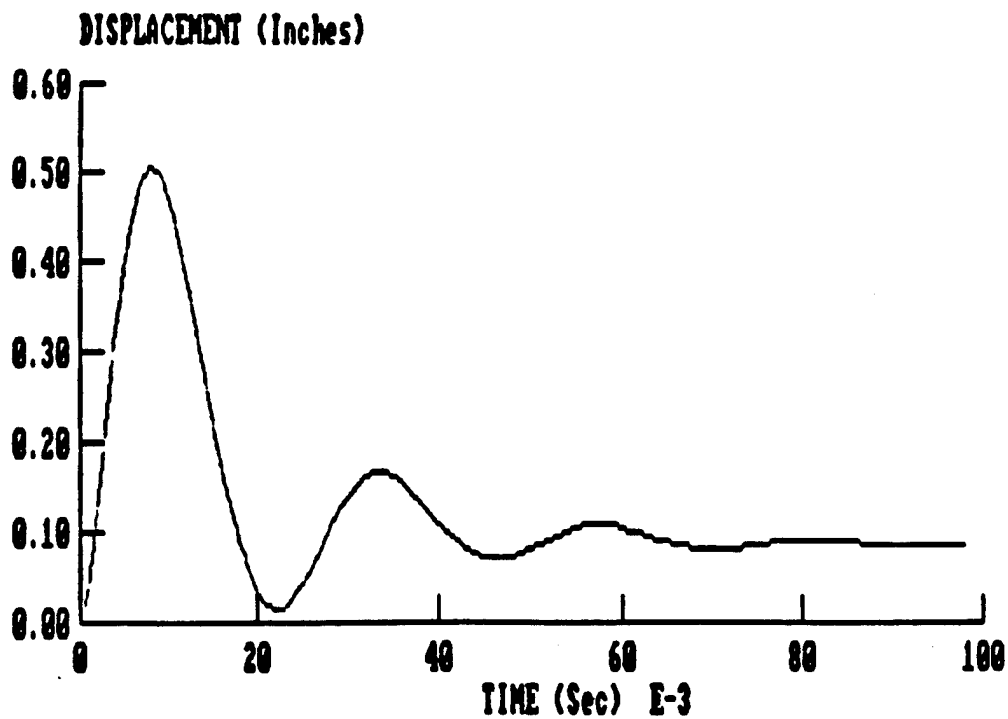
Figure 65.   SASDE Analysis Results, IDF Test 6.

89
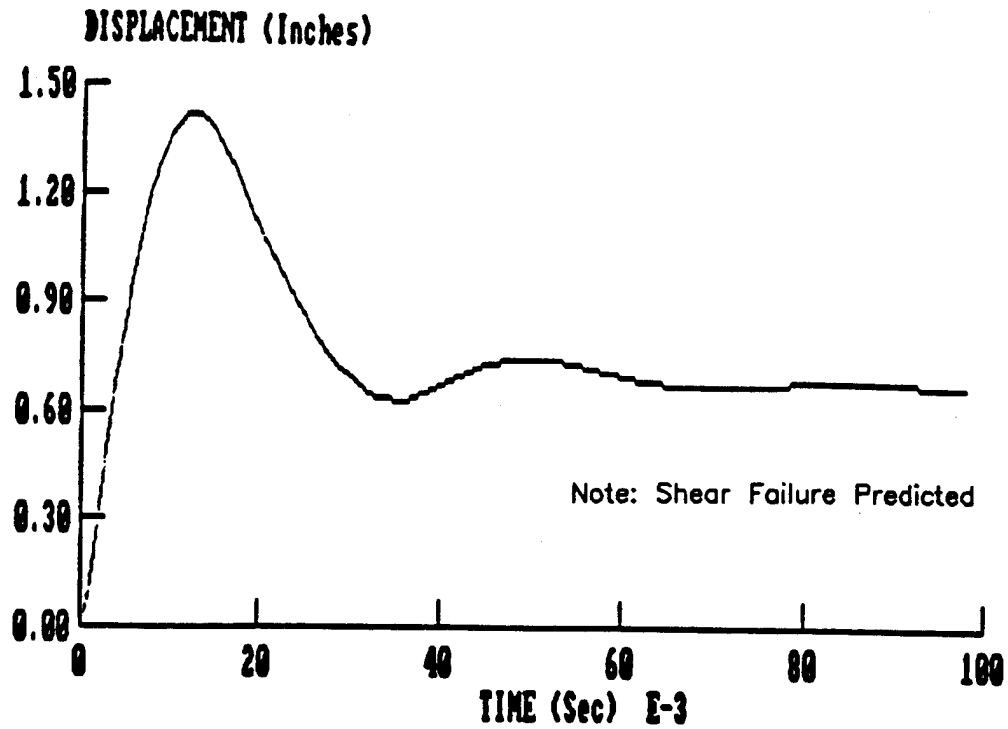
Figure 66. SASDE Analysis Results, IDF Test 7.
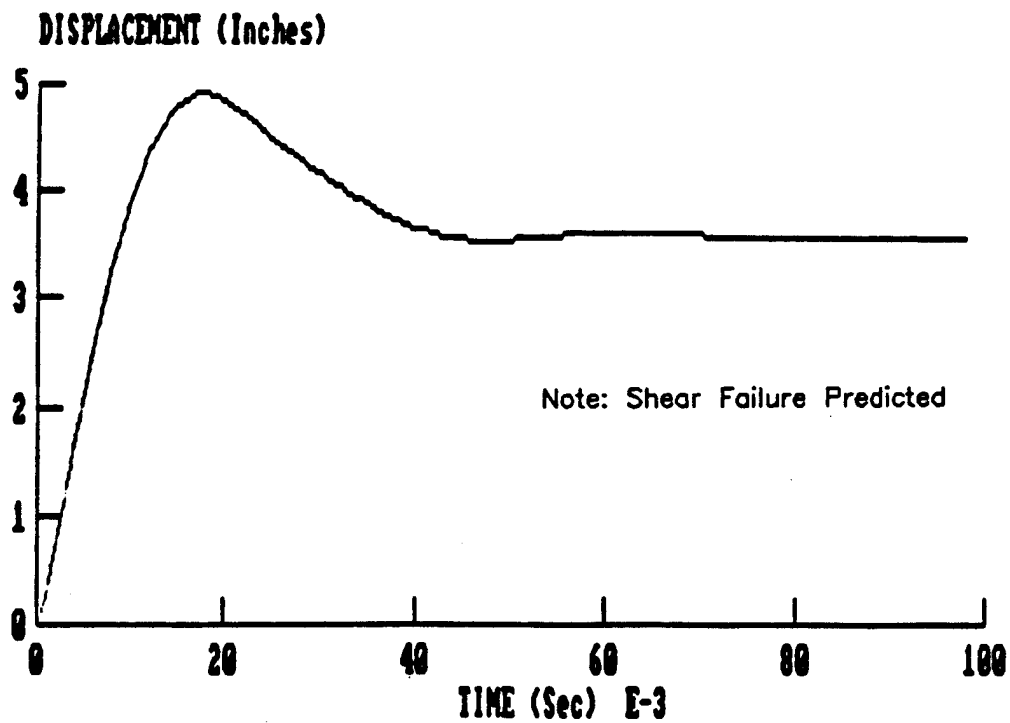
Figure 67. SASDE Analysis Results, IDF Test 8 With MF = 0.33.

90

DISPLACEMENT (Inches)

Note: Shear Failure Predicted

TIME (Sec) E-3
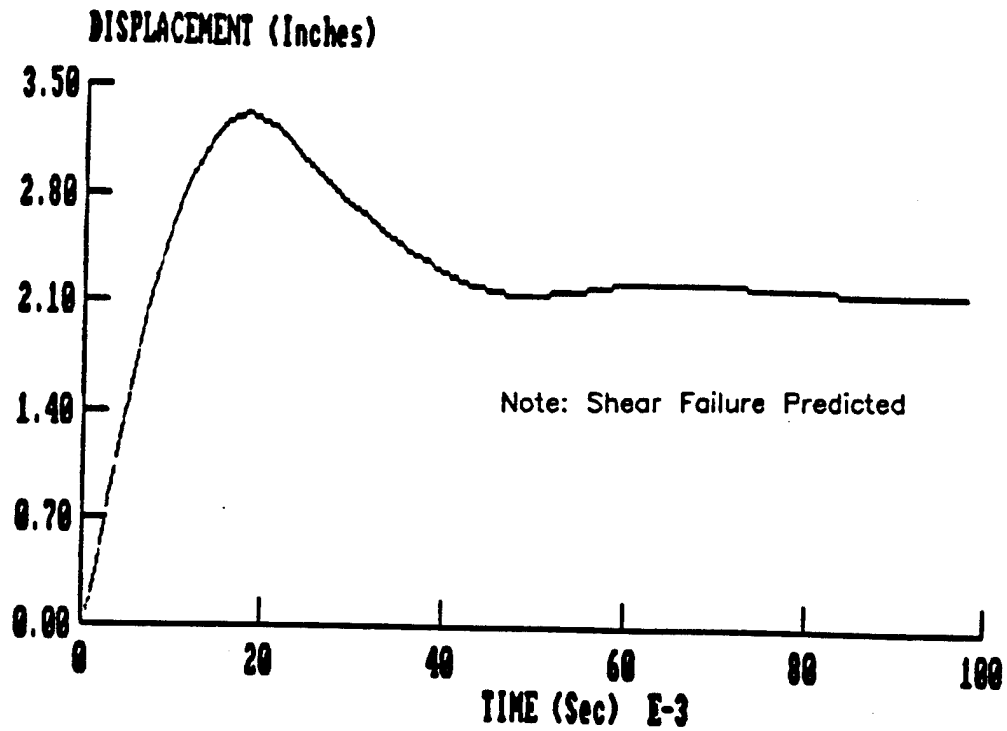
Figure 68.   SASDE Analysis Results, IDF Test 8 With MF = 0.50.

DISPLACEMENT (Inches)

Note: Shear Failure Predicted

TIME (Sec) E-3
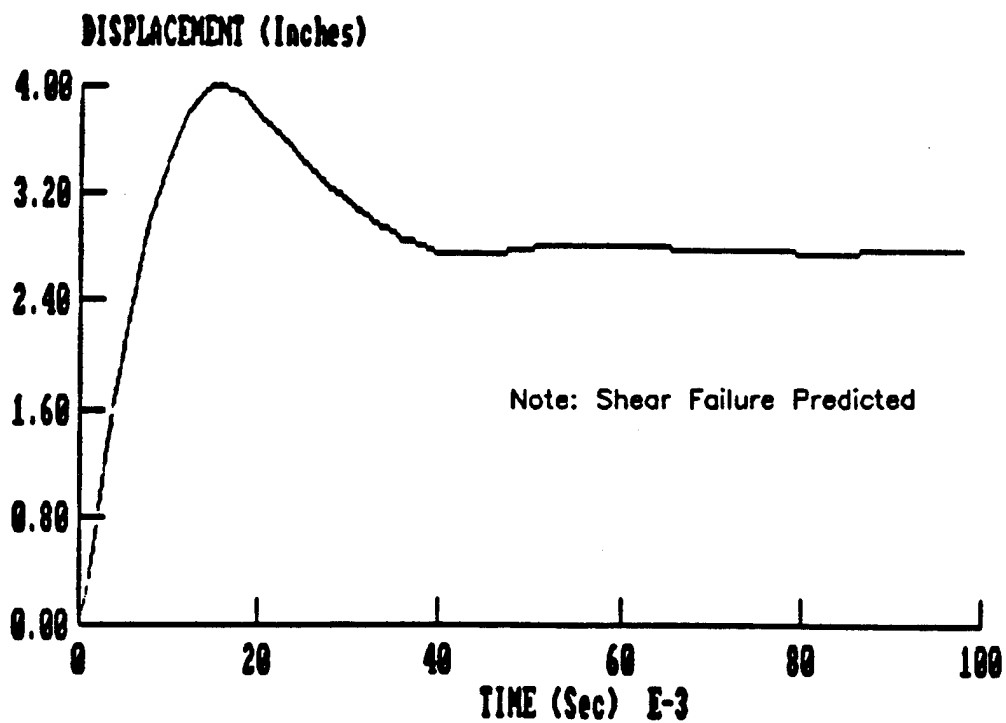
Figure 69.   SASDE Analysis Results, IDF Test 9 With MF = 0.33.

91
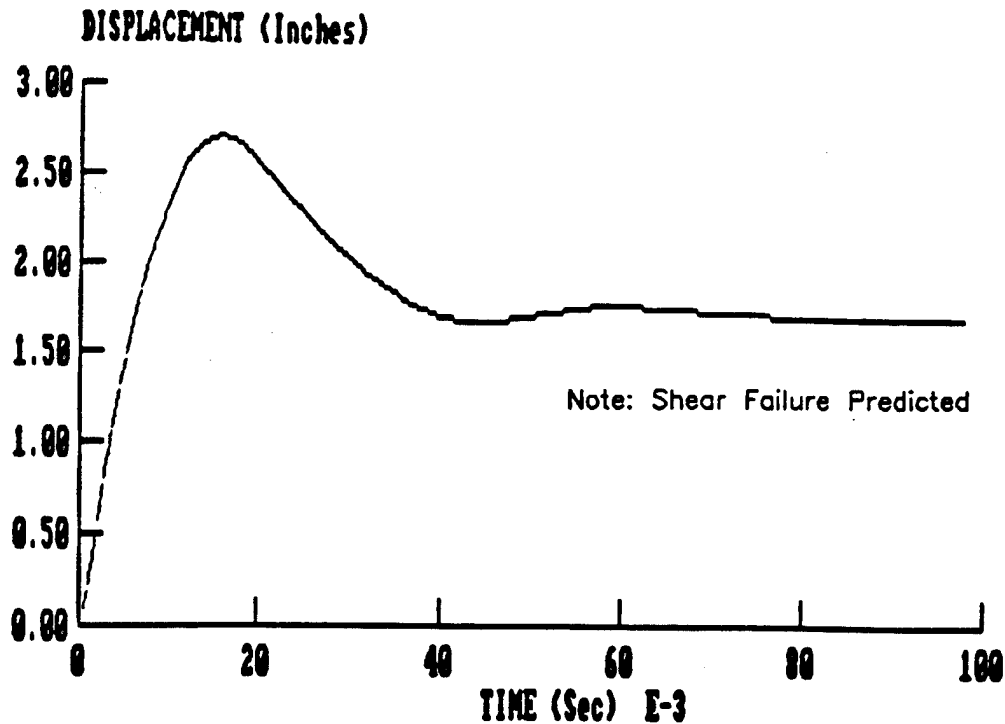
Figure 70. SASDE Analysis Results, IDF Test 9 With MF = 0.50.

5, respectively. Those computed residual deflections are accumulated in column 6, and can be compared with the comparable measured values of column 7. Such a comparison will indicate that, for Tests 1-4, the calculated residual deflections are significantly smaller than are the measured values. For Tests 5, 6, and 7 the measured and computed residuals are comparable, and for Test 8, the comparison has little meaning because the loading function used in that analysis was a theoretical one. For Test 9, the computed value is invalid, because the failure was in shear, which was predicted by SASDE, rather than in flexure. But in making these comparisons, care must be taken so unjustified conclusions are not reached. It must be remembered that the computed results were based on a contrived resistance function and lateral support stiffnesses.

C.   APPLICATION OF THE PROGRAM TO THE TYNDALL STRUCTURES

Against the background of experience gained in the application of this program to the IDF structures as discussed in the preceding section, the Tyndall test walls were idealized for analysis by SASDE only as one-way slabs spanning in the vertical direction, and the geometric data required for input into the program are as shown on Figure 36 and Tables 10 and 11. As was done for the IDF structures, the NSL option in the program was selected for use.

Although the program requires the specification of the concrete cover on the reinforcing steel bars on both the inside and outside faces of the slabs, which quantities are different, it also requires the specification of only one

92

set of "d" and "d'"values, depths to the centers of the tension and compression steel. Because the slabs are of constant thickness, different concrete cover on the inside and outside faces would produce different sets of "d" and "d'" values for the center and end regions of the slabs. In the absence of other guidance, "d" and "d'" values appropriate to the positive moment regions of the slabs were used in these studies. In a similar vein, the program assumes that the slabs are supported in the same manner at each end and that the reinforcement is the same on both faces of the slab. Except for the difference in concrete cover on the steel bars, those conditions are met for these slabs.

The material properties required by the program include the static compressive strength of the concrete (4275 psi, 28 day value), and the static yield strength (60,000 psi), and the yield (0.00207) and ultimate (0.18) strains of the reinforcing steel.

The dynamic characteristics of the slabs that are required as input to the program include the following:

Mass Factor:	0.5
Strain rate strength enhancement factor for concrete:	1.3
Strain rate strength enhancement factor for steel:	1.3
Resistance enhancement factor:	1.3
Fraction of critical damping	0.05
"Beta", as used in the dynamic response integration:	0.1666
Lateral Support Stiffness	0.01 lb-in./in.

In contrast to the situation that existed for the SASDE analyses of the IDF structures, but for unclear reasons, SASDE ran successfully for the Tyndall structures with realistically low lateral support stiffnesses.

The flexural resistance functions that were generated by the program for each of the two test walls (Tests 6 and 10), using the input data that are summarized above, are shown in Figures 71 and 72. It will be observed that those resistance levels are significantly higher than were the comparable resistances as used in the UofI and the BIGGS programs. The explanation for the significantly higher resistances generated by SASDE is not fully understood, because the resistances are computed internally by the program. However, as discussed in the preceding section, it seems likely that those higher resistances are a result of moment capacity augmentation that results from some in-plane forces that are computed to be developed in the walls as they deflect out of their initial planes.

The loadings used in the exercise of this program were the same as those that were used with the UofI program, and are shown in Figures 51 and 52 for the south and north walls, respectively. The maximum deflections computed using those loadings and the resistance functions noted above are summarized in Table 14. As would be expected, the maximum deflections computed using SASDE are
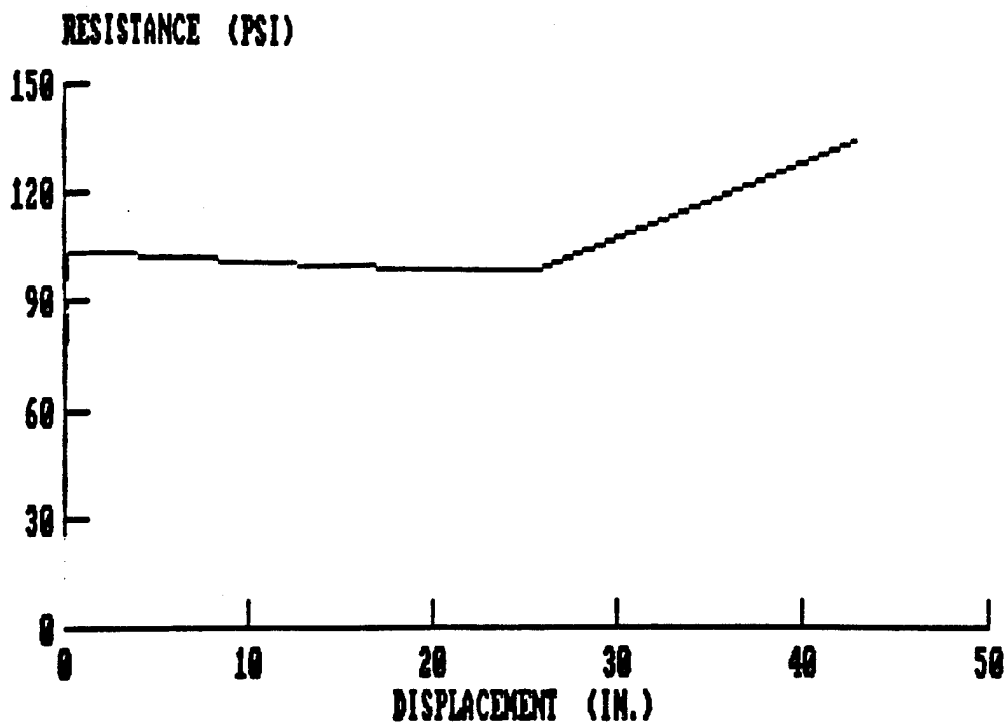
RESISTANCE (PSI)

Figure 71.   Flexural Resistance Function Generated by SASDE for South Wall of
             Tyndall Structure.
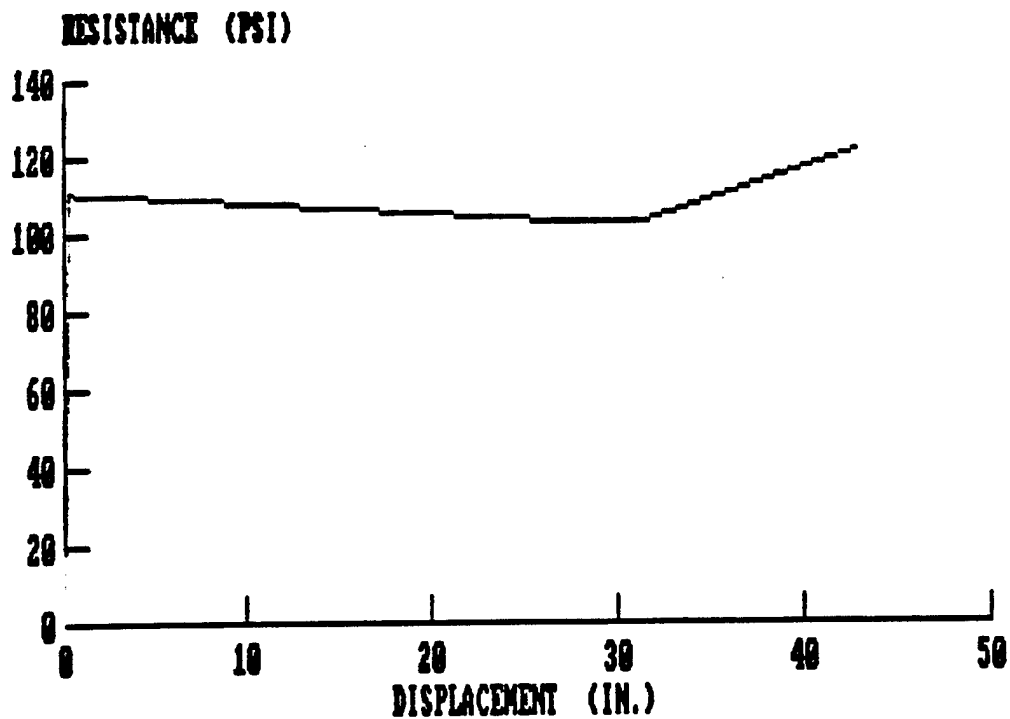
RESISTANCE (PSI)

Figure 72.   Flexural Resistance Function Generated by SASDE for North Wall of
             Tyndall Structure.

94

significantly smaller than are the comparable deflections computed by the UofI program (see Table 12), the differences resulting primarily from the higher resistances and damping factors (the UofI program assumes zero damping) that are used in SASDE.

TABLE 14. COMPARISON OF MEASURED AND COMPUTED RESPONSES OF THE TYNDALL AFB STRUCTURES USING THE SASDE PROGRAM.

Wall	Measured maximum deflection (in.)	Computed maximum deflection (in.)		
		Loading A	Loading B	Loading C
South	2.46	2.45	3.85	0.91
North	1.94	1.14	3.04	0.76

SECTION VI
PREDICTION OF THE BEHAVIOR OF THE TEST STRUCTURES USING BIGGS

A.   BRIEF DESCRIPTION OF THE PROGRAM

BIGGS, as described in Reference 30, is similar in many respects to the programs described in Sections IV and V. It, too, presumes the structural element (beam or slab) that has been subjected to a dynamically applied load normal to the plane in which it lies, to respond as a SDOF system. It is, quite simply, a computer solution of the SDOF idealizations of beams and slabs as described by Dr. John M. Biggs, for whom the program is named (Reference 3). As indicated in Reference 10, the program was developed by Wilfred Baker Engineering, Inc., of San Antonio, TX.

Briefly summarized, this program requires that the following information be provided as input into the program to describe the SDOF idealization being analyzed.

(1) The *total mass* of the system, for both the deflection and the rebound phases of response. The responding mass need not be the same for these two phases.

(2) A *multilinear loading function* which is given as a series of load-time pairs, the number of such pairs not to exceed 20. Such a function is illustrated in Figure 73. The forces must be given as the *total* forces that are applied to the element.

Notes:
(1) P_0 and t_0 must be zero.
(2) "n" has maximum value of 20.
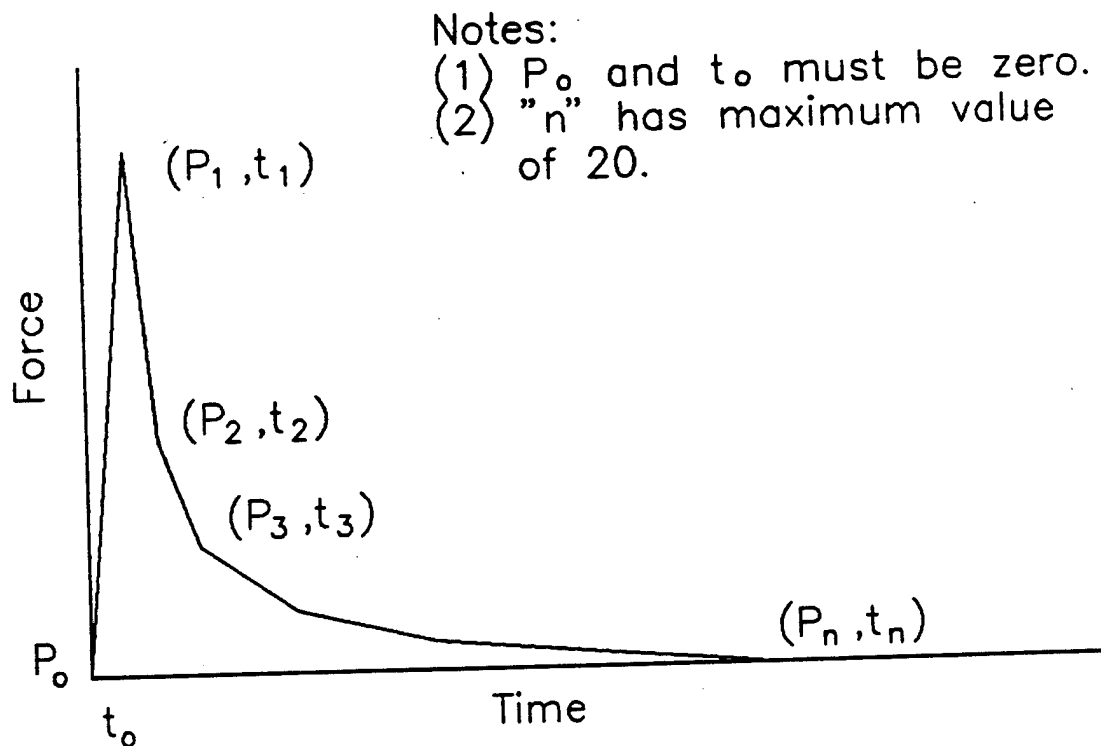
Figure 73.   Generalized BIGGS Loading Function.

(3) A *bilinear or trilinear resistance function* of the form illustrated in Figure 74 (a) and (b), in which the final element has a slope of zero. More complex functions such as that shown in Figure 74(c) can also be handled with this program, but to do so the complex function must be replaced with an equivalent bilinear function as shown; the yield deflection, y_{eE}, is determined such that total areas under the actual function and the idealized function are equal.

It is appropriate to note here that, although the program as written will handle a trilinear resistance of the form shown in Figure 74(b) directly, that function can also be replaced by an equivalent bilinear function in the same way that was described above for the quadri-linear function of Figure 74(c) without significant loss in computational accuracy. Indeed, except for deflections that are less than the deflection at which the fully plastic resistance is developed, the deflections computed using the actual resistance function and its bilinear idealization will be essentially equal.

To be consistent with the loading function, the input resistance levels must be given as *total* forces. The resistance function data are input into the program as slopes of the elastic and the elastic-plastic segments of the functions, and the magnitudes of the forces that define the intersections of these segments. As noted above, the final element must have a slope of zero.

4. The *load-mass factors* for the system, which relate the idealized SDOF system to the real distributed mass system of which it is, computationally, the equivalent. As noted in the preceding chapters, and as discussed at length in Reference 3, for any given element, these factors change during response as the element approaches the fully plastic phases. Values of these factors for a wide variety of commonly occurring beams and slabs are given in Tables 5.1-5.6 of Reference 3.

5. *Shear Constants*, which provide for computation of the dynamic reactions of the system. As observed in Reference 30, when referring to Reference 3, "Biggs notes that dynamic reactions of real structural elements do not equal the reactions in equivalent SDOF systems. He develops an approximate method of determining dynamic reactions based on a distribution of inertia forces identical to the static deformed shape of the element for the specified load distribution. This method results in a dynamic reaction or shear force F." These approximate expressions for the dynamic reactions, as developed by Biggs for the various beam and slab elements that he treats, are contained in Tables 51-56 of Reference 3. The BIGGS program requires that the coefficients of F and R, as they appear in those tabulated expressions, be given directly as input into the program.

6. *Initial Conditions.* Although for most blast loading and response problems, the responding element is initially at rest with zero displacement and zero velocity, this program permits the user to enter initial displacements and velocities other than zero.

7. *Viscous Damping.* The program requires that a damping factor, expressed as a percentage of critical damping for the system, be given directly as input. From the initial response of a beam or slab to its maximum deflection, the effect
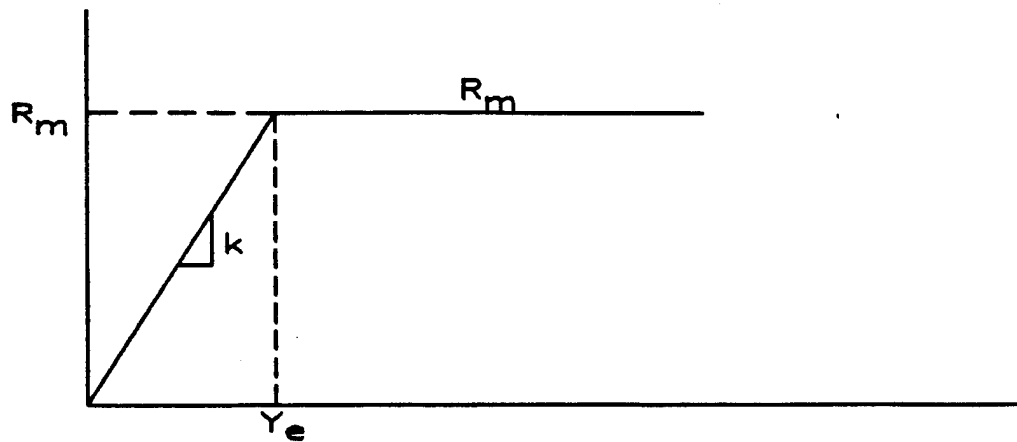
(a) Bi-Linear Elasto-Plastic
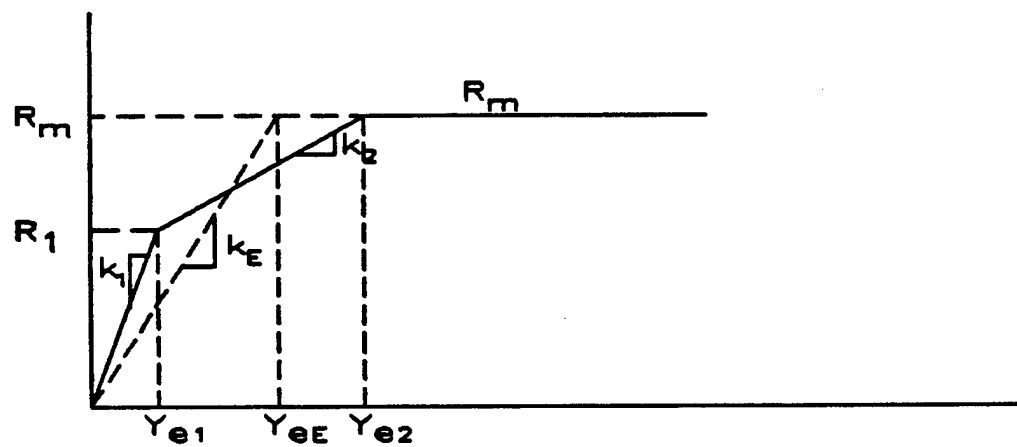
(b) Tri-Linear Elasto-Plastic
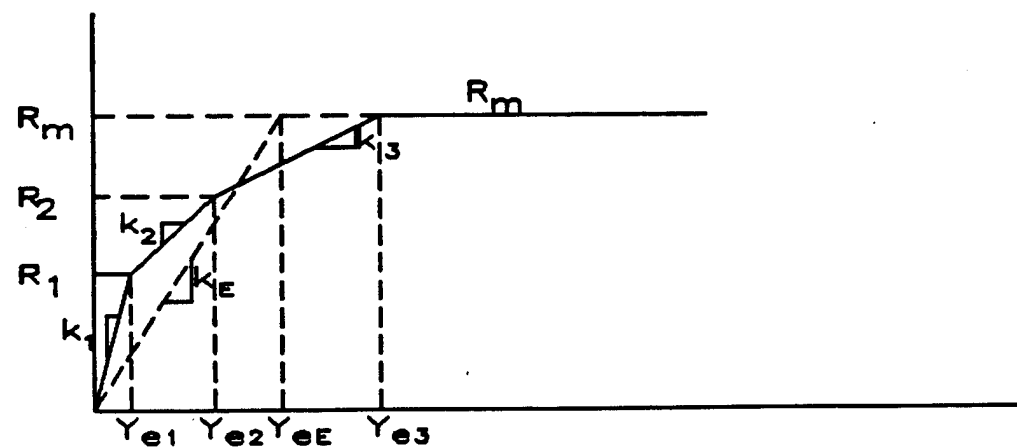
(c) Quadra-Linear Elasto-Plastic

Figure 74.   Typical BIGGS Resistance Functions.

of damping should normally be quite small; values of zero to 5 percent are reasonable estimates.

8. *Integration Time Step.* The integration time step to be used in the dynamic response analysis may be selected by the user of the program, but it must be small enough to ensure computational stability of the analysis. In general, the smaller the integration time step, the greater the accuracy, but the longer the computation time. For excessively small steps, the increase in accuracy is negligible. Biggs recommends that the time step be set equal to approximately one-tenth of the shorter of the period of vibration of the system or the shortest linear increment of the loading function.

Having entered all of the data that are required to define the dynamic characteristics of the structural element to be analyzed, and the loading to which it is to be subjected, the analyst has only to select "Compute Response" from the appropriate menu provided in the program to cause the response analysis to be carried out.

After the analysis is complete, the program provides the user with an opportunity to view the results as a detailed tabulation of the displacement, the force, the resistance, and the dynamic reactions for each time step, and/or to have those tabulated quantities plotted as functions of time. Additionally, the analyst may elect to have the input data, the total output data, and/or a summary of the output data printed for a permanent record.

B.   APPLICATION OF THE PROGRAM TO THE IDF STRUCTURES

This program was easily applied to the IDF structures and yielded generally satisfactory results. Initially, for comparative purposes, the idealization developed in Section IV for the UofI program was used as input for the BIGGS program. Because BIGGS requires that masses, resistances, and loads be input as *total* quantities, while the UofI program employed these quantities expressed in units per square inch of slab surface area, it was necessary to multiply UofI program quantities of Section IV by the surface area of the wall, which was taken as 120 x 276 inches, or 33,120 in². Input data thus determined are as shown in Table 15, which is a printout of the input used to get a BIGGS solution that was comparable to the Test 1 solution obtained in the Section IV analysis. Similar printouts could have been obtained for all other Section IV analyses, but they would differ from that of Table 15 only in the loading histories that are given.

To facilitate interpretation of the data shown in Table 15, it should be noted that the table is a copy of the input data printout as provided by the BIGGS program, and was designed for use with a trilinear resistance function of the form shown in Figure 74(b). Consequently, because the case being treated here is a bilinear idealization, the elastic-plastic yield forces are taken to be equal to the elastic yield forces. It should be further noted that, to be consistent with the assumptions made in the Section IV analyses, a load-mass factor of 0.61 was used here for all portions of response history, and that the dynamic characteristics were assumed to be the same during both the positive and the rebound phases of response. Similarly, because they are required by the

99

TABLE 15.   SUMMARY OF INPUT DATA FOR BIGGS REPRESENTATION OF
UofI MODEL FOR IDF TEST 1.

Positive Phase Mass . . . . 1.169×10^2
Rebound Phase Mass . . . . 1.169×10^2
Positive Phase Elastic Load Mass Factor . . . . 6.100×10^{-1}
Positive Phase Elastic-Plastic Load Mass Factor . . . . 6.100×10^{-1}
Positive Phase Plastic Load Mass Factor . . . . 6.100×10^{-1}
Rebound Phase Elastic Load Mass Factor . . . . 6.100×10^{-1}
Rebound Phase Elastic-Plastic Load Mass Factor . . . . 6.100×10^{-1}
Rebound Phase Plastic Load Mass Factor . . . . 6.100×10^{-1}
Positive Phase Elastic Spring Constant . . . . 7.205×10^6
Rebound Phase Elastic Spring Constant . . . . 7.205×10^6
Positive Phase Elastic-Plastic Spring Constant . . . . 0.000×10^0
Rebound Phase Elastic-Plastic Spring Constant . . . . 0.000×10^0
Positive Phase Elastic Yield . . . . 1.101×10^6
Positive Phase Elastic-Plastic Yield . . . . 1.101×10^6
Rebound Phase Elastic Yield . . . . 1.101×10^6
Rebound Phase Elastic-Plastic Yield . . . . 1.101×10^6
Fraction of Viscous Damping . . . . 5.000×10^{-2}
Number of Force-Time History Pairs   12

Force	Time	Force	Time
0.000×10^0	0.000×10^0	4.140×10^5	3.560×10^{-3}
1.040×10^6	0.000×10^0	3.113×10^5	4.450×10^{-3}
9.340×10^5	5.900×10^{-4}	2.087×10^5	5.930×10^{-3}
8.084×10^5	1.180×10^{-3}	1.027×10^5	7.400×10^{-3}
6.227×10^5	2.360×10^{-3}	0.000×10^0	8.600×10^{-3}
5.200×10^5	2.960×10^{-3}	0.000×10^0	1.000×10^{-2}

Initial displacement . . . . 0.000×10^0
Initial Velocity 0.000×10^0
Positive Phase Short Shear Constant F . . . . 4.000×10^{-2}
Positive Phase Short Shear Constant R . . . . 8.000×10^{-2}
Positive Phase Long Shear Constant F . . . . 1.100×10^{-1}
Positive Phase Long Shear Constant R . . . . 2.700×10^{-1}
Rebound Phase Short Shear Constant F . . . . 4.000×10^{-2}
Rebound Phase Short Shear Constant R . . . . 8.000×10^{-2}
Rebound Phase Long Shear Constant F . . . . 1.100×10^{-1}
Rebound Phase Long Shear Constant R . . . . 2.700×10^{-1}
Integration Time Step (sec) . . . . 0.100×10^{-5}
Number of Response Cycles Evaluated . . . . 5.000×10^0
Positive Phase Period (sec) . . . . 1.977×10^{-2}
Rebound Phase Period (sec) . . . . 1.977×10^{-2}

BIGGS program, the dynamic shear coefficients used were taken from the Biggs'
recommended values of Table 55 of Reference 3, for an aspect ratio of 0.5
(because values for an aspect ratio of 0.3 were not given), even though there
were no comparable quantities in the Section IV analyses.

The results obtained from the BIGGS analyses of the UofI idealizations are
compared with the UofI program results in Table 16. As should be expected, the
two sets of results are essentially the same. Because the input loading and the
resistance functions were the same, the results should be identical, except for
small differences that develop as a consequence of differences in the integration
procedures that are employed by the two programs.

Illustrations of the graphical output provided by the BIGGS program are
shown in Figures 75 and 76 which are for IDF Tests 1 and 4, respectively.
Similar output was obtained from the analyses of all other tests.

TABLE 16.   COMPARISON OF UofI AND BIGGS PROGRAM RESULTS
USING ZERO DAMPING AND UofI RESISTANCE FUNCTION.

Test	UofI Program		BIGGS Program	
	Maximum Defl. (in)	Residual Defl. (in)	Maximum Defl. (in)	Residual Defl. (in)
1	0.128	0	0.130	0
2	0.217	0.064	0.222	0.69
3	0.377	0.224	0.389	0.236
4	0.461	0.308	0.476	0.323
5	0.168	0.015	0.171	0.018
6	0.522	0.369	0.539	0.386
7	1.392	1.239	1.443	1.280
8	---	---	---	---
9	3.027	2.874	3.141	2.988

Equiv. Elastic Displac. = 1.528E-01   Max Force = 1.040E+06
Max Displacement = 1.197E-01   Min Force = 0.000E+00
Min Displacement = -1.019E-01   Max Resistance = 8.628E+05
Time of Max Displacement = 7.224E-03   Min Resistance = -7.343E+05
Time of Min Displacement = 1.722E-02   Max Shear A = 7.443E+04
MU = 7.836E-01   Min Shear A = -5.875E+04
                                         Max Shear B = 2.474E+05
                                         Min Shear B = -1.983E+05
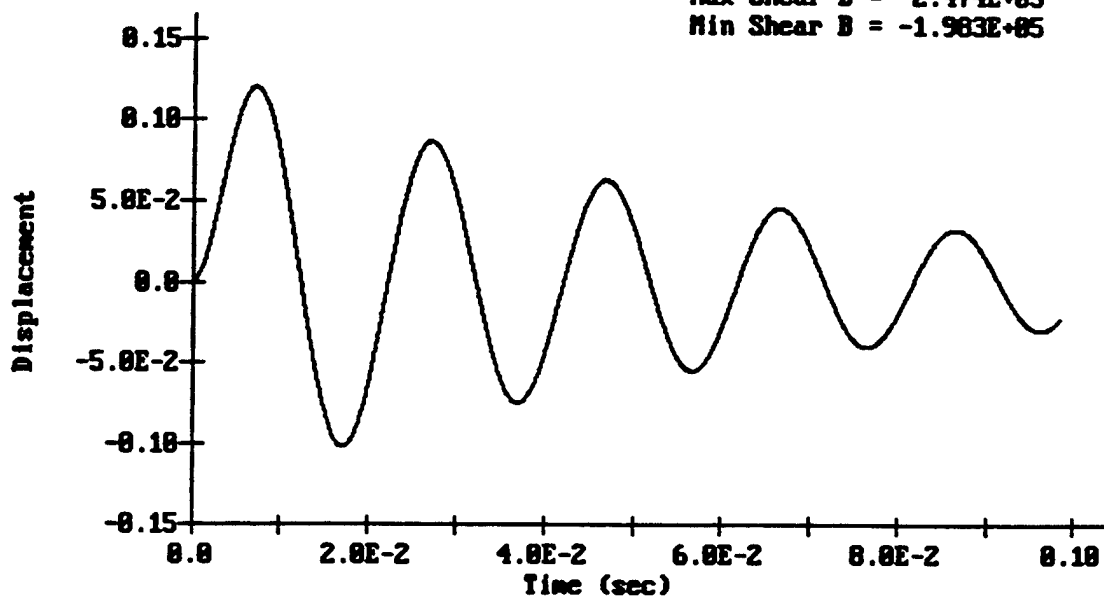
Figure 75.   Output from BIGGS' Analysis of UofI Idealization for IDF Test 1.

101

Equiv. Elastic Displac. = 1.528E-01   Max Force = 1.467E+07
Max Displacement = 4.100E-01   Min Force = 0.000E+00
Min Displacement = 4.467E-05   Max Resistance = 1.101E+06
Time of Max Displacement = 7.497E-03   Min Resistance = -9.400E+05
Time of Min Displacement = 2.100E-05   Max Shear A = 5.692E+05
MU = 2.603E+00   Min Shear A = -7.526E+04
                                       Max Shear B = 1.565E+06
                                       Min Shear B = -2.540E+05
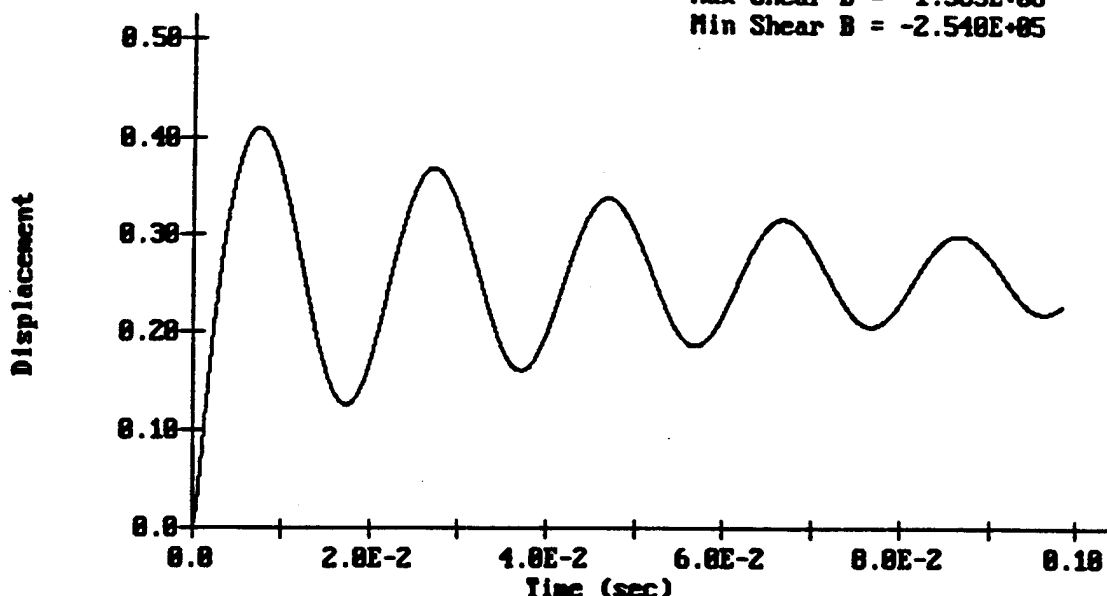
Figure 76. Output from BIGGS' Analysis of UofI Idealization for IDF Test 4.

The BIGGS program was also run using a trilinear resistance function and load-mass factors as recommended by Biggs in Table 55 of Reference 3, which was developed for a symmetrically reinforced, two-way slab that was fully restrained against rotation along all four edges. Clearly, this does not correctly represent the wall of the IDF test structure under study because, as described in Section II, the wall was not fully restrained against rotation at its base, nor was its vertical reinforcement the same at the top and the bottom. However, by taking as the negative moment along the long sides of the wall a value equal to the average of the negative moments at the top and bottom of the wall, the case represented can be said to be a reasonable approximation of the wall under study.

Treated in this manner, and using the values recommended for a slab with an aspect ratio of 0.5 (because data for an aspect ratio of 0.3 were not provided), input data for the wall as shown in Table 17 were developed. Because, even at an aspect ratio of 0.5, the dominant slab resistance is as a one-way slab in the short span direction, use of the resistance data for an aspect ratio of 0.5 instead of 0.3 should have a negligible effect on the results. As will be observed, the loading function shown in Table 17 is the same as the loading function of Table 15, because both represent input functions for IDF Test 1. The

102

TABLE 17.   SUMMARY OF INPUT DATA FOR BIGGS TRILINEAR IDEALIZATION
OF IDF STRUCTURE FOR TEST 1.

Positive Phase Mass . . . . 1.169×10^2
Rebound Phase Mass   . . . . 1.169×10^2
Positive Phase Elastic Load Mass Factor . . . . 7.200×10^{-1}
Positive Phase Elastic-Plastic Load Mass Factor . . . . 7.500×10^{-1}
Positive Phase Plastic Load Mass Factor . . . . 5.900×10^{-1}
Rebound Phase Elastic Load Mass Factor   . . . . 7.200×10^{-1}
Rebound Phase Elastic-Plastic Load Mass Factor   . . . . 7.500×10^{-1}
Rebound Phase Plastic Load Mass Factor   . . . . 5.900×10^{-1}
Positive Phase Elastic Spring Constant   . . . . 3.678×10^7
Rebound Phase Elastic Spring Constant . . . . 3.678×10^7
Positive Phase Elastic-Plastic Spring Constant   . . . . 9.171×10^6
Rebound Phase Elastic-Plastic Spring Constant . . . . 9.171×10^6
Positive Phase Elastic Yield . . . . 6.391×10^5
Positive Phase Elastic-Plastic Yield . . . . 1.172×10^6
Rebound Phase Elastic Yield . . . . 6.391×10^5
Rebound Phase Elastic-Plastic Yield . . . . 1.172×10^6
Fraction of Viscous Damping . . . . 5.000×10^{-2}
Number of Force-Time History Pairs   12

Force	Time	Force	Time
0.000×10^0	0.000×10^0	4.140×10^5	3.560×10^{-3}
1.040×10^6	0.000×10^0	3.113×10^5	4.450×10^{-3}
9.340×10^5	5.900×10^{-4}	2.087×10^5	5.930×10^{-3}
8.048×10^5	1.180×10^{-3}	1.027×10^5	7.400×10^{-3}
6.227×10^5	2.360×10^{-3}	0.000×10^0	8.600×10^{-3}
5.200×10^5	2.960×10^{-3}	0.000×10^0	1.000×10^{-2}

Initial displacement   . . . . 0.000×10^0
Initial Velocity . . . . 0.000×10^0
Positive Phase Short Shear Constant F . . . . 4.000×10^{-2}
Positive Phase Short Shear Constant R . . . . 8.000×10^{-2}
Positive Phase Long Shear Constant F . . . . 1.100×10^{-1}
Positive Phase Long Shear Constant R . . . . 2.700×10^{-1}
Rebound Phase Short Shear Constant F . . . . 4.000×10^{-2}
Rebound Phase Short Shear Constant R . . . . 8.000×10^{-2}
Rebound Phase Long Shear Constant F . . . . 1.100×10^{-1}
Rebound Phase Long Shear Constant R . . . . 2.700×10^{-1}
Integration Time Step (sec) . . . . 2.100×10^{-5}
Number of Response Cycles Evaluated . . . . 5.000×10^0
Positive Phase Period (sec) . . . . 9.505×10^{-3}
Rebound Phase Period (sec) . . . . 9.505×10^{-3}

results of the analysis produced by the input of Table 17 are shown on Figure 77,
and the results from a similar analysis for Test 4 are shown, for illustrative
purposes, in Figure 78. The deflection results from the trilinear BIGGS analyses
of all of the tests in this series are summarized also in Table 18, along with
the results obtained in comparable parallel analyses.

     To demonstrate the general adequacy of equivalent bilinear representations
of more complex resistance functions, the analyses of the trilinear idealizations
discussed above were rerun using an equivalent bilinear function, the elastic
yield capacity of which was the same as the elastic-plastic yield capacity of the
trilinear function, and the equivalent elastic slope of which was determined as
described in Section VI.A to make the areas under the two functions equal at a
deflection equal to the elastic-plastic yield deflection in the trilinear
function.
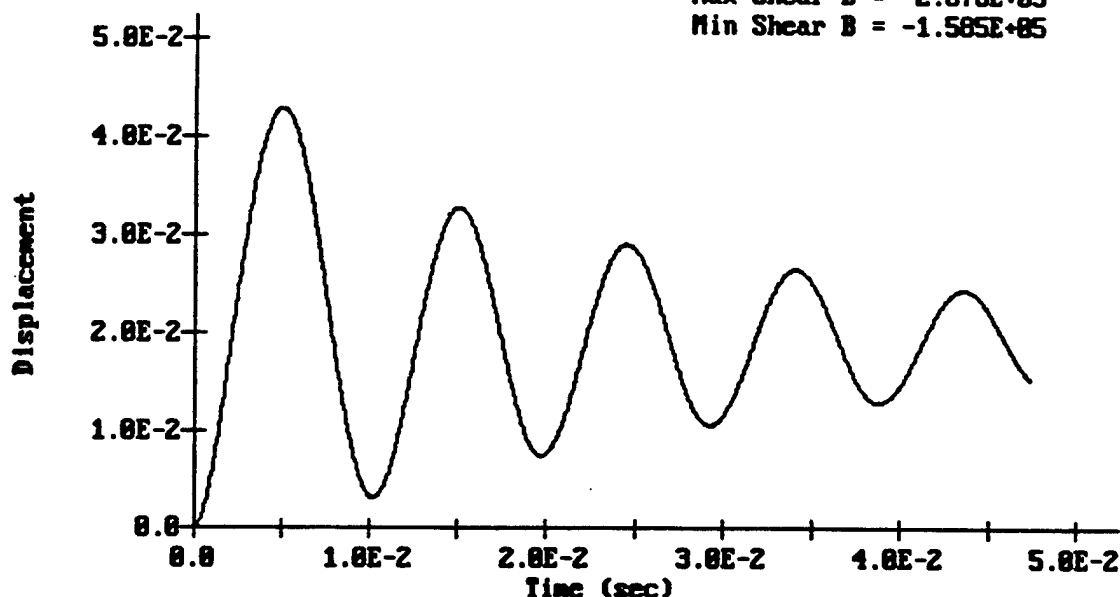
Figure 77. Output from BIGGS' Analysis of Trilinear Idealization of IDF Test 1.

Shown in Table 19 is a summary of the input data for the equivalent bilinear analysis of Test 1, and a summary of the results of this analysis is shown in Figure 79. Similarly, for illustrative and comparative purposes, the output from the corresponding analysis for Test 4 is shown in Figure 80. Summary deflection data from the BIGGS analysis of all of the IDF tests in this series, using the equivalent bilinear resistance function, are also contained in Table 19.

As is apparent from the data contained in Table 19, there are significant differences in the deflections as predicted using the resistance function of Section IV and those that are predicted using a resistance function formulated as recommended in Reference 3. As expected, the deflections predicted using the resistance function of Section IV are larger than those predicted using the BIGGS' resistance, because the former resistance (yield value of 33.3 psi) is smaller than the latter resistance (yield value of 35.4 psi). The differences are further exacerbated because the elastic slope of the UofI function is much smaller than is the elastic slope of the BIGGS' function. Hence, the differences observed in the deflection predictions result not from conceptual or program differences, but from differences in the input resistance functions.

104

Equiv. Elastic Displac. = 5.170E-02   Max Force = 1.467E+07
Max Displacement = 2.396E-01   Min Force = 0.000E+00
Min Displacement = 3.783E-05   Max Resistance = 1.172E+06
Time of Max Displacement = 5.670E-03   Min Resistance = -7.483E+05
Time of Min Displacement = 2.100E-05   Max Shear A = 5.693E+05
MU = 4.634E+00   Min Shear A = -5.987E+04
                                        Max Shear B = 1.566E+06
                                        Min Shear B = -2.021E+05
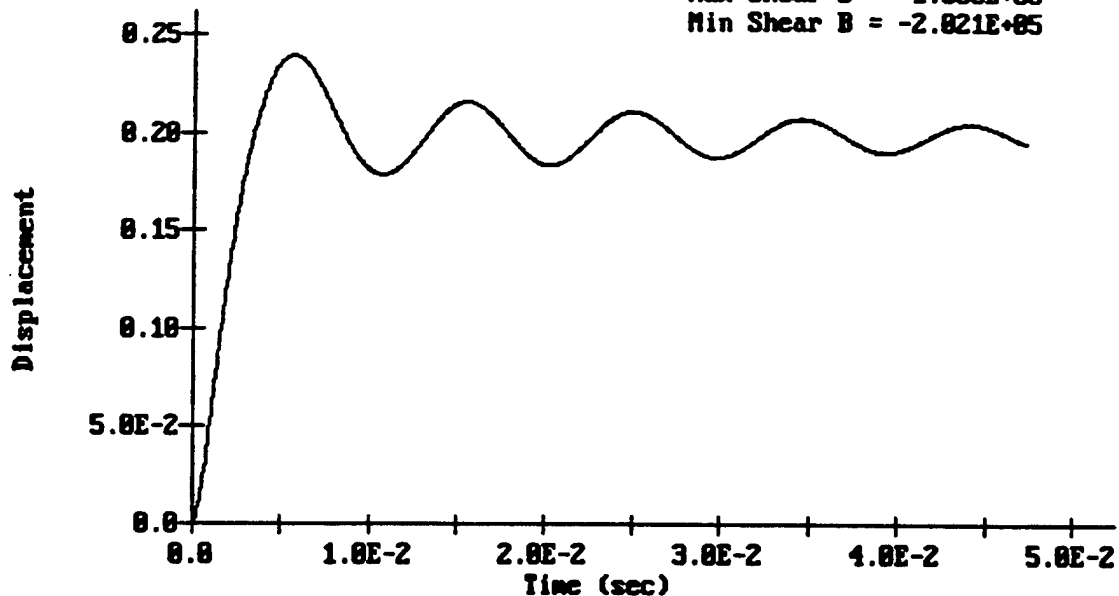
Figure 78. Output from BIGGS' Analysis of Trilinear Idealization of IDF Test 4.

TABLE 18. COMPARISON OF BIGGS PROGRAM RESULTS USING 5 PERCENT
DAMPING AND DIFFERENT RESISTANCE IDEALIZATIONS.

Test	UofI Resistance		BIGGS' Resistance			
			Trilinear		Equiv. Bilinear	
	Max Defl. (in)	Resid. Defl. (in)	Max Defl. (in)	Resid. Defl (in)	Max Defl. (in)	Resid. Defl. (in)
1	0.120	0	0.043	0	0.050	0
2	0.201	0.048	0.107	0.055	0.111	0.059
3	0.340	0.187	0.195	0.144	0.207	0.155
4	0.410	0.257	0.240	0.188	0.255	0.204
5	0.160	0.007	0.0674	0.013	0.066	0.015
6	0.459	0.306	0.259	0.207	0.280	0.228
7	1.126	0.973	0.675	0.623	0.752	0.701
8	---	---	---	---	---	---
9	2.227	2.074	1.313	1.488	1.488	1.436

105

TABLE 19.   INPUT DATA FOR BIGGS EQUIVALENT BILINEAR IDEALIZATION
OF THE IDF STRUCTURE WALL.

Positive Phase Mass . . . . 1.169×10^2
Rebound Phase Mass . . . . 1.169×10^2
Positive Phase Elastic Load Mass Factor . . . . 7.200×10^{-1}
Positive Phase Elastic-Plastic Load Mass Factor . . . . 5.900×10^{-1}
Positive Phase Plastic Load Mass Factor . . . . 5.900×10^{-1}
Rebound Phase Elastic Load Mass Factor . . . . 7.200×10^{-1}
Rebound Phase Elastic-Plastic Load Mass Factor . . . . 5.900×10^{-1}
Rebound Phase Plastic Load Mass Factor . . . . 5.900×10^{-1}
Positive Phase Elastic Spring Constant . . . . 2.266×10^7
Rebound Phase Elastic Spring Constant . . . . 2.266×10^7
Positive Phase Elastic-Plastic Spring Constant . . . . 0.000×10^0
Rebound Phase Elastic-Plastic Spring Constant . . . . 0.000×10^0
Positive Phase Elastic Yield . . . . 1.172×10^6
Positive Phase Elastic-Plastic Yield . . . . 1.172×10^6
Rebound Phase Elastic Yield . . . . 1.172×10^6
Rebound Phase Elastic-Plastic Yield . . . . 1.172×10^6
Fraction of Viscous Damping . . . . 5.000×10^{-2}
Number of Force-Time History Pairs   12

Force	Time	Force	Time
0.000×10^0	0.000×10^0	4.140×10^5	3.560×10^{-3}
1.040×10^6	0.000×10^0	3.113×10^5	4.450×10^{-3}
9.340×10^5	5.900×10^{-4}	2.087×10^5	5.930×10^{-3}
8.048×10^5	1.180×10^{-3}	1.027×10^5	7.400×10^{-3}
6.227×10^5	2.360×10^{-3}	0.000×10^0	8.600×10^{-3}
5.200×10^5	2.960×10^{-3}	0.000×10^0	1.000×10^{-2}

Initial Displacement . . . . 0.000×10^0
Initial Velocity . . . . 0.000×10^0
Positive Phase Short Shear Constant F . . . . 4.000×10^{-2}
Positive Phase Short Shear Constant R . . . . 8.000×10^{-2}
Positive Phase Long Shear Constant F . . . . 1.100×10^{-1}
Positive Phase Long Shear Constant R . . . . 2.700×10^{-1}
Rebound Phase Short Shear Constant F . . . . 4.000×10^{-2}
Rebound Phase Short Shear Constant R . . . . 8.000×10^{-2}
Rebound Phase Long Shear Constant F . . . . 1.100×10^{-1}
Rebound Phase Long Shear Constant R . . . . 2.700×10^{-1}
Integration Time Step (sec) . . . . 2.100×10^{-5}
Number of Response Cycles Evaluated . . . . 5.000×10^0
Positive Phase Period (sec) . . . . 1.211×10^{-2}
Rebound Phase Period (sec) . . . . 1.211×10^{-2}

Determining which is the most nearly correct resistance function is another
matter. Because the UofI function more nearly reflected the actual reinforcement
patterns and support conditions than did the BIGGS' function, the maximum
resistance estimated for the UofI function is probably closer to the actual yield
resistance of the wall. But the UofI function presumes a much flatter initial
slope than does the BIGGS' function and, therefore, is an inadequate
representation of the response of the structure at small deflections. For large
deflections, well into the plastic region, both procedures will give
approximately the same absolute maximum deflections.

Hence, for general purposes, either program can be used to obtain
satisfactory results; it is necessary only that the user understand the data
being input into them to define the idealized SDOF system to be analyzed, and be

106

Equiv. Elastic Displac. = 5.172E-02   Max Force = 1.040E+06
Max Displacement = 5.010E-02   Min Force = 0.000E+00
Min Displacement = -3.740E-02   Max Resistance = 1.135E+06
Time of Max Displacement = 4.051E-03   Min Resistance = -8.475E+05
Time of Min Displacement = 1.134E-02   Max Shear A = 1.023E+05
MU = 9.687E-01   Min Shear A = -6.700E+04
                                       Max Shear B = 3.300E+05
                                       Min Shear B = -2.288E+05
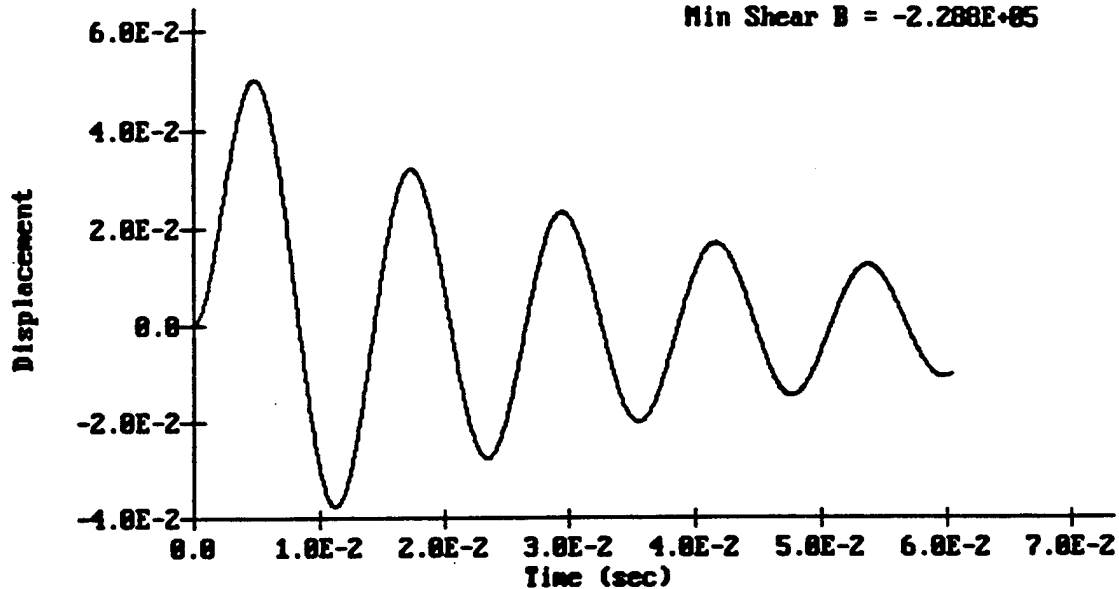
Figure 79. Output from BIGGS' Analysis of Equivalent Bilinear Idealization of IDF Test 1.

able to interpret correctly the deflections computed. From a user perspective, the BIGGS program would normally be preferred because of the very user-friendly manner in which it is presented and the comprehensiveness and versatility of its output. It does, however, possess one characteristic that can restrict quite severely its general usefulness: it can deal only with a resistance function that has a final slope of zero.

Hence, it cannot be used to analyze slabs or beams whose early resistances are amplified as a consequence of in-plane forces that may develop during their early deflection histories, and which subsequently decay to the much smaller levels. Similarly, it cannot be used to compute deflections that are beyond the fully plastic flexural response domain, perhaps in a tension membrane region in which the resistance takes on a positive slope, after an earlier zero, or possibly negative slope. In contrast, the UofI program can handle a variety of multilinear resistances, and is not restricted in this manner. However, except for this deficiency, the BIGGS program will be found to be generally preferable.

107

Equiv. Elastic Displac. = 5.172E-02   Max Force = 1.467E+07
Max Displacement = 2.553E-01   Min Force = 0.000E+00
Min Displacement = 3.783E-05   Max Resistance = 1.172E+06
Time of Max Displacement = 5.901E-03   Min Resistance = -1.001E+06
Time of Min Displacement = 2.100E-05   Max Shear A = 5.693E+05
MU = 4.935E+00   Min Shear A = -8.011E+04
                                        Max Shear B = 1.565E+06
                                        Min Shear B = -2.704E+05
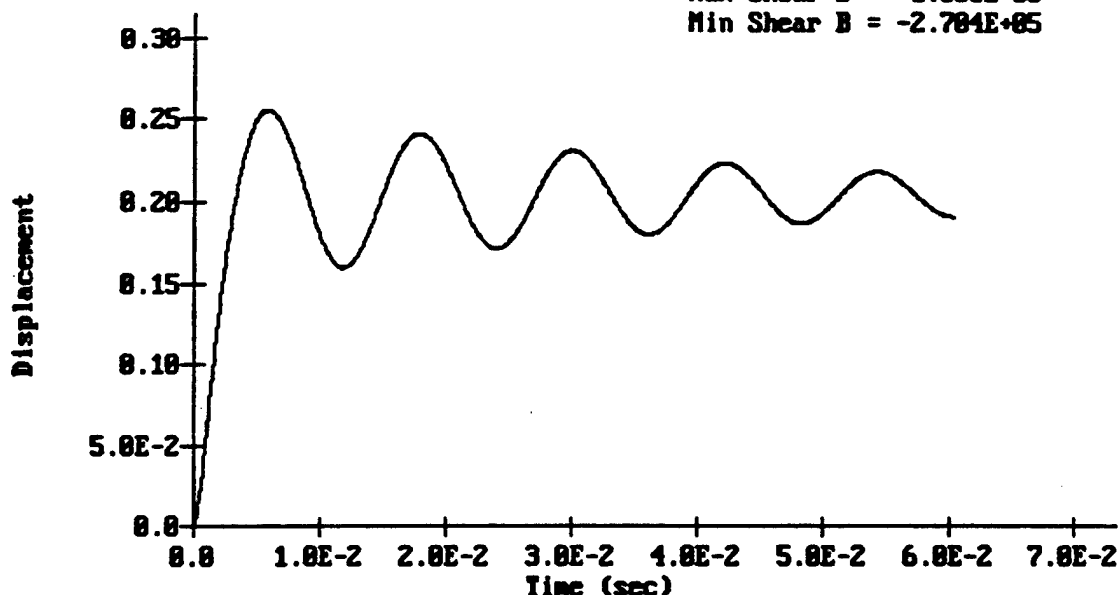
Figure 80. Output from BIGGS' Analysis of Equivalent Bilinear Idealization of IDF Test 4.

C. APPLICATION OF THE PROGRAM TO THE TYNDALL STRUCTURES

The NATO test walls were analyzed using the BIGGS program in the same manner that it was used to analyze the IDF structures. Actually, because the Tyndall test walls (as idealized) were symmetrically supported and reinforced, in contrast to the unsymmetrical reinforcement and support conditions that existed for the IDF structures, the BIGGS program could be applied somewhat more easily to the Tyndall walls.

As observed in the earlier description of the BIGGS program, the numerical integration scheme employed by it is the same as the one used by the UofI program. Consequently, if the same resistance functions, loading functions, and dynamic characteristics of the walls are input into both programs, the computed responses should also be essentially the same. To confirm that this situation existed for the Tyndall walls, and, thereby, to confirm that both programs were being used correctly, the Tyndall walls were analyzed by BIGGS using the same wall resistance and dynamic characteristics, and the same loadings that were used for the IDF structures. Because, as noted earlier, the BIGGS program requires

108

the use of total forces in both the resistance and forcing functions, those quantities were determined for this comparative study by multiplying the resistance and loading unit force values used in the UofI analyses by the area of the loaded wall, which, for the idealized wall, was 158 x 519.5 inches, or 82,081 square inches.

Summaries of the input data thus determined for the south and north walls of the Tyndall structures are given in Tables 20 and 21, respectively, for loading cases (a). As noted above, those loading cases were determined by multiplying the (a) loads as shown in Figures 51 and 52 by 82,081 square inches. The input data for the (b) and (c) loads of Figures 51 and 52 were identical to those given in Tables 20 and 21 except for the loading functions used.

The results obtained from these analyses are compared with their UofI counterparts in Table 22, in which it will be observed that the BIGGS program results, with zero damping, agree exactly with the corresponding UofI results. As noted above, this agreement was to be expected. Shown also in this table, for comparative purposes, are the maximum deflections that would be computed if 5 percent critical damping is introduced, all other input data remaining unchanged. As will be observed, even this modest level of damping reduces the expected maximum deflections quite significantly.

The BIGGS program was also applied to the Tyndall test walls using trilinear resistance functions whose coordinates were computed directly from the equations provided by Biggs in Table 5.5 of Reference 3. Use of the equations given in that table will introduce some error, because they assume that all the slabs are fixed against rotation on all four edges. Because the idealized slabs are fixed only in the short direction, being simply supported in the long direction, the resistances computed from those equations should be somewhat higher than they really are. Additionally, to use the relations provided in that table, it was necessary to use an aspect ratio of 0.5, which is the smallest ratio for which data are given. Because the aspect ratio of the idealized wall is only 0.3, use of a ratio of 0.5 will also result in small overestimates of the resistances of the walls. As a consequence, deflections computed on these bases will be somewhat smaller than they should be. Input data developed in this way are summarized in Tables 23 and 24 for the south and north walls, respectively. The maximum deflections computed in this manner are summarized in Table 25.

For further comparative purposes, the walls were also analyzed by BIGGS using the trilinear, one-way slab resistance relationships provided in Table 5.2 of Reference 3, the results of which are also shown in Table 25. The input data for the one-way slab idealizations used in these BIGGS analyses are shown in Tables 26 and 27. Interestingly, as shown in Table 25, the maximum deflections computed by BIGGS for the two-way and one-way idealizations are practically identical. Because the resistance computed for the one-way idealization is smaller than that computed for the two-way idealization, the one-way idealization should result in slightly larger predicted deflections. That was not the case and it appears to be a result of the different load-mass factors that are used in the two idealizations. Though puzzling, this apparent anomaly is not believed

Positive Phase Mass	4.703×10^{2}
Rebound Phase Mass	4.703×10^{2}
Positive Phase Elastic Load Mass Factor	6.600×10^{-1}
Positive Phase Elastic-Plastic Load Mass Factor	6.600×10^{-1}
Positive Phase Plastic Load Mass Factor	6.600×10^{-1}
Rebound Phase Elastic Load Mass Factor	6.600×10^{-1}
Rebound Phase Elastic-Plastic Load Mass Factor	6.600×10^{-1}
Rebound Phase Plastic Load Mass Factor	6.600×10^{-1}
Positive Phase Elastic Spring Constant	2.369×10^{7}
Rebound Phase Elastic Spring Constant	2.369×10^{7}
Positive Phase Elastic-Plastic Spring Constant	$0.000 \times 10^{+0}$
Rebound Phase Elastic-Plastic Spring Constant	$0.000 \times 10^{+0}$
Positive Phase Elastic Yield	5.965×10^{6}
Positive Phase Elastic-Plastic Yield	5.965×10^{6}
Rebound Phase Elastic Yield	5.965×10^{6}
Rebound Phase Elastic-Plastic Yield	5.965×10^{6}
Fraction of Viscous Damping	0.000×10^{-2}
Number of Force-Time History Pairs	3

Force	Time
0.000×10^{0}	$0.000 \times 10^{+0}$
2.323×10^{8}	$0.000 \times 10^{+0}$
0.000×10^{0}	9.000×10^{-4}

Initial displacement	$0.000 \times 10^{+0}$
Initial Velocity	$0.000 \times 10^{+0}$
Positive Phase Short Shear Constant F	4.000×10^{-2}
Positive Phase Short Shear Constant R	8.000×10^{-2}
Positive Phase Long Shear Constant F	1.100×10^{-1}
Positive Phase Long Shear Constant R	2.700×10^{-1}
Rebound Phase Short Shear Constant F	4.000×10^{-2}
Rebound Phase Short Shear Constant R	8.000×10^{-2}
Rebound Phase Long Shear Constant F	1.100×10^{-1}
Rebound Phase Long Shear Constant R	2.700×10^{-1}
Integration Time Step (sec)	1.000×10^{-5}
Number of Response Cycles Evaluated	$5.000 \times 10^{+0}$
Positive Phase Period (sec)	2.274×10^{-2}
Rebound Phase Period (sec)	2.274×10^{-2}

to be a concern because, as observed earlier, because of its low aspect ratio, the slab behavior is dominated by its one-way action. Hence, the computed deflection as a one-way slab should be only slightly larger than the deflection computed using a two-way idealization.

TABLE 21. INPUT DATA FOR BIGGS ANALYSIS OF NORTH WALL OF
TYNDALL STRUCTURE FOR LOADING A AND UofI RESISTANCE FUNCTION.

Positive Phase Mass . . . . 5.811×10^2
Rebound Phase Mass . . . . 5.811×10^2
Positive Phase Elastic Load Mass Factor . . . . 6.600×10^{-1}
Positive Phase Elastic-Plastic Load Mass Factor . . . . 6.600×10^{-1}
Positive Phase Plastic Load Mass Factor . . . . 6.600×10^{-1}
Rebound Phase Elastic Load Mass Factor . . . . 6.600×10^{-1}
Rebound Phase Elastic-Plastic Load Mass Factor . . . . 6.600×10^{-1}
Rebound Phase Plastic Load Mass Factor . . . . 6.600×10^{-1}
Positive Phase Elastic Spring Constant . . . . 3.092×10^7
Rebound Phase Elastic Spring Constant . . . . 3.092×10^7
Positive Phase Elastic-Plastic Spring Constant . . . . $0.000 \times 10^{+0}$
Rebound Phase Elastic-Plastic Spring Constant . . . . $0.000 \times 10^{+0}$
Positive Phase Elastic Yield . . . . 6.666×10^6
Positive Phase Elastic-Plastic Yield . . . . 6.666×10^6
Rebound Phase Elastic Yield . . . . 6.666×10^6
Rebound Phase Elastic-Plastic Yield . . . . 6.666×10^6
Fraction of Viscous Damping . . . . 0.000×10^0
Number of Force-Time History Pairs 3

Force	Time
0.000×10^0	$0.000 \times 10^{+0}$
8.208×10^7	$0.000 \times 10^{+0}$
$0.000 \times 10^{+0}$	1.500×10^{-3}

Initial Displacement . . . . $0.000 \times 10^{+0}$
Initial Velocity . . . . $0.000 \times 10^{+0}$
Positive Phase Short Shear Constant F . . . . 4.000×10^{-2}
Positive Phase Short Shear Constant R . . . . 8.000×10^{-2}
Positive Phase Long Shear Constant F . . . . 1.100×10^{-1}
Positive Phase Long Shear Constant R . . . . 2.700×10^{-1}
Rebound Phase Short Shear Constant F . . . . 4.000×10^{-2}
Rebound Phase Short Shear Constant R . . . . 8.000×10^{-2}
Rebound Phase Long Shear Constant F . . . . 1.100×10^{-1}
Rebound Phase Long Shear Constant R . . . . 2.700×10^{-1}
Integration Time Step (sec) . . . . 1.000×10^{-5}
Number of Response Cycles Evaluated . . . . $5.000 \times 10^{+0}$
Positive Phase Period (sec) . . . . 2.213×10^{-2}
Rebound Phase Period (sec) . . . . 2.213×10^{-2}

111

	Computed Maximum Deflection, in.								
	Loading A			Loading B			Loading C		
	UofI	BIGGS		UofI	BIGGS		UofI	BIGGS	
Damp.[a]	0.0	0.0	0.05	0.0	0.0	0.05	0.0	0.0	0.05
South wall	3.07	3.07	2.33	5.00	5.00	3.56	1.14	1.14	0.95
North wall	1.30	1.30	1.06	3.64	3.64	2.65	0.84	0.84	0.71

[a]Fraction of critical damping used in the computations.

TABLE 23. INPUT DATA FOR BIGGS ANALYSIS OF SOUTH WALL OF TYNDALL STRUCTURE AS A TWO-WAY SLAB WITH TRILINEAR RESISTANCE FUNCTION.

Positive Phase Mass	4.703×10^2
Rebound Phase Mass	4.703×10^2
Positive Phase Elastic Load Mass Factor	7.200×10^{-1}
Positive Phase Elastic-Plastic Load Mass Factor	7.500×10^{-1}
Positive Phase Plastic Load Mass Factor	5.900×10^{-1}
Rebound Phase Elastic Load Mass Factor	7.200×10^{-1}
Rebound Phase Elastic-Plastic Load Mass Factor	7.500×10^{-1}
Rebound Phase Plastic Load Mass Factor	5.900×10^{-1}
Positive Phase Elastic Spring Constant	8.495×10^7
Rebound Phase Elastic Spring Constant	8.495×10^7
Positive Phase Elastic-Plastic Spring Constant	$2.118 \times 10^{+7}$
Rebound Phase Elastic-Plastic Spring Constant	$2.118 \times 10^{+7}$
Positive Phase Elastic Yield	2.851×10^6
Positive Phase Elastic-Plastic Yield	6.715×10^6
Rebound Phase Elastic Yield	2.851×10^6
Rebound Phase Elastic-Plastic Yield	6.715×10^6
Fraction of Viscous Damping	5.000×10^{-2}
Number of Force-Time History Pairs	3

Force	Time
0.000×10^0	$0.000 \times 10^{+0}$
2.323×10^8	$0.000 \times 10^{+0}$
0.000×10^0	9.000×10^{-4}

Initial Displacement	$0.000 \times 10^{+0}$
Initial Velocity	$0.000 \times 10^{+0}$
Positive Phase Short Shear Constant F	4.000×10^{-2}
Positive Phase Short Shear Constant R	8.000×10^{-2}
Positive Phase Long Shear Constant F	1.100×10^{-1}
Positive Phase Long Shear Constant R	2.700×10^{-1}
Rebound Phase Short Shear Constant F	4.000×10^{-2}
Rebound Phase Short Shear Constant R	8.000×10^{-2}
Rebound Phase Long Shear Constant F	1.100×10^{-1}
Rebound Phase Long Shear Constant R	2.700×10^{-1}
Integration Time Step (sec)	1.000×10^{-5}
Number of Response Cycles Evaluated	$5.000 \times 10^{+0}$
Positive Phase Period (sec)	1.254×10^{-2}
Rebound Phase Period (sec)	1.254×10^{-2}

TABLE 24.   INPUT DATA FOR BIGGS ANALYSIS OF NORTH WALL OF TYNDALL STRUCTURE
           AS A TWO-WAY SLAB WITH TRILINEAR RESISTANCE FUNCTION.

Positive Phase Mass . . . . 5.811x10^2
Rebound Phase Mass . . . . 5.811x10^2
Positive Phase Elastic Load Mass Factor . . . . 7.200x10^{-1}
Positive Phase Elastic-Plastic Load Mass Factor . . . . 5.900x10^{-1}
Positive Phase Plastic Load Mass Factor . . . . 5.900x10^{-1}
Rebound Phase Elastic Load Mass Factor . . . . 7.200x10^{-1}
Rebound Phase Elastic-Plastic Load Mass Factor . . . . 5.900x10^{-1}
Rebound Phase Plastic Load Mass Factor . . . . 5.900x10^{-1}
Positive Phase Elastic Spring Constant . . . . 1.560x10^8
Rebound Phase Elastic Spring Constant . . . . 1.560x10^8
Positive Phase Elastic-Plastic Spring Constant . . . . 3.884x10^{+7}
Rebound Phase Elastic-Plastic Spring Constant . . . . 3.884x10^{+7}
Positive Phase Elastic Yield . . . . 2.963x10^6
Positive Phase Elastic-Plastic Yield . . . . 7.605x10^6
Rebound Phase Elastic Yield . . . . 2.963x10^6
Rebound Phase Elastic-Plastic Yield . . . . 7.605x10^6
Fraction of Viscous Damping . . . . 5.000x10^{-2}
Number of Force-Time History Pairs 3

                        Force   Time
                        0.000x10^0 0.000x10^{+0}
                        1.888x10^8 0.000x10^{+0}
                        0.000x10^0 8.280x10^{-4}

Initial Displacement . . . . 0.000x10^{+0}
Initial Velocity . . . . 0.000x10^{+0}
Positive Phase Short Shear Constant F . . . . 4.000x10^{-2}
Positive Phase Short Shear Constant R . . . . 8.000x10^{-2}
Positive Phase Long Shear Constant F . . . . 1.100x10^{-1}
Positive Phase Long Shear Constant R . . . . 2.700x10^{-1}
Rebound Phase Short Shear Constant F . . . . 4.000x10^{-2}
Rebound Phase Short Shear Constant R . . . . 8.000x10^{-2}
Rebound Phase Long Shear Constant F . . . . 1.100x10^{-1}
Rebound Phase Long Shear Constant R . . . . 2.700x10^{-1}
Integration Time Step (sec) . . . . 1.000x10^{-5}
Number of Response Cycles Evaluated . . . . 5.000x10^{+0}
Positive Phase Period (sec) . . . . 1.029x10^{-2}
Rebound Phase Period (sec) . . . . 1.029x10^{-2}

TABLE 25. COMPARISON OF MEASURED AND COMPUTED RESPONSES OF THE TYNDALL WALLS USING THE BIGGS PROGRAM WITH TRILINEAR RESISTANCE FUNCTION AND 5% DAMPING.

Wall	Meas-ured defl-ection (in.)	Computed maximum deflection, in.					
		Idealized as two-way slab			Idealized as one-way slab		
		Load A	Load B	Load C	Load A	Load B	Load C
South	2.46	1.48	2.21	0.63	1.50	2.22	0.63
North	1.94	0.71	1.75	0.48	0.70	1.61	0.47

TABLE 26. INPUT DATA FOR BIGGS ANALYSIS OF SOUTH WALL OF TYNDALL STRUCTURE AS A ONE-WAY SLAB WITH TRILINEAR RESISTANCE FUNCTION.

Positive Phase Mass . . . . 4.703×10^2
Rebound Phase Mass . . . . 4.703×10^2
Positive Phase Elastic Load Mass Factor . . . . 7.700×10^{-1}
Positive Phase Elastic-Plastic Load Mass Factor . . . . 7.800×10^{-1}
Positive Phase Plastic Load Mass Factor . . . . 6.600×10^{-1}
Rebound Phase Elastic Load Mass Factor . . . . 7.700×10^{-1}
Rebound Phase Elastic-Plastic Load Mass Factor . . . . 7.800×10^{-1}
Rebound Phase Plastic Load Mass Factor . . . . 6.600×10^{-1}
Positive Phase Elastic Spring Constant . . . . 1.330×10^8
Rebound Phase Elastic Spring Constant . . . . 1.330×10^8
Positive Phase Elastic-Plastic Spring Constant . . . . 2.661×10^7
Rebound Phase Elastic-Plastic Spring Constant . . . . 2.661×10^7
Positive Phase Elastic Yield . . . . 3.725×10^6
Positive Phase Elastic-Plastic Yield . . . . 5.496×10^6
Rebound Phase Elastic Yield . . . . 3.725×10^6
Rebound Phase Elastic-Plastic Yield . . . . 5.496×10^6
Fraction of Viscous Damping . . . . 5.000×10^{-2}
Number of Force-Time History Pairs 3

Force   Time
0.000×10^0 $0.000 \times 10^{+0}$
2.323×10^8 $0.000 \times 10^{+0}$
0.000×10^0 9.000×10^{-4}

Initial Displacement . . . . $0.000 \times 10^{+0}$
Initial Velocity . . . . $0.000 \times 10^{+0}$
Positive Phase Short Shear Constant F . . . . 1.200×10^{-1}
Positive Phase Short Shear Constant R . . . . 3.800×10^{-1}
Positive Phase Long Shear Constant F . . . . 1.100×10^{-1}
Positive Phase Long Shear Constant R . . . . 2.700×10^{-1}
Rebound Phase Short Shear Constant F . . . . 1.200×10^{-1}
Rebound Phase Short Shear Constant R . . . . 3.800×10^{-1}
Rebound Phase Long Shear Constant F . . . . 1.100×10^{-1}
Rebound Phase Long Shear Constant R . . . . 2.700×10^{-1}
Integration Time Step (sec) . . . . 1.000×10^{-5}
Number of Response Cycles Evaluated . . . . $5.000 \times 10^{+0}$
Positive Phase Period (sec) . . . . 1.037×10^{-2}
Rebound Phase Period (sec) . . . . 1.037×10^{-2}

114

TABLE 27.   INPUT DATA FOR BIGGS ANALYSIS OF NORTH WALL OF TYNDALL STRUCTURE
            AS A ONE-WAY SLAB WITH TRILINEAR RESISTANCE FUNCTION.

```
Positive Phase Mass . . . . . . . . . . . . . . . . . . . . .  5.811x10²
Rebound Phase Mass  . . . . . . . . . . . . . . . . . . . . .  5.811x10²
Positive Phase Elastic Load Mass Factor . . . . . . . . . . .  7.700x10⁻¹
Positive Phase Elastic-Plastic Load Mass Factor . . . . . . .  5.800x10⁻¹
Positive Phase Plastic Load Mass Factor . . . . . . . . . . .  6.600x10⁻¹
Rebound Phase Elastic Load Mass Factor . . . . . . . . . . .   7.700x10⁻¹
Rebound Phase Elastic-Plastic Load Mass Factor  . . . . . . .  5.800x10⁻¹
Rebound Phase Plastic Load Mass Factor  . . . . . . . . . . .  6.600x10⁻¹
Positive Phase Elastic Spring Constant  . . . . . . . . . . .  2.440x10⁸
Rebound Phase Elastic Spring Constant . . . . . . . . . . . .  2.440x10⁸
Positive Phase Elastic-Plastic Spring Constant  . . . . . . .  4.879x10⁺⁷
Rebound Phase Elastic-Plastic Spring Constant . . . . . . . .  4.879x10⁺⁷
Positive Phase Elastic Yield  . . . . . . . . . . . . . . . .  3.871x10⁶
Positive Phase Elastic-Plastic Yield  . . . . . . . . . . . .  5.590x10⁶
Rebound Phase Elastic Yield . . . . . . . . . . . . . . . . .  3.871x10⁶
Rebound Phase Elastic-Plastic Yield . . . . . . . . . . . . .  5.590x10⁶
Fraction of Viscous Damping . . . . . . . . . . . . . . . . .  5.000x10⁻²
Number of Force-Time History Pairs  . . . . . . . . . . . . .  3
```

```
                    Force          Time
                    0.000x10⁰      0.000x10⁺⁰
                    1.888x10⁸      0.000x10⁺⁰
                    0.000x10⁰      8.280x10⁻⁴
```

```
Initial displacement  . . . . . . . . . . . . . . . . . . . .  0.000x10⁺⁰
Initial Velocity  . . . . . . . . . . . . . . . . . . . . . .  0.000x10⁺⁰
Positive Phase Short Shear Constant F . . . . . . . . . . . .  1.200x10⁻¹
Positive Phase Short Shear Constant R . . . . . . . . . . . .  3.800x10⁻¹
Positive Phase Long Shear Constant F  . . . . . . . . . . . .  1.100x10⁻¹
Positive Phase Long Shear Constant R  . . . . . . . . . . . .  2.700x10⁻¹
Rebound Phase Short Shear Constant F  . . . . . . . . . . . .  1.200x10⁻¹
Rebound Phase Short Shear Constant R  . . . . . . . . . . . .  3.800x10⁻¹
Rebound Phase Long Shear Constant F . . . . . . . . . . . . .  1.100x10⁻¹
Rebound Phase Long Shear Constant R . . . . . . . . . . . . .  2.700x10⁻¹
Integration Time Step (sec) . . . . . . . . . . . . . . . . .  1.000x10⁻⁵
Number of Response Cycles Evaluated . . . . . . . . . . . . .  5.000x10⁺⁰
Positive Phase Period (sec) . . . . . . . . . . . . . . . . .  8.509x10⁻³
Rebound Phase Period (sec)  . . . . . . . . . . . . . . . . .  8.509x10⁻³
```

SECTION VII
PREDICTION OF THE BEHAVIOR OF THE TEST STRUCTURES USING BLAST

A.   BRIEF DESCRIPTION OF THE PROGRAM

BLAST is a program that was prepared for the Physical Security Division of the U.S. Department of State by the Transportation Systems Center of the Research and Special Programs Administration, U.S. Department of Transportation. The work was performed under the direction of Herbert H. Gould, Chief, Vehicle Crashworthiness Division. Staff members of the U.S. Naval Civil Engineering Laboratory, Port Hueneme, CA, and of the U.S. Army Waterways Experiment Station, Vicksburg, MS, also provided assistance during development of the program.

The program was intended to be a simplified, easy-to-use procedure for the assessment of the vulnerabilities of building wall panels to damage by high explosive air blast pressure loadings. It considers walls of reinforced concrete (with or without cut-outs), bearing walls (either infilled or bearing), and glass panels made of a variety of glazing materials. The program is interactive, and displays the results in both tabular and graphical form. For the convenience of the users of the program, its authors have provided both a *Users Manual* and a *Technical Manual*, References 31 and 32, respectively. The program runs under the DOS operating system.

A detailed understanding of computers is not required to use the program successfully, nor is extensive knowledge of structural engineering or of air blast loading phenomenology required to understand and interpret the results produced by the program. However, a reasonable knowledge of structures and of blast loading phenomenology is necessary for the user of the program to understand the assumptions and idealizations that are implicit in it and, therefore, to appreciate the significance of uncertainties and approximations that may exist in the definition of the element being analyzed. In other words, intelligent use of the program to analyze a structural element whose geometry, support conditions, and/or internal resistance characteristics differed significantly from the idealized elements assumed by the program would require a reasonable level of competence in structural engineering.

Only symmetrical wall panels that are supported on all edges by a nondeflecting structural system are considered. It is assumed that the supporting structural system is capable of withstanding the forces imparted to it as the panel being supported responds to the air blast forces to which it is being subjected. Each panel that is analyzed is assumed to be an independent unit, structurally unrelated to any of the other panels under review. The panels were idealized for dynamic analysis as SDOF systems in essentially the same manner as each of the programs that were described in the preceding chapters. The dynamic model employed was developed as described by Biggs in Reference 3 for slab-type elements. Conceptually, then, this program is very similar to the other programs that have already been reviewed.

To use the program, the analyst is required to provide the following minimal information as initial input:

(a) The external dimensions of the panel (wall element) being studied. (This information is provided by entering the rectangular coordinates of the corners of the panel, these coordinates being expressed with reference to an arbitrary set of axes selected by the analyst).

(b) The material (glass, masonry [infilled or bearing], or reinforced concrete) of which the panel is made.

(c) The size (pounds of TNT) of the explosive charge.

(d) The location of the charge with respect to the panel, expressed as the coordinates of the location of the charge given with reference to the same axes that were used to define the corners of the panel.

With this information (and, in the case of glass walls, with more specific definition of the type of glazing in the panel, and making use of built-in default values for panel thicknesses and material properties) the program can proceed to develop an idealized SDOF model, generate the blast pressure loading function that is to be imposed upon the panel, carry out an iterative dynamic analysis of the responding element, and predict the maximum deflection of the panel that might be expected. However, if more detailed or better information about the panel thickness and/or the properties of the materials of which it is made is available, the program allows the analyst to enter this "better" data, which the program will then use, instead of the default values, to compute the equivalent mass and the resistance function of the SDOF model of the panel. Brief descriptions of the bases that are used in this program to generate the required resistance functions are given in the following paragraphs.

For *reinforced concrete panels*, the program assumes rotational fixity of all edges, with the same percentage of reinforcing steel being used on both faces and in both directions. The conventional, trilinear, flexural resistance function is then developed, using yield-line theory. The ultimate resistance is the uniformly applied pressure that would be required to develop the fully plastic moment along all of the negative and positive moment yield lines simultaneously.

If the panel has a cut-out, the program requires that the size of the cut-out be entered as a percentage of the total surface area of the panel, assumes the cut-out to have the same aspect ratio as does the panel and to be located symmetrically in the center of the panel, and, using yield-line theory, then computes the resistance function of the remaining slab. In this analysis, it assumes that the cut-out is covered with unbroken material (perhaps glazing, which will be or has been analyzed separately) and that the pressure that is applied to the area of the cut-out is carried by the slab as a line-load along the edges of the cut-out.

For a slab without cut-out, the SDOF transformation factors used by the program are those that are provided by Biggs for a fixed-edged plate in Reference 3. For slabs with cut-outs, these transformation factors are evaluated by the

program individually for each case, using the physical definitions of these factors as given by Biggs.

For *glass panels*, the analyst is required to specify one of the following types of glazing:

- Thermally tempered glass
- Polycarbonate
- Semitempered glass
- Annealed glass
- Herculite II
- Plate glass
- Annealed glass (abraded)
- Tempered glass (abraded)

For each of these materials, the program contains default values of thickness and strength properties which it will use to compute a resistance function for the panel, unless other, presumably better, values of these quantities are provided by the analyst. Using the work of Moore (Reference 33) and of Meyers (Reference 34), the program then computes the resistance function, assuming that the panels are simply supported and are free to rotate and to move in the plane of the panel. The dynamic SDOF equivalence factors are taken as given by Biggs in Reference 3 for small deflection plate behavior.

For *masonry panels*, the program is designed to analyze both infilled and bearing walls that are made of either brick or concrete blocks. Only unreinforced masonry construction is considered. As for the other materials, the program includes default values for the wall thickness and for the mortar and brick or block properties, but provides convenient opportunity for the analyst to replace any or all of those default values with better data, if better data are available. For bearing walls, the number of stories above the panel being analyzed is required as additional input.

The resistance functions for the walls are computed on the basis of one-way flexural response. This assumption will underestimate the strength of the panel because most panels will derive some strength augmentation from two-way action, such augmentation being especially pronounced in square, infilled panels.

For infilled walls, the resistance functions are generated using the arching action theory of masonry walls as developed by McDowell, McKee, and Sevin in Reference 35, and the dynamic transformation factors used were those as proposed by Biggs (Reference 3) for the plastic regime of simple beam behavior. For bearing walls, the resistance is taken as the flexural strength, determined on the basis of the tensile strength of the mortar, as augmented by the in-plane force produced by the weight of the stories above the panel being analyzed.

The blast pressure loading is generated within the program for each analysis as the reflected pressure pulse that is produced by the detonation of a hemispherical charge of specified size (pounds of TNT) at a specified distance from, and at a given angle of incidence with respect to, the center of the panel. The loading pulse thus generated takes into account the variation of reflection factor as a function of both the incident peak pressure and the angle of

118

incidence of the blast wave with the panel surface. It is not possible to enter a prescribed pressure-time curve.

B. APPLICATION OF THE PROGRAM TO THE IDF STRUCTURES

Because the IDF test walls were not the symmetrically supported, symmetrically reinforced slabs that BLAST assumes, it was necessary, before entering the wall properties to be used instead of the default values of the program, to determine an "equivalent" uniform reinforcement percentage. This percentage, when applied in both directions on both sides of the slab, would produce an ultimate flexural capacity that was about the same as the comparable value determined for the UofI and BIGGS solutions. Consequently, by selecting dynamic yield stresses for the concrete and steel of 5200 psi and 41,000 psi, respectively, which are the same as the comparable values that were used in the other programs, it was determined by back-calculation that a uniform reinforcement percentage of 0.233, when used with a cover on the steel of 0.9 inch and assuming full edge fixity, would produce an ultimate flexural resistance of the slab of about 34 psi. This reinforcement ratio and cover is different from that used in the program BIGGS, but it was necessary to make this modification to obtain the same yield resistance of about 34 psi. Because this value is reasonably close to the resistance levels used in the UofI and the BIGGS programs, the results produced by BLAST, using this resistance, should be roughly comparable to the corresponding results that were produced by the other two programs under comparable loadings. But, because of the unique nature of SASDE, as described in Section V, one could not reasonably expect the BLAST and SASDE results to agree.

The resistance function thus generated, which is shown in Figure 81, was assumed to apply for all of the IDF tests, and the program was run to determine the maximum deflection of the wall in each of the tests. The results of the analysis for Test 1, which are illustrative of the output that was generated by the program for each of the test runs, are shown in Table 28 and Figures 82 and 83.

The pressure pulses shown in Figure 82, which were generated by BLAST for Test 1, are typical of the loading pulses used by this program. The exponentially decaying pulses shown on that figure are the incident and reflected pressure pulses computed by the program to exist at the center of the wall as a consequence of the detonation of a 189.3-pound hemispherical charge of TNT (the equivalent of the actual charge of 181 pounds of Composition B that was actually used in the tests) on the ground surface at a distance of 49.2 feet from the wall. Shown also on that figure are the impulse-equivalent triangular pulses of the incident and reflected pressures that are used by the program as the load functions instead of the theoretical exponentially decaying pulses. The program permits the analyst to select either the incident pressure or the reflected pressure as the loading function to be used in the analysis. Clearly, for the IDF structures, the reflected pressure pulses were used.

119

FORCE-DEFL CURVE OF CONCRETE PANEL # 2, THICKNESS=15.70 IN, C/C= 0.%
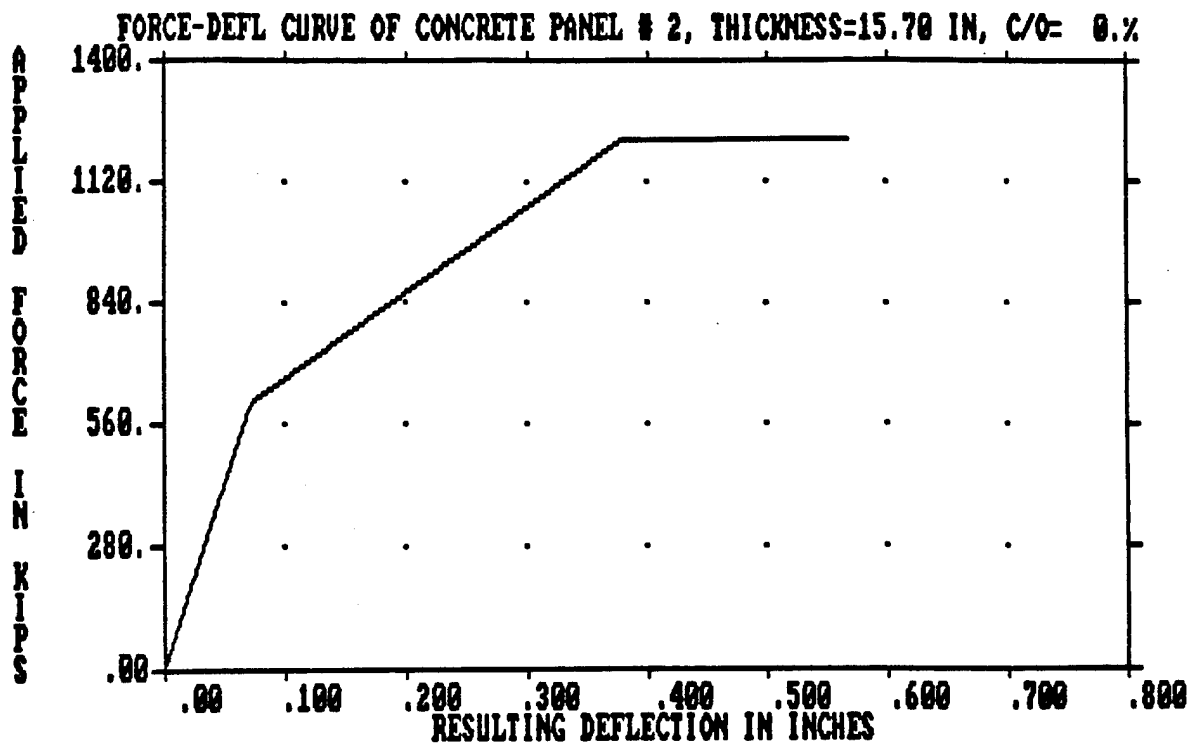
Figure 81. Resistance Function Calculated by BLAST for the IDF Wall Tests.

The maximum deflections of the wall as predicted by BLAST in each of the tests are shown in Table 29. Shown also in that table for comparative purposes are corresponding maximum deflections that were predicted by the UofI program using theoretical reflected pressure impulse loadings. The reflected pressure impulses used in the UofI solutions were computed external to the program, but they were computed from the same reference source as were the internally computed pressures of BLAST. Hence, they should have been equal for each test and, as will be observed from the data of Table 29, they were essentially equal. As will also be observed from studying the data of Table 29, the maximum deflections predicted by the two programs are also in good agreement. The differences between these maximum deflections result from the slightly larger loading impulses as determined for the UofI program (see the tabulation), the small difference in yield resistance as used in the two programs (33.5 psi for the UofI versus 36.0 psi for BLAST), and the fact that BLAST assumed the loads to be applied as equivalent triangles while UofI used the computed, exponentially decaying pulses. The latter effect is of little or no consequence as long as the duration of the equivalent impulse triangle is small relative to the period of vibration of the responding element, but it becomes significant when the duration of the loading triangle becomes greater than about one-quarter to one-third the natural period. Its effect is clearly visible in Test 5 for which the equivalent triangular impulse duration was 9.1 milliseconds which is almost half of the 20-millisecond natural period of the wall.

120

C.   APPLICATION OF THE PROGRAM TO THE TYNDALL STRUCTURES

BLAST was applied to the test walls of the Tyndall structures in essentially the manner in which it was used to analyze the IDF structures. Because the test walls were neither fully fixed on all four edges nor reinforced equally in both directions, which conditions are assumed by BLAST, to obtain results that might be reasonably comparable to those given by other programs reviewed here, it was necessary to determine artificial reinforcement percentages which, if used on both faces in both directions of the slabs, would produce resistance levels that closely approximated the resistance levels that were used by the other programs. (It will be recalled that this same situation existed in the application of BLAST to the IDF structures.) Using the dimensions of the idealized slab as defined earlier (158 x 519.5 inches), and the material properties used in other analyses, uniform reinforcement ratios of 0.0020 and 0.0014, with average concrete cover of 2.00 inches on both the inside and outside faces of the walls, were found to produce yield resistances as computed by BLAST

TABLE 28. SUMMARY OF RESULTS PROVIDED BY BLAST FOR IDF TEST 1.

BLAST parameters--without perimeter wall	
Weight of TNT	189.3 lbs
Distance from panel	49.3 ft
Angle of incidence	5.8 deg
Shock front arrival time	19.46 msec
Shock front velocity	1481.6 ft/sec
Incident peak pressure	12.95 psi
Incident pulse duration	13.73 msec
Incident equiv. pulse duration	8.19
Incident impulse	53.05 psi-msec
Incident pulse decay coeff.	1.795
Reflected peak pressure	34.13 psi
Reflected pulse duration	13.73 msec
Reflected equiv. pulse duration	7.00 msec
Reflected impulse	119.51 psi-msec
Reflected pulse decay coeff.	2.466

Results of BLAST on concrete Panel #2	
Reflected wave--TNT weight	189.3 lbs
Without perimeter wall--distance	49.3 ft
Angle	5.8 deg
Height of Panel	10.00 ft
Length of Panel	24.30 ft
Thickness of panel	15.70 in.
Percent cut-out	0.0 %
Equivalent elastic defl. limit	0.216 in.
Edge rotation (fails at 2.0 deg)	0.172 deg
Maximum dynamic center deflection	0.146 in.
Ductility ratio	0.678
If ductility ratio less than 1.0	No panel failure
If ratio between 1.0 and 5.0	Partial failure
If ratio more than 5.0	Total failure

121

INCIDENT AND REFLECTED PRESSURE: WGT= 189. DIS= 49. ANG= 5.8
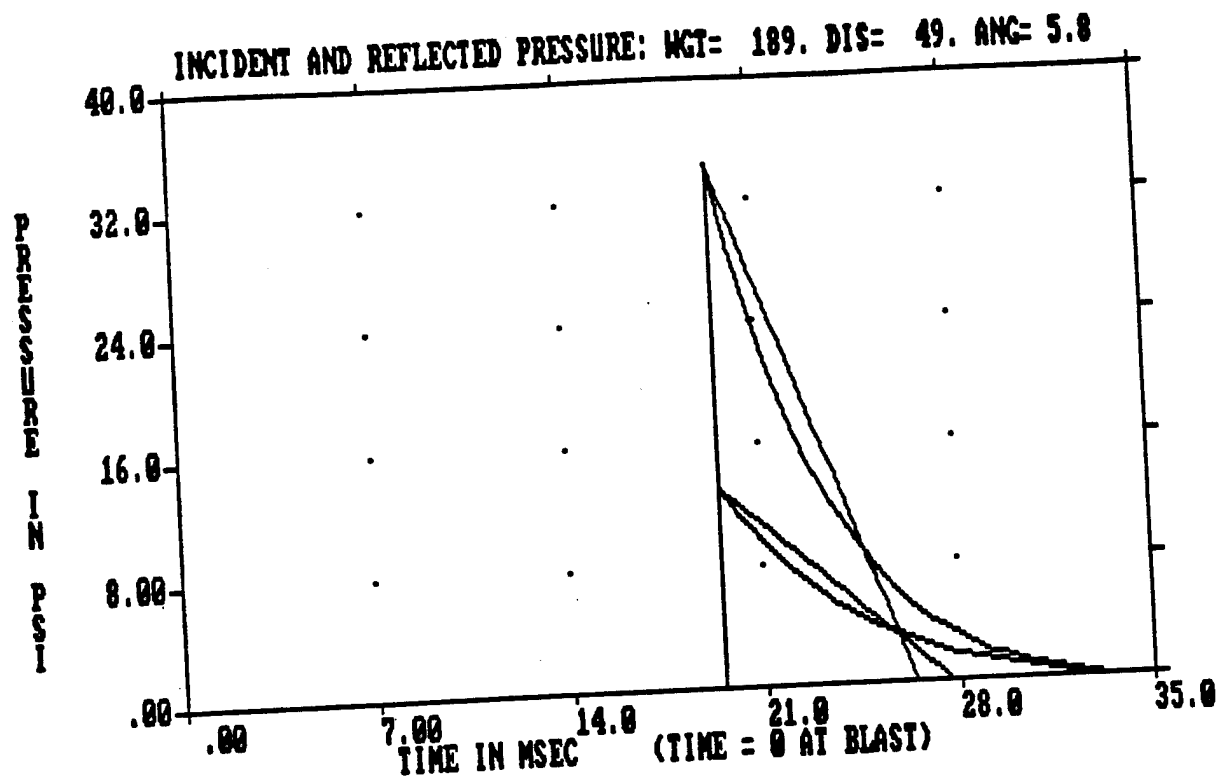
Figure 82. Theoretical Incident and Reflected Pressure Pulses at the Center of the Wall for IDF Test 1 as Generated by BLAST.

RESPONSE OF PANEL # 2, WGT= 189.,DIS= 49.,ANG= 5.8,THKNSS=15.700 IN
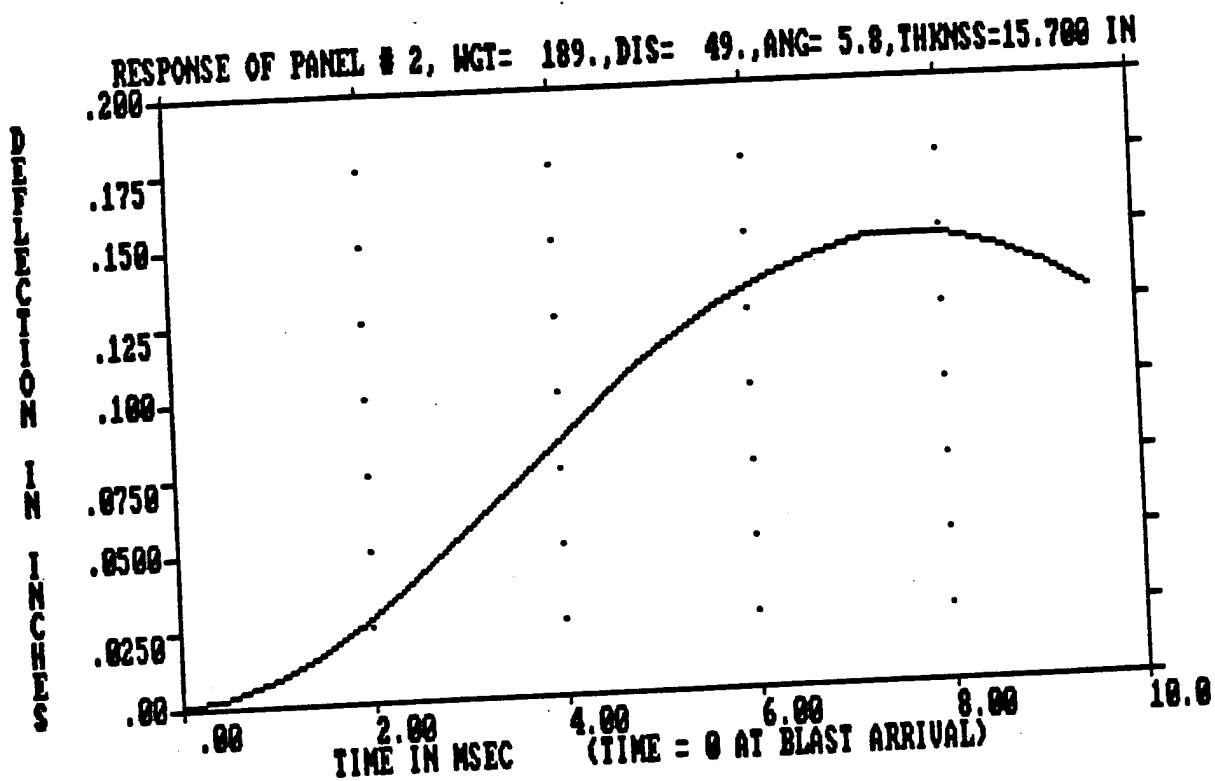
Figure 83. Displacement-Time Response for IDF Test 1 as Calculated by BLAST.

122

TABLE 29. SUMMARY OF BLAST RESULTS AND COMPARISON WITH UofI PROGRAMS RESULTS.

Test No.	Range[a]	BLAST		UofI Program	
		Refl. Imp. (psi-ms)	Max. Defl. (in)	Refl. Imp. (psi-ms)	Max. Defl. (in)
1	49.5	120	0.145	123	0.135
2	33.1	188	0.314	197	0.293
3	23.5	281	0.609	301	0.674
4	17.2	410	1.27	450	1.52
5	65.8	194	0.260	200	0.204
6	49.5	271	0.502	280	0.448
7	33.1	435	1.27	457	1.37
8	23.5	661	2.97	715	3.52
9	17.2	969	6.28	1091	8.09

[a]Distance from the location of the charge to the center of the test wall

of about 77 psi and 82 psi for the south and north walls, respectively. These resistances, which can be compared with the UofI program values of 73 psi and 81 psi, respectively, are shown in Figures 84 and 85. The resistance levels depicted in those figures are expressed in terms of total forces on the wall, and are related to the comparable unit forces by the surface area of the wall, 82,081 square inches.

For convenient reference, the parameters used by BLAST to arrive at those resistance functions are summarized in Table 30.

The loadings on the walls are generated by the program on the basis of input data that include an explosive charge of specified type and size, the location of that charge with respect to the wall being loaded, and the dimensions of the wall. With this input data, it appears that the program then computes loading at the midpoint of the wall, taking into account both the distance from the charge to that midpoint and the angle of incidence with which the advancing shock front impinges on the walls at their midpoints.

The assumed loading function is shown in Figure 86. Because this loading was determined at the center of the wall, taking into account the angle of incidence of the blast, it should be somewhat less severe than are the loadings shown in Figures 51(b) and 52(b), which were computed for the same charge size at the same location but assumed the pressure fronts to impinge normally on the walls. Similarly, it should be somewhat more severe than the loadings shown in Figures 51(c) and 52(c), which attempted to represent an average of the reflected impulse loadings over the entire wall areas, taking into account, albeit somewhat crudely, the variations in the angles of incidence from point to point across the

FORCE-DEFL CURVE OF CONCRETE PANEL # 4, THICKNESS=25.50 IN, C/O= 0.%
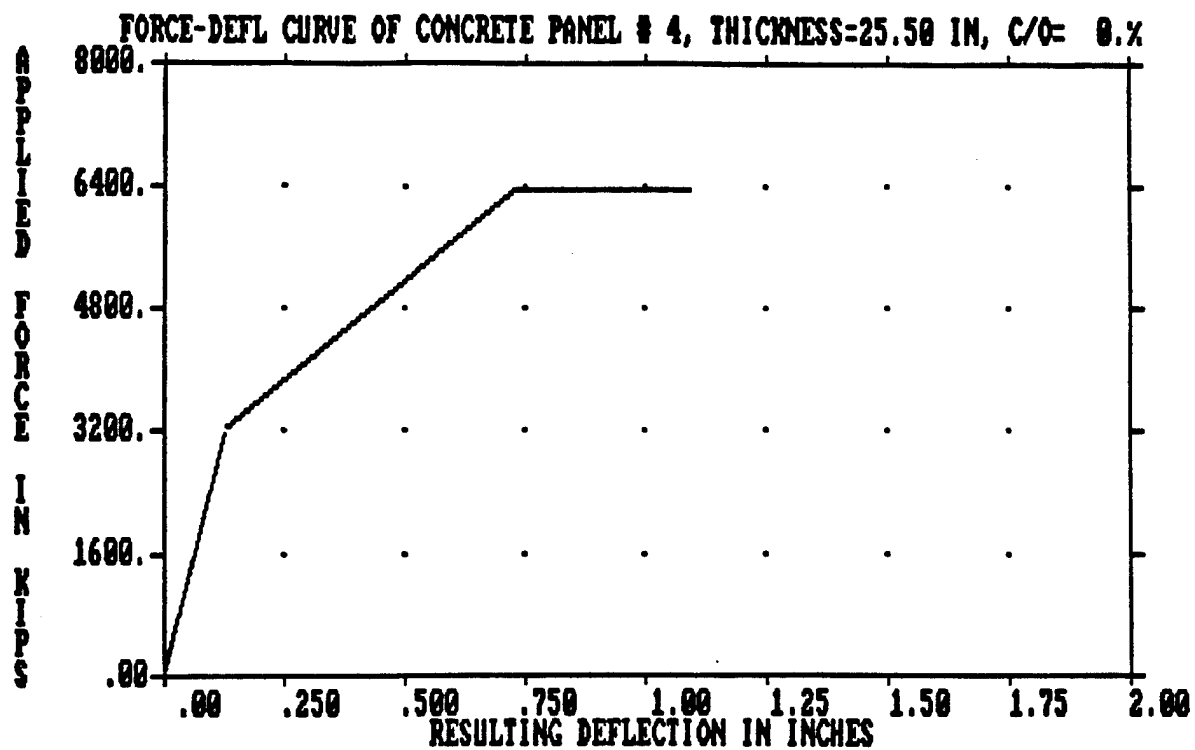
Figure 84.   Resistance Function Generated by BLAST for the South Wall of the Tyndall Structure.

FORCE-DEFL CURVE OF CONCRETE PANEL # 2, THICKNESS=31.50 IN, C/O= 0.%
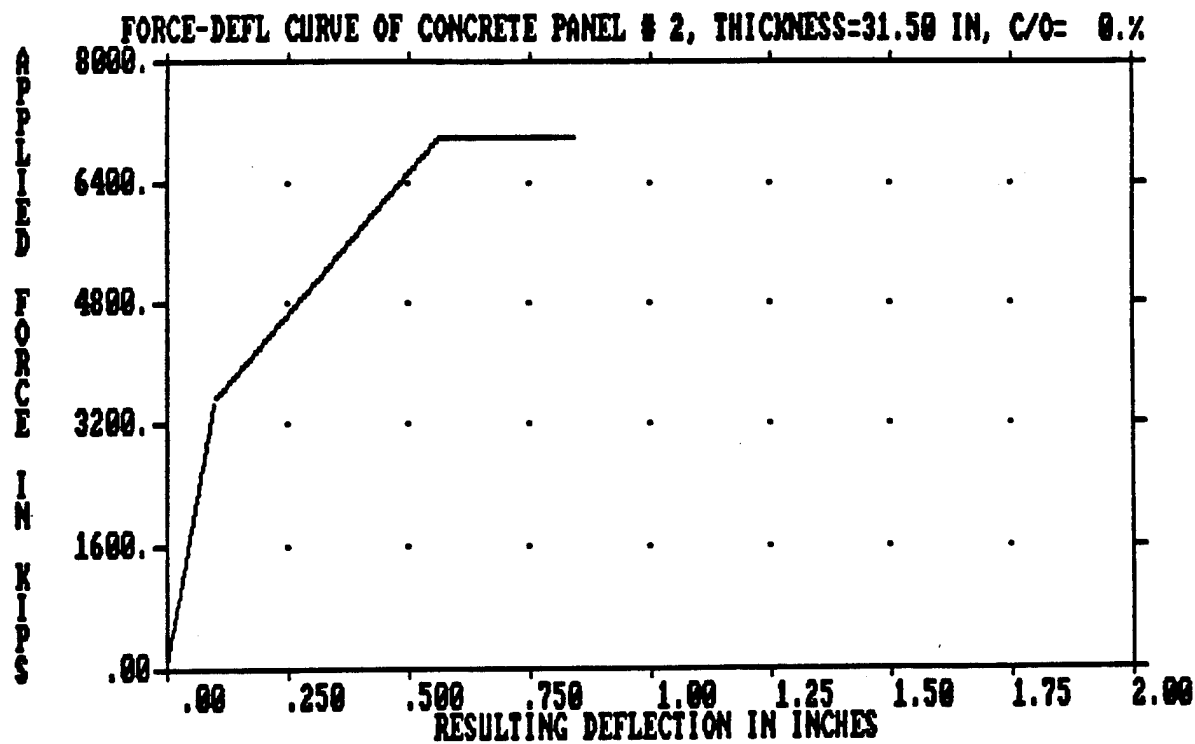
Figure 85.   Resistance Function Generated by BLAST for the North Wall of the Tyndall Structure.

TABLE 30.   PARAMETERS USED BY BLAST TO DETERMINE RESISTANCE FUNCTIONS.

Parameter	South Wall	North Wall
Short span length, in.	158.0	158.0
Long span length, in.	519.5	519.5
Total slab thickness, in.	25.5	31.5
Dynamic yield strength of steel, psi	78,000	78,000
Dynamic yield strength of conc., psi	6,947	6,947
Modulus of elasticity for steel, psi	29,000,000	29,000,000
Modulus of elasticity for conc., psi	3,726,259	3,726,259
Steel reinforcement ratio	0.0020	0.0014
Average conc. cover on reinf. in	2.0	2.0

surfaces of the walls. With a peak pressure of about 2800 psi and a selected impulse of about 1000 psi-ms, the loading pulse of Figure 86 is seen to lie between the loadings represented by pressure pulses (b) and (c) of Figures 51 and 52.

Applying the loading function of Figure 86 to the resistance functions of Figures 84 and 85, and using damping factors of 0.05, the maximum deflections of the south and north walls were computed by BLAST to be 2.44 and 1.81 inches, respectively, as shown in Figures 87 and 88. As would be expected, these values fall between the corresponding maximum deflections as computed by the other programs for loadings (b) and (c) of Figures 51 and 52.
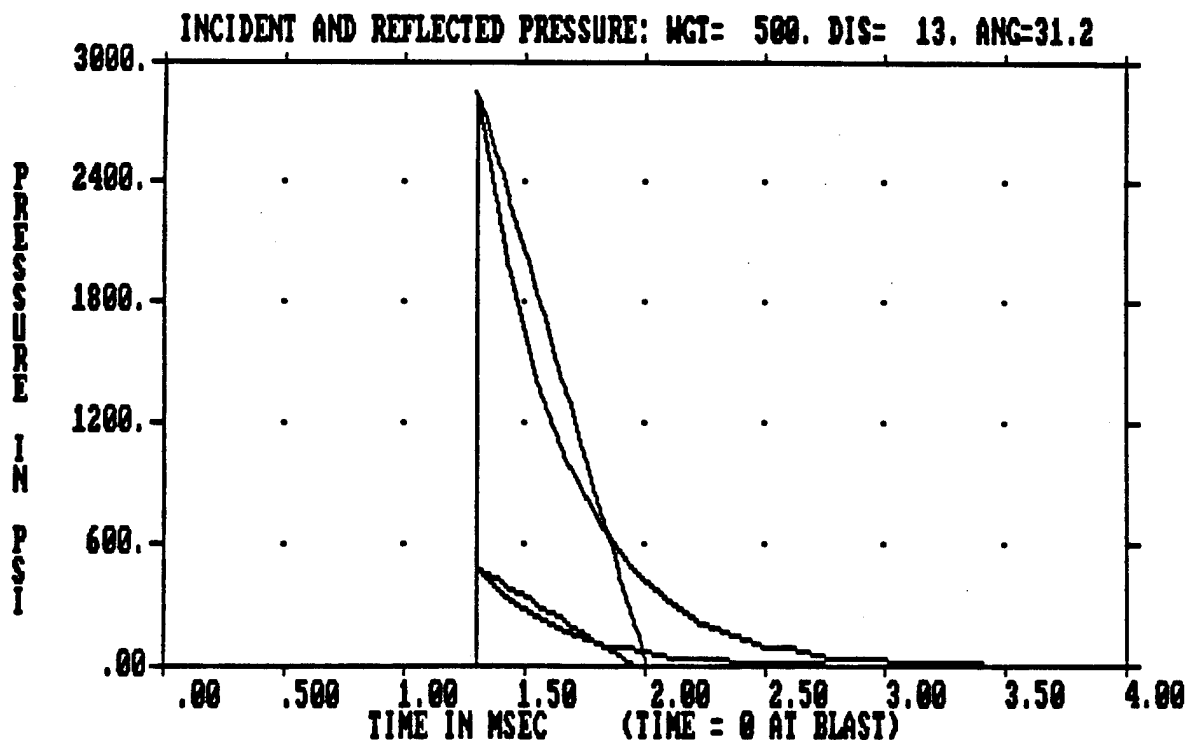
Figure 86.   Loading Functions Generated by BLAST for Both Walls of the Tyndall Structure.
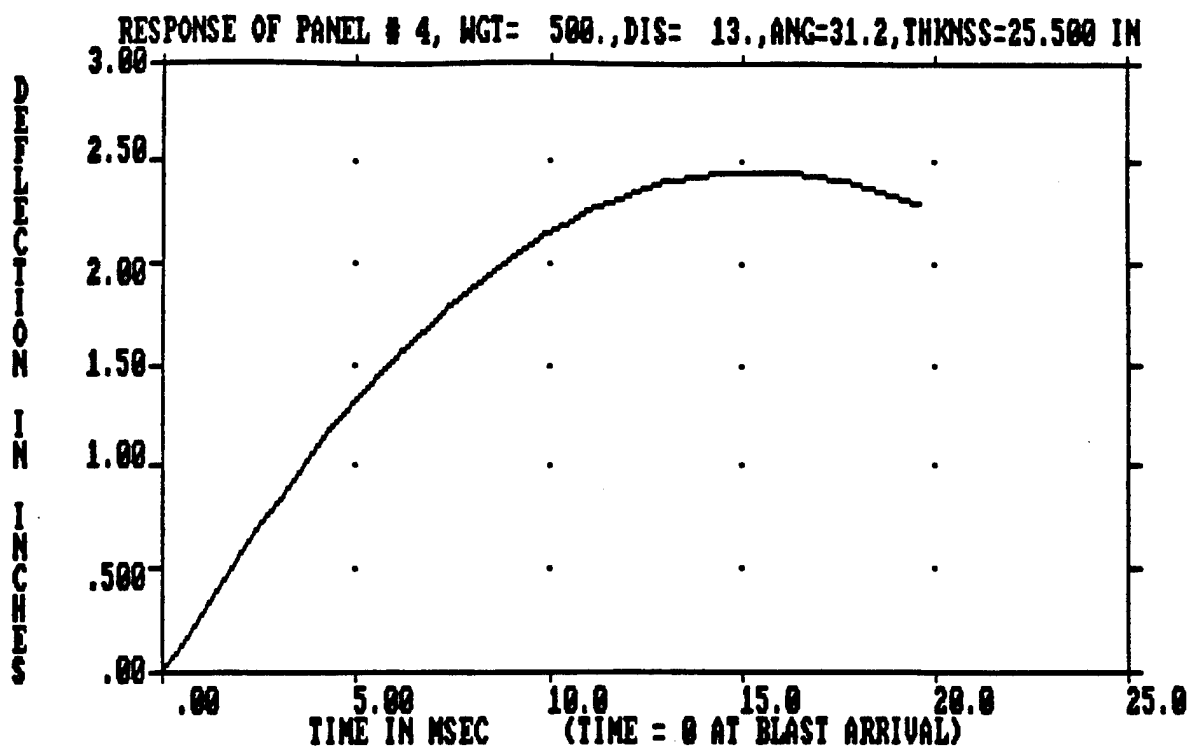
Figure 87.   Response of the South Wall of the Tyndall Structure as Computed by
             BLAST.
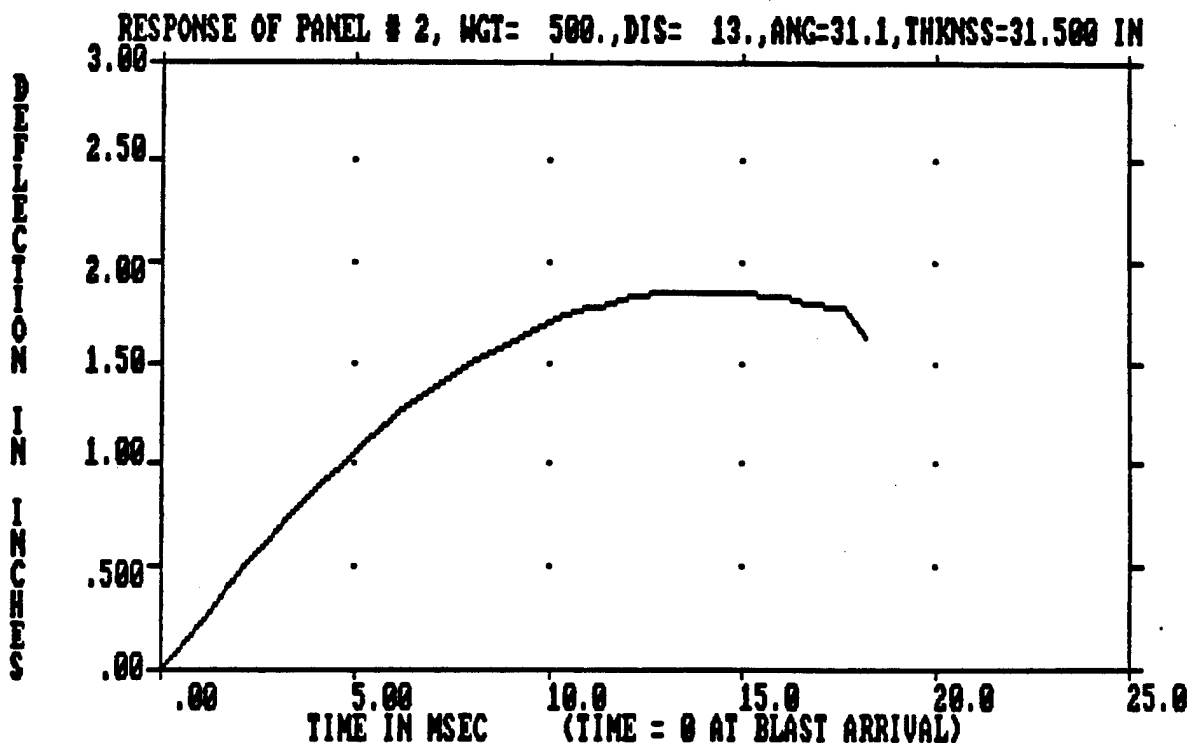
Figure 88.   Response of the North Wall of the Tyndall Structure as Computed by
             BLAST.

126

SECTION VIII

NONLINEAR FINITE ELEMENT MODELING OF TEST STRUCTURES

A. INTRODUCTION

In addition to performing a comparative study of SDOF microcomputer models, a number of nonlinear dynamic finite element analyses (NDFEA) of the test structures were performed. The objective of the NDFEA was to determine the feasibility of using such procedures in the design process, either instead of or as a complement to the SDOF procedures.

The code selected for the NDFEA was Automated Dynamic Incremental Nonlinear Analysis (ADINA), which was developed and is marketed by ADINA R&D Inc., Watertown, MA. The selection was heavily influenced by two factors. First, Headquarters Air Force Civil Engineering Support Agency (HQ AFCESA) is already involved with ADINA applications, so there is a degree of corporate familiarity with ADINA. Second, ADINA is one of the few commercial finite element codes available with a detailed concrete material modeling capability. This was viewed as a valuable program feature. This report documents the authors' experiences in using ADINA to analyze the IDF Structure (Tests 1, 2, 3, and 4) and two of the Tyndall AFB Structure tests (Tests 6 and 10). Because of the complexity of ADINA's use in the analyses, a brief description of its features as they apply to NDFEA of reinforced concrete structures is presented. (Should the reader not wish to review this description, he or she may proceed directly to Section VIII, paragraph B.6, to review the analyses conducted in this study.)

B. GENERAL DESCRIPTION OF THE FINITE ELEMENT MODELING PROCEDURES USED IN ADINA

1. Overview

ADINA is a multipurpose finite element program, although, as its name implies, its real strengths are its nonlinear and dynamic analysis capabilities. It possesses a broad selection of element types, material models, and static and dynamic solution schemes. In particular, it has a sophisticated concrete material model that supports analysis of concrete or geotechnical materials.

Although ADINA provides a number of advantages, the analyst is posed with a number of complexities that must be addressed via judicious use of *engineering judgement*. A 1982 state of the art report (Reference 47, p. 26) summarized these complexities; they have not changed significantly in the ensuing 10 years:

(a) There are two distinctly different materials to be modeled, steel and concrete. While steel material properties are generally well defined, concrete material properties are much less well defined and subject to wide variability.

(b) Concrete in actual structures is subjected to complex multiaxial stress states. Its behavior in such states is still not well understood.

(c) With its inherently low tensile strength, concrete cracks under relatively low tensile stresses. As cracks propagate in a reinforced concrete

member, its local stresses and displacements, and its global behavior and strength, change.

(d) Bond between reinforcement and concrete deteriorates with increasing and/or cyclic load.

(e) Concrete material properties vary with time. While creep is not a major issue in the analyses reported here, the strain rate-dependence of concrete stress-strain behavior is very significant.

(f) Shear stress transfer after tensile cracking has occurred is a complex combination of load transfer mechanisms.

These complexities lead to a highly complicated, nonlinear analysis procedure. There are added factors in the explosives effects arena that are associated with structural load mechanisms.

In Reference 37, Bathe et al., note that nonlinear finite element analysis of reinforced concrete is not well accepted, due to the above noted problems, the expense of nonlinear dynamic analysis, and the difficulties associated with numerical stability and computational accuracy.

2.   Element Types Used in the Analyses

To simulate a reinforced concrete structure, an analyst desires to model both the steel reinforcement properties and the concrete material properties, and their interactions. The approach used depends largely upon the information sought. While some analysts have developed *smeared* models that in some way combine the properties of the steel reinforcement and the concrete into equivalent single material properties, the ability to model the two materials separately can provide more flexibility to the analyst when both steel and concrete behavior (and associated bond mechanisms) need to be observed, as would be the case in design. The element types found in ADINA accommodate this modeling approach.

A truss, or line, element is available for reinforcing bar modeling. The truss element transmits force in uniaxial tension or compression only. The contribution of the reinforcement stiffness to overall structural stiffness is accomplished by superposition of the reinforcing bar stiffness directly on the solid element (concrete) stiffness matrix (Reference 47, p. 164). The relatively low volume of reinforcement in the structures analyzed led the authors to neglect reducing the structure's concrete volume that was displaced by the reinforcement. For dynamic analysis, the truss element mass matrix may be lumped or consistent (Reference 36). In lumped mass matrices, element masses are "lumped" in equal amounts at element nodes; in consistent mass matrices, element masses are distributed in accordance with the isoparametric shape functions for the element. The consistent formulation includes both translational and rotational degrees of freedom, while the lumped formulation only includes translational degrees of freedom. The consistent formulation is generally more accurate, but more computationally demanding, than the lumped formulation. The truss element can be used with linear or nonlinear material properties, and it is available in 2,

3, or 4 node options (Figure 89), with the 3 and 4 node options typically used in conjunction with higher order solid concrete elements.

While this study uses truss elements to simulate discrete reinforcing bars, it would also be possible to use other element types found in ADINA to create smeared reinforcing layers of isotropic or anisotropic materials. For the analyses reported here, individual truss element cross-sectional areas were based upon the reinforcement percentages in the test structures; the truss elements were sized to provide proper reinforcement percentages in the analytical models, given that bar "spacing" in the ADINA model would be driven by concrete, or solid, element sizes. The truss elements in the models were located as closely as possible to the centerline positions for the reinforcing bars shown in design drawings.

To model concrete material, ADINA requires that two- or three-dimensional solid isoparametric elements be used. The two-dimensional, or planar, elements, in 3, 4, 6, and 8 node options, are available for plane stress, plane strain, or axisymmetric analyses. This study uses the two-dimensional elements in plane strain to model one-way slab action in the structure. Three-dimensional solid elements are available in 8, 20, 21, and 27 node quadrilateral variants, as well as tetrahedral shapes. The three-dimensional elements are used in the study to a limited extent to model both one-way and two-way slab behavior. Figure 90 illustrates the 8-node planar and 20-node three-dimensional elements used in the study.

Isoparametric elements are used mainly because of the ease of adjusting the number of element nodes and order of Gaussian integration (Reference 38). As pointed out in Reference 36, the 9-node planar and 27-node three-dimensional solid elements are most accurate, but they are also most costly to use. For this study, the 8-node planar and 20-node three-dimensional elements are used to balance computational cost and accuracy. These elements provide quadratic definitions of element edge shapes and displacements, which are more accurate than the linear representation afforded by 4-node planar and 8-node three-dimensional elements. Linear elements have the associated disadvantage of self-induced parasitic shear, making them too stiff in bending (Reference 50, p. 197). In Reference 42, comparative analyses were made in which a structure was modelled with quadratic elements and then with linear elements (with a refined mesh that yielded the same number of degrees of freedom as the quadratic element model). The linear model was found to be considerably stiffer than the quadratic model when shear-induced deformations became significant.

In Reference 36, Bathe recommends that element height-to-length (h/L) ratios not exceed 10. This recommendation is in keeping with conventional wisdom concerning element compactness. Large h/L ratios lead to excessive element stiffness (Reference 50, p. 197).

While ADINA allows the analyst to employ reduced integration rules, full Gaussian numerical integration is employed in both the planar and three-dimensional models in this study. Full integration involves 9 integration points (3 x 3) in planar elements and 27 integration points (3 x 3 x 3) in three-dimensional solid elements. ADINA provides stress and strain data for all
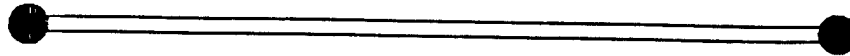
Two Node Truss Element
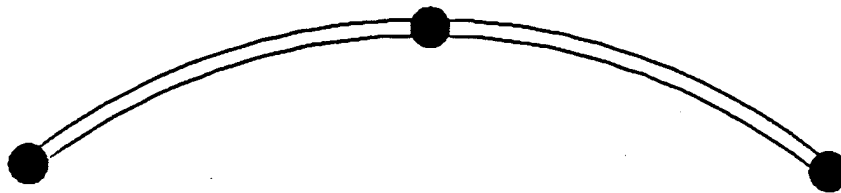
Three Node Truss Element
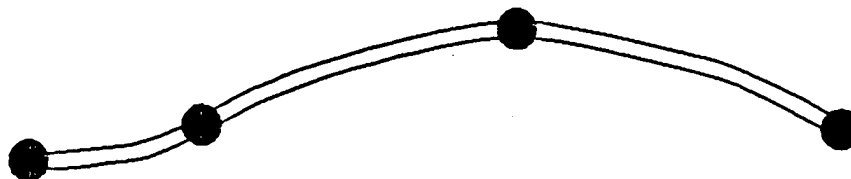
Four Node Truss Element

Figure 89.   Truss Elements Used in ADINA Models.
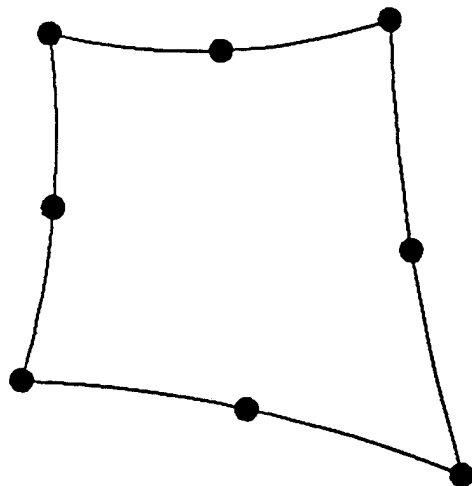
Eight Node Two—Dimensional Solid Element
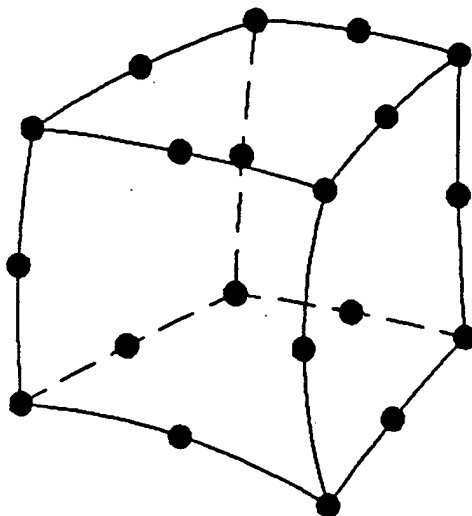
Twenty Node Three—Dimensional Solid Element

Figure 90. Solid Elements Used in Concrete Models.

element integration points. There is a slight drawback in the use of full integration: elements tend to be slightly stiffer than in reduced order integration (Reference 50, p. 197). However, when a consistent, rather than lumped, mass matrix is used, as is done here, full integration is needed for its exact evaluation (Reference 49, p. 284). Consistent mass matrices are employed because they are considered to be more accurate than lumped mass matrices when implicit direct time integration methods are used for dynamic analysis (Reference 50, p. 415). More significantly, for anticipated highly nonlinear material behavior, higher order integration permits better simulation of actual material nonlinearities, because the number of integration, or information, points is larger (Reference 49, p. 401).

One of the numerous complicated phenomena associated with modeling reinforced concrete structures is the interaction between the reinforcement and concrete, known commonly as *bond*. As a structural member is loaded, the original bonding breaks down, permitting reinforcement *slippage* to occur and altering structural response. Numerous attempts to model the bond-slippage effects appear in the literature. Normally, a linkage element is provided between the elements representing steel and those representing concrete. The linkage is given material properties that enable slippage to occur. In Reference 42, one such model is presented, with the linkage elements given essentially elastic-plastic properties. Other models do not attempt to simulate bond-slip faithfully and simply join the reinforcing elements rigidly to the concrete elements. Because the objective of this study is to analyze overall structural behavior, rather than micromechanics, and because the available test data being used for reference do not provide highly detailed structural information, the study adopts a simplified approach of rigidly joining the truss and solid elements at nodal points.

Reference 42 indicates that less computational difficulty arises when reinforcement elements are located through solid element Gauss points. However, because of the added geometric modeling complexity this would entail, this study places reinforcement along nodal lines in the solid element model.

A final element type used to analyze the Tyndall AFB structure is the linear spring element. ADINA permits the use of either linear or rotational spring elements. The elements may be used to link adjacent finite element nodes, or they may be used to link finite element nodes to supports. In these analyses, the linear spring elements are used to link the ends of the wall sections to their supports. Various spring stiffnesses are used in different analyses, to examine the effects of in-plane forces in the walls that are induced by the resistances of the connecting roof and floor slabs.

In conjunction with the spring elements, the authors used another modeling feature available in ADINA, that of establishing constraints, where certain nodes are designated as *master* nodes and others are designated as *slave* nodes. For any designated degree of freedom, the slave node is tied to the master node via a linear function. The slave's movement is a fixed percentage of the master's movement. The authors have used this feature to model the rotational stiffness provided by the connecting roof and floor slabs.

3. Material Properties Used in the Finite Element Models

ADINA provides a broad selection of material models. For the truss elements used to simulate reinforcement in this study, two models are most applicable. There is a linear elastic model, with no yield points, and there is a *plastic* model. The plastic model is a bilinear function (Figure 91), with user-defined moduli. By using a zero (flat) or very low slope for the second portion of the bilinear model, with the slope change (*yield*) point's occurring at the yield stress and strain for the steel type used, the elastic and postelastic, prestrain hardening behavior of the reinforcement can be modelled well. Because concrete compression crushing and tension cracking behavior is expected to govern the ultimate strength of the structure, omitting steel strain hardening does not pose a serious limitation. In this model, unloading after yield follows a path parallel to the initial elastic portion of the stress-strain curve, thus approximating the hysteresis characteristic of steel behavior.

A key feature of ADINA for the present study is its incorporation of a comprehensive concrete material model. The model uses experimental research results in its formulation. Its key features are a nonlinear stress-strain relation, including compressive strain softening; failure envelopes that define tensile cracking and compressive crushing; and postcracking/crushing behavior.
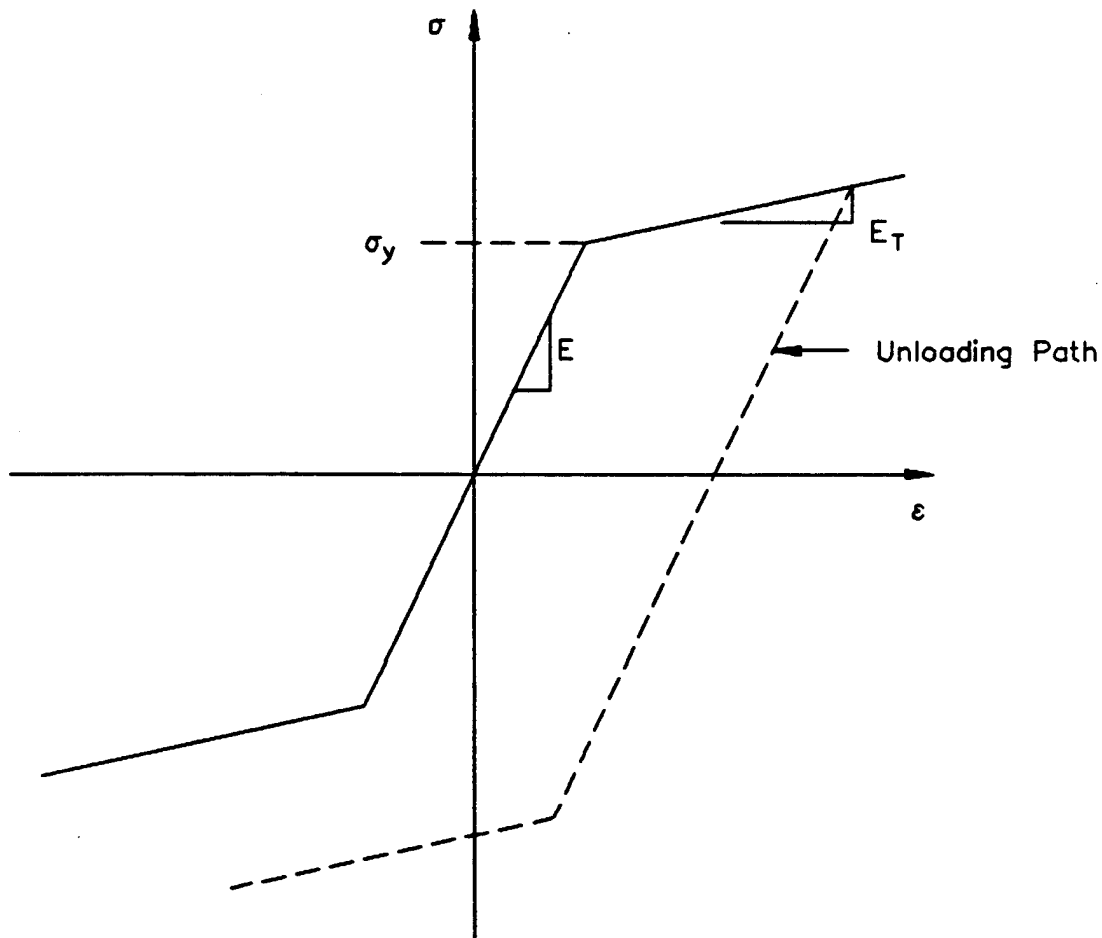
Figure 91. Bilinear Model Used To Simulate Steel Behavior.

133

References 36-39 provide detailed descriptions of the modeling approach. This report summarizes the basic characteristics of the model in the paragraphs that follow, using those references, particularly Reference 37.

To better visualize the procedures used in the ADINA concrete model, it is helpful to review briefly the incremental stress-strain computations at a single load or time step, t, in an analysis using the finite element method. In this review, the general notation of Reference 50 is used. For simplicity in this initial discussion, inertia (mass) effects are excluded, so the formulation best resembles a static load case. First, each element stiffness matrix must be formed:

$$\{\Delta u_t\} = [N]\{\Delta d_t\}$$

$$\{\Delta \varepsilon_t\} = [\partial][\Delta u_t] = [\partial][N]\{\Delta d_t\} = [B]\{\Delta d_t\}, \quad [B] = [\partial][N]$$

$$[k_t] = \int [B]^T[E_t][B] \, Vol \tag{7}$$

where, $\{\Delta u_t\}$ = incremental displacements within element, time t
$\quad$ $[N]$ = isoparametric shape functions
$\quad$ $\{\Delta d_t\}$ = element incremental nodal displacements, step t
$\quad$ $\{\Delta \varepsilon_t\}$ = incremental strains within element, step t
$\quad$ $[\partial]$ = differential operator
$\quad$ $[E_t]$ = tangent stress-strain operator, step t
$\quad$ $[B]^T$ = transpose of $[B]$
$\quad$ $[k_t]$ = element tangent stiffness, step t
$\quad$ Vol = element volume

From the element tangent stiffness matrices, the total structure tangent stiffness matrix is formed (n = number of elements in structural model):

$$[K_t] = \sum_{i=1}^{n} [k_{t,i}]$$

For the entire structure:

$$\{\Delta D_t\} = [K_t]^{-1}\{\Delta R_t\} \tag{8}$$

where, $\{\Delta D_t\}$ = incremental nodal displacements, step t
$\quad$ $[K_t]$ = structural tangent stiffness, step t
$\quad$ $\{\Delta R_t\}$ = incremental nodal loads, step t

Once all nodal displacements are determined for the time or load step, the displacements for the nodes of each element may be extracted and, for each element:

$$\{\Delta \sigma_t\} = [E_t]\{\Delta \varepsilon_t\} = [E_t][B]\{\Delta d_t\} \tag{9}$$

where, $\{\Delta \sigma_t\}$ = incremental element stresses, step t

ADINA bases concrete's multiaxial stress-strain relationships upon the conventional uniaxial concrete stress-strain model (Figure 92). In tension, the model is linear until the concrete's tensile failure point. In compression, the model uses a third-order curve-fit to the nonlinear stress-strain curve, up to the ultimate compressive crushing condition in the material. Any prefailure unloading in either the tensile or compressive regions follows a path parallelling the initial linear portion of the curve.

At any given time or load step, and at each integration point within each finite element at that step, in an analysis, ADINA determines the three principal stresses and corresponding strains. Using the already defined uniaxial model, the uniaxial stress-strain curve slopes (or Young's moduli) are determined for each of the three principal stress directions. These moduli, associated shear moduli, and off-diagonal terms governed by Poisson's Ratio, are used in the appropriate locations in the finite element stress-strain matrix to derive the element stiffness matrix at that time or load step. In this manner, the three-dimensional properties of the material are treated orthotropically in the directions of the three principal stresses. Similarly, for each new load or time step increment, the new three dimensional stress state is determined by evaluating the
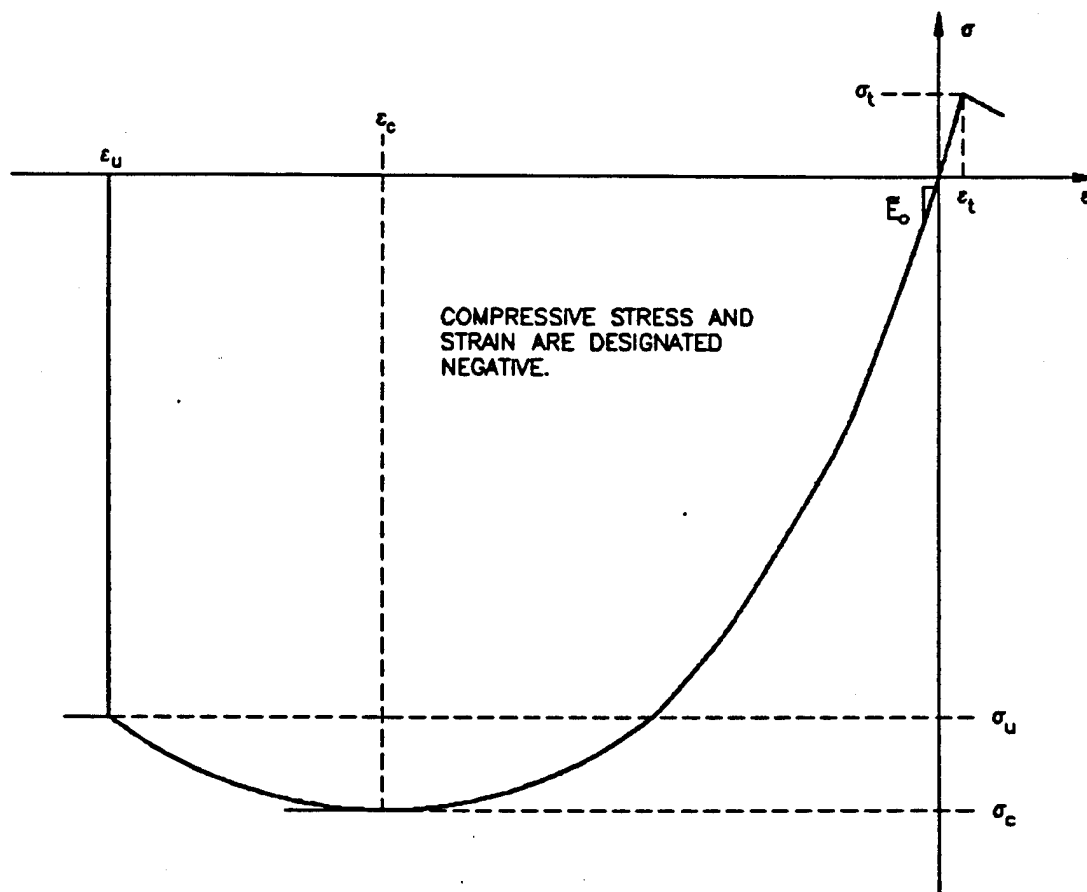
Figure 92. Uniaxial Stress-Strain Relation Used in ADINA Concrete Model.

135

uniaxial stress-strain relations for each of the three principal stress directions, which change as the stress state changes.

The tendency of concrete to develop tensile cracking and compressive crushing dictates that the material model must have clearly defined failure envelopes and postfailure performance simulations. ADINA incorporates tensile and compressive material failure envelopes that simulate experimental results; the triaxial tensile failure envelope employed is shown in Figure 93; the triaxial compressive failure envelope is shown in Figure 94. Figure 94 is a planar view of a portion of the compressive failure surface; each of the six curves shown represents a section through the solid formed by the three-dimensional failure surface. While the tensile region is represented by linear functions, the compressive failure envelope is nonlinear and relies upon the input of 24 normalized (with respect to the unconfined uniaxial compressive strength, f_c') stress values. Those values would need to be based on experimental data, if the concrete in the analysis is to be an accurate model. Very little compressive test data exists in this form, so the user faces uncertainty when determining appropriate input values. ADINA has two sets of experimentally-based default values for these variables, which are known as "KUPFER" and "SANDIA." A comparison of these two envelopes is shown in Figure 95. It is possible that neither of the experiments upon which these default values are based accurately replicates the needed material characteristics. It is noteworthy that, during an analysis, if ADINA computes the smallest (in magnitude, not sign) principal compressive stress to be larger in magnitude than the principal stress defined by curve 6 in Figures 94 and 95, the program terminates. It is indirectly indicating that the computations lie outside the "known" behavior of the material. For this study, the authors relied primarily on the "SANDIA" model.

Other failure surface formulations have been developed by other researchers; a more general example, which is less dependent on detailed experimental data, and originally discussed by Khan and Saugy (Reference 45), is presented by Bathe et al., in Reference 38.

$$\sqrt{I_2} + \left(\frac{n-1}{2n-1}\right) I_1 + \left(\frac{n}{2n-1}\right) f_c' = 0$$

$$I_1 = \sigma_1 + \sigma_2 + \sigma_3$$

$$I_2 = \left(\frac{3}{2}\right) [(\sigma_1 - \overline{\sigma})]^2 + (\sigma_2 - \overline{\sigma})^2 + (\sigma_3 - \overline{\sigma})^2]$$

$$\overline{\sigma} = \left(\frac{1}{3}\right) (\sigma_1 + \sigma_2 + \sigma_3)$$

$$n = \frac{biaxial\ f_c'}{uniaxial\ f_c'} \approx 1.25 \tag{10}$$

Figure 96 illustrates the failure surface formed by these equations.

136

The two triaxial failure envelopes, tensile and compressive, must be considered in concert and are difficult to interpret in their three-dimensional form. In a more easily understood portrayal, Figure 97 reduces the complexities of the two failure surfaces to a biaxial condition (where the third principal stress is maintained at a constant value) that is easier to interpret.

For each load or time step, at each numerical integration point in an element, ADINA determines whether the stress state lies inside or outside the appropriate tensile or compressive failure surfaces. This check is performed by first calculating the three principal stresses. In the tensile region, it is a simple matter of checking whether the stress state lies inside or outside the failure envelope.

Because the three-dimensional stress state must be resolved into three uniaxial models, the compression region is more complicated to analyze. Once the
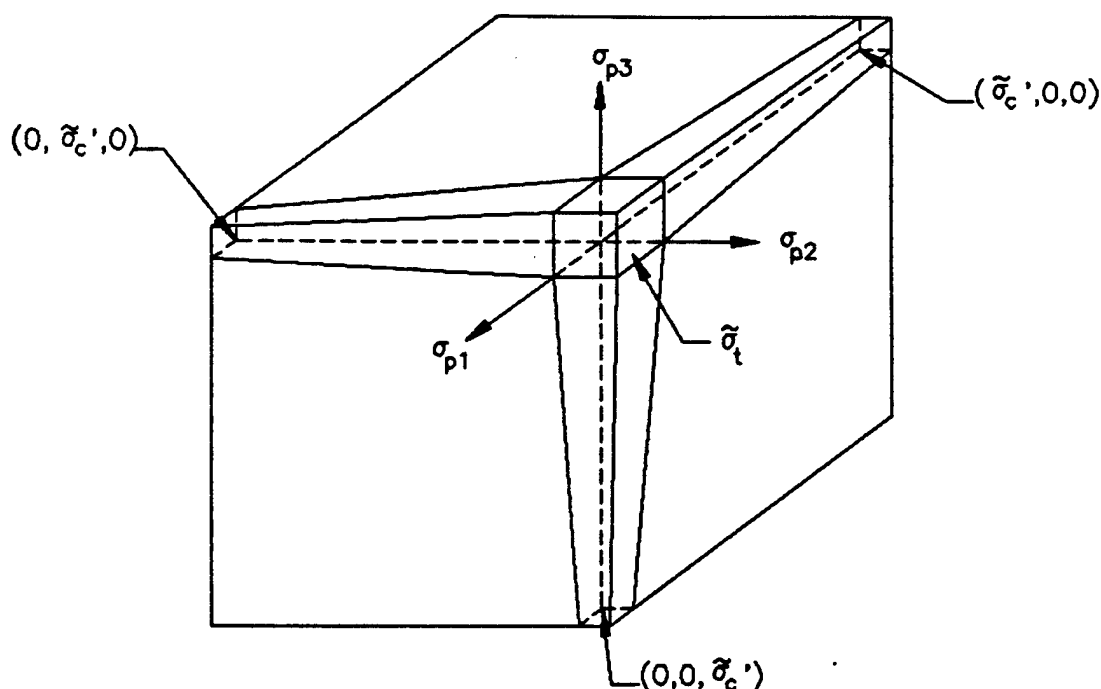
$\tilde{\sigma}_t$ = MAXIMUM TENSILE STRESS UNDER MULTIAXIAL CONDITIONS

$\tilde{\sigma}_c'$ = COMPRESSIVE FAILURE STRESS UNDER MULTIAXIAL CONDITIONS

σ_{p1} , σ_{p2} , σ_{p3} = PRINCIPAL STRESSED IN DIRECTIONS 1, 2, AND 3

Figure 93.   Triaxial Tensile Failure Envelope of ADINA Concrete Model.
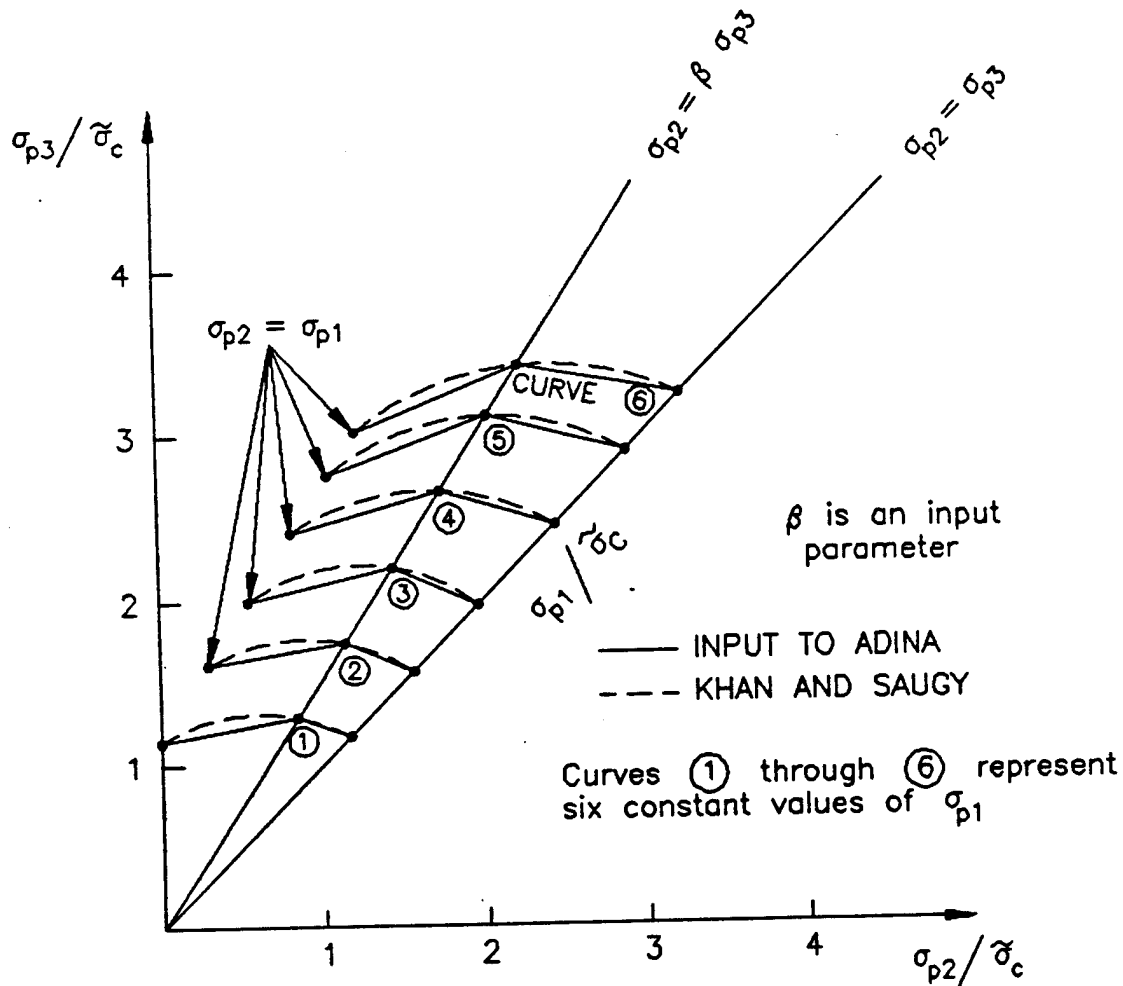
Figure 94. Triaxial Compressive Failure Envelope.

three principal stresses are calculated, ADINA modifies the three uniaxial strength property sets to establish the material strength in the triaxial stress state. Using the two computed compressive stresses that are smallest in magnitude, the failure envelope is used to determine the stress required in the third principal stress direction to cause a crushing failure. If the ratio of the failure stress to the computed stress is less than one, then crushing failure is deemed to have occurred. If the ratio exceeds one, it is used to determine the effective strength increase due to the confinement provided by the triaxial stress state. To provide this strength enhancement in the uniaxial stress-strain curve used in the model, ADINA modifies the curve as shown in Figure 98. For the principal stress direction in question:

$$\sigma'_c = \gamma_1 \sigma_c \quad (Failure\ surface)$$

138
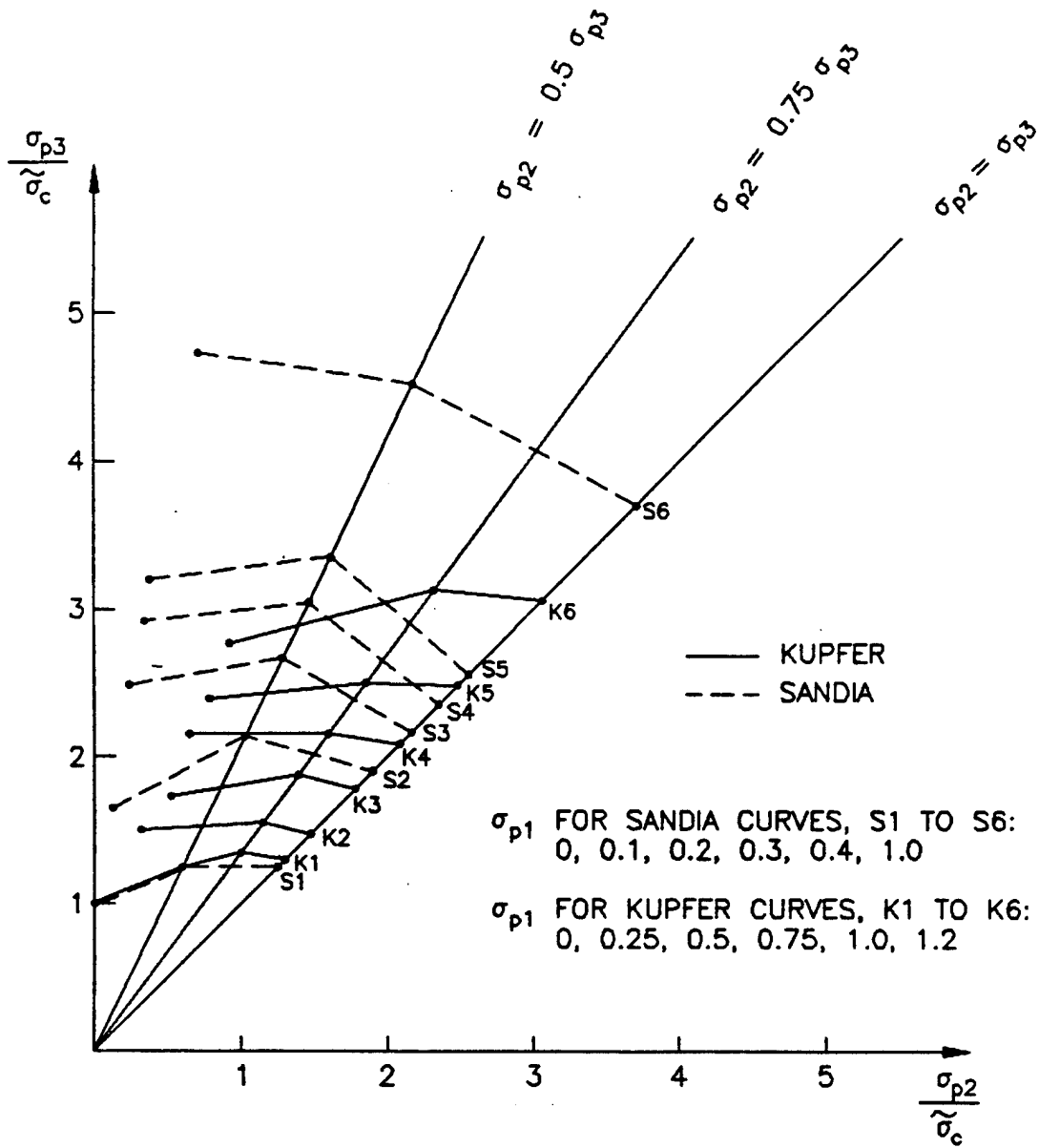
Figure 95. Comparison of Triaxial Compressive Failure Envelopes ADINA "KUPFER" and "SANDIA" Models.

$$\sigma_u' = \gamma_1 \sigma_u$$

$$\varepsilon_c' = (C_1 \gamma_1^2 + C_2 \gamma_1) \varepsilon_c$$

$$\varepsilon_u' = (C_1 \gamma_1^2 + C_2 \gamma_1) \varepsilon_u \tag{11}$$

where, σ_c' = peak (crushing) stress, triaxial stress state

σ_c = peak (crushing) stress, uniaxial stress state

σ_u' = ultimate stress, triaxial stress state

139
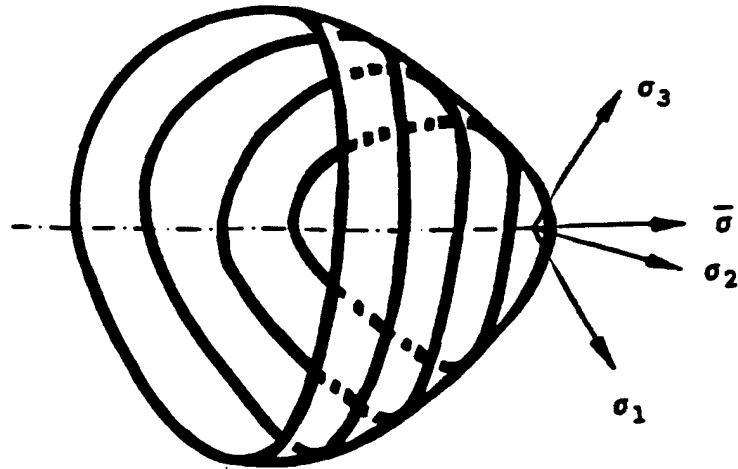
Figure 96.   Khan and Saugy Triaxial Failure Surface for Concrete.
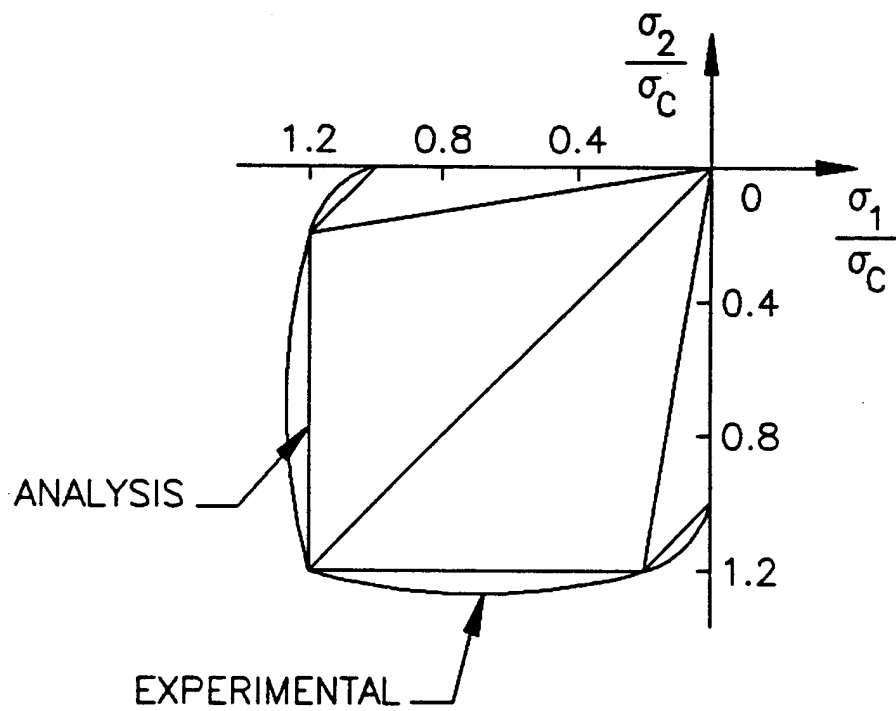
Figure 97.   Biaxial Concrete Compressive Failure Envelope.
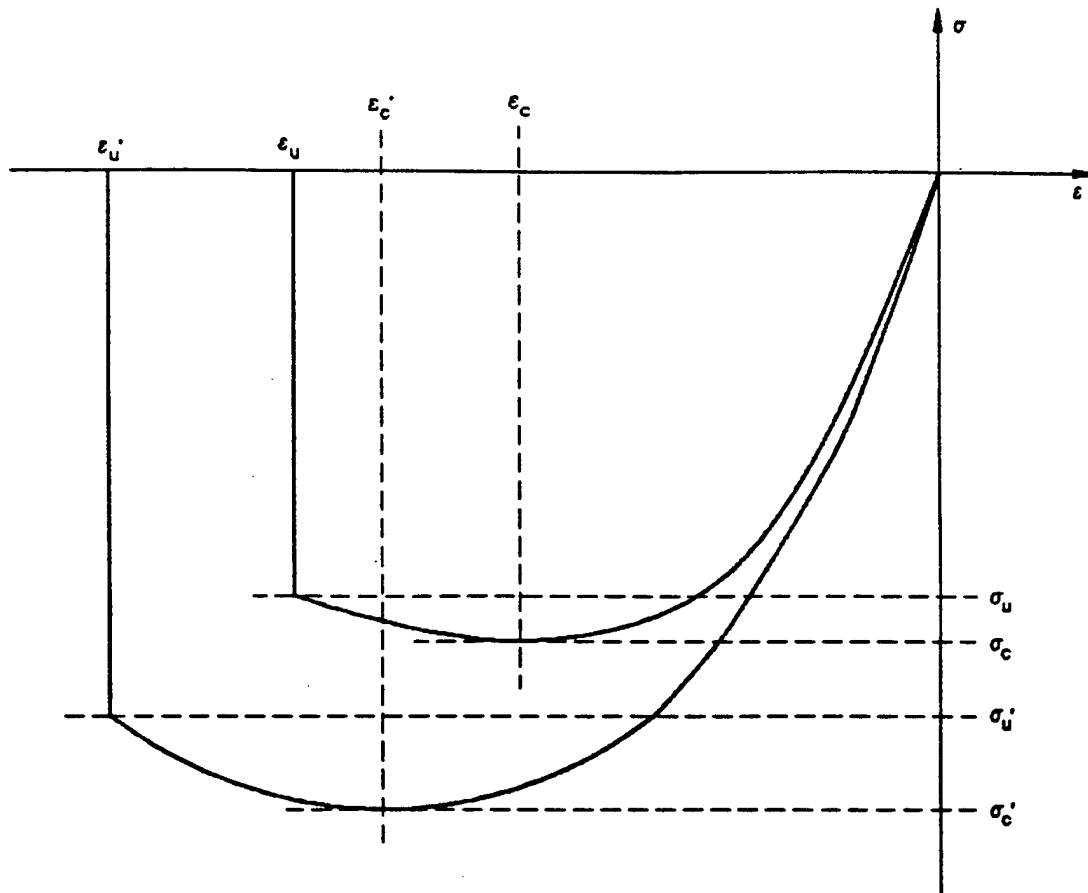
Figure 98. Evaluation of One-Dimensional Stress-Strain Law Under
Multiaxial Compressive Stress Conditions.

σ_u = ultimate stress, uniaxial stress state

γ_1 = ratio, peak triaxial/peak uniaxial stress

ε_c' = strain at crushing onset, triaxial stress state

ε_c = strain at crushing onset, uniaxial stress state

ε_u' = ultimate strain, triaxial stress state

ε_u = ultimate strain, uniaxial stress state

C_1 = constant, ADINA default = 1.4

C_2 = constant, ADINA default = -0.4

The two constants shown relate the crushing and ultimate strains in the triaxial
stress state with those of the uniaxial stress state; without clarifying
experimental data, the user would be inclined to use the default values in the
program.

In regions of combined tensile and compressive principal stresses, the
tensile stresses reduce the compressive stresses required to produce crushing
failure, and the compressive stresses reduce the tensile stresses required to
produce cracking.

141

In the postfailure regions, the calculation procedure changes. After tensile failure occurs at an integration point, a failure plane is assumed to form at that point. To implement this numerically, ADINA reduces the stiffness normal to the failure plane and the shear stiffness in the failure plane to lower values. These reductions' physical meaning can be thought of in the following manner: when a crack forms in the concrete, its ability to carry a normal tensile force at that point effectively goes to zero, and the crack will also reduce the shear capacity at that point. In assembling the element stiffness matrix for the next time or load step, the element stress-strain matrix, matrix E, is formed using reduced normal and shear moduli values, thus weakening the structure.

In ADINA, the normal stiffness (i.e., the modulus normal to the failure plane, or crack) is reduced to a default value of 0.01 percent of the initial uniaxial Young's modulus, and the shear stiffness is reduced to a default value of 50 percent of the initial uniaxial shear modulus (about 21 percent of the initial uniaxial Young's modulus); the user may override the defaults. Poisson's ratio-effected terms in the E matrix are also modified. The default value for the normal stiffness is set to a small non-zero value to avoid a singularity in the stiffness matrix; it is zero for all practical purposes. All analyses reported here used the default value of reduced normal stiffness.

The reduced shear stiffness is more subjective and might therefore be adjusted in some instances. In the manner in which it is used in finite element analysis, the shear stiffness reflects the ability of an element to transfer shear at a point. As discussed in Reference 41, shear transfer after cracking occurs as a result of crack face roughness, the amount of reinforcement crossing the crack, the crack width, concrete strength, and reinforcement dowel action. The shear reduction chosen by the analyst is thus actually characterizing the combined effects of all these factors. In analyses dominated by shear response, as might be the case in blast load analysis, the postcracking shear modulus is therefore significant. Reference 41 indicates that the effective postcracking shear modulus approaches zero asymptotically, with an effective minimum of about 5 percent of the uncracked modulus. Reference 52 adopts a calculational approach that would reduce the shear stiffness to about 15 percent (vs the 21 percent default value in ADINA) of the initial uniaxial Young's modulus. Reference 47 provides a detailed discussion of the different philosophies used to develop postcracking shear behavior models. Most of the analyses reported here maintained the default value of reduced shear stiffness. Where exceptional difficulty in maintaining numerical stability occurred, the models were strengthened by increasing the stiffness.

Once nodal displacements are determined using the weakened postcracking stiffness matrix, ADINA uses a separate parallel procedure to calculate the effective stresses at the integration points where tensile failure has occurred. Figure 99 illustrates key features of the procedure used for calculating stresses from strains. Beyond the tensile failure (cracking) point on the stress-strain curve, the model allows a controlled softening (effectively simulating crack propagation) to occur by forcing normal and shear stresses to decrease linearly

over the region bounded by the tensile failure strain and a user-specified maximum strain. The stress normal to the failure plane decreases to zero over the range, while the shear stress decreases to the value used in the E matrix formulation described above. Stresses at the point are then calculated using a *modified* E matrix. A full description of the formulation of the modified E matrix may be found in Reference 37. For this discussion, the key features are shown in Figure 99. They are:

E_f = Young's modulus, normal across failure plane

$\tilde{E}_o$ = initial Young's modulus

σ_t = tensile cracking stress

ε_t = strain at cracking stress

ε_m = maximum strain when zero stress is reached = $\xi \varepsilon_t$

ξ = XSI = measure of fracture energy, user-specified constant (ADINA)

σ_T, ε_T = stress, strain at time T

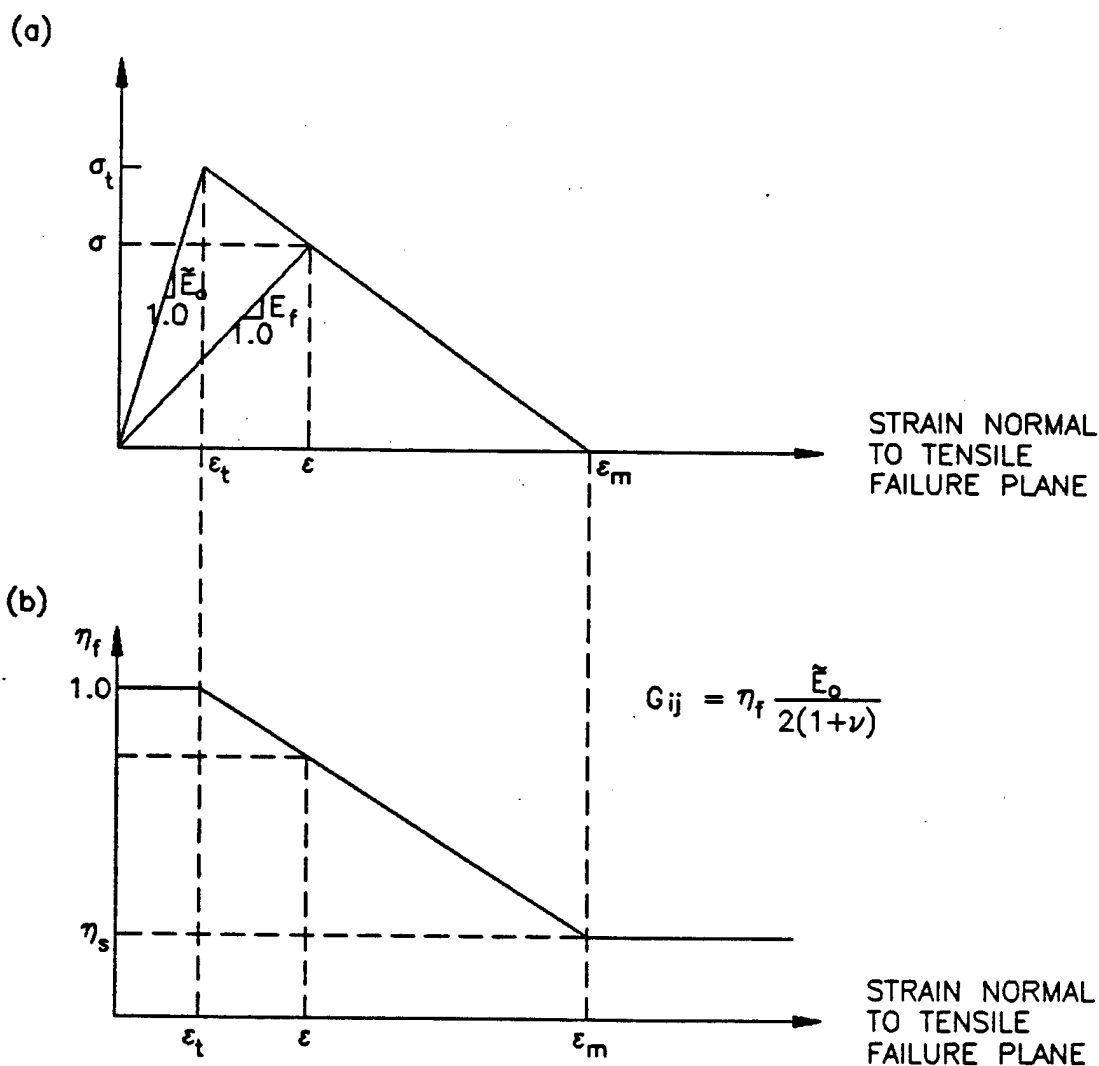$$G_{ij} = \eta_f \frac{\tilde{E}_o}{2(1+\nu)}$$

Figure 99.   Moduli for Stress Calculation After Tensile Failure, (a) Young's Modulus, (b) Shear Modulus.

143

η_a = shear stiffness reduction factor, as described above

η_f = multiplier, see Figure 99

It is important to distinguish between the modified E matrix used to calculate stress at a point and the E matrix used to analyze displacements. The significance of the element stress calculations using the modified E matrix lies in the equilibrium iteration procedure that accompanies the nonlinear analysis. The equilibrium iteration procedure will be described briefly later in this report. To summarize detailed discussions found in Reference 47, the reduced stresses that are calculated using the modified E matrix are used to calculate a *residual stress vector* for each element, which is the difference between the stresses the material would sustain at the calculated strain state using the precracking E matrix and the lower postcracking stresses the material sustains using the modified E matrix. These stress residuals are integrated over the element volumes to form a structural load vector. For each element:

$$\{p_r\} = \int [B]^T \{\sigma_r\} \, Vol \qquad (12)$$

where, $\{p_r\}$ = "residual" load vector

$\{\sigma_r\}$ = "residual stresses" vector

$[B]^T$, Vol : defined previously

The residual load vectors for all elements are summed to form a vector of out-of-balance forces that must be included in the equilibrium calculations. The cracking process causes a redistribution of the total stress normal to the cracking plane that must be accommodated numerically, where force from weakened integration points must be shifted to stronger points. Reference 47 describes the impact of this procedure on the overall analysis. Two of the description's more significant points are that, first, the key feature seems to be the actual cracking strength, not postcracking behavior. After cracking occurs, reinforcement properties are stated to be more significant in influencing overall behavior. The authors' experiences indicate that the postcracking concrete behavior is actually significant. After *all* cracking has occurred, the steel behavior does dominate, but this will happen very late in the structural response. Before this happens, it is likely that numerical instabilities will accrue. Second, element size is a factor. When a crack occurs at even a single integration point, it weakens the entire element and, because of stress redistributions, increases strains at other integration points in the element (hence propagating the crack). Therefore, a crack's forming in a large element has the effect of softening a relatively larger portion of a structure than in a smaller element.

Simulating the postcracking concrete material behavior is clearly a complex aspect of the ADINA concrete model. To understand its significance more fully, it is helpful to review key factors in developing the postcracking model. There are three basic components in the crack modeling process (Reference 52): crack initiation, crack representation, and crack propagation. ADINA uses the aforementioned failure envelopes to establish crack initiation.

In general, there are two crack representation schemes commonly used in finite element analysis of concrete structures: *discrete* cracking models and *smeared* cracking models (Reference 52). In discrete cracking models, individual cracks are frequently simulated using predefined crack orientations that follow mesh lines. Such models are typically used to study micromechanics, such as crack tip growth. They require detailed knowledge of crack tip kinematics and can introduce extreme complexity to numerical analysis. ADINA adopts the smeared cracking model approach. In it, cracking is addressed in overall structural response, not through individual crack mechanisms. The postcracking behavior of the material is modeled in an average sense. By reducing the appropriate stress-strain moduli, the average behavior of the volume around an integration point is softened as if cracks were propagating through the region. Mathematically, the procedure imposes discontinuities in the stress field without making the displacement field discontinuous (Reference 52). This simplifies computations as compared to discrete cracking models, but it also provides a more objective material response law, because most actual concrete material tests (e.g., standard compressive cylinders) measure overall response, rather than localized crack region conditions (Reference 41).

The smeared crack approach to postcracking response involves two related physical phenomena that models should address, *tension softening* and *tension stiffening*. Tension softening is a characterization of the effects of crack formation on the average stress-strain response of the concrete material in tension. As its name implies, the cracked material responds globally as if it were softening under load (Reference 41). In laboratory tests of unreinforced tension specimens with fixed crack spacings, s, stress-displacement curves have the form shown in Figure 100. The area under the curve in Figure 100 is a measure of the fracture energy in the concrete material. It may be equated to the triangular stress-strain function used by ADINA (Figure 99) in the following manner:

$$G_f = \textit{Fracture energy} = \textit{Area under curve, Figure} \ 100 \qquad (13)$$

where, $\quad 0.29 \ \text{lb/in.} \le G_f \le 1.45 \ \text{lb/in.}$

For the ADINA stress-strain function (Figure 99), then:

$$G_f = \frac{1}{2}\sigma_t \varepsilon_m s \qquad (14)$$

where, $\quad$ s = crack spacing

Therefore,

$$\varepsilon_m = \frac{2G_f}{\sigma_t s} = \xi \varepsilon_t$$

and,

$$\xi = \frac{2G_f}{\sigma_t \varepsilon_t s} = \frac{2G_f \tilde{E}_0}{(\sigma_t)^2 s}$$

145
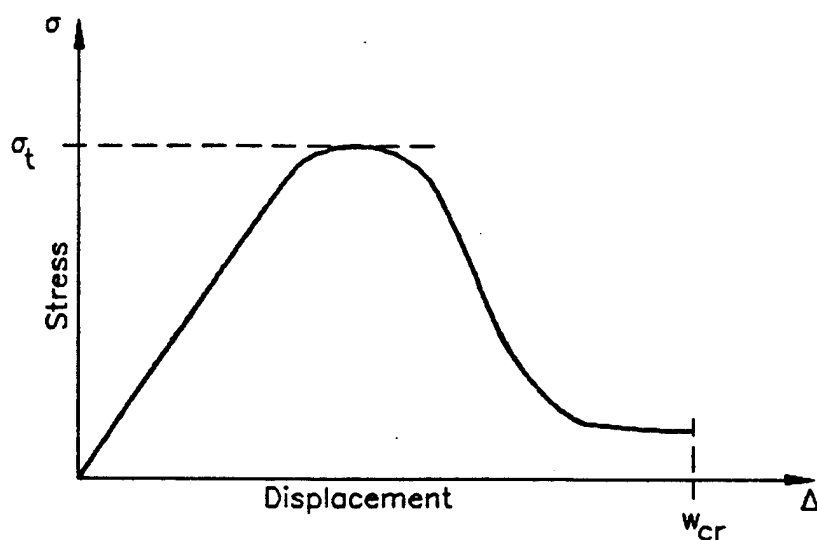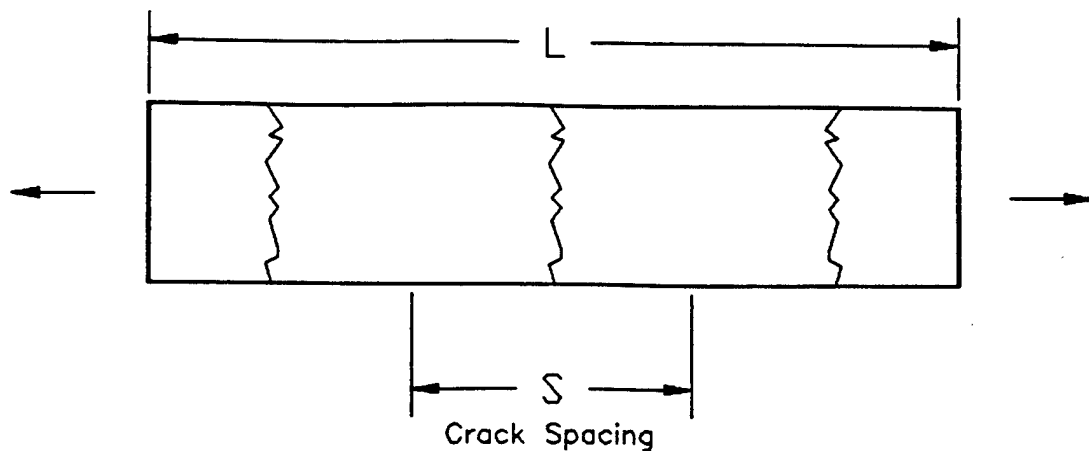
Displacement Curve,
Crack Width, w_{cr}

Figure 100. Unreinforced Tension Specimen Tests.

This procedure, explained in Reference 41, assumes that the energy absorbed by the material in forming a unit area of crack is constant and that the strain between adjacent cracks is uniform. In Reference 51, this model, known as linear softening, is shown as one of four tension softening models (see Figure 101). The bilinear model shown in Figure 101 is stated to represent most accurately average concrete behavior. The linear model used in ADINA yields a stiffer element than does the bilinear or discontinuous model. Reference 54 reports on the use of an exponential decay function for the tensile stress-strain model in the postcracking region. That report's authors directly inserted the model into the ADINA source code. This model lowers the fracture energy, but Reference 54 indicates that the exponential decay model still produced a stiffer postcracking response than was measured in structural load tests.

146
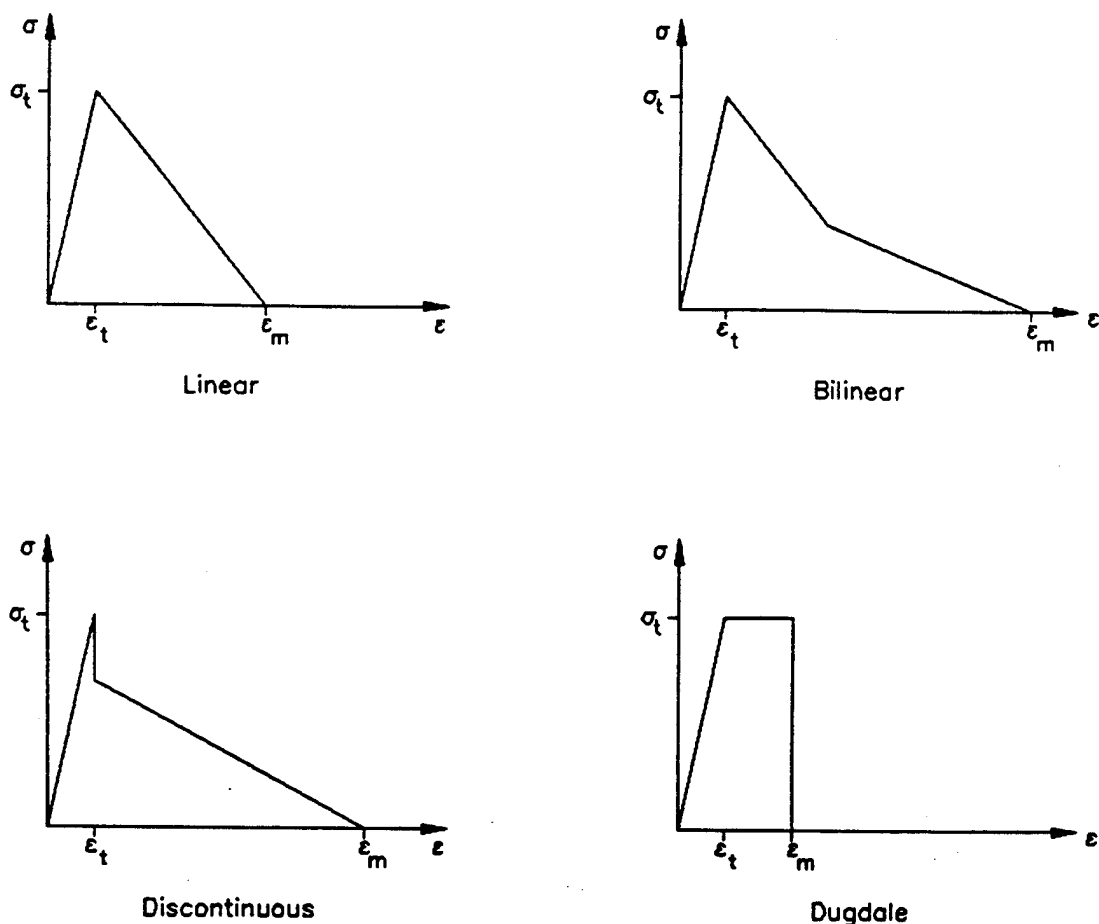
Figure 101. Concrete Tension Softening Models.

With the linear model used in ADINA, the analyst can adjust the maximum tensile strain at zero stress, but the above shows that accurate analysis requires knowledge of the fracture energy and anticipated crack spacing (which in turn will be affected in the model by element size and degree of Gaussian integration), as well as the uniaxial tensile strength. An increased maximum tensile strain at zero stress, without adjustment of other variables, results in a direct increase in total fracture energy. Reference 51 describes the effect of increasing the available fracture energy in this manner. Both peak load and failure displacement will increase, but the increase is less than directly proportional to the fracture energy increase. Increased fracture energy also tends to broaden the peak region of the load-deflection curve for a structure (Reference 51). The magnitude of the maximum strain at zero stress is reported to lie over a wide range. Reference 52 reports that various researchers have found ξ to range from 5 to 25. The reference also mentions that maximum strains lie typically in the range of 0.0015 to 0.0020. ADINA essentially considers a range for ξ of one to eight. The authors performed limited parametric studies on the effects of varying ξ, but most analyses used a value of eight, to provide increased computational stability.

147

Tension stiffening is a separate, but related, postcracking phenomenon. Reference 41 characterizes tension stiffening as the effects of interaction between steel reinforcement and concrete in the postcracking region. In a physical sense, the phenomenon is a function of crack spacing, reinforcement volume, and bond (Reference 41). Tension stiffening is recognition that the remaining intact concrete between cracks can transmit tension. Neglecting tension stiffening tends to lead to underestimated stiffness (Reference 52). Figure 102 illustrates the stress distributions that lead to tension stiffening. Two approaches to incorporating tension stiffening in material models are presented in Reference 52. Figure 103 shows the first approach, whereby the reinforcement stiffness is increased incrementally to include indirect effects of the concrete stiffness. Figure 104 shows the second approach, where the concrete tensile softening curve is modified. ADINA uses the linear postcracking stress-strain function in the modified E matrix, thus considering the phenomenon. Adjusting the maximum tensile strain at zero stress reflects tension stiffening effects. ADINA therefore incorporates both tension stiffening and tension softening effects in the postcracking, modified E matrix, formulation. As can be seen in this brief description, the two phenomena may place conflicting demands on the postcracking characterization.

In the process described above, ADINA indicates that a failure plane, or crack, has formed perpendicular to the appropriate principal stress direction at that integration point; this actually signifies that the tensile cracking or failure stress has been exceeded. Tensile failure at an integration point can occur in one, two, or three orthogonal directions. As new failure planes, or cracks, form at an integration point, each new failure plane fixes that respective stress direction. The second failure plane to form at an integration point is orthogonal to the first; after two failure planes have formed, the direction of the third is fixed as orthogonal to the other two. This procedure affects both the stress and displacement calculations, because the failure planes remain fixed once formed, and tensile principal stress directions at affected integration points can no longer rotate freely.

In the compressive region, failure at an integration point is determined to have occurred if a multiaxial stress condition falls outside the compressive failure surface. Upon a compressive, or crushing, failure, the material is assumed to behave isotropically. The slope of the uniaxial stress-strain curve becomes negative until the ultimate stress point is reached, at which time the material is assumed to be completely crushed, and all stresses at the integration point are set to zero (Reference 37); see Figure 98. This material characteristic again represents system, not micromechanic, behavior. Because compression softening is a system property, it can be influenced by the presence of reinforcement. In particular, shear-related reinforcement (stirrups, etc.) can be expected to provide confinement that increases system strength and ductility.

ADINA also accommodates load histories that traverse from tension to compression, and vice versa. For example, a tensile crack can close and assume a subsequent compressive stress. The primary irreversible occurrence is crushing
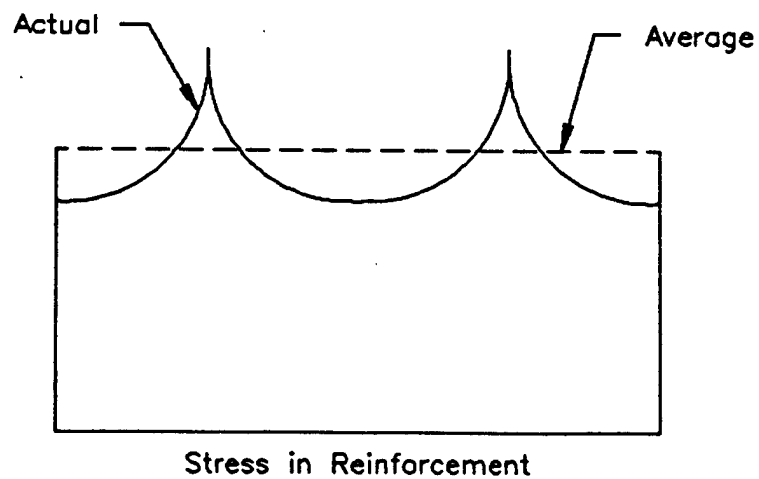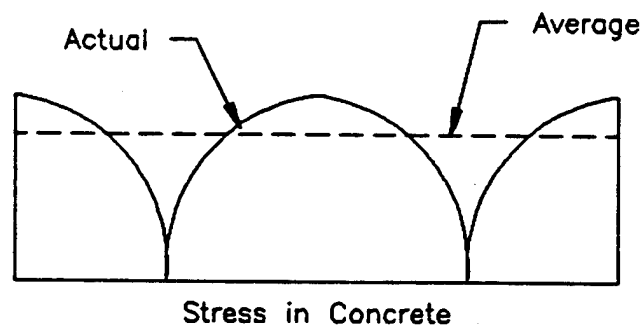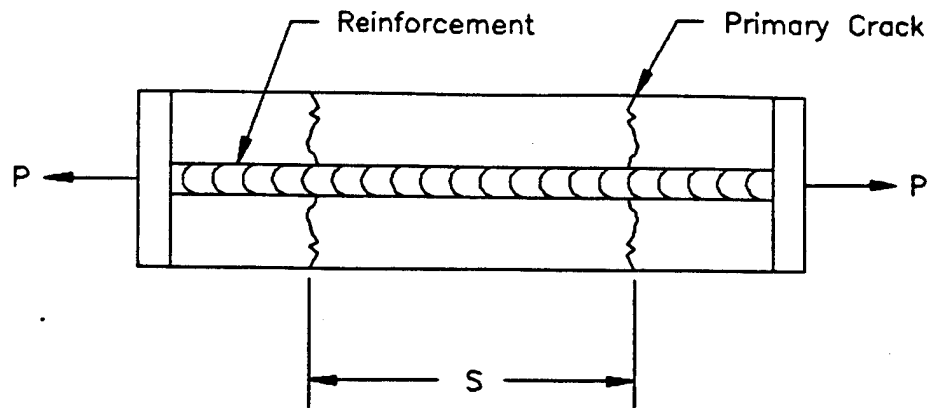
Figure 102. Stress Distribution in a Cracked Reinforced Concrete Element
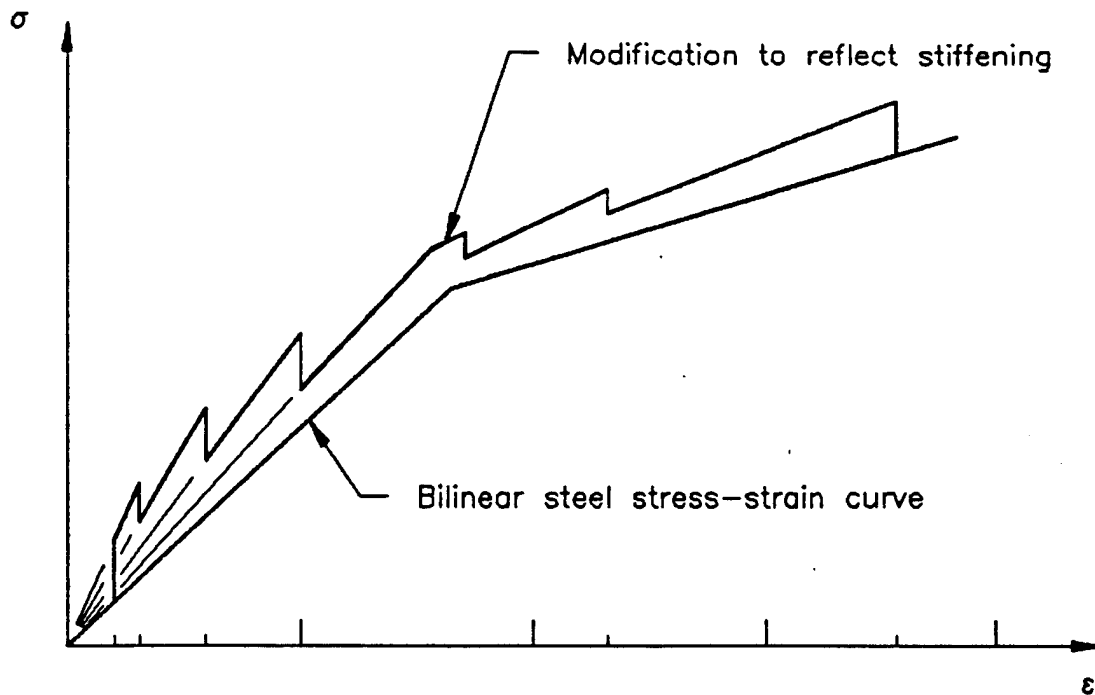that Lead to Tension Stiffening Effects.

149

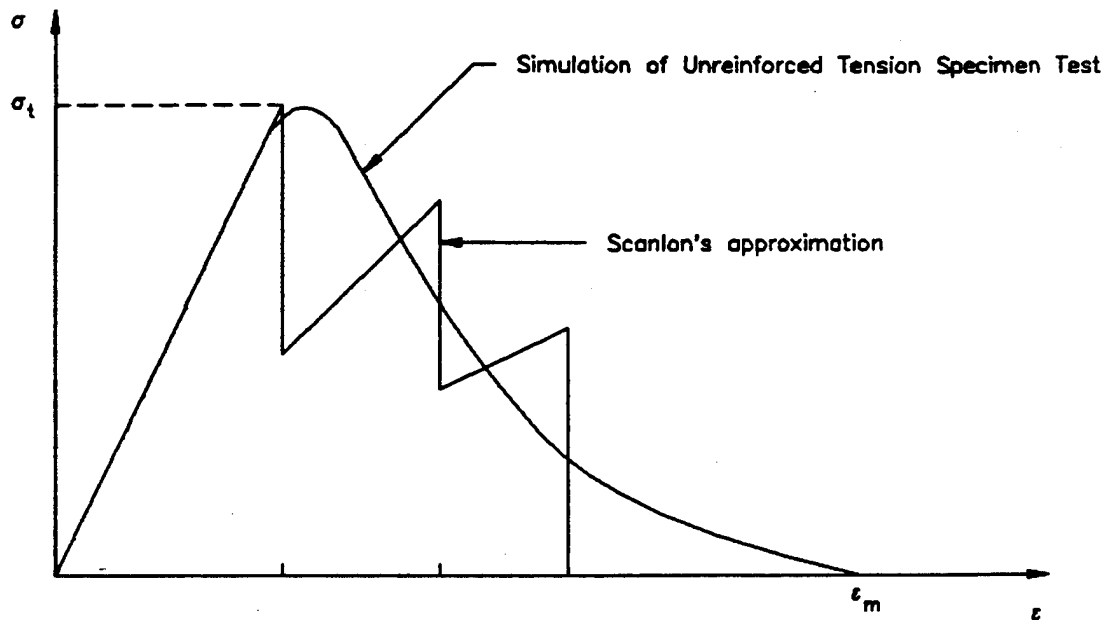Figure 103. Tension Stiffening via Modifying Stress-Strain Diagram of Reinforcing Steel.

Figure 104. Tension Stiffening via Modified Concrete Stress-Strain Model.

150

failure; once that occurs, the material is incapable of further load-transmission, although its mass is still carried in dynamic calculations. Reference 37 summarizes the procedures used for load reversal calculations. In most instances, as the concrete unloads from a tensile or compressive stress level back to a condition of zero stress, the initial uniaxial Young's modulus is used to establish the unloading path.

ADINA permits two approaches to modeling Poisson's ratio effects. In either approach, the user may input the ratio deemed most appropriate; values of 0.15-0.20 are typically used for concrete. In the first approach, Poisson's ratio is held constant throughout the analysis. In the second, Poisson's ratio varies from its initial value to a maximum of 0.42, according to Reference 36:

$$v_s = v_f - (v_f - v)\sqrt{1 - \left(\frac{\gamma_2 - \gamma_a}{1 - \gamma_a}\right)^2} \qquad (15)$$

where,
v_s = Poisson's ratio at given stress state
v = user-specified Poisson's ratio, normally $\approx$ 0.15-0.20
v_f = maximum value of Poisson's ratio at failure = 0.42 for ADINA
$\gamma_2 = \dfrac{\text{maximum compressive stress}}{f_c'} \leq \gamma_a$
γ_a = 0.7

This simulates the observed behavior of compression test specimens, in which the material first compacts and then dilates due to internal microcracking (Reference 52). From observation, ADINA initiates dilatation when the largest compressive stress exceeds 70 percent of f_c'. For the studies reported here, Poisson's ratio was held constant at 0.17.

The user must also input several uniaxial stress-strain properties and the mass density of the material. The stress-strain properties include the initial tangent, or Young's, modulus at zero strain, the tensile strength, maximum compressive stress (f_c'), with corresponding strain, and the ultimate, or failure, stress, with corresponding strain. As is most often the case, the authors only had the unconfined compressive strength, f_c', from the concrete in the test structures. Other values were estimated largely from empirical data found in the literature. Aside from the usual lack of data needed for determining the various input parameters, ADINA also does not provide any means for considering the effects of strain rate on the material properties. Conventional wisdom holds that material strength properties increase with higher strain rates, as will be generated by blast loading. Unpublished data furnished the authors by Dr. C.A. Ross, HQ AFCESA, show that uniaxial Split Hopkinson Pressure Bar tests indicate increases of tensile and compressive strengths, and prefailure compressive strains, with higher load rates. The authors attempted to account for strain rate effects by adjusting yield, ultimate, and/or crushing stresses and strains in the material models. This approach emulates the approximate procedures to account for rate effects that are found in military design manuals.

4. System Damping Characteristics

In structural dynamics calculations, the energy dissipation that occurs in structural motion and damage is modeled using structural damping mechanisms. Dissipation is actually the aggregation of several energy loss mechanisms, including elastic-plastic hysterisis (e.g., steel reinforcing), material softening via cracking and crushing (e.g., concrete), and friction. In both SDOF modeling and in finite element analysis, it is common to approximate the real damping mechanisms with artificial viscous damping mechanisms, which are actually based on fluid mechanics principles.

ADINA permits the use of two viscous damping mechanisms. Either of the two may be used alone, or they may be summed. First, individual "dashpot" dampers may be attached to element nodes; the synthesized effects of all dampers form the structural damping matrix, [C]. The second method is Rayleigh, or proportional, damping, where the damping matrix is a linear combination of the structural stiffness and mass matrices:

$$[C_R] = \alpha[K] + \beta[M] \tag{16}$$

where, $[C_R]$ = Rayleigh damping

In this equation α and β are constants that are determined by knowing the relationship between viscous damping and frequency (see Reference 50) at two significant natural system frequencies. In either of the ADINA schemes, one must have knowledge of equivalent viscous damping to be able to implement the scheme effectively. In addition, for Rayleigh damping, ADINA uses only the linear portion of the stiffness matrix; the concrete model is decidedly nonlinear. Viscous damping does not faithfully replicate true physical damping, especially as damping increases with structural deterioration. Adding the damping functions also increases computational effort.

In using the ADINA concrete model, with its cracking and crushing features, and the hysteritic steel material behavior, several of the physical energy dissipation mechanisms are modeled, if only approximately, so using added viscous damping is not necessary. Beyond these factors, there is also the practical consideration that damping does not significantly affect the initial peak dynamic response or the permanent inelastic deformation (although added viscous damping may cause oscillations to damp out more quickly). The analyses reported here therefore have omitted viscous damping mechanisms.

5. General Program Features Used in Dynamic Calculations

a. Time Integration Procedures

ADINA provides the user with a choice of three time integration procedures: explicit time integration using the central difference technique, and implicit time integration using either the Newmark Beta or Wilson Theta techniques. All three of the methods involve finite difference approximations to the equations of motion.

In explicit time integration, force equilibrium at time "t" is used to calculate displacements at time "t+Δt." Ignoring damping (for simplicity in description):

$$[M]\{\ddot{D}_t\} = \{R_t\} - \{F_t\} \tag{17}$$

where, $[M]$ = system masses

$\{\ddot{D}_t\}$ = nodal accelerations, time t

$\{R_t\}$ = external nodal loads, time t

$\{F_t\}$ = internal nodal forces, time t

In a typical finite difference form (ignoring damping):

$$\frac{1}{\Delta t^2}[M]\{D_{t+\Delta t}\} = \{R_t\} - [K_{s,t}]\{D_t\} + \frac{1}{\Delta t^2}[M](2\{D_t\} - \{D_{t-\Delta t}\}) \tag{18}$$

where, $\{D_t\}$ = displacement, time t

$\{D_{t+\Delta t}\}$ = displacement, time t+Δt

$\{D_{t-\Delta t}\}$ = displacement, time t-Δt

$[K_{s,t}]$ = structural secant stiffness, time t

The primary advantage of the explicit method is that neither the full mass nor the full system stiffness matrix need be calculated (Reference 49) in a typical analysis. In particular, the complete stiffness matrix is not required to compute the internal nodal force vector. Instead, the element stiffness matrices may be analyzed individually to develop it. This is very straightforward in linear analysis and some types of nonlinear analysis, and it greatly reduces computational requirements and associated time. The nonlinearity of the ADINA concrete model requires that both strains and stresses be calculated, so the entire structure stiffness matrix must be reformed to compute the internal forces accurately, negating the advantages of explicit integration. The explicit method is conditionally stable with respect to the maximum time step used.

In implicit time integration, force equilibrium at time "t+Δt" is used to calculate displacements at time "t+Δt." Again, ignoring damping:

$$[M_{t+\Delta t}]\{\ddot{D}_{t+\Delta t}\} + [K_{s,t+\Delta t}]\{D_{t+\Delta t}\} = \{R_{t+\Delta t}\} \tag{19}$$

In a typical finite difference form:

$$[K_{t+\Delta t}^{eff}]\{D_{t+\Delta t}\} = \{R_{t+\Delta t}^{eff}\} \tag{20}$$

where, $[K_{t+\Delta t}^{eff}] = a_0[M] + [K_{s,t+\Delta t}]$

$\{R_{t+\Delta t}^{eff}\} = \{R_{t+\Delta t}\} + [M](a_0\{D_t\} + a_2\{\dot{D}_t\} + a_3\{\ddot{D}_t\})$

a_0, a_2, a_3 = constants, defined later

153

With a material nonlinearity such as the concrete model:

$$[K_{s,t+\Delta t}] = f \, \{D_{t+\Delta t}\}$$

Therefore, equilibrium iteration at frequent intervals must occur, where an assumed displacement is used to calculate an estimate for the updated stiffness matrix. The displacement is then computed using the estimated updated stiffness matrix. The estimated and computed new displacements and related forces are compared. Recalculations occur until a designated tolerance between estimated and computed values is met.

While detailed discussions of the Newmark Beta and Wilson Theta methods may be found in structural dynamics texts, their implementation in the finite difference expressions may be summarized by examining the constants in Equations (19) and (20).

In the Newmark Beta method, the change in acceleration over each time interval, Δt, may be defined in a number of ways: constant (equal to the acceleration at the beginning of the interval, for the first half of the interval, and equal to the acceleration at the end of the interval, for the second half of the interval), average (equal to average of the acceleration at the beginning and the acceleration at the end of the interval), or linear (varied linearly from the acceleration at the beginning to the acceleration at the end of the interval). The assumed acceleration variation effects on Equations (19) and (20) are defined by the constants:

$$a_0 = \frac{1}{\alpha(\Delta t)^2}$$

$$a_2 = \frac{1}{\alpha(\Delta t)}$$

$$a_3 = \left(\frac{1}{2\alpha}\right) - 1 \qquad\qquad (21)$$

where, $\quad \alpha = \frac{1}{6}$, linear acceleration

$\qquad\qquad \alpha = \frac{1}{4}$, average acceleration

$\qquad\qquad \alpha = \frac{1}{8}$, constant acceleration

In the Wilson Theta method, linear acceleration variation is assumed over an interval from time "t" to time "t+$\theta\Delta t$." In the finite difference equations:

$$a_0 = \frac{6}{[\theta(\Delta t)]^2}$$

$$a_2 = \frac{6}{[\theta(\Delta t)]}$$

$$a_3 = 2 \qquad\qquad (22)$$

154

where,   Θ = multiplier for time step, Δt, which yields total
                time of linear acceleration

The Newmark Beta method is unconditionally stable with respect to time step size when an assumed average acceleration function is used. Therefore, this study has adopted its use in an attempt to minimize instability problems.

Reference 36 notes that, in nonlinear solutions, in particular, convergence during equilibrium iteration is often assisted by the inertia forces present, which tend to smooth out nonlinearities caused by material properties. However, the extreme nonlinearity caused by the combined effects of the concrete and steel models may still cause convergence problems. To minimize convergence difficulties, Reference 36 recommends:

$$\Delta t \leq \frac{0.20}{\omega_{co}} \qquad (23)$$

where, ω_{co} = highest structural frequency of interest

b.   Equilibrium Iteration Procedures

With the implicit time integration schemes, and with the high degree of nonlinearity present in the structural models, equilibrium iterations are required at each time step to ensure solution accuracy, avoid error accumulation, and minimize solution instability. The analyst must examine the tradeoffs between small time steps and frequency of equilibrium iteration. ADINA provides three primary equilibrium iteration techniques from which the analyst may choose: full Newton-Raphson iteration, modified Newton-Raphson iteration, and the BFGS (Broyden, Fletcher, Goldfarb, Shanno) method.

References 40 and 49 provide detailed explanations of the three equilibrium iteration techniques. They are described briefly below, as excerpted from the detailed explanations.

With the equilibrium iteration schemes, the equations of motion are expressed in incremental form. As well as the other schemes, the Newton-Raphson technique involves using the tangent stiffness matrix rather than the secant stiffness matrix, from the previous iteration step in the finite element calculations:

$$[M]\{\ddot{U}^i_{t+\Delta t}\} + [K^{i-1}_{T,t+\Delta t}]\{\Delta U^i\} \approx \{R_{t+\Delta t}\} - \{F^{i-1}_{t+\Delta t}\} \qquad (24)$$

where, $[K^{i-1}_{T,t+\Delta t}]$ = structural tangent stiffness, iteration i-1, time t+Δt, etc.

$\{\Delta U^i\}$ = $\{U^{i-1}_{t+\Delta t}\}$ - $\{U^i_{t+\Delta t}\}$ = incremental displacement, iteration i, time t+Δ

155

To start the equilibrium iterations at a given time step:

$$[K_{T,t+\Delta t}^0] = [K_{T,t}^{final}] \qquad (25)$$

$$\{F_{t+\Delta t}^0\} = \{F_t^{final}\} = Internal\ forces, time\ t$$

$$\{U_{t+\Delta t}^0\} = \{U_t^{final}\} = System\ displacements,\ time\ t$$

In the modified Newton-Raphson technique, the stiffness matrix is not reformed at every iteration. Rather, the stiffness matrix is updated only periodically, based on computed equilibrium configurations. In the Newton-Raphson calculations, as summarized above, the continuously updated stiffness matrix is replaced by the periodically updated (at some designated time interval) stiffness matrix:

$$[K_{T,t+\Delta t}^{i-1}] \rightarrow [K_{T,\tau}] \qquad (26)$$

where, τ = accepted equilibrium configuration load/time step

The BFGS method is known as a matrix update or quasi-Newton method. The stiffness matrix is again updated at predesignated periodic intervals; instead of complete reformation, the inverse of the stiffness matrix is updated without directly manipulating the stiffness matrix itself:

$$[K_{T,t+\Delta t}^i]^{-1} = \{A^i\}^T [K_{T,t+\Delta t}^{i-1}]^{-1} \{A^i\} \qquad (27)$$

where, $\{A^i\}$ = f (known nodal forces, known nodal displacements)

This brief explanation of the three equilibrium iteration techniques, upon reflection, shows that full Newton-Raphson iteration is the most computationally expensive of the techniques, because of its frequent complete stiffness matrix updates. Because of its frequent updates, however, it is usually the most effective technique when high degrees of nonlinearity are present. Reference 36 indicates the BFGS method is effective with moderate nonlinearities, while the modified Newton-Raphson technique is effective when only mild nonlinearities are present.

Reference 40 lists several significant factors concerning the modified Newton-Raphson and BFGS techniques. First, the analyst must balance solution accuracy with computational demand in deciding on the frequency of stiffness matrix update. The degree of system nonlinearity will bear heavily on the

decision (i.e., the greater the nonlinearity, the more often updates are required). Second, there are two prominent computational problems associated with the modified Newton-Raphson technique. The technique will converge slowly, requiring many iterations, when the structural system being analyzed softens suddenly (as is the case when steel reinforcement transitions from elastic to plastic behavior). If the system under analysis stiffens, divergence can actually occur. Stiffening occurs in both the steel and concrete material models in ADINA when stress reversals occur (unloading curves generally follow the initial tangent Young's modulus). Based on the authors' experiences, the modified Newton-Raphson technique is of limited value in the type of analysis undertaken here, because of the high degree of nonlinear material response. Stiffness matrix updates must be frequent to minimize numerical instabilities. Third, while the BFGS method seems to present no serious convergence or divergence difficulties, a large number of equilibrium iterations may be required for sufficient accuracy.

In Equation (24) describing the Newton-Raphson procedure, an approximation was indicated in the finite element equations. In theory, exact equality is desired, but, in practice, the analyst must be willing to accept some degree of approximation in order to minimize the number of equilibrium iterations performed. ADINA provides the analyst with several options for checking how well the approximation is converging on the exact solution for the time step. These options involve checking certain calculated quantities against convergence criteria with user-specified tolerances. For undamped systems, the convergence checks are as follows (Reference 36):

(1)   Energy convergence criterion:

$$\frac{\{\Delta U^i\}^T(\{R_{t+\Delta t}\} - [M]\{\ddot{U}_{t+\Delta t}^{i-1}\} - \{F_{t+\Delta t}^{i-1}\})}{\{\Delta U^1\}^T(\{R_{t+\Delta t}\} - [M]\{\ddot{U}^0\} - \{F_t^{final}\})} \leq ETOL \tag{28}$$

where,   ETOL = energy convergence tolerance

(2)   Force and moment convergence criteria:

$$\|\{R_{t+\Delta t}\} - [M]\{\ddot{U}_{t+\Delta t}^{i-1}\} - \{F_{t+\Delta t}^{i-1}\}\|_2 \leq RNORM*RTOL \tag{29}$$

where,   RNORM = reference force quantity, user-specified
            RTOL = force convergence tolerance

(3)   Translational and rotational convergence criteria:

$$\|\{\Delta U^i\}\|_2 \leq DNORM*DTOL$$

157

where,   DNORM = reference displacement, user-specified
          DTOL = displacement tolerance

The latter two sets of criteria are expressed as Euclidean vector norms, which are of the scalar form (Reference 49):

$$\| v \|_2 = \left(\sum_{j=1}^{n} |v_j|^2 \right)^{\frac{1}{2}} \tag{30}$$

Reference 40 discusses the above convergence criteria; the discussion is briefly summarized here. Selecting appropriate convergence criteria and convergence tolerances is critical in nonlinear analysis. If the tolerance is too loose, results are likely to be inaccurate, whereas, if it is too tight, too much computation may occur for relatively little gain in accuracy.

The translational and rotational convergence criteria have been found to be ill-behaved in nonlinear modeling, so they are not generally used. The force and moment convergence criteria ignore displacements, so they can lead to highly inaccurate results (for example, when the Young's tangent modulus is small, force differentials may be small, while corresponding displacements may be quite large). Note that, for the displacement (translation, rotation) and force (force, moment) convergence checks, ADINA separates the translational and rotational quantities, to keep units consistent.

The energy convergence criterion therefore seems to be the most effective single convergence criterion to use in nonlinear analysis. This criterion includes both force and displacement quantities, so it at least indirectly accounts for the accuracy of both. Reference 40 suggests ETOL = 0.001 (ADINA default value) to check for convergence and ETOL = 1.0 to check for divergence. The authors used the energy convergence criterion in all analyses reported here.

Note finally that the analyst chooses the maximum number of equilibrium iterations that will be allowed at a particular time step. If ADINA reaches this limit without meeting the convergence tolerance, the computations are terminated, accompanied by an appropriate message to the analyst.

6.   Description of Finite Element Models Used in Analyses
      a.   General

The purpose of the finite element analyses performed for the project was to assess the general applicability of ADINA in the design of above-ground reinforced concrete protective structures subjected to airblast effects. There are two primary reasons why the finite element procedure might be used instead of the less rigorous SDOF models. First, greater analytical accuracy might be possible. Second, more detailed design-related information might be gained from the finite element modeling process. ADINA was used in specific trial cases for both the IDF and the Tyndall AFB structures; the trial cases were chosen to provide specific information about different variables in the modeling process.

158

In modeling both the IDF and the Tyndall AFB structures, the authors concentrated on analyzing the wall behavior in the region affected locally by the airblast from a nearby conventional explosive detonation. The wall sections were modeled alone, without added elements for adjacent walls, roofs, or floors. Field test data for above-ground structures indicate that these walls are of primary concern in structural design. The increased fidelity and volume of relevant information that would be gained by modeling the abutting elements seemed to be outweighed by the increase in computational demand that would occur as a consequence of their addition. Rather, the authors attempted to incorporate the anticipated flexural and in-plane resistance effects of the adjoining elements in the support conditions used in the wall analyses. As partial validation of this hypothesis, the authors examined roof and floor displacement data in the IDF Test 4. The data were obtained by double integration of acceleration-time histories at accelerometer locations at the midspans of the roof and floor sections adjoining the test wall. There was almost no vertical floor movement; peak displacements were approximately 0.05 inch (recall that the floor slab was not cast integrally with the wall). Peak vertical roof displacements were approximately 0.25 inch to 0.70 inch, depending on the baseline shift technique employed in reducing the data. In the clear roof span of approximately 22 feet, these displacements represent modest rotations of 0.15 to 0.45 degree, assuming all midspan vertical movement is due to support rotation. Posttest observations were insufficiently detailed to ascertain whether yielding was more prevalent in the wall than in the roof. Peak horizontal floor and roof displacements were approximately 0.02 inch to 0.05 inch. The authors concluded that these displacements were small enough to assume relative (to the wall) rigidity of the roof and floor elements in modeling the support conditions. Comparable data in the Tyndall AFB structure were not readily available.

b. IDF Structure

The IDF structure had three distinguishing structural configuration features. First, the wall section was not cast integrally with the floor slab. Second, the outside vertical reinforcement volume was increased in the near-roofline region over that in the midspan to ground level region. It is likely that the facility designers foresaw the added flexural tension in this region that would be induced by blast loads. Third, the inside vertical reinforcement volume is larger than the outside volume, in likely anticipation of the positive midspan moments caused by airblast. As in the Tyndall AFB structure, horizontal reinforcement is uniform on both faces and in smaller volume than the vertical steel. Flexural response is anticipated to be dominated by one-way action spanning vertically. Details of the construction may be found in Section II. The ADINA models were able to replicate these configurations faithfully, while none of the SDOF models could do so.

For all analyses of the IDF structure, the wall was considered to be "fixed" at the top and (for two-way analysis) at adjoining walls (Figure 105).
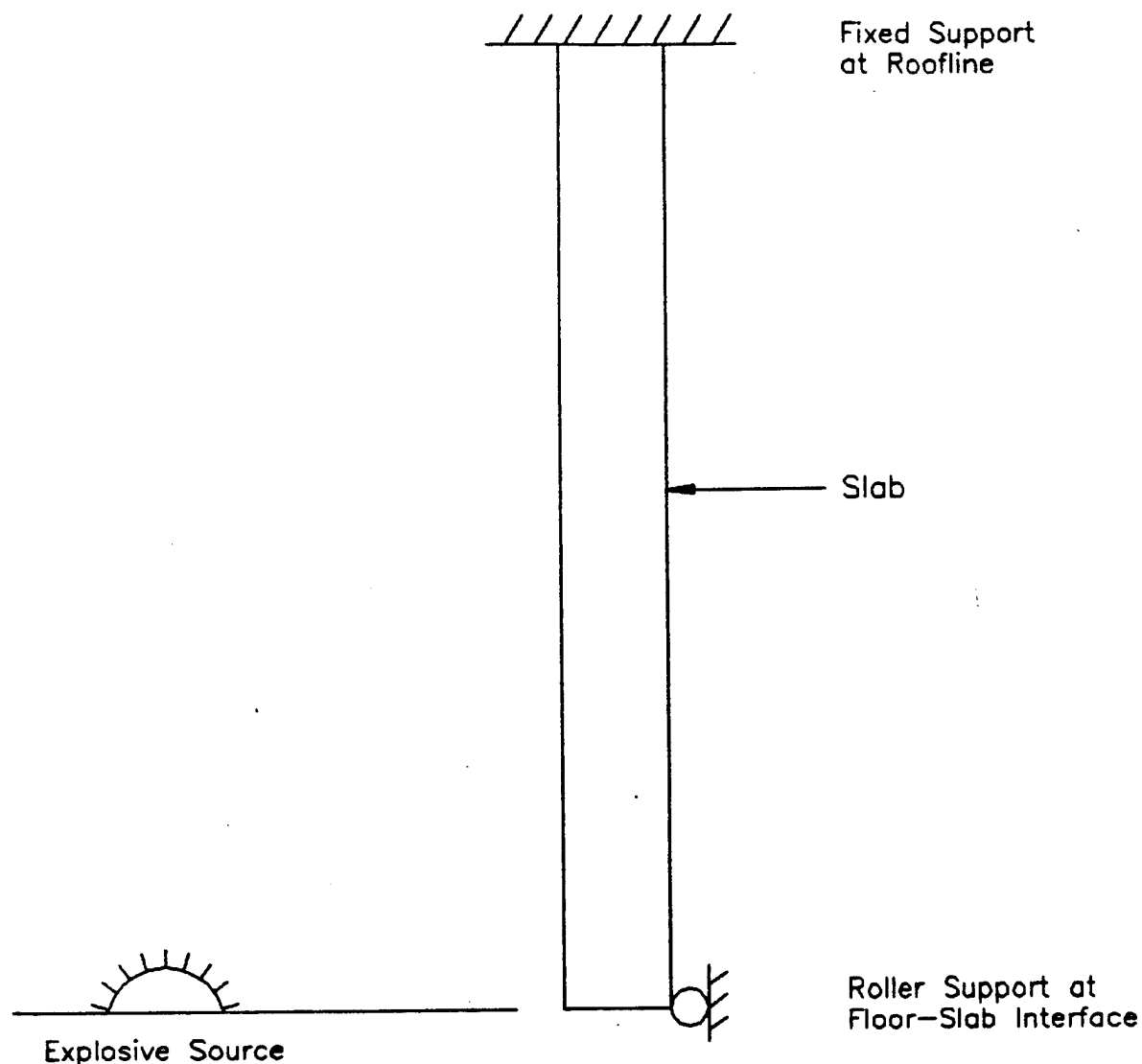
159

Figure 105. Idealization of IDF Structure for Finite Element Analyses.

The wall was considered supported by a horizontal knife edge at its base, where it abutted the floor. Appropriate nodal degrees of freedom were fixed to implement the assumed support conditions. While not detailed here, some nodes in the region of total fixity were released to minimize stress concentrations in the fixed end region. Figure 105 shows the idealization assumed by the authors.

Because the wall clear width (approximately 23 feet) exceeded twice its clear height (approximately 10 feet), and the transient airblast load is most severe in the region directly opposite the charge, the authors presumed one-way action in the vertical span would dominate the response. To minimize computational demand, therefore, most of the analyses were run as one-way slab models. Four different one-way slab models were developed. Three models used two-dimensional (2D) solid elements, in plane strain, while the fourth used three-dimensional (3D) solid elements.

160

The three 2D models all used eight node elements to represent the concrete material. Vertical reinforcement was represented by three-node truss elements directly connected at all node points to respective solid elements. Because of the planar nature of the analyses, horizontal reinforcement was not modeled. All three models used six solid elements through their depths, four of which were between the vertical reinforcement layers and two of which represented concrete cover over the reinforcement. The four elements between the reinforcement layers had individual thicknesses of 3.43 inches, with three integration points each through the thickness. The three models used three different element lengths (6 inches, 12 inches, and 20 inches) to analyze moment and shear gradient effects and to analyze element aspect ratio stiffness effects. The models were designated IDF-2D-20, IDF-2D-10, and IDF-2D-6, respectively; see Figures 106-108. The wall clear span was rounded to 10 feet, from the actual 9.8 feet, a slight approximation, in the models to make element lengths even, and thus more interpretable, in English units. In planar analysis, ADINA defaults to a unit thickness, 1 inch in these analyses. The vertical reinforcement volume for the 1 inch width was based on the reinforcement percentages used in the actual structure.

The fourth one-way slab model, IDF-3D-1W (Figure 109), was composed of a one element width of 20-node 3D solid elements. The element width was 12 inches, representing a 12-inch width of wall directly opposite the explosive. Four elements were used through the wall thickness, with two elements between reinforcement layers. The two elements between the reinforcement layers were each 6.85 inches thick. There were 10 elements along the 10-foot wall length. For each of the primary reinforcement planes, vertical reinforcement consisted of three-node truss elements along the node lines formed by the edges of the solid element width, and two-node truss elements along the node line formed by the solid element midside nodes. Horizontal reinforcement was also placed in the two reinforcement planes; three-node and two-node truss elements were used at appropriate solid element node lines. The horizontal and vertical reinforcement were both joined rigidly to the solid elements at nodes. All nodes on each side of the 12-inch width were fixed in the plane of the wall, to simulate plane strain, except at the end support nodes (which were fixed as needed to simulate the support conditions). These side nodes were otherwise free to move.

One two-way slab model, IDF-3D-2W (Figure 110) was constructed in an attempt to validate the assumed dominance of one-way action. Even the relatively simple two-way model analysis was so computationally demanding when using the concrete material model as to make its use impractical in a design effort. The authors note that less complicated material behavior could be used for elements outside the most severely loaded region, thus reducing the analytical demand somewhat. With the placement of the explosive at midwidth of the structure, symmetry about midwidth was used. From wall midwidth to the connecting wall, 11 3D solid element widths were used. Each element width was 12 inches, for a total wall width of 22 feet (vs the 23 feet actually used). The connecting wall was considered to be a fixed support, while the centerline at wall midwidth
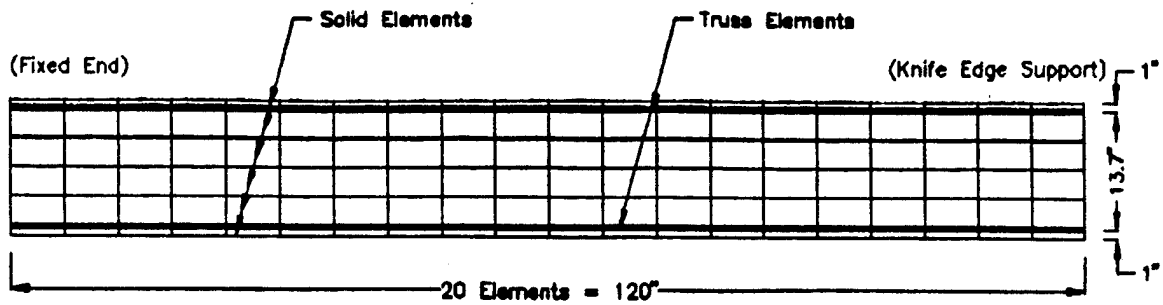
161

Figure 106. Geometric Model Used in IDF-2D-6.
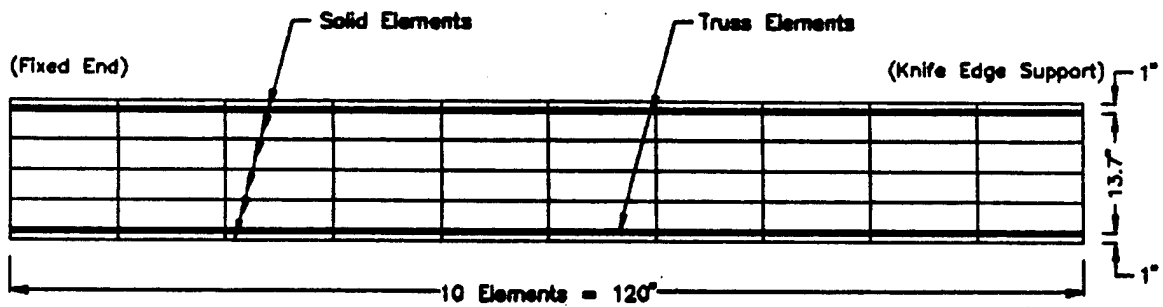

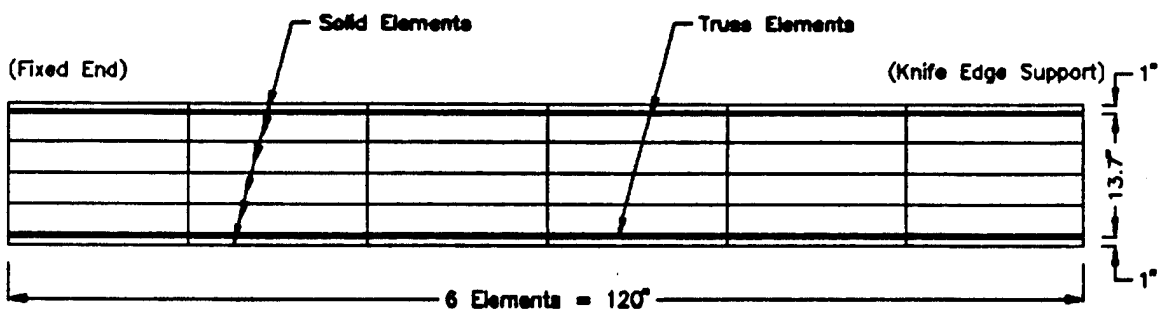Figure 107. Geometric Model Used in IDF-2D-10.

Figure 108. Geometric Model Used in IDF-2D-20.

162
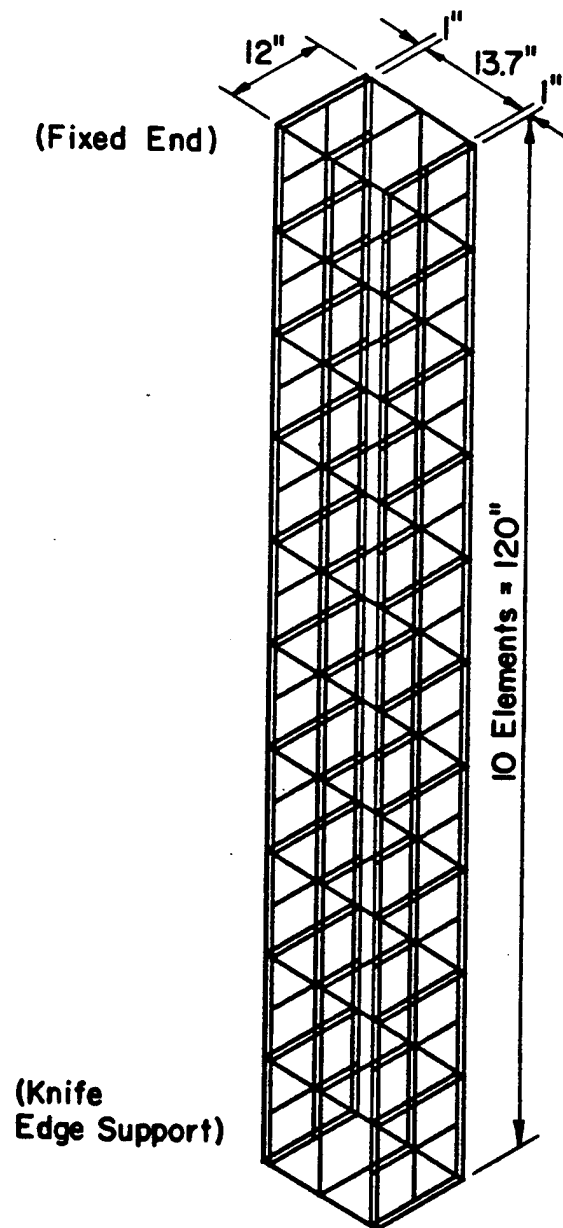
Figure 109. Geometric Model Used in IDF-3D-1W.

restricted in-plane movement only. Otherwise the two-way slab model was constructed in the same manner as the 3D one-way slab model.

c. Tyndall AFB Structure

The Tyndall AFB structure, because of its experimental nature, had several distinctly different wall sections around its perimeter. The sections exposed in Tests 6 and 10 were used for the ADINA analyses. Those wall sections most closely resembled the IDF structure. (See Section III for a more complete description of construction details.) However, there were major differences in the IDF and Tyndall AFB tests. The Tyndall wall sections were relatively thicker

than the IDF sections. The Tyndall wall section thickness to clear span ratio (t/h) was 0.16 in Test 6 and 0.20 in Test 10, whereas the IDF t/h was 0.13. In addition, the explosive charges were larger, were cased, had more slender cylindrical aspect ratios, and were located closer to the structure in the Tyndall tests than the IDF tests. The authors therefore anticipated a more dominant shear response in the Tyndall structure than in the IDF structure. Tyndall Tests 6 and 10 were both modeled; the blast parameters were the same, but wall section details were different.
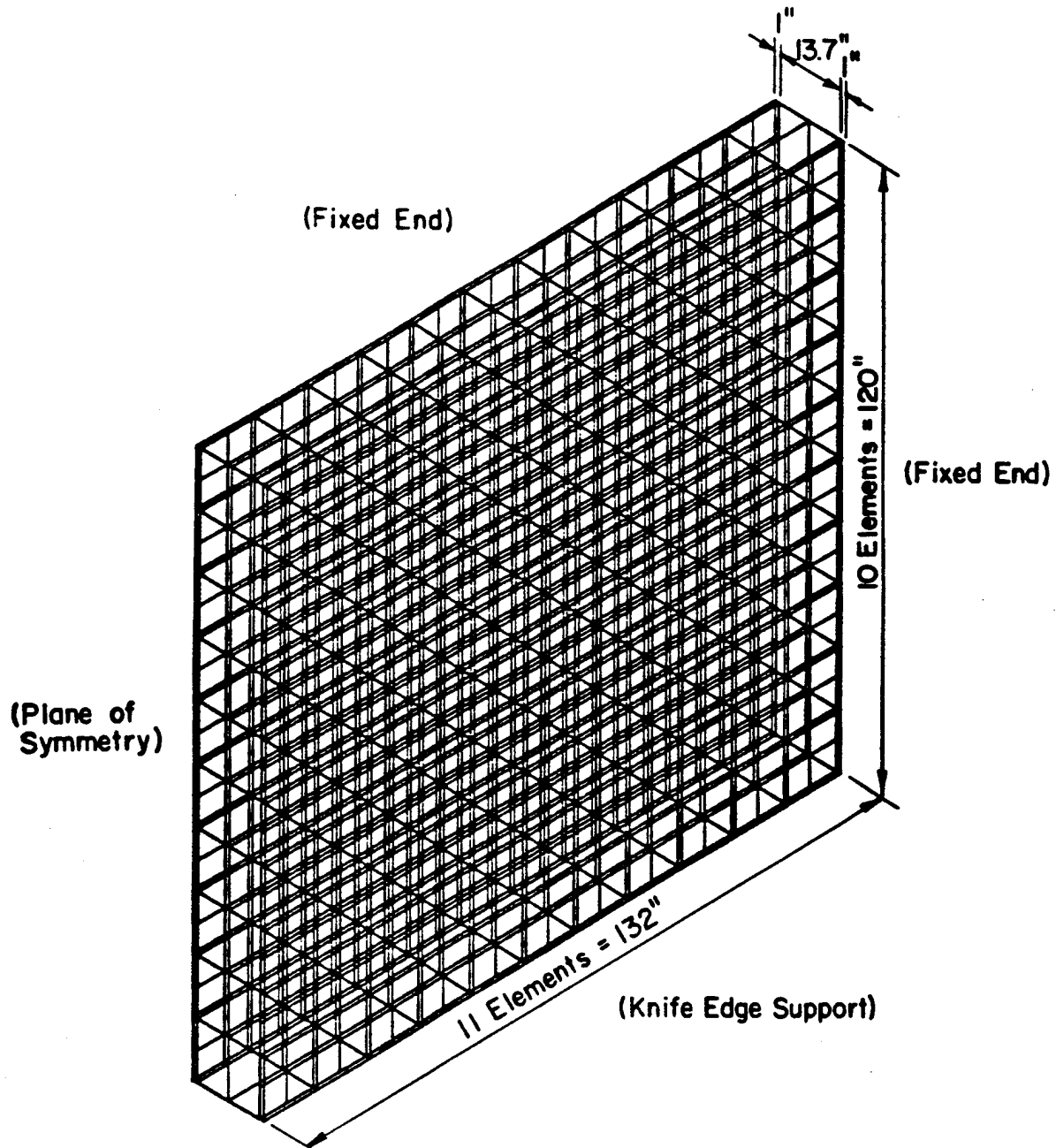

Figure 110. Geometric Model Used in IDF-3D-2W.

164

The Tyndall structure had several construction details other than those listed above that provided opportunity to use different modeling parameters. First, the wall section was cast integrally with the connecting roof and floor slab sections. In addition to extending flexural reinforcement into the roof and floor slabs, diagonal bars were added in the joint regions. Second, while inner and outer wall reinforcement layers had equal steel volumes, their concrete cover thicknesses differed, resulting in somewhat different positive and negative flexural and shear capacities. Third, the presence of doorways near each wall end, and the large wall clear width, approximately 48 feet, when compared to a vertical clear span of 13 feet, led the authors to assume one-way action in the vertical span would dominate structural response. Finally, stirrups were provided over the full height of the wall; U.S. military construction practice includes stirrups for confining primary reinforcement and providing added shear resistance.

For all analyses of the Tyndall AFB structure, the wall was considered to respond in one-way action. Based on earlier experience with the IDF structure, only plane strain analyses were run, using the 2D 8-node solid elements to model the concrete material and two and three-node truss elements to model the reinforcement.

Although only the wall clear span was modeled, the authors examined the effects of end restraints induced by the connecting slab elements. At each end of the clear span, a knife edge horizontal support restricted all horizontal movement. It was assumed that the axial stiffnesses of the floor and roof slabs, and the total mass of the facility, were sufficient to prevent any significant horizontal translation of the wall at the supports. Cursory analyses of the floor and roof slabs showed them to be very stiff in both flexure and axial compression. Therefore, the ends of the wall were fixed against rotation. Because there has been discussion of in-plane resistance provided by adjoining elements (the microcomputer model SASDE includes in-plane effects), the in-plane movement of the slab was not prohibited for some of the analyses. Rather, linear springs were added to the model in its connection to the fixed support. A succession of analyses using different spring stiffnesses then examined the in-plane force effects. As with the IDF structure, it was necessary to relax some of the assumed nodal fixities at the supports to minimize stress concentrations in the models. Figure 111 portrays the assumed structural configuration.

Three models were constructed. The first, designated Tyndall-South (Figure 112), modeled the 25.5-inch thick wall section of Test 6. Vertical reinforcement was represented by three-node truss elements directly connected at all nodes to respective solid elements. Horizontal reinforcement was not modeled because of the planar nature of the analyses. Three-node truss elements were also used to model the stirrups. They were placed along the interelement lines (12-inch spacing) of the solid elements and joined the inner and outer vertical reinforcement layers. Two-node truss elements modeled the corner diagonal bars and joined vertical reinforcement nodes replicating the configuration in the prototype structure. The model used five solid elements through its depth, three
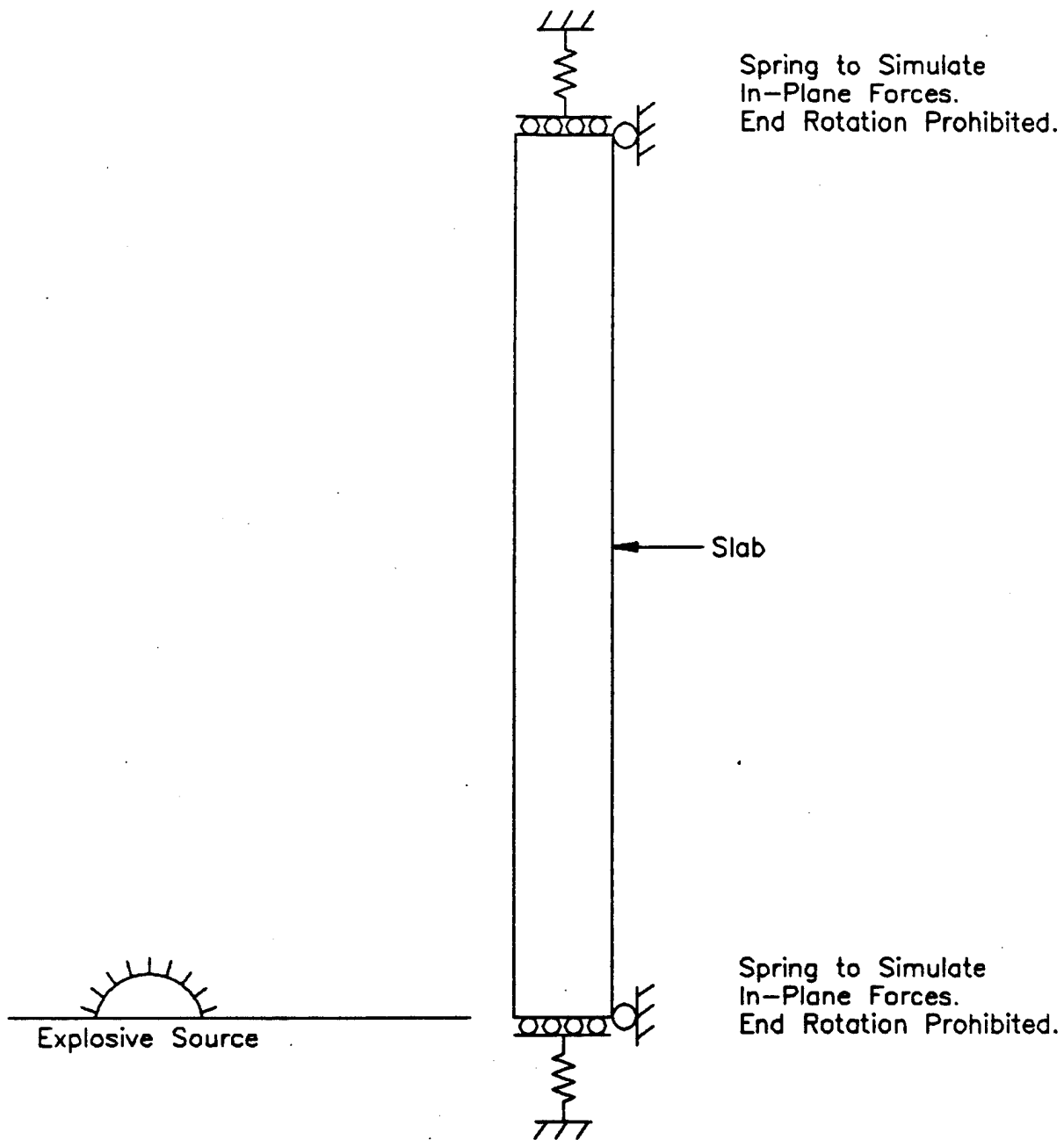
165

Figure 111. Idealization of Tyndall AFB Structure for Finite Element Analyses.

of which were between the vertical reinforcement layers and two of which represented the concrete cover over the reinforcement. The elements between the reinforcement layers had individual thicknesses of 7.05 inches. Each solid element was 12 inches long; with 13 elements, the wall clear span was 13 feet, vs the actual clear span of 13 feet 2 inches. This approximation would have negligible effects on analysis results but would make element lengths even for better interpretation of results. In planar analysis, ADINA defaults to a unit thickness, 1 inch here. The reinforcement volume for a 1-inch width was based on the prototype percentages.
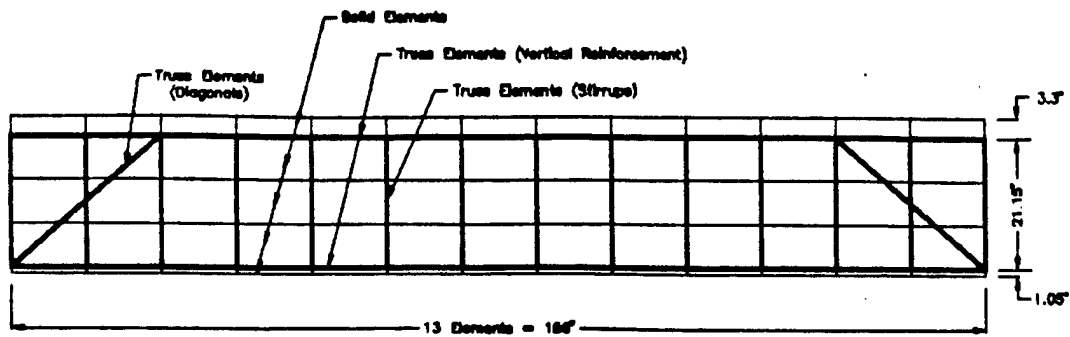
Figure 112. Geometric Model Used in Tyndall-South.

Two models of the north wall were constructed. The first, Tyndall-North-1 (Figure 113), is essentially the same as Tyndall-South, except that the three solid elements between the vertical reinforcement layers were each 9.05 inches thick. Model Tyndall-North-2 (Figure 114) was the same as Tyndall-North-1, except that a finer element mesh was used. Along the length, 26 elements, each 6 inches long, were used. Through the depth, between the vertical reinforcement layers, six elements, each 4.525 inches thick, were used.

d.   Geometric Modeling

The ADINA software package comes with its own pre- and postprocessing capabilities. ADINA-IN is used as a preprocessor to develop ADINA finite element models; ADINA-PLOT is used as a postprocessor. For the 2D IDF analyses, ADINA-IN was used directly. Its geometric data input involves a specified language structure. When the authors developed the 3D IDF models and all Tyndall models, they used an alternate approach made available by ADINA R&D. A supplemental ADINA software package, TRANSOR, translates a neutral file output by a separate commercial preprocessor, PATRAN, into a format accepted by ADINA-IN. PATRAN provides a more straightforward model construction process, with real-time model visualization, than is currently available in ADINA-IN.
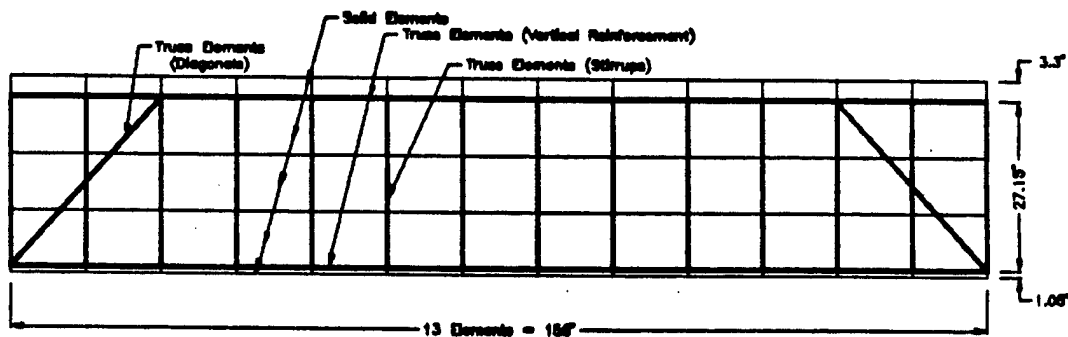

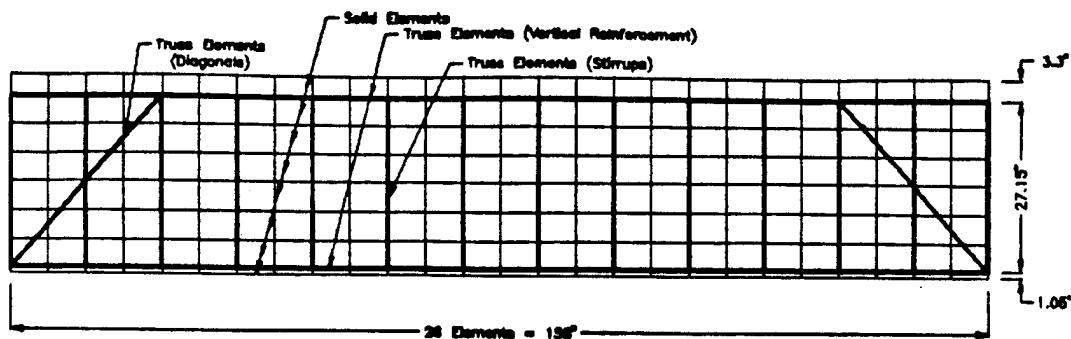Figure 113. Geometric Model Used in Tyndall-North-1.

167

Figure 114. Geometric Model Used in Tyndall-North-2.

e. Material Properties

Material properties used in all ADINA models closely paralleled those used in the microcomputer models discussed previously. Where noteworthy deviations were made, the following paragraphs mention them. In particular, it was necessary to raise the concrete strength properties in numerous instances above those that were used in the microcomputer models (or in the prototype structures) to allow ADINA to overcome numerical instabilities.

C. PARAMETER STUDIES WITH ADINA

The effects of several parameters that influence the solutions obtained with ADINA were investigated to better understand the applicability of the program to the analysis of impulsive transient pressure loading. These parameters are related to loading function, geometric modeling, and material behavior. Both static and dynamic solutions were compared for a number of test cases, for three reasons: the influence of some parameters may be more easily compared with static load analysis, some parameters' influence may not be the same for both static and dynamic loading, and numerical instabilities in the nonlinear dynamic analyses can be avoided in static analyses.

Large displacements are acceptable for some applications of protective structure design. It would therefore be desirable to have the static solutions continue into the range of several inches of wall deflection or the dynamic solutions continue until structural motions damp out well enough to estimate a residual displacement. In some of the dynamic analyses this occurred, but in many others the program became unstable and stopped after yielding but before the deflections became large. Several months of experience with ADINA were required to gain partial understanding of ways to avoid the premature stoppage. Also, when the three dimensional elements were used for both the one-way and two-way slab models, the computer run times became so long that it was not possible to obtain the full pressure-deflection history or time history on the available workstations. Toward the end of the study, access to ADINA was obtained on a supercomputer and a few longer runs were possible. Initial runs were made on a workstation network.

168

1. Effect of Loading Parameters

The manner in which the loading is applied and the shape of the loading function affect the deformed shape of the slab and consequently the stress distribution in the concrete and the reinforcement. The 10x6 element mesh IDF model (Model: IDF-2D-10) was used to study the effect of the manner in which the dynamic pressure was applied. The models used in this section are shown in Figures 106-114.

The model was loaded in three different ways. First, a dynamic uniform pressure over the outside surface was applied with the magnitude and pressure-time function measured at the midpoint of the wall in the IDF Test 4 (Loading A). This is consistent with assumptions frequently made in SDOF models. However, in reality the pressure reaches the lower portion of the wall first and then travels upward. The increased distance from the charge and the changing angle of incidence reduce the pressure magnitude and delay the time of arrival. Two additional solutions were obtained to assess this effect. The second loading assumed the pressure to start at the bottom of the wall (the ground level) and to travel up the wall using the measured pressures as a guide but using a multilinear approximation to the theoretical exponential decay of pressure as the wave moves along the wall, with the same pressure time curve at the midheight as that used in the uniform loading case (Loading B). There is evidence, however, that the lower portion of the wall is subjected to additional pressure due to the build up of the wave at the ground (Reference 56), and so this effect was modeled in the third loading using the enhancement of pressure near the bottom of the wall suggested by the reference. The movement and change in peak pressure of the wave along the wall was the same as in the second case, except that the pressure at the bottom of the wall was increased (Loading C). The three pressure loadings are shown in Figure 115.

Figure 116 shows the deflection-time history for the three different loadings on the wall. The primary observation is that the maximum deflections are different, therefore indicating that the pressure-time curve measured at the midpoint of the wall is not a meaningful average pressure to apply to obtain an equivalent response; it underpredicts the response. If a uniform pressure over the loaded surface was desired, it would be necessary to develop other criteria to obtain an equivalent loading. Except for this, Figure 116 would indicate that the overall response is similar. However, the internal forces and stresses in the slab may be even more affected by the loading. In addition, the enhanced pressure near the bottom of the wall (Loading C) further increases its deflection, and thus the stresses in the materials.

Figure 117 shows the deflected shape of the slab at 0.5 and 10.0 ms when the load is applied uniformly over the surface (Loading A). At 0.5 ms the deflections are small, but the shape is such that the midportion of the slab is perfectly flat and all the deformation has occurred near the ends as shown in Figure 117a. This occurs because the slab has not had sufficient time to develop significant response in flexure in 0.5 ms; the flexural period of the unyielded slab is approximately 20 ms. The pressure has pushed the slab inward, deforming
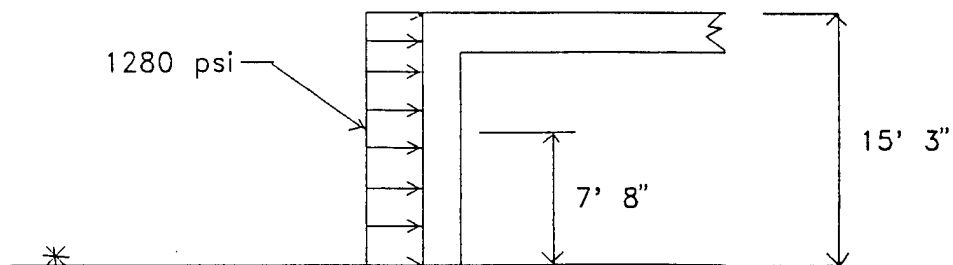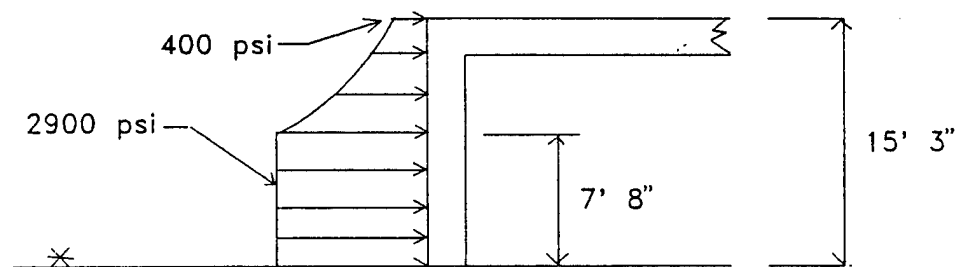
(a)   Loading A, Uniform pressure measured at midheight.
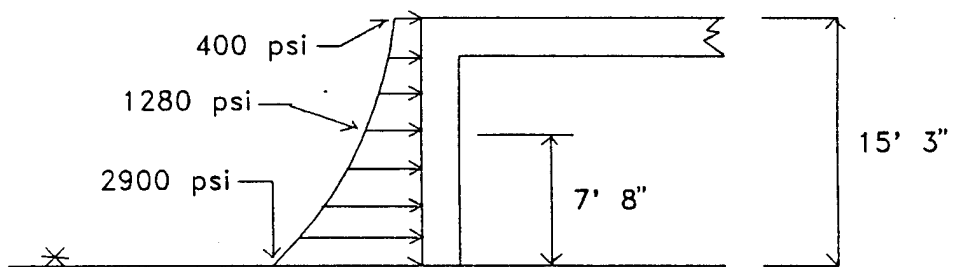
(b)   Loading B, Theoretical pressure decay that matches measured value at midheight.

(c)   Loading C, Enhanced pressure at the lower portion of the wall.

Figure 115. Three Wall Pressure Distributions Considered in the Parameter Study.
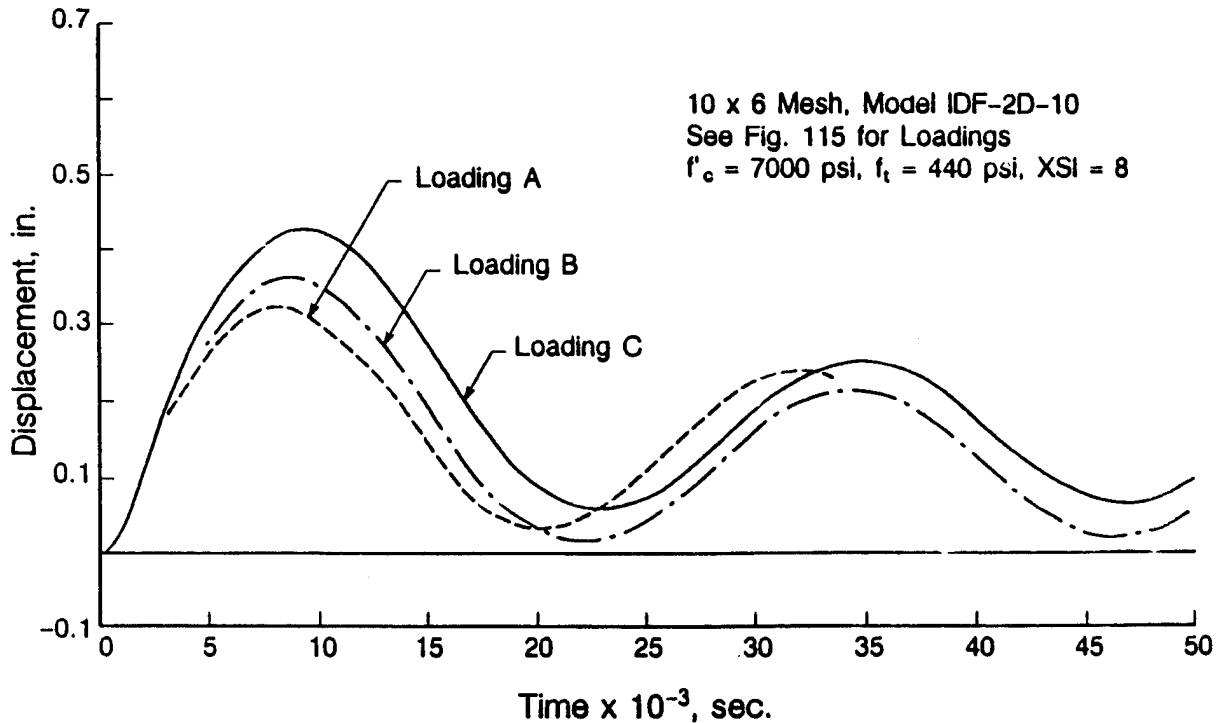
170

Figure 116. Effect of Loading Distribution on the IDF Wall Model.

the end regions in shear. This behavior has been observed in numerous tests (Reference 57) in which the end regions failed in direct shear. If failure does not occur in direct shear the response continues in flexure and the deformed shape of Figure 117(b) develops.

Figure 118 shows the deformed shape of the slab at 0.5 and 10.0 ms with the transient Loading B. The pressure is applied first to the bottom elements near the pinned end of the slab and then travels upward toward the fixed end. Figure 118(b) shows the deformed shape at 0.5 ms when the pressure has pushed the end of the beam inward. Pressure has been applied only to the bottom seven elements, and the three rows of elements near the fixed end have not had pressure applied to them nor have they had time to respond from pressure applied to the other elements. At this time, there is still pressure on the bottom elements, as the pressure-time history is 1.0 ms long at this location. The deflections are small, but the pressure is greatest at the bottom of the wall and may be sufficient to cause a shear failure before the energy absorbing capability of the flexural behavior can be developed. This is what actually occurred in the IDF Test 9 discussed earlier. At 10 ms (Figure 118(a)) the deflected shape is similar to that from the previous loading, but the maximum deflection is somewhat larger.

Figure 119 shows the deformed shape of the slab at 0.5, 1.0, 1.5 and 10.0 ms with the transient pressure that has been enhanced near the bottom of the wall (Loading C) engulfing the slab from the right end in the figure. This loading
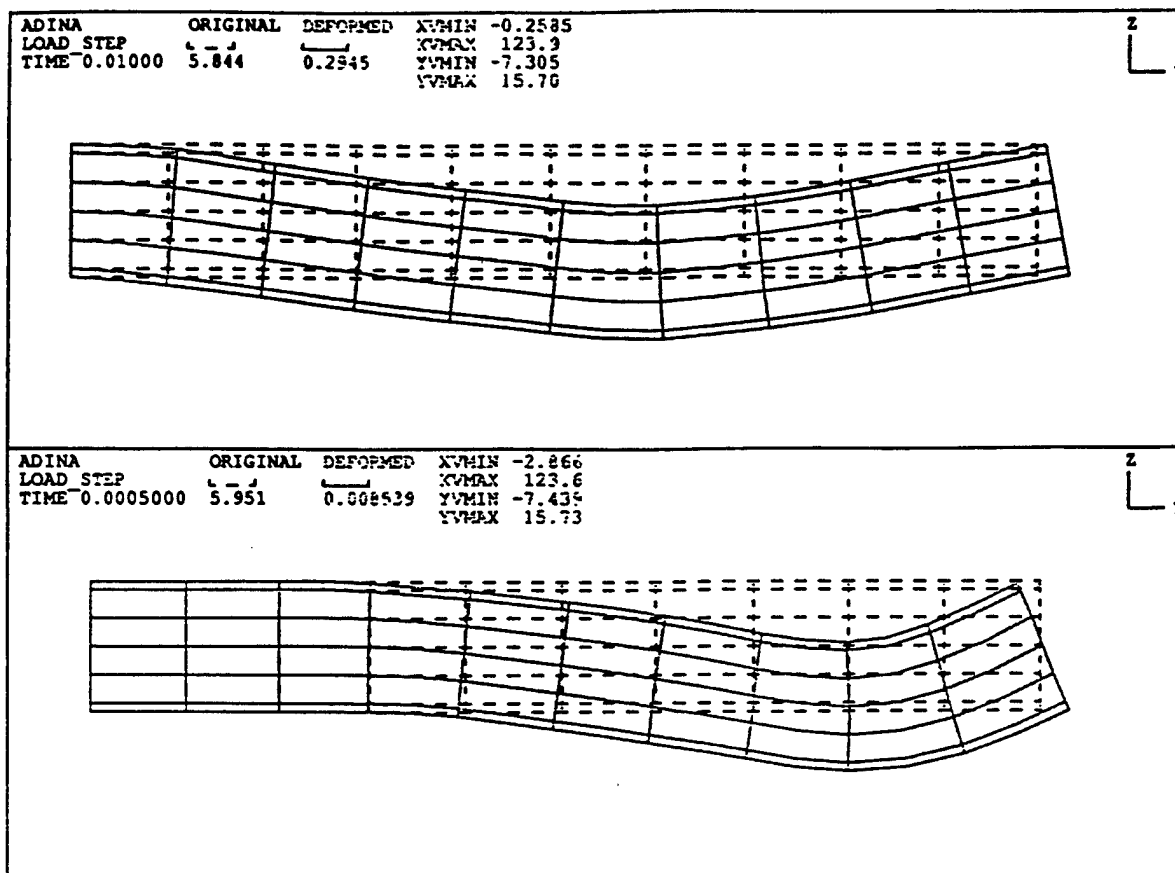
171
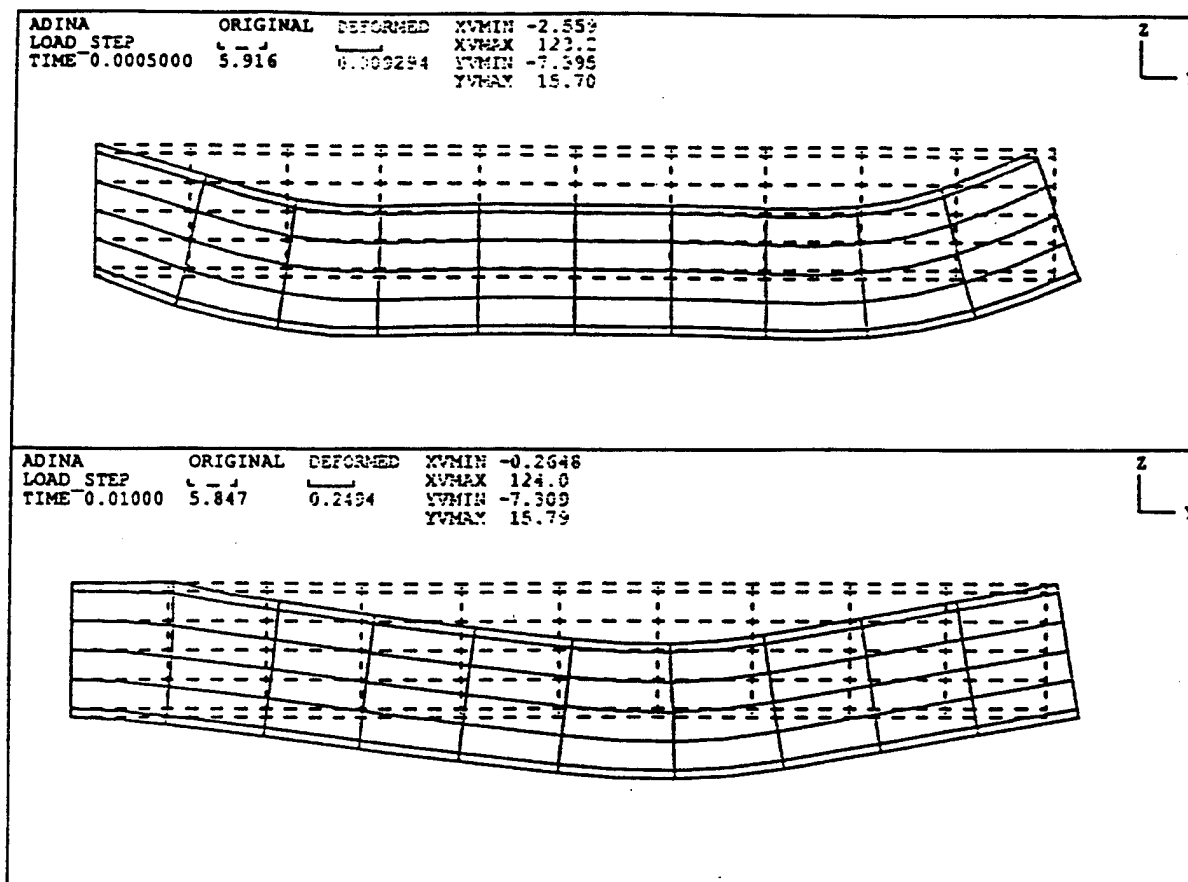
10x6 Mesh, Model IDF-2D-10, f'_c= 7000 psi, f_t = 440 psi, XSI = 8

Figure 117. Deformed Shapes of the IDF Wall at Two Times With the Uniform Loading A.

has the same effect as that discussed above, but the initial loading is larger and therefore the deformation is larger at any given time. The high shear at the pinned support and the delay in response at the top (fixed) end of the slab is similar.   Also the change in shape is clearer here because there are more different response times represented.   At 0.5 ms the maximum deflection occurs at the second element from the pinned end; at 1.0 ms the maximum deflection has moved to the third element. At 1.5 ms the point of maximum deflection has moved very little, but the beam has deformed much more between the maximum deflection point and the fixed end.   At 10.0 ms the maximum deflection has moved to the fifth element from the pinned end and the shape is similar to that expected in the flexural mode.   This is approximately the time that the peak deflection occurred (Figure 116).

These comparisons emphasize the uncertainty associated with the loading that should be applied to a slab if a simplified uniform time-dependent pressure is to be used.   It is clear that applying a uniform pressure history at the center of the slab does not provide the correct response when a nonuniform

172

10x6 Mesh, Model IDF-2D-10, $f_c' = 7000$ psi, $f_t = 440$ psi, XSI = 8

Figure 118.   Deformed Shape of the IDF Wall at Two Times With the Transient Loading B.

transient pressure is the actual loading. These studies also show that the transient loading can be modeled with the finite element program and therefore provide a means for investigating the uniform loading that will provide the correct maximum overall response, or to study the slab behavior with transient loading. A study of the deformed shape at very early times in the slab response shows that direct shear at the supports is a failure mode that could result in failure before the flexural response can occur. This occurs because the frequency of response in shear is very high, and the loading at the edge depends on the peak pressure at the initially loaded edge rather than on an average pressure that occurs over the entire slab that drives the flexural response. Thus, the shear failure could occur in cases in which a flexural failure would not have occurred. Numerous field tests have corroborated this observation.

2.   Effect of Tensile Strength of the Concrete

One of the most uncertain and critical material properties in the test slabs is the tensile strength of the concrete. There are many reasons for this
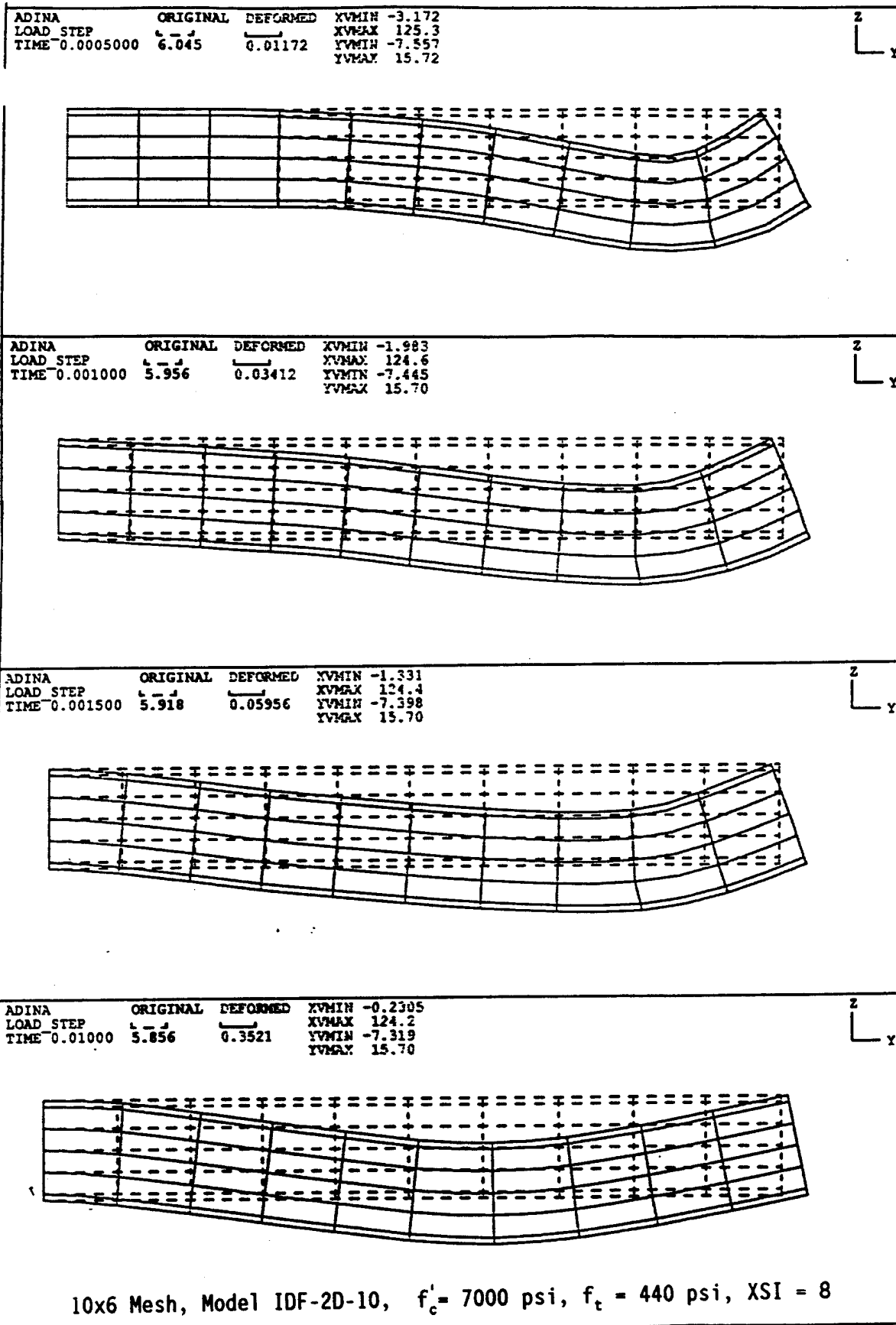
173

ADINA   ORIGINAL   DEFORMED   XVMIN -3.172
LOAD STEP   XVMAX 125.3
TIME 0.0005000 6.045   0.01172   YVMIN -7.557
                                     YVMAX 15.72

ADINA   ORIGINAL   DEFORMED   XVMIN -1.983
LOAD STEP   XVMAX 124.6
TIME 0.001000   5.956   0.03412   YVMIN -7.445
                                     YVMAX 15.70

ADINA   ORIGINAL   DEFORMED   XVMIN -1.331
LOAD STEP   XVMAX 124.4
TIME 0.001500   5.918   0.05956   YVMIN -7.398
                                     YVMAX 15.70

ADINA   ORIGINAL   DEFORMED   XVMIN -0.2305
LOAD STEP   XVMAX 124.2
TIME 0.01000   5.856   0.3521   YVMIN -7.319
                                     YVMAX 15.70

10x6 Mesh, Model IDF-2D-10, f_c'= 7000 psi, f_t = 440 psi, XSI = 8

Figure 119. Deformed Shape of the IDF Wall at Four Times With the Transient
Loading C.

174

uncertainty. There is a normal broad scatter in the tensile strengths of concrete that depend on the mix, aggregate, curing conditions, and such. Also, shrinkage may cause cracking on the surface that can initiate tensile cracks, resulting in a lower effective tensile strength. This can occur especially when it is hot and dry during curing, as was likely in the IDF structures. In addition, when there are repeated severe loadings, as in the case of the IDF structural tests, there may be some cracking from the previous loadings that results in a lower effective tensile strength in subsequent tests. Thus, to model this behavior in the finite element analysis it may be reasonable to lower the tensile strength for those tests that follow earlier ones.

To investigate the effect of concrete tensile strength on the finite element model several solutions were obtained using identical concrete material parameters except for the tensile strength. This was done first for the thicker Tyndall structure wall with static loading, and then for the IDF wall with the transient dynamic loading.

The pressure-deflection curves for the thicker Tyndall wall 13x5 element model (Model: Tyndall-North-1) subjected to static loading and with concrete tensile strengths of 300 and 600 psi are shown in Figure 120. The knee of the curve for 300 psi strength occurs at one-half of the pressure of that for the 600 psi curve, indicating clearly that the knee results from tensile cracking. After cracking has extended to the neutral axis of the slab, the curves tend to merge. However, there is considerably more area under the 600 psi tensile strength curve, and therefore that model has more energy absorbing capacity. It can be expected that this parameter would then affect the dynamic response, though the effect would be less as the overall deflection increases because the difference in area under the pressure-deflection curve would become a smaller part of the total area as the deflection increases.

The effect of cracking of the concrete under static loading on the reinforcement stress is shown in Figure 121 where the midspan and fixed support tensile reinforcement stresses are shown for both cases. When the concrete cracks at the level of the reinforcement, the stress is transferred to the bars, and the stress increases rapidly. This begins at a pressure of about 50 psi for the case with 300 psi concrete tensile strength and at a pressure of about 100 psi for the case with 600 psi. The concrete cracks first at the support and so the reinforcement stress starts to increase there first. When cracking begins at the midspan, the reinforcement stress increases more rapidly because the slab is then not as stiff, allowing deflections to increase quickly.

The pressure-displacement curve for the 300 psi tensile strength case (Figure 120) shows an irregular transition between initiation of cracking at about 55 psi pressure and yield of the reinforcement. This type of gradual transition does not occur for the 600 psi tensile strength case, and the initiation of cracking is very close to the pressure at which the steel has yielded. This occurs because in the latter case the cracking capacity of the slab is about the same as the fully cracked section capacity at yield. Thus, when cracking occurs the critical sections go directly to the cracked section
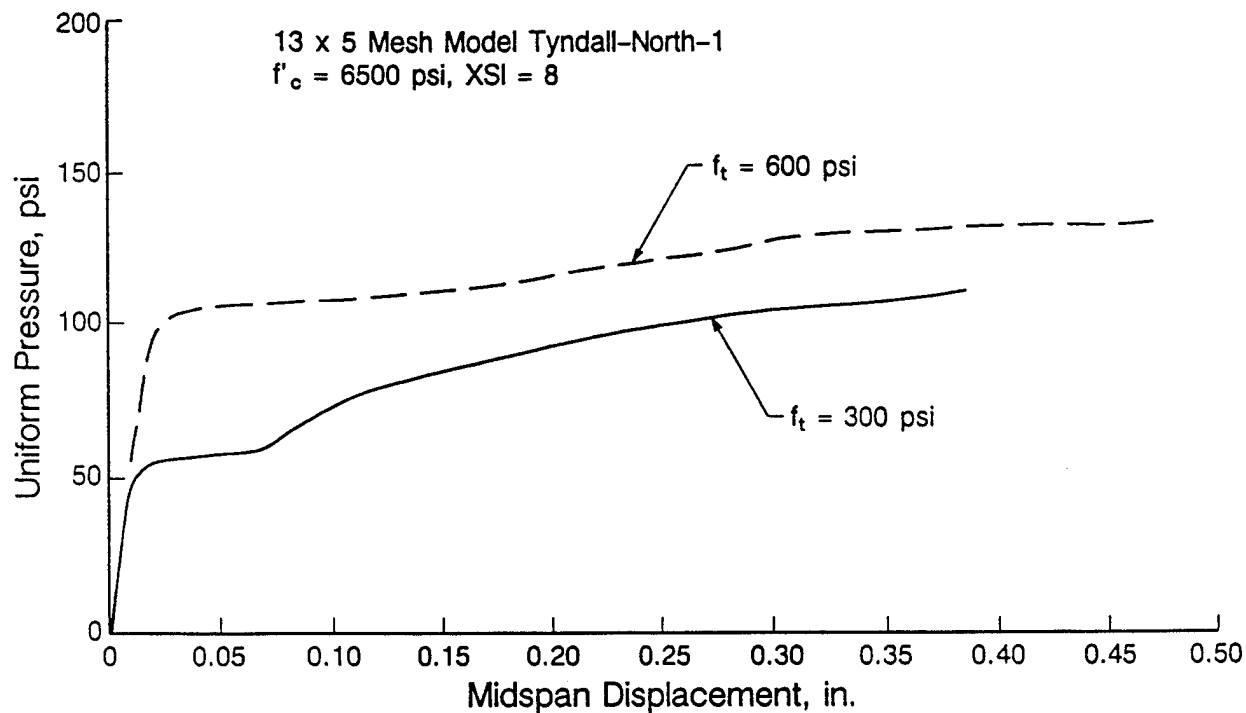
Figure 120. Effect of Concrete Tensile Strength on the 13x5 Element Tyndall North Wall Model with Static Load.
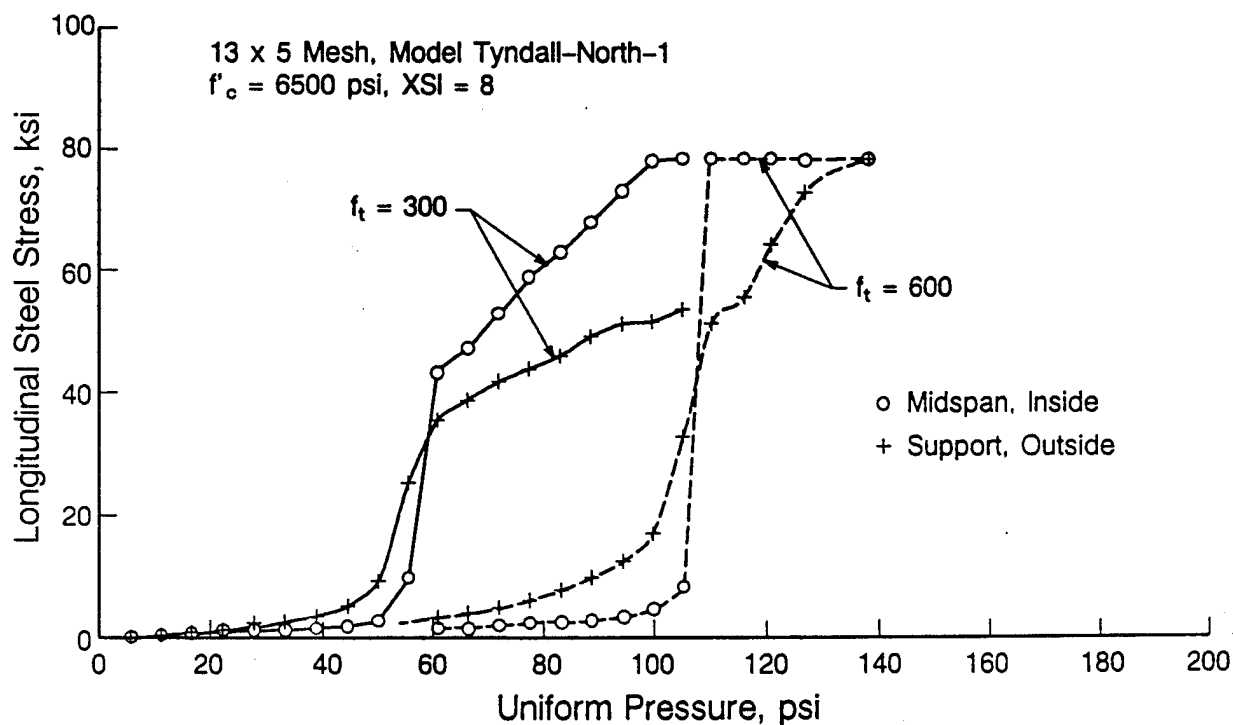

Figure 121. Effect of Concrete Cracking on the Reinforcement Stress for the 13x5 Element Tyndall North Wall Model With Static Loading.

176

capacity with the reinforcement yielding, because the sections are so lightly reinforced. A more heavily reinforced structure would respond differently. These observations of the behavior indicate that the finite element model does portray the details of behavior of a concrete slab that have been observed in static tests.

To investigate the effect of concrete tensile strength on the dynamic behavior, several solutions were obtained with different concrete tensile strengths while holding other parameters constant, using the 10x6 element mesh IDF wall model (Model: IDF-2D-10) and the Test 4 transient loading. The displacement-time curves for four tensile strengths and for XSI = 1.0 are shown in Figure 122. It is clear that the tensile strength has a marked effect on the maximum displacement reached by the slab as well as the time at which the maximum displacement occurs. The effect on static response and the energy absorbing capacity of the beam can explain the differences in dynamic response.

These studies indicate that the tensile strength of the concrete is an important parameter in the displacement-time response and reinforcement stresses of the slab. It affects the overall behavior and the details of the internal forces, and therefore must be selected with care. In normal design techniques, concrete unconfined compressive strength is usually the dominant concrete design
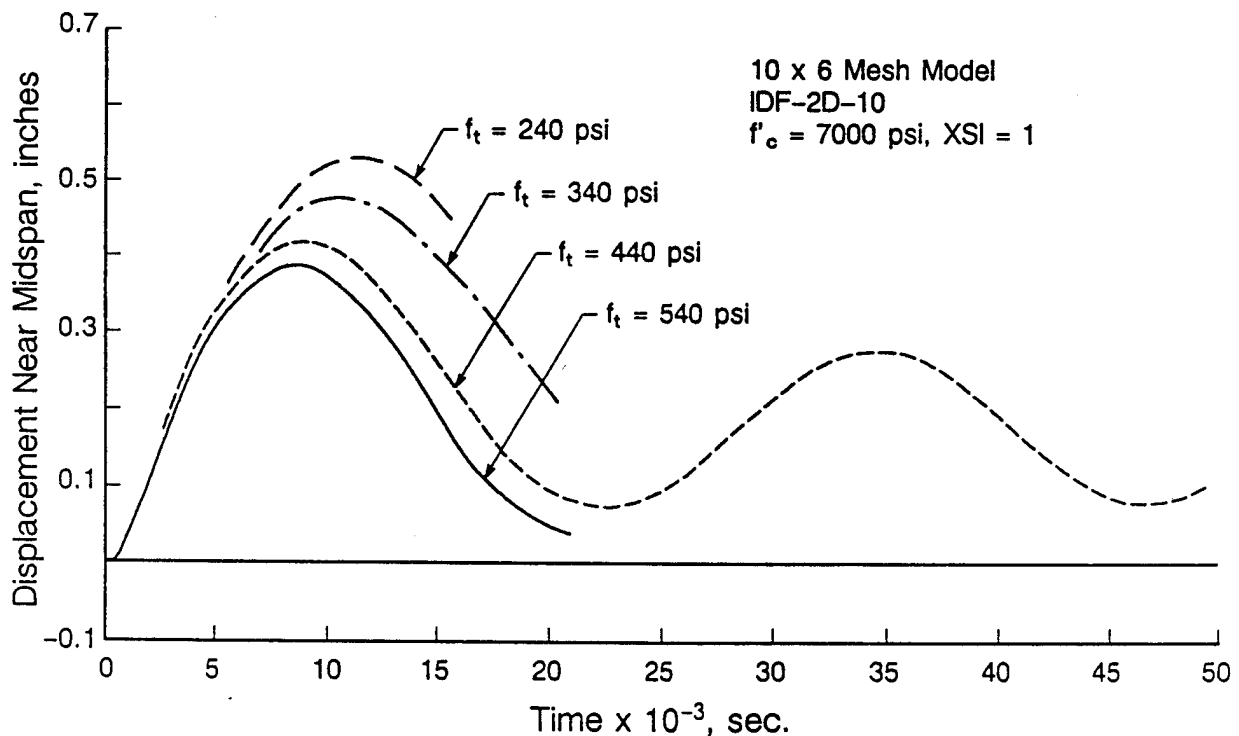

Figure 122. Effect of Concrete Tensile Strength on the 10x6 Element IDF Model With Transient Loading.

177

parameter, with tensile strength being expressed as an empirical function of compressive strength. This leads to rather gross approximations of tensile strength that can have major effects on analysis results. It was suggested that for overall response the effect of previous damage could be approximated by selecting a progressively lower tensile strength for studies such as the IDF tests. This procedure was implemented here with a modest degree of success. However, it is difficult to predict what the reduction in yield stress should be, and this technique would not be as effective in predicting the detailed internal forces due to precracking. The analyses reported here also fail to indicate a clear *recipe* that one might use for all blast load analyses.

ADINA has the option of restarting a problem with some of its input parameters changed. Therefore, it would be possible to run a simulation of the first test that would result in cracking of the model, change the loading to that of the second test, and then restart the solution process. The geometry of the model containing the precracking and residual deformation would be preserved in the restarted problem, and this could be continued through the test series. This process would only be justified for very special studies, however.

3. Effect of XSI Parameter in the Concrete Model

The XSI parameter in the concrete model is discussed in Section VIII-2D-B, and represents the amount of tension softening after cracking. Static analyses using the model for the thicker Tyndall structure test wall were used to study the effect of this parameter. The study was extended to include two mesh configurations and then to the dynamic solutions using the IDF model with 10x6 element mesh.

Figure 123 shows the effect of three values of XSI on the static load-deflection behavior of the 26x8 element mesh model of the thicker Tyndall wall (Model: Tyndall-North-2). The initial portion of the curve is changed by this parameter with a reduction of deflection at a given load as XSI is increased. Each solution begins with the same linear slope, but XSI affects the loading at which the curves deviate from linearity. This deviation results from an effective first cracking of the concrete. XSI influences the onset and propagation of effective cracking even though the tensile strength of the concrete is the same for each of these solutions. Increasing XSI slows the propagation of cracking, effectively increasing the strength of the concrete in tension beyond first cracking as shown by the larger uniform pressure at any given deflection when the XSI is larger.

Figure 123b shows the full pressure-deflection curves for 1000 load steps in each solution. The slopes and deflections are quite different at the ends of each run. Plots of the reinforcement stresses (not shown here) show when the stress has reached tension yield at the midspan and ends, and when plastic hinges have formed at these locations. This occurs at 110 psi for the case of XSI of 4.5, for example, and the load-deflection curve might be expected to remain relatively flat beyond this point. However, it continues to rise, indicating
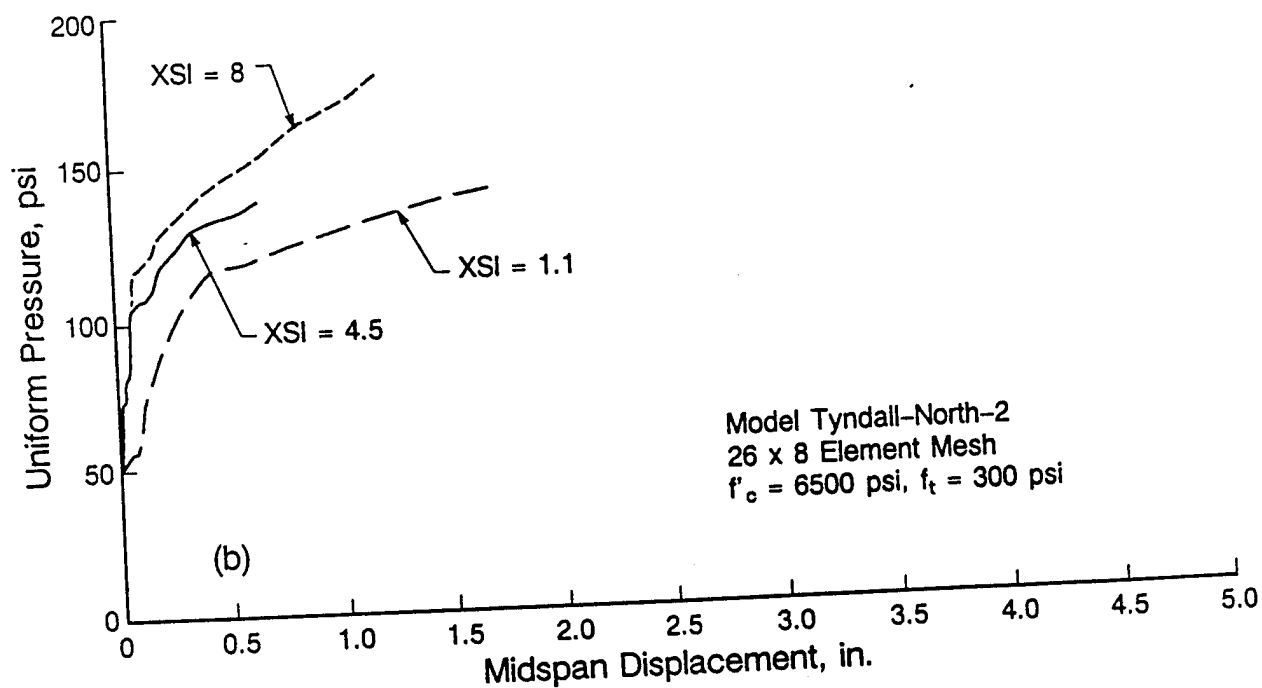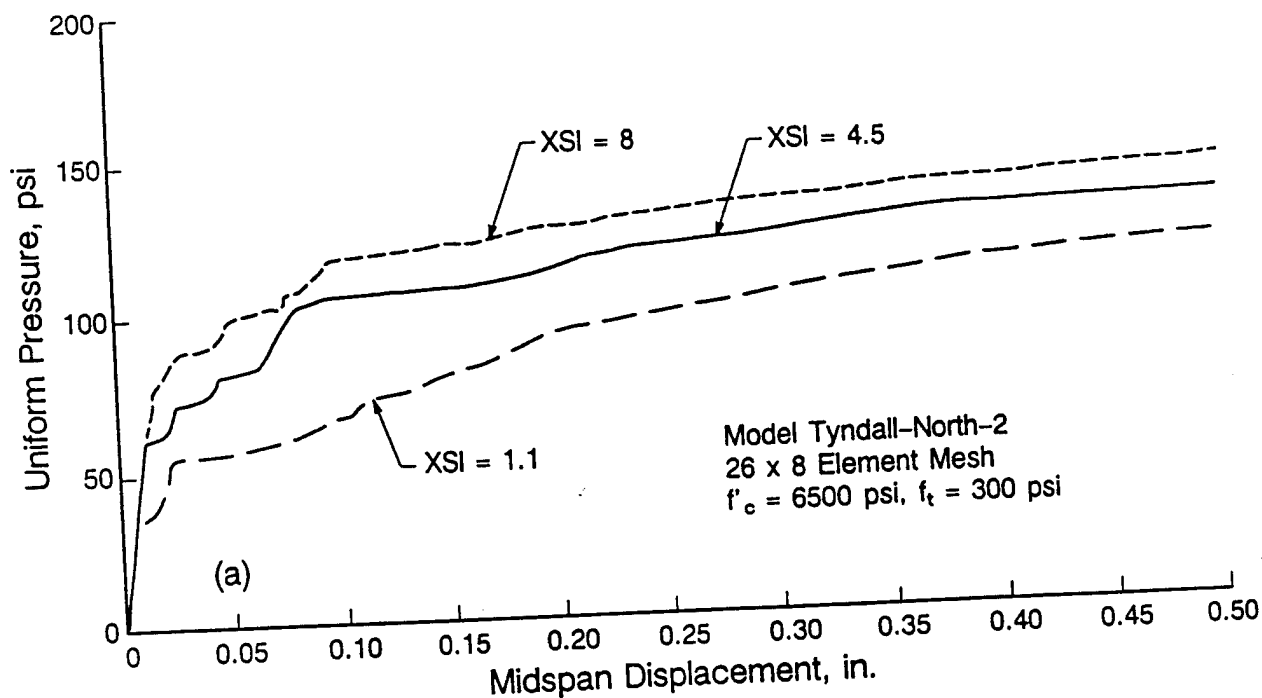
Figure 123. Effect of XSI on the Response of the 26x8 Element Tyndall North Wall Model with Static Loading.

179

that the moment-curvature function is not flat at the plastic hinges, and the resistance continues to increase.

Figure 124 shows the effect of XSI on the static load-deflection behavior for the 13x5 element model of the slab (Model: Tyndall-North-1). As before, increasing XSI has slowed crack propagation, thus increasing the effective cracking load, but not nearly as much as for the 26x8 element mesh shown in Figure 123. The larger XSI has increased the moment capacity as the crack continues to propagate, providing a moment after the reinforcement yields well above the value calculated using conventional hand calculations.

The influence of XSI is not the same for the two mesh configurations as shown further in Figure 125. At a value of XSI = 1.1 the curves are similar in shape, except that the pressure reached at larger deflections is somewhat higher for the finer 26x8 element mesh.

In general, the curves for the 13x5 element mesh fall below those for the 26x8 element mesh, with an equal XSI, and the curves for the smaller XSI fall below those for the larger XSI. The reason for this effect of XSI is shown by the cracking patterns in the 26x8 mesh model for solutions with XSI equal to 4.5 and 8.0 shown in Figure 126. These figures are drawn for the same load levels for the two models, 139 psi. The short parallel lines indicate cracking, and from the comparison, the regions at the inflection points that are not cracked are wider for the XSI = 8 case. That is, the larger XSI localized the cracking more at the midspan and ends while the smaller XSI diffused the cracking over a larger area, especially near midspan. The lower XSI causes a more rapid decrease in concrete tensile force capacity, which causes the reinforcement stress to be larger at a lower load, and the diffusion of cracking causes it to be spread over a longer length of the reinforcing bars, both of which result in a larger deflection at a given load level.

The discussion of XSI in Section VIII-B describes how this factor is used in the program, and the discussion above provides an indication of the effect that it has on the slab models. It is difficult to determine the proper value to use in a particular case, as it depends on the characteristics of the structure being studied as well as the mesh used in some cases, and perhaps on other factors. It appears that a larger XSI may be appropriate during the initial cracking stages of response to promote localization of cracking, but, after cracking has progressed through the beam a low value is appropriate to reduce the influence of tension stress across cracks that apparently causes the capacity to continue to increase after the reinforcement has yielded. A low value of XSI did not always cause the pressure-deflection curve to flatten after yielding of the reinforcement, so there are other factors that affect the resistance after yielding also.

4.   Effect of Element Mesh

The effect of mesh configuration was first investigated using static solutions with the Tyndall wall model with the 13x5 element mesh (Model: Tyndall-North-1) and with the 26x8 element mesh (Model: Tyndall-North-2). Dynamic
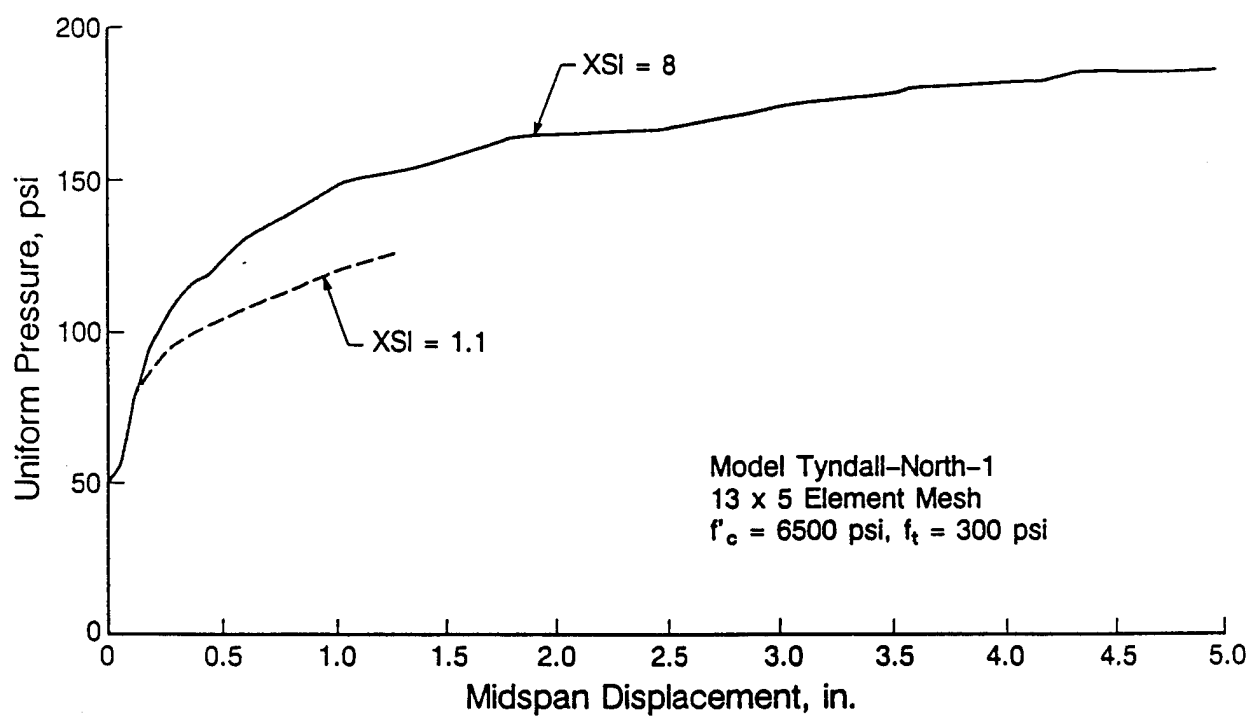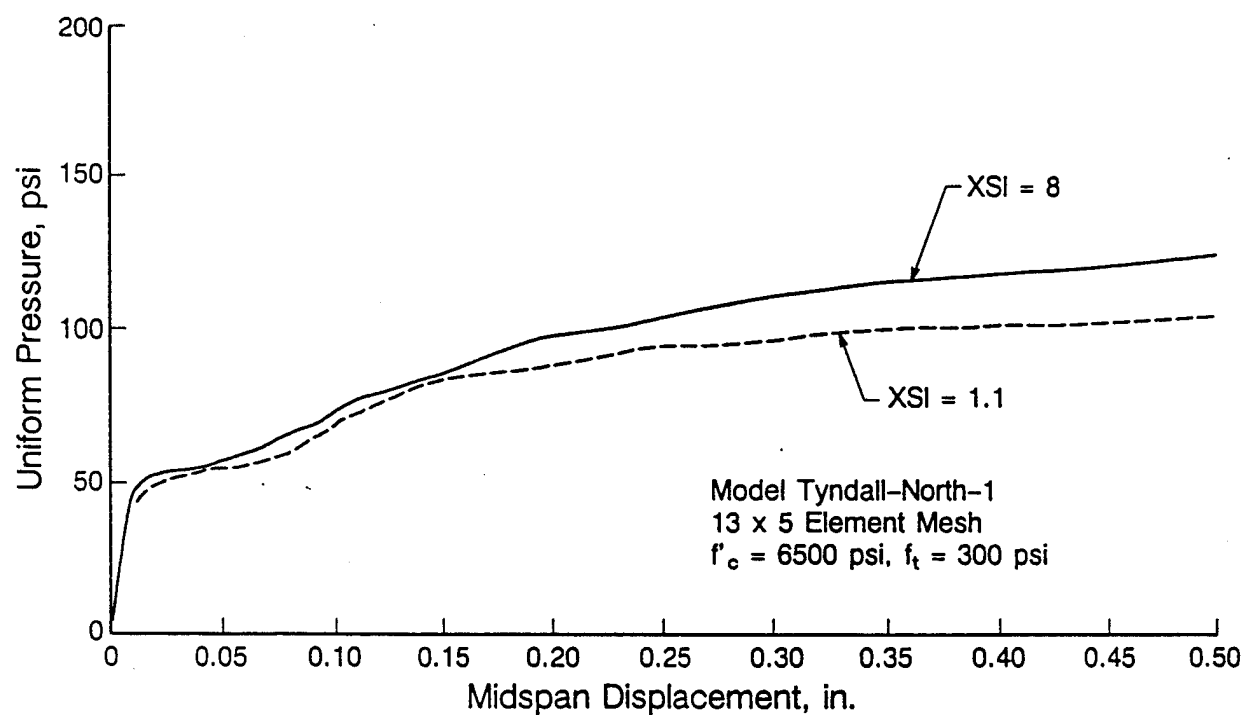
Figure 124. Effect of XSI of the Response of the 13x5 Element Tyndall North Wall
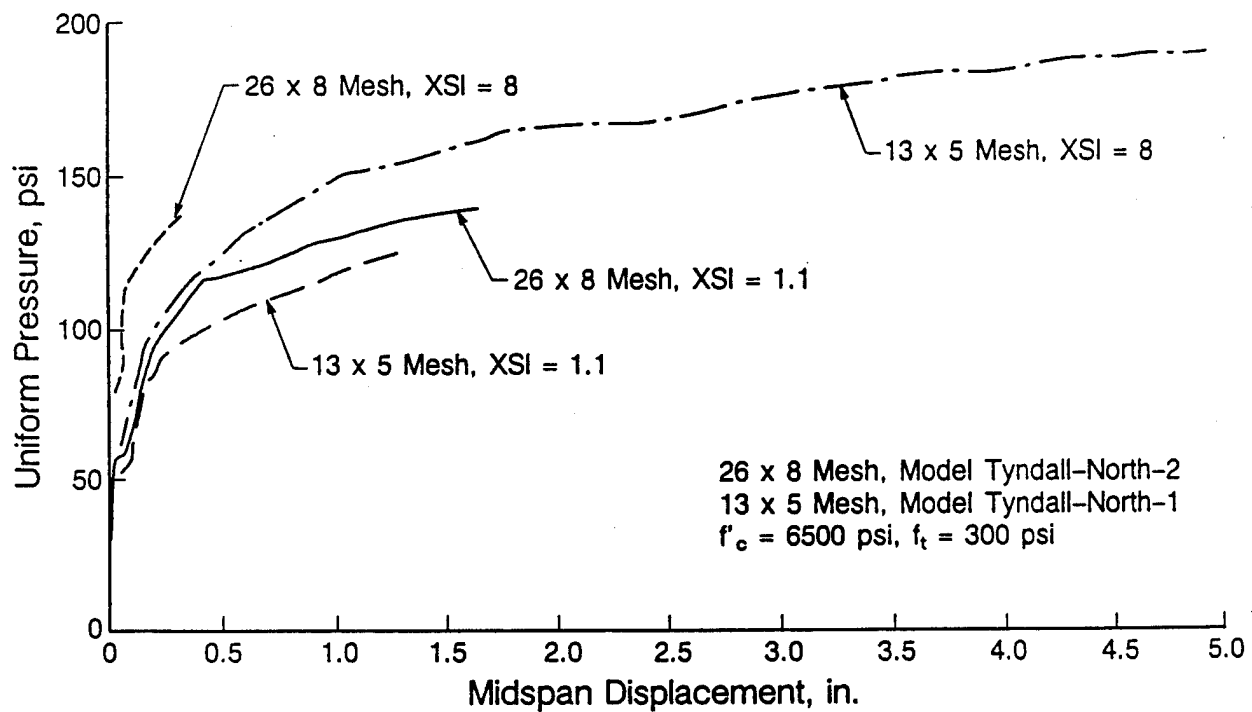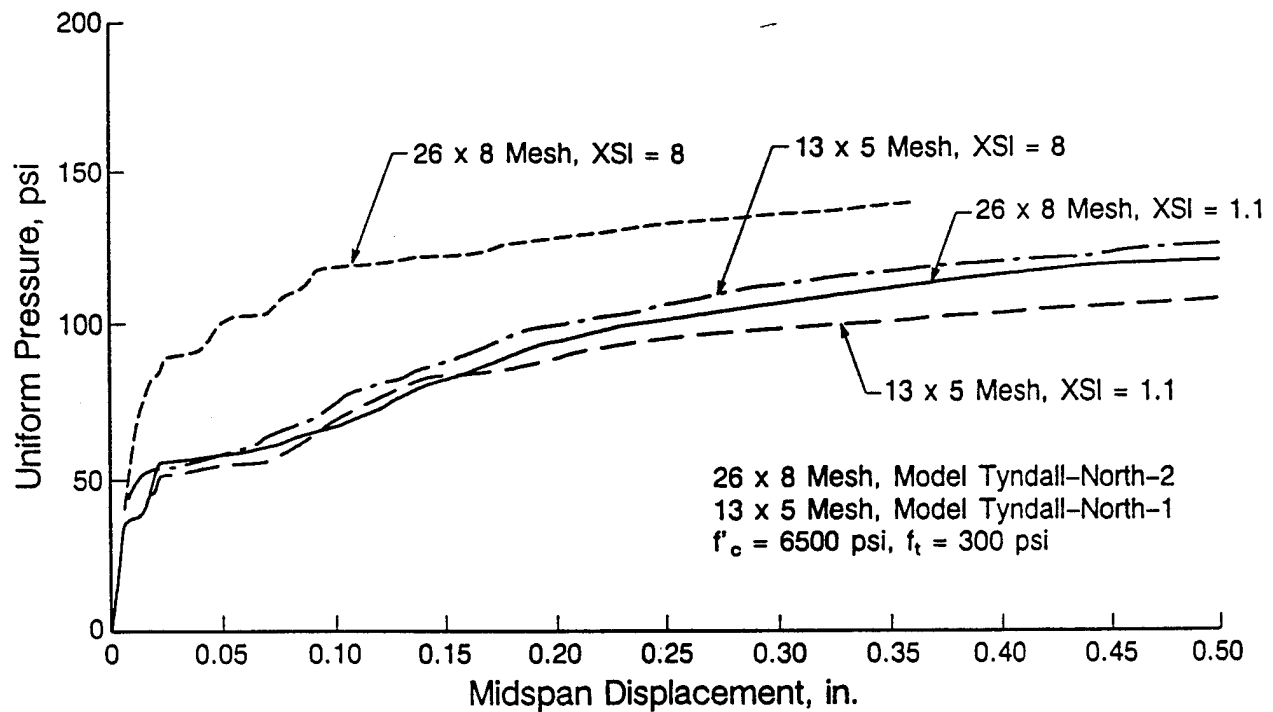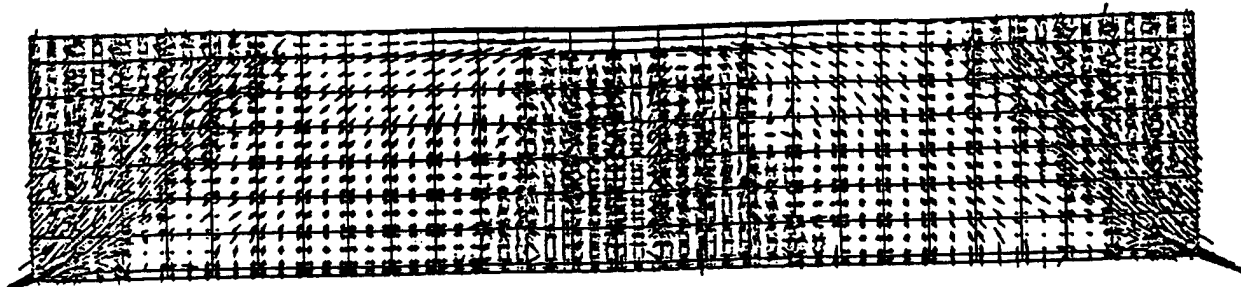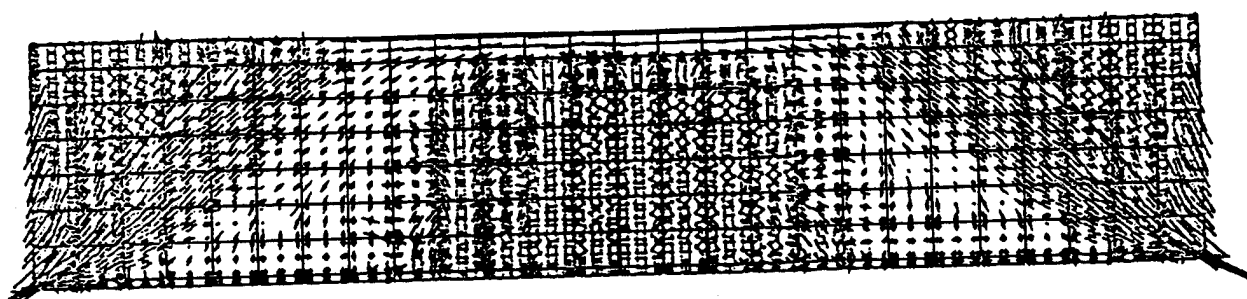Model with Static Loading.

181

Figure 125. Comparison of Effects of XSI on the 26x8 and 13x5 Element Tyndall North Wall Models.

(a) XSI = 8

26x8 Mesh, Model tyndall-North-2
$f'_c = 6500$ psi, $f_t = 600$ psi, pressure = 75 psi

(b) xsi = 4.5

Figure 126. Effect of XSI on the Crack Pattern for the 26x8 Element Tyndall North Wall Model.

solutions were also obtained with the IDF slab models with 20x6, 10x6, and 6x6 element meshes (Models: IDF-2D-20, IDF-2D-10, and IDF-2D-6) for comparison with this loading.

Figure 127 compares the load-deflection curves for the thicker Tyndall structure wall models with 13x5 and 26x8 element meshes and with XSI = 8.0. The initial stiffness of the two models is identical. The finer mesh provides a higher strength after the reinforcement yields, and the coarser mesh provides a sharper knee on the load-deflection curve. The reason for the sharper knee on the curve can be seen from the plot of stress in the longitudinal reinforcement shown in Figure 128. Yielding of the slab begins at a lower applied pressure, resulting in an increase in the reinforcement stress for the 26x8 element mesh model at this lower pressure. The initial yield point may be influenced by mesh size as follows: The coarser mesh results in locating the first numerical integration points found inside the reinforcement layer at a depth that results in lower tensile strains than for the corresponding points in the finer mesh example. Thus, the finer mesh induces first cracking somewhat earlier than the coarse mesh. Though the slab yields at a larger applied pressure for the 13x5 element mesh model, the increase to yield stress is more abrupt, so full yield
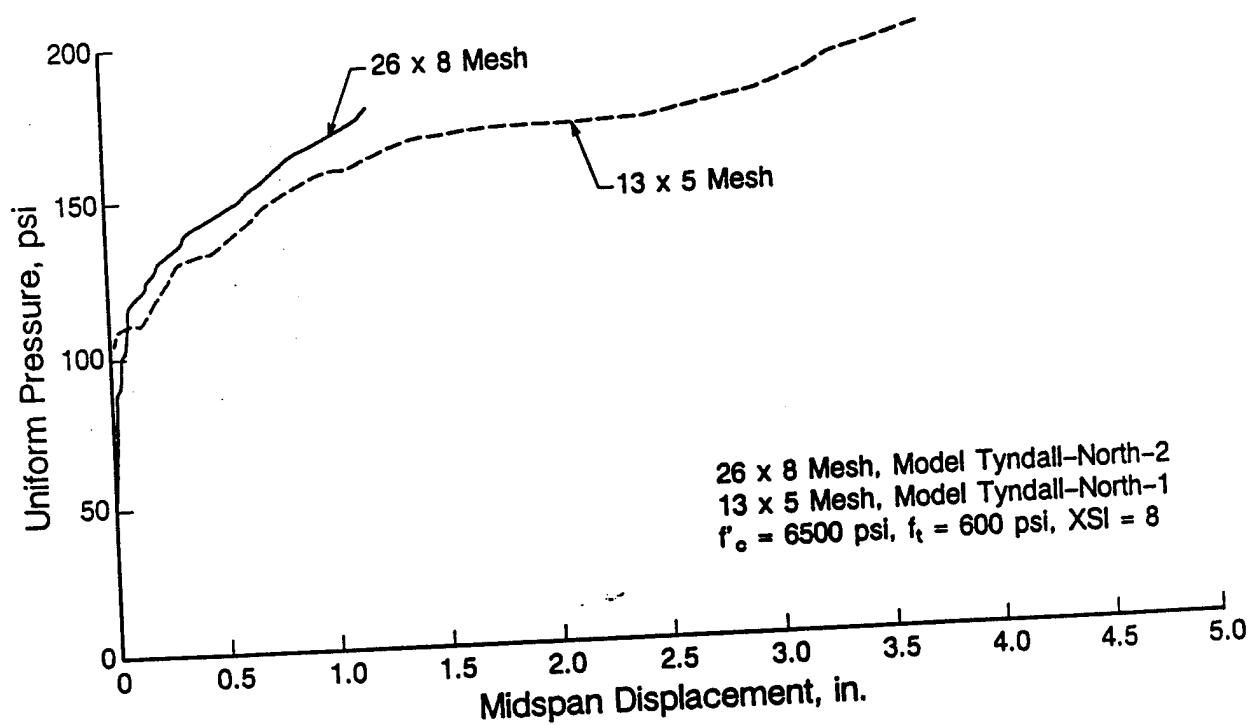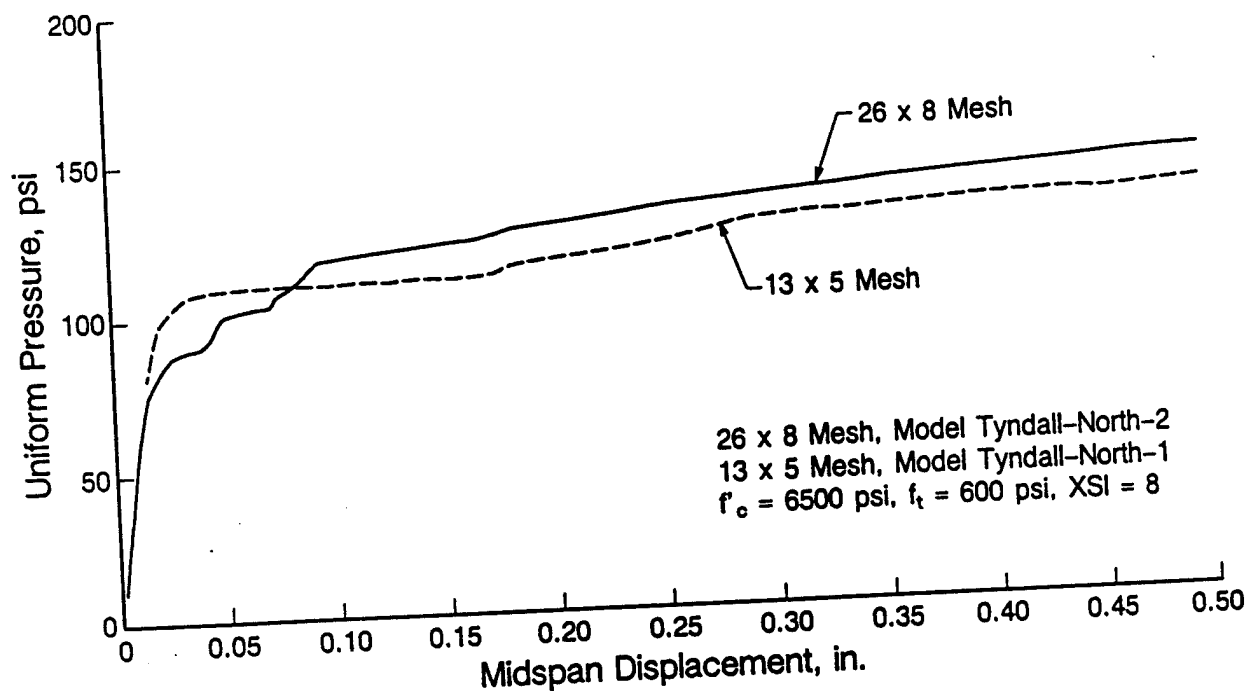
183

Figure 127. Comparison of Effect of Mesh (26x8, 13x5) With Two Values of XSI for the Tyndall North Wall Models.
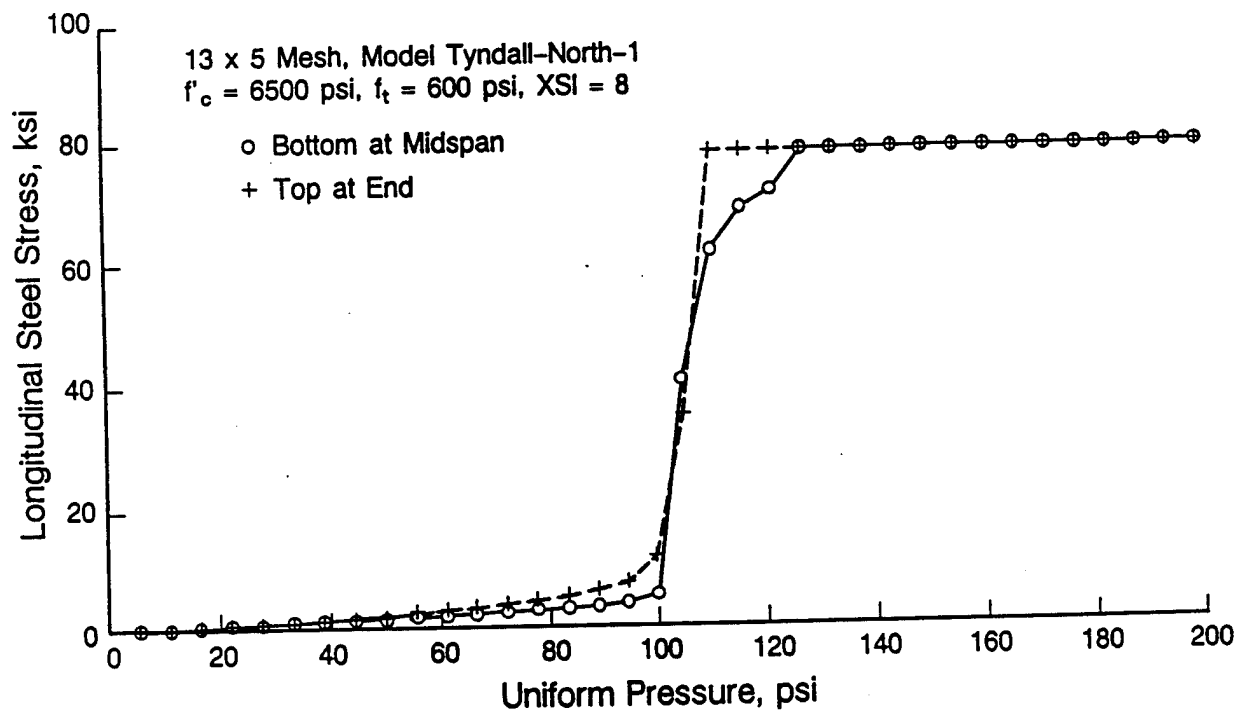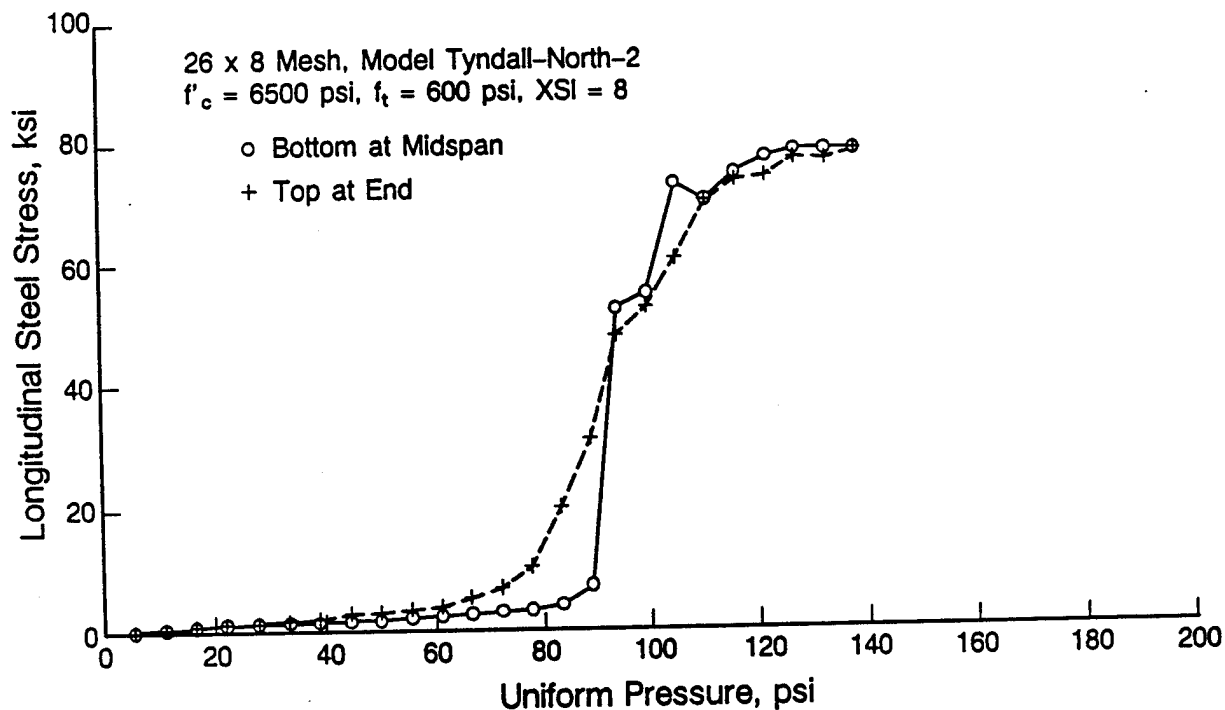
Figure 128. Effect of Mesh (26x8, 13x5) on the Reinforcement Stress for the Tyndall North Wall Model.

is reached at about the same pressure. Also, this abrupt transition to yield stress in the reinforcement causes the sharp knee of the load-deflection curve, because cracking and yield occur at essentially the same applied pressure.

A larger applied pressure at a given displacement after the reinforcement has yielded must result from larger moments at the midspan and ends of the one way slab in the 26x8 mesh model. This difference in yield strength at a given displacement can also be viewed as a difference in displacement at a given external pressure, in which case the 13x5 element mesh model deforms considerably more. Figure 129 shows the cracking pattern in the two models at 139 psi applied pressure. The regions that are cracked near midspan do not appear very different in the two cases, but at the ends near the top the cracked region is larger in the 13x5 element model, exposing a longer length of reinforcement to yield stress. This would lead to larger deflections at this pressure level for the 13x5 element model.

Dynamic solutions using the IDF slab models were obtained for three different meshes as well. In each case there were six elements through the depth with one element outside the reinforcement on each face and four elements between the layers of reinforcement. Longitudinally there were 6, 10, and 20 elements. The Test 4 transient Loading C was used.

The deflection-time curves for these three solutions are shown in Figure 130. There is an increase in maximum displacement as the mesh becomes finer; however, the difference is only 6 percent between the 10x6 element mesh and the 20x6 element mesh. This trend agrees with the general observation that, in finite element analysis, the coarser mesh is stiffer. It is reasonable to assume that there would be less change for grids finer than the 20x6 mesh, and that the optimum lies somewhere between the 10x6 and 20x6 meshes, and depends on the criteria used.

These solutions resulted in rather small deflections, from 0.4 to 0.5 inch However, from observing the reinforcement stress-time plots, the reinforcement has yielded at a deflection slightly over 0.1 in. This comparison includes behavior in the plastic range, but does not include large deflections.

In this comparison of the effects of mesh the finer mesh size sustained the largest maximum dynamic deformation. The previous comparison with static loading showed that the finer mesh had a larger resistance after yielding; with a larger resistance it might be expected that a smaller maximum dynamic deflection would occur, but this was not the case. There are other differences between the static and dynamic models in this comparison. The value of XSI was the same, but the static model grid varied in both directions (depth and length) while the dynamic model grid varied only in the longitudinal direction, the concrete tensile strengths were different, and the aspect ratio of the elements were different. Thus, conclusions about the effect of grid on the static vs. dynamic behavior cannot be drawn from this comparison.

Not surprisingly these studies show that the mesh used can have a major effect on the results obtained from the finite element analysis, and therefore, the mesh should be optimized for the particular problem. It is known that a
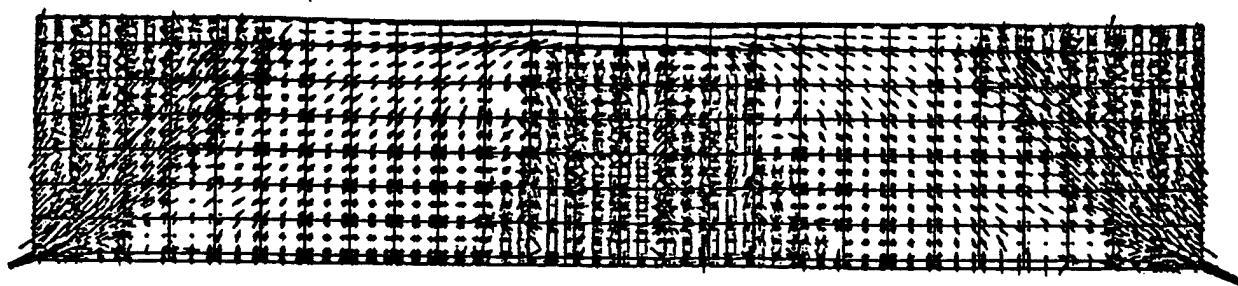
(a) 26x8 Mesh, Model Tyndall-North-2

$$f'_c = 6500 \text{ psi}, \quad f_t = 600 \text{ psi}, \quad XSI = 8$$

(b) 13x5 Mesh, Model Tyndall-North-1

Figure 129. Effect of Mesh (28x6, 13x5) on the Crack Pattern for the Tyndall North Wall Model.

finer mesh generally provides more accurate results. On the other hand computer running time increases drastically with the number of elements, so a careful balance of running time and accuracy required must be reached.

5.   Effect of In-Plane Support Stiffness

Walls must be attached to other parts of a structure at their edges for support; the adjoining structural elements will generally provide some resistance to movement in the direction of the plane of the wall as well as perpendicular to the wall. The in-plane resistance in both the IDF and Tyndall test structures is provided by the roof slabs of the structures at the top edge and by side walls at the ends. The bottom of the IDF wall was attached to shallow footings and the Tyndall wall was integral with a basement wall and floor slab at the bottom. In-plane resistance at the top edge results from bending of the roof slab in the direction parallel to the wall and perpendicular to it and therefore varies along the top edge of the wall. In addition to varying along the edge of the wall, the resistance would be difficult to estimate because there is also the inertia of the roof slab that causes resistance to movement that is not included in the
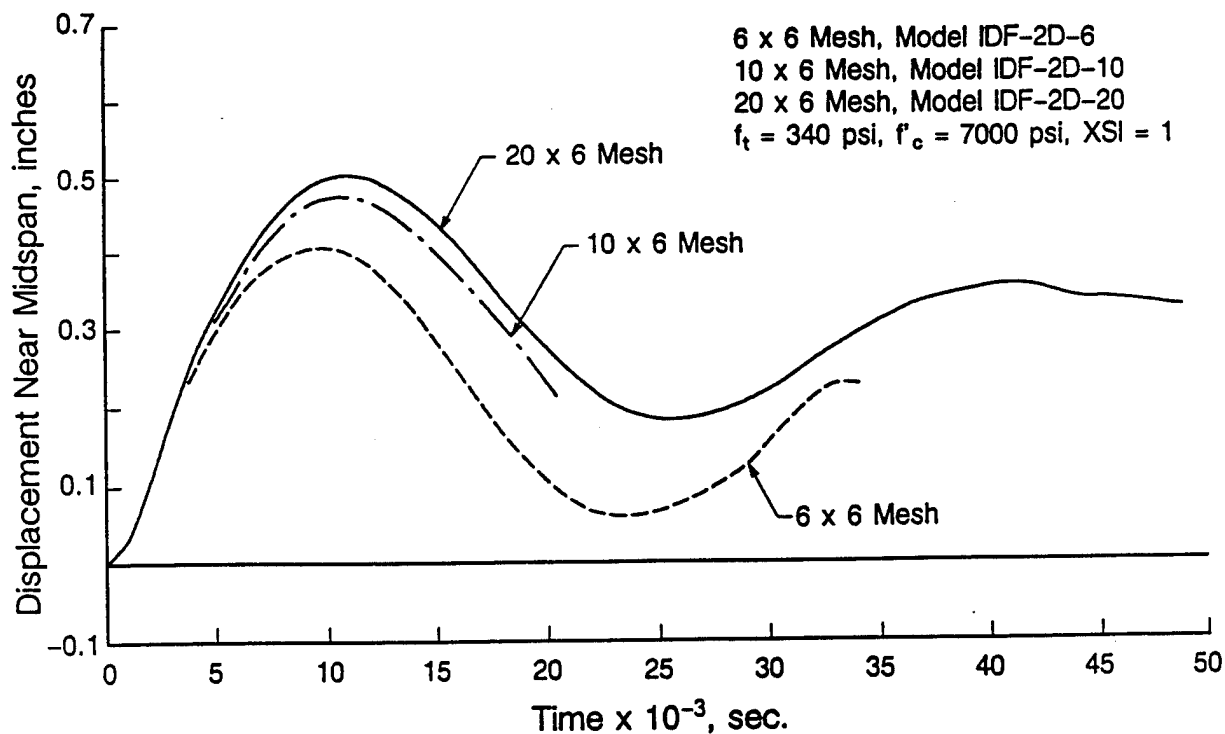
187

Figure 130. Effect of Mesh (6x6, 10x6, 20x6) on Response of the IDF Models With Transient Loading.

model. After the pressure wave reaches the roof slab it applies a downward pressure, causing an in-plane compression in the wall as well.

A series of problems using the Tyndall wall one-way model (Model: Tyndall-North-1) was performed to study the effect of the in-plane stiffness of the edge supports on the overall static response and to provide some means of validating the in-plane force modeling in SASDE. The finite element model of the one-way slab is for 1.0 inch of slab width. Approximate calculations of in-plane stiffness provided by the supports vary from one to 5 kips/in./in. of width, depending on the assumptions made. Attachment to the lower floor and basement wall at the bottom and to the roof slab at the top provides considerable resistance to rotation at these edges, and therefore they were assumed fixed against rotation. Linear springs were placed at each end of the beam at the nodes to which the inside face primary reinforcement was attached; fixity against rotation was obtained by rigidly linking the nodes at the ends so they would move in the in-plane direction the same as these end nodes.

Figure 131 shows the static analysis pressure-displacement curves for the Tyndall structure thick wall model for spring stiffnesses of 0.0, 1.7, and 5.1 kips/in.; these curves show no effect of the springs through the linear portion of the response and well into the yield portion. Only beyond about 0.5 inch deflection does the resistance begin to increase, though it appears that the effect could become significant at large displacements. There is one problem
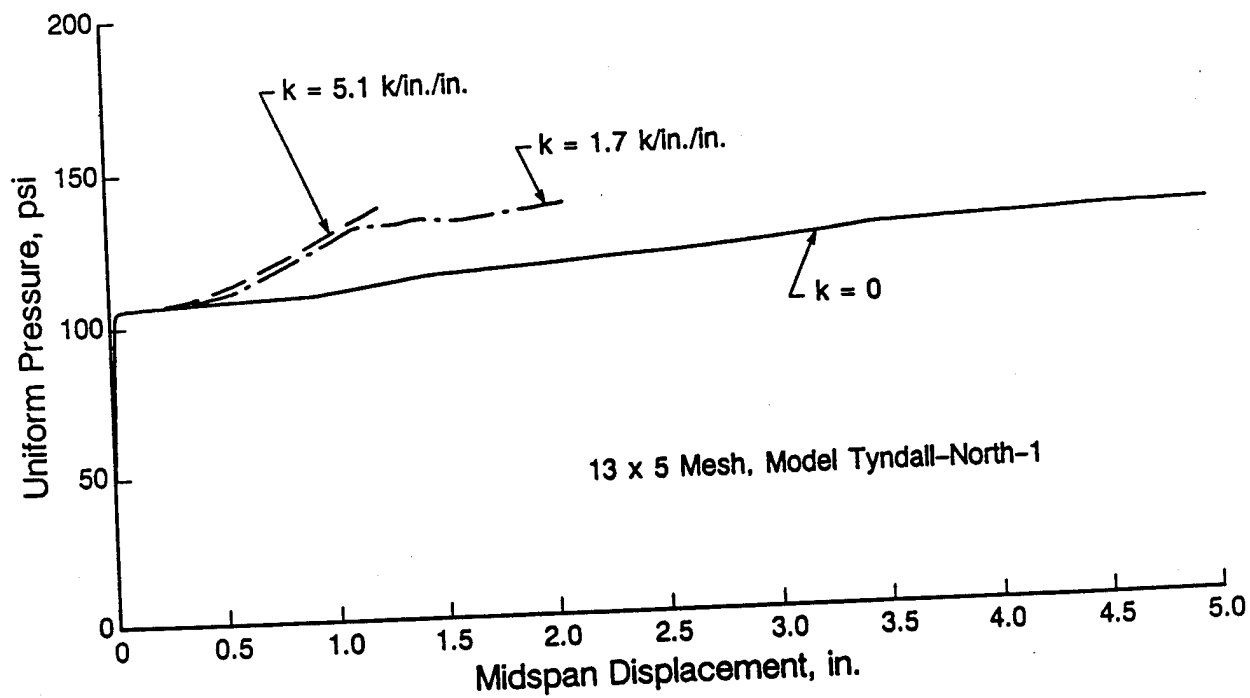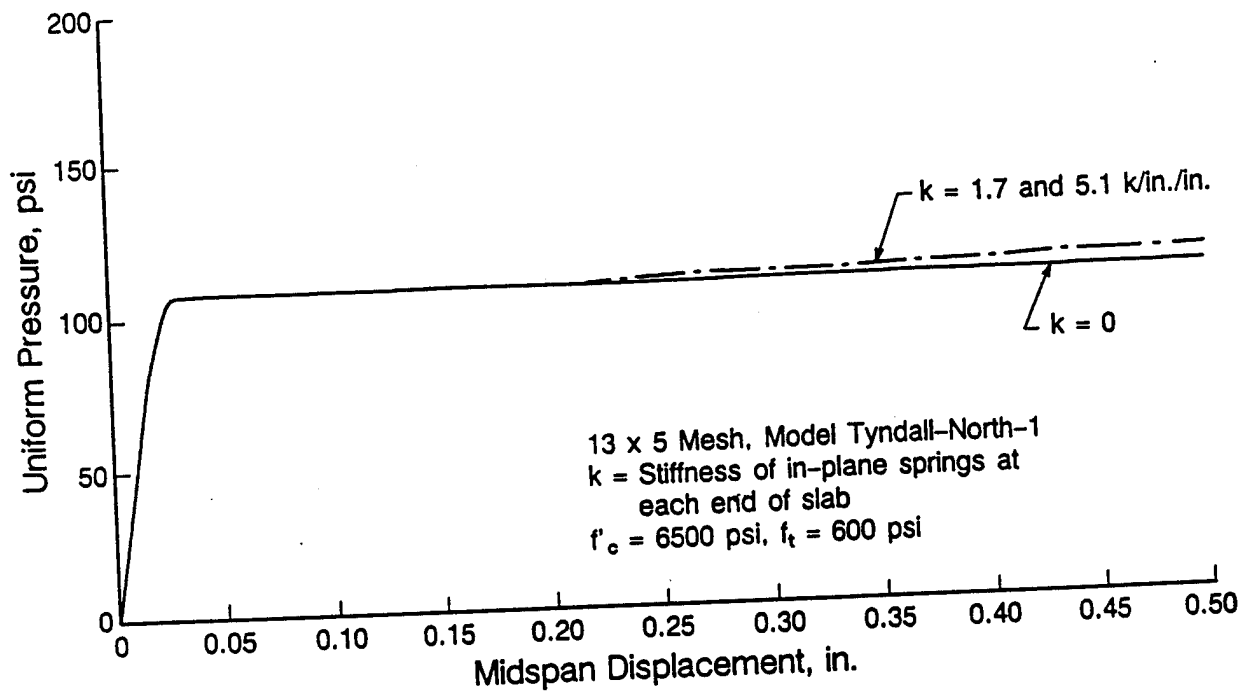
Figure 131. Effect of In-Plane Support Stiffness on Static Response of the Tyndall North Wall Model.

189

with this conclusion, however. The springs are linear and the load in them can continue to increase; in reality the in-plane resistance due to the roof slab flexure would have a plateau due to yielding of the reinforcement in it as well, and so there would be a limit to the in-plane resisting force. Also, the pressure wave reached the roof in about 2 ms, and the deflection is less than 0.5 inch at this time. Therefore, during the time when the in-plane stiffness can be modeled with a spring, the influence of the spring is very small. Beyond this time, when the pressure is applied to the roof, the in-plane force should be modeled with a time dependent force from pressure on the roof and a constant force due to flexure of the roof slab that has yielded.

The effect of in-plane forces on the slab shown in Figure 131 can be explained by observing the in-plane displacement of the ends of the slab. There is no significant movement outward of the ends of the slab until the reinforcement yields in tension. When this occurs, the slab elongates by allowing the ends to move outward. At this point in the response, there is a considerable amount of tension cracking, and a significant amount of arch action develops in the slab with the inside (bottom) reinforcement acting as the tie. The in-plane spring provides additional force to help the reinforcement supply the tie force to the arch. Measured displacements in the Tyndall structure tests were 1.9 to 2.5 inches, so the in-plane resistance could become a significant factor in the response.

6.   Effect of Concrete Compression Curve Parameters

The uniaxial unconfined stress-strain curve for the concrete in compression is defined by several ADINA input parameters. Some of the parameters were varied to determine their overall effect on the dynamic displacement-time response of the IDF slab model with the 10x6 element mesh (Model: IDF-2D-10).

Figure 132 shows two curves in which the first solution was obtained with a compressive strength of 7000 psi and the second used an increased strength of 9000 psi. The same strains at peak stress and ultimate stress, 0.0035 and 0.0075, were used in both. The former problem ran to 50 ms while the latter did not. The larger compressive strength decreased the peak deflection slightly at 10 ms, and decreased the recovery displacement at about 23 ms by a slightly larger amount. The result of this effect would be a slight decrease in the peak response and a very small increase in the residual deflection after the slab has come to rest.

Figure 132 also shows two curves in which the same compressive strength of 7000 psi is used but the strains at peak and ultimate stresses are different while the initial modulus remained the same. If the curve with strains of 0.002 and 0.0045 is considered the base for comparison, then increasing these strains increased the peak deflection at 10 ms, and increased very slightly the recovery at 23 ms. The effect on the peak deflection was the same amount as increasing the compressive strength from 7000 to 9000 psi.

The compressive stress-strain curve parameters have an effect on the peak displacement, but it is not as large as some of the other parameters
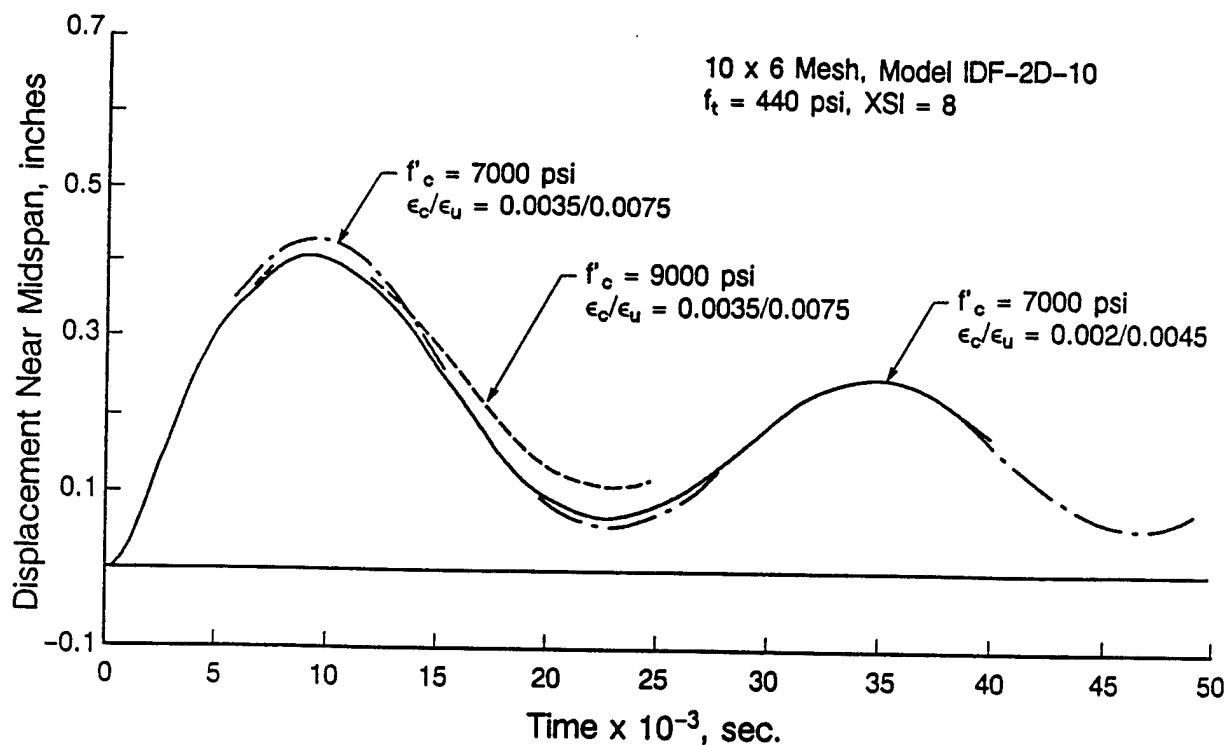
Figure 132. Effect of Compression Curve Parameters on Static Response of the 10x6 Element IDF Model.

investigated. There is some evidence from dynamic material testing that the peak compressive strength and the ultimate strength occur at larger strains under dynamic loading than they do in conventional static tests. For this reason most of the studies with the concrete model in ADINA were carried out with the 0.0045 and 0.0075 values of strain discussed above. Also, the expected static concrete compressive strength was increased by 30 percent to account for the dynamic strain rate effects.

7. Effect of Diagonal End Bars

In the Tyndall structure walls a diagonal reinforcing bar was used to link the outside main reinforcing bars with the supporting roof and floor slabs as shown in Figures 112-114. These bars at the ends of the 13x5 element mesh one-way slab model of the thicker Tyndall wall (Model: Tyndall-North-1) were removed to determine the effect on response with the static loading. The pressure-deflection curves with and without the diagonal bars are compared in Figure 133, where the response is essentially identical to a deflection of about 0.25 inch. Beyond this point in the response, the deflection is larger when the diagonal bars are not present, but the difference is not large within the limits of the data.

The stresses in the diagonal bars are shown in Figure 134 and explain the reason for this behavior. There is essentially no stress in the diagonal bars

191

until the applied pressure reaches 100 psi (Figure 134(b)), and then they start to pick up tensile stress. The stress in the longitudinal bars is shown in Figure 134(a), and indicates that the diagonal bars start to pick up stress when the longitudinal bars become plastic, which is when they begin to elongate significantly.

The deformed shape in Figure 135 helps explain why the diagonal bars are not stressed immediately and why they go into tension. This shape occurred when the response was well into the yield range. The lower attachment point is at the end of the longitudinal reinforcement and moves outward (longitudinally) in the figure while the top attachment point moves downward in the figure. Apparently the movements are the same so there is no change in length of the bar until the inside longitudinal reinforcement starts to yield; when yielding begins, the bottom attachment point moves outward more than the top point moves down, resulting in an elongation of the diagonal bar.

The end conditions in the model represent an ideal rotation free support that can move outward freely. The actual condition in the structure allows some rotation, that would change the diagonal bar force. However, these solutions indicate that the bars may not be stressed as expected and that the behavior can be simulated with the finite element model. It would be possible to extend the model to include part of the roof slab and floor so that the end conditions are more accurately simulated. This comparison was not extended to the dynamic
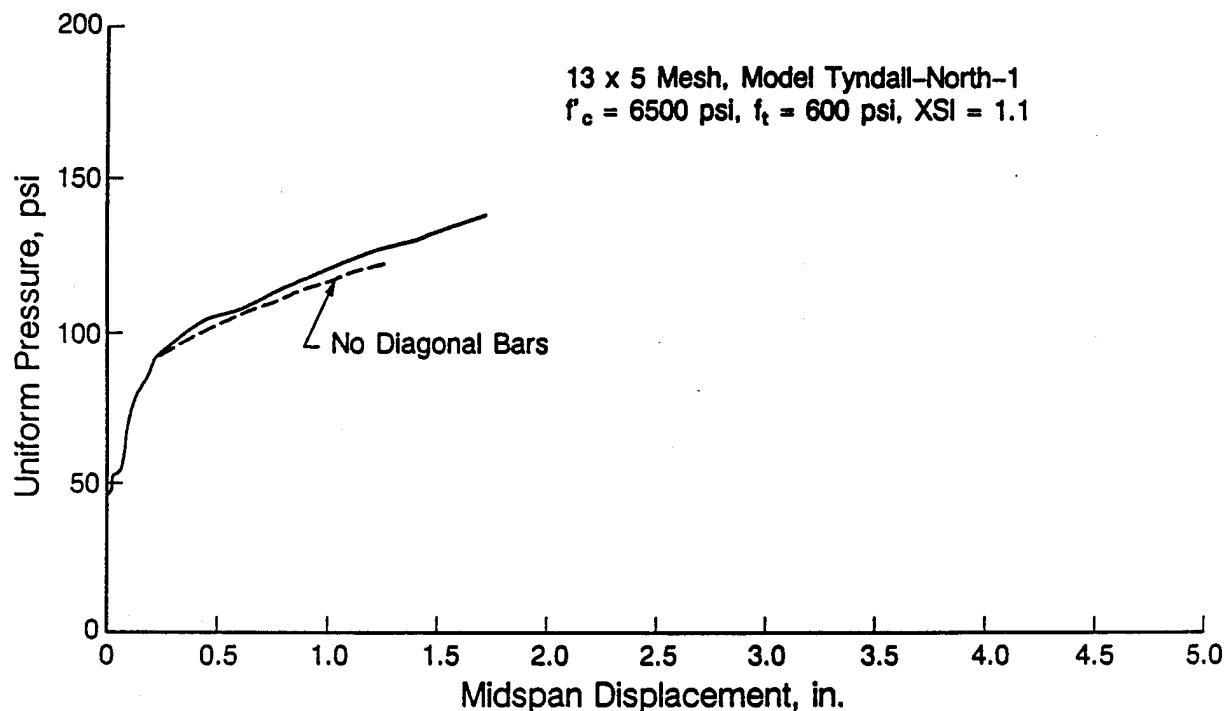

Figure 133. Effect of Diagonal End Bars on Response of the 13x5 Element Tyndall North Wall Model.
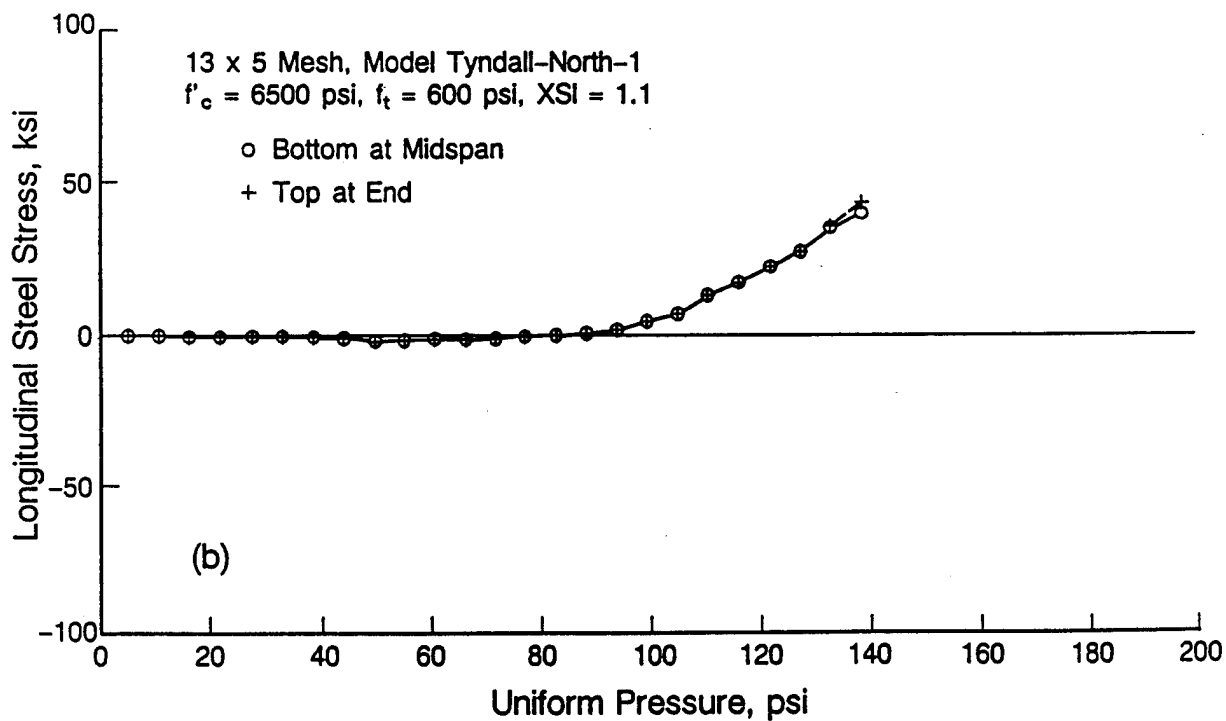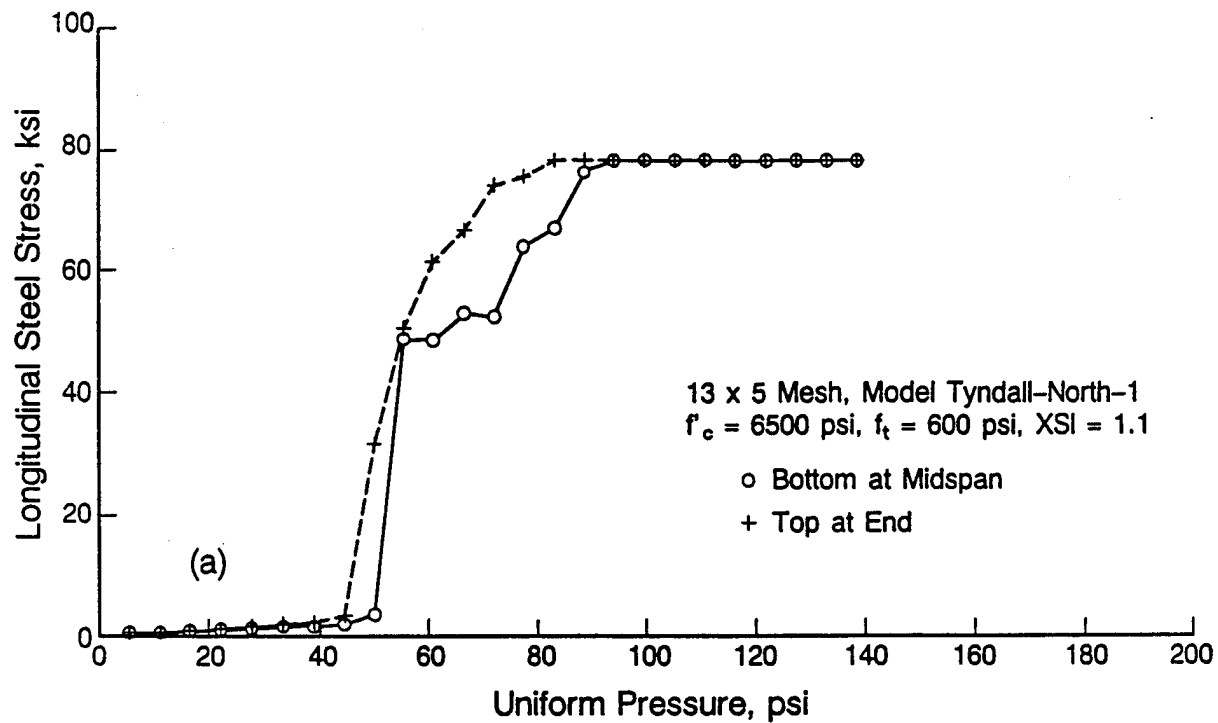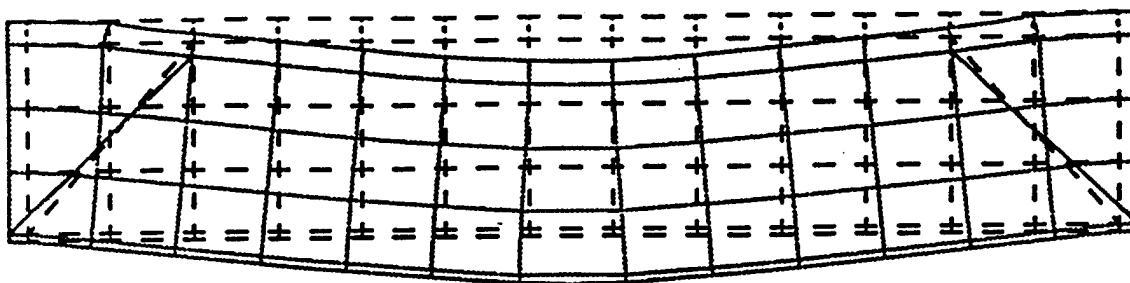
192

Figure 134. Reinforcing Bar Stresses for the 13x5 Element Tyndall North Wall Model With Diagonal End Bars.

193

13x5 Mesh, Model Tyndall-Northe-1
$f'_c = 6500$ psi, $f^t = 600$ psi, XSI = 1.1

Figure 135. Deformed Shape of the Tyndall North Wall Model With Diagonal Bars and Static Loading.

analysis.   The dynamic response has more initial shear at the ends so the diagonal bar stress may be quite different.

8.   Two Dimensional vs Three Dimensional Elements

If a three dimensional model of the wall is to be used in an analysis, three dimensional finite elements must be used.   The question then arises concerning possible differences in behavior of the three and two dimensional elements in the models under consideration.   These differences might arise in initial stiffness, in the interaction of the concrete material model with the elements, and in boundary condition effects.

The two element types were compared with two static solutions of the one way slab representation of the IDF wall using the two dimensional elements (Model: IDF-2D-10) and the three dimensional elements (Model: IDF-3D-1W).   The 2D element model is a 10x6 grid with 20 node elements.   Between reinforcing bars through the thickness there are two elements in the 3D element model and four elements in the 2D element model.   Thus the grids are not the same for the two element types.   The 3D elements were restrained by the boundary conditions to a plane strain condition normal to the plane of bending, and the 2D element model was specified as a plane strain problem.

Figure 136 compares the pressure-displacement curves for the two solutions, and shows that they are comparable up to a displacement of 0.20 inch though the linear stiffness of the 3D model is slightly larger.   However, between a displacement of 0.2 and 0.3 inch the 3D model suddenly increased its resistance and then abruptly locked up.   This comparison indicates that the material model may be more sensitive when the 3D element model is used, and it may be necessary to use a smaller pressure increment in static analyses or a smaller time step in dynamic analyses.

A yield pressure of 36 psi is obtained from Figure 136 for the IDF wall and a yield displacement of about 0.05 inch.   In Section IV-B-1-a the yield pressure and yield displacement calculated with procedures recommended by the design

194

manuals were 33.3 psi and 0.15 inch, respectively. Though the yield pressures compare well, the maximum displacements are different by a factor of three.

A three dimensional element model of one-half of the entire wall was also developed in an attempt to model two-way behavior in the structure. A single static analysis consumed over 20 hours of cray CPU time and indicated that both stiffness and strength parameters were noticeably higher than in the one-way analyses.

9.   Comparison With Test Data

One objective of the examination of the test data and various programs was to see if the programs would provide a reasonable prediction of the actual behavior. Previous discussion of the test data has cast some uncertainty on the pressures measured and on the response measurements consisting of the integrated accelerations and the residual deformations. Also, the discussion in previous sections indicate that there are uncertain parameters within the program that can affect the results. However, a prediction of response was run for the IDF Tests 1-4 and for the two Tyndall structure walls using the best estimates of the input quantities.

The IDF test predictions were run using the one way slab model 10x6 element mesh (Model: IDF-2D-10) and the pressures measured at midheight and reported in Section II-D-2. The theoretical distribution of peak pressure over the height
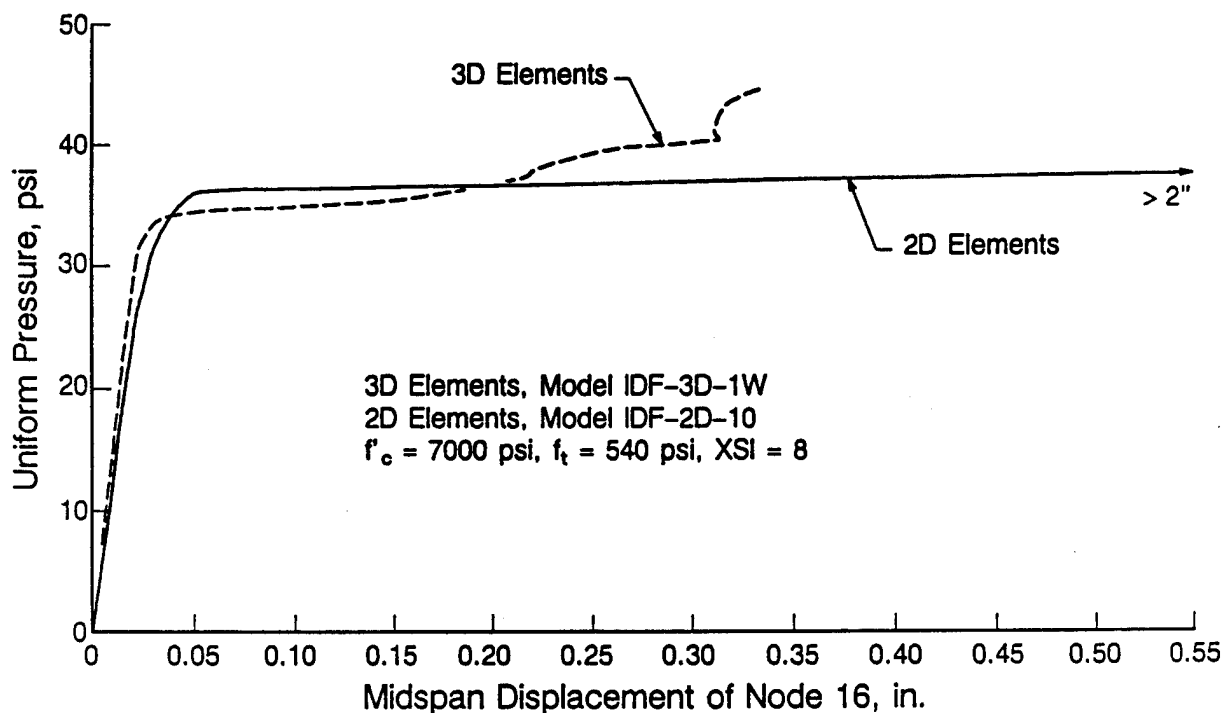

Figure 136. Comparison of Static Response of the IDF One-Way Wall Models With 2D and 3D Elements.

195

of the wall was calculated and scaled to match this central pressure (Appendix B). The theoretical arrival times for each element were then assigned to the pressure on each element to provide the transient nature of the loading. The tensile strength of the concrete was arbitrarily reduced for successive tests to account for cracking from previous loadings.

Displacement-time curves for each of the IDF Tests 1-4 are shown in Figure 137; each solution was obtained without initial displacements. If it is assumed that the residual displacements can be summed, as shown in the third column of the summary in Figure 137, then these residuals can be compared with the measured values in the fourth column of the summary. The resulting residual displacements compare quite well.

The Tyndall structure wall slabs were treated in a manner similar to that described above for the IDF walls, but the maximum dynamic displacements will be compared because this information is available for the tests from scratch gages. One-way slab models with the 13x5 element mesh were used for the two slabs (Models: Tyndall-South and Tyndall-North-1). The enhanced pressure function (Loading C) described in Figure 115 was applied to both of the wall models.

To get the thick wall model (north wall) to run, it was necessary to increase the factor SHEFAC in the material model; it defines the shear stiffness of a cracked element. The default value is 0.5 and it was increased to 0.85. Also the compressive strength of the concrete was increased to 14.0 ksi. The loading was treated in two different ways for this solution. In one case the pressure-time curves applied to each element were given the exponential decay calculated with the program WALLPLOT. In the other case the pressure-time function was linear from the peak reflected pressure to zero with the duration calculated so the impulse under the curve was the same. The resulting deflection-time curves are shown in Figure 138.

The curve calculated with the linear pressure-time functions gave a larger deflection as shown in Figure 138. It is speculated that this occurred because the linear pressure-time curves apply more impulse to the wall at an earlier time. The reason for this is that the exponential pulse duration for the high peak pressure curves at the bottom of the wall was 4.5 ms and is very steep, and for the linear functions it was only about 0.75 ms. The transit time across the wall is only about 2 ms.

Using the same pressure-time functions for the thin wall (south wall) model, it was not possible to obtain a solution, even with the increased shear factor, compressive strength, and a few other modifications that were tried. The solution only ran to 1.5 ms, at which time it stopped. Many reinforcing bars had yielded at the fixed ends and at the center. There were many elements in the high compression stress regions that indicated crushing and most of the rest of them had tension cracking. At the end of the solution the maximum deflection was 0.24 inch but there had not been sufficient time for a flexural response of this magnitude. However, this deflection is about 8 times the yield deflection of the static load deflection curve, which is shown in Figure 131 to be about 0.03 inch.

10 x 6 Mesh, Model IDF-2D-10
f'_c = 7000 psi
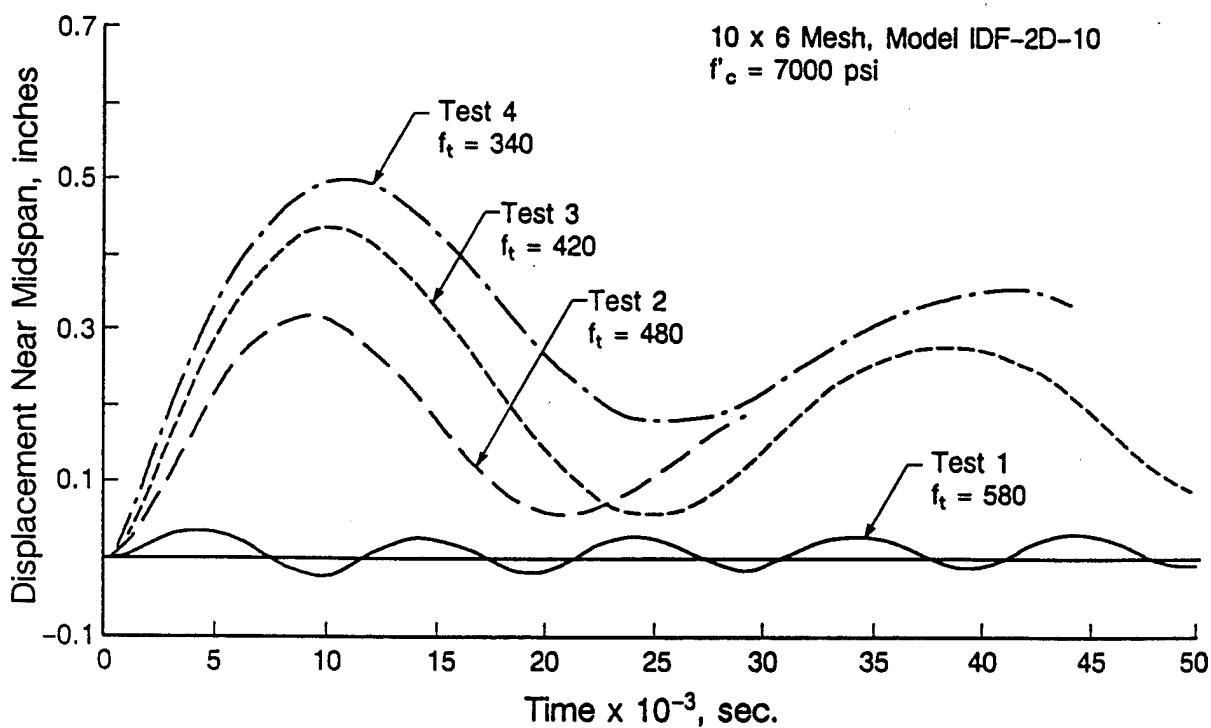
Test	Calculated Residual Displ., in.	Summation of Calc.Resid. Displ., in.	Measured Residual Displ., in.	f_t, psi	Peak Pressure Midht. psi
1	0	0	0	580	34
2	0.13(est)	0.13	0.2	480	142
3	0.16	0.29	0.3	420	288
4	0.26	0.55	0.6	340	443

Figure 137. Comparison of IDF Tests 1-4 ADINA Predictions With Measured Residual Displacements.

A solution for a longer time was possible for the thin (south) wall model when in-plane springs with k = 1.7 k/in./in. were added to the model as described in Section VIII-C-5. The resulting curve is shown in Figure 138, and the effect of adding these springs on the static pressure-deflection curve is shown in Figure 131. Adding the springs increased the resistance. They have the effect of increasing the effective amount of reinforcement, and therefore reducing the dynamic peak deflection.
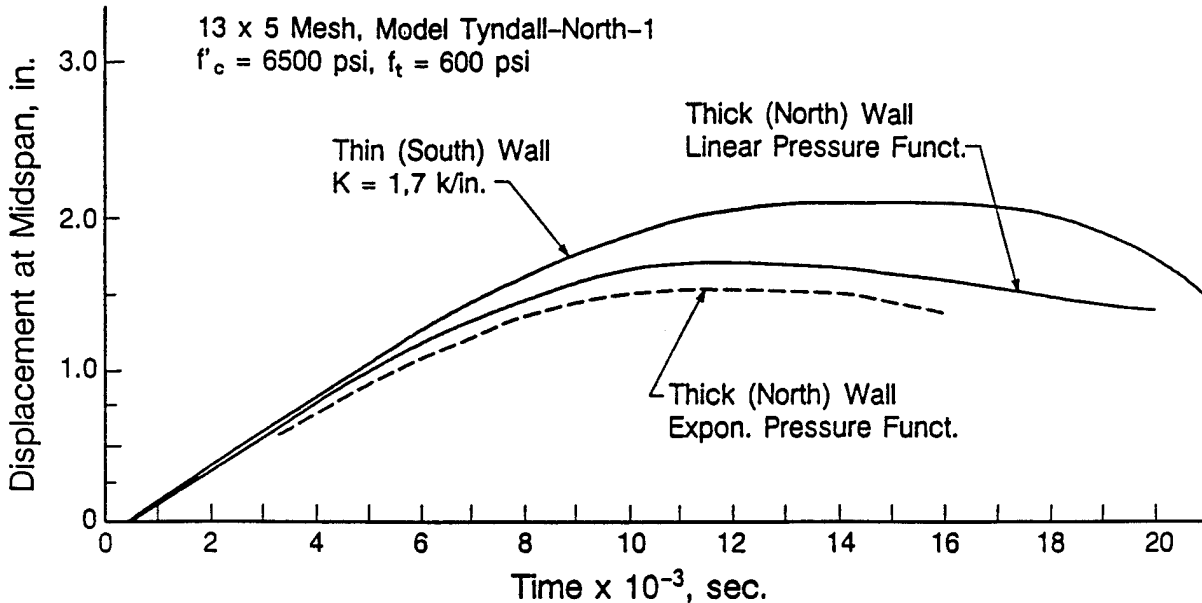
Figure 138. Comparison of Tyndall Tests ADINA Predictions With Measured Peak Dynamic Displacements.

The thin (south) wall experienced about 2.5 inches of deflection and considerable flexural cracking and interior spalling. It is not clear whether the extent of damage to the wall from this particular loading can be predicted from the original finite element solution that did not run past 1.5 ms; the solution results would clearly indicate some kind of failure. On the other hand, the actual structure would be considered failed only for certain types of applications. It cracked extensively, but it did not breech and let gasses pass through it. The final deflection could not be predicted because the material model would not let the solution continue. The computer solution may, therefore, have predicted more concrete damage than actually occurred, though other interpretations are certainly possible.

The peak measured dynamic deflections for the thin and thick walls were approximately 2.5 inches and 1.7-1.9 inches, respectively. These maximum deflections were obtained from scratch gages. The calculated values were about 2.1 inches (with in-plane springs) for the thin wall and 1.5 inches for the thick wall (using the more realistic exponential pressure-time loading curves). In view of the uncertainties, these are reasonable agreements, but they are not better than those obtained by some of the SDOF programs. Thus, if the deflection response is all that is needed to predict adequacy of the design, then the SDOF program requires a lot less work. However, there is the potential for gaining a lot of additional information from the finite element solution if it is needed. This includes information about the concrete and reinforcement stresses as well

198

as more detailed information about the effect of the transient application of the pressure. In this study, stresses were not analyzed in-depth, because there was no actual test data on material strains to use for comparison. It is important to note that accurate stress histories are more difficult to obtain with finite element calculations than are displacement histories.

SECTION IX
SUMMARY AND CONCLUSIONS

A.   INTRODUCTION

As stated in Section I, the primary objectives of this study are:

(1)   To evaluate the data taken in the IDF field tests.

(2)   To use the IDF test data and data taken in similar tests at Tyndall Air Force Base to evaluate the applicability of several currently available SDOF microcomputer programs to the analysis of the response of structural elements to the blast pressure effects of conventional HE weapons.

(3)   To use the IDF and Tyndall test data to assess the applicability of a comprehensive finite element computer program to the analysis of the response of structural elements to the blast pressure effects of conventional HE weapons.

The extent to which each of these objectives has been achieved is summarized briefly in the following paragraphs.

B.   EVALUATION OF IDF TEST DATA

Although two structures were tested in the IDF program, detailed loading and response measurements were taken on only Structure 1 which was subjected to the effects of bare HE charges. For Structure 2, which was subjected to the blast effects of conventional cased charges, primarily verbal descriptions and pictures of the damage inflicted on the walls of the structure were reported. Based on the experience in interpreting structural data, no detailed effort to interpret Structure 2 data was made. Hence, only the data taken in the tests of Structure 1 were considered in this study.

Structure 1 was subjected to nine tests, four on one wall and five on another, presumably identical, wall. For each of these tests, three reflected pressure measurements on the wall and one free-field pressure measurement to the side of, but in the plane of, the wall were measured. Additionally, for each test, acceleration measurements were attempted on the inside center and bottom of the loaded wall and on the roof. No time-dependent deflections were measured, but the residual deflection at the center of the wall was measured after each test, and verbal descriptions of the condition of the wall following each test were also recorded. The results of the pressure and acceleration measurements are summarized in Tables 5 and 6, respectively. The residual deflections at the center of the wall and the verbal descriptions of the condition of the wall following each test are given in Table 3.

As will be observed from the data contained in Table 5, most of the pressure gages did produce reducible records but several of these records disagree significantly with theoretical pressure predictions. The measured and theoretical pressure data are compared in Figures 13, 14, 15, and 16, from which it will be observed that the measured and predicted peak reflected pressures agreed quite well except for the very close-in loading cases. Because of the

200

difficulty of measuring accurately extremely high pressure spikes, disagreements between measured and computed values under such conditions should probably not be unexpected. Regrettably, substantial disagreement existed between the measured and computed impulses at all loading levels for Tests 1-4. In contrast, quite good agreement between the measured and computed impulse values was obtained for Tests 5, 6, and 7, which were the less severe loading cases for the second wall. No reliable impulse data were obtained for Tests 8 or 9, so no comparison with measured values was possible.

Because both types of pressure gages that were employed and the theoretical prediction equations that were used had previously demonstrated their reliability, it was impossible to decide which of these impulse values more accurately reflected the actual loadings to which the walls were subjected. As will be noted below, efforts to resolve this issue by comparing the maximum deflections that were computed using both the measured and computed impulses with the measured residual deflections were also unsuccessful.

The measured residual deflections at the centers of the loaded walls were compared with predicted maximum deflections of these walls with mixed results. While reasonably good agreement between the measured deflections in Tests 1-4 and the deflections computed for these tests using theoretical impulse data was obtained, similar agreement was not observed in the other tests. This lack of agreement between measured and computed responses of the walls is further complicated by the fact that residual responses of zero were reported for Tests 5 and 6 for which the loadings were measured as being substantially higher than were the loadings in Tests 1 and 2, for which measurable residual deflections were recorded. Such an anomaly is especially confusing because both walls were presumably identical. But because the test walls were built as conventional structures rather than to the exacting specifications of a research instrument, perhaps they were not identical, in which case the apparent anomaly may, in fact, not be an anomaly. It might be further noted that, because the test walls were not built to research tolerances, there is no assurance that the inside surfaces of the walls, on which the residual deflections were measured, were initially true vertical planes. Consequently, the accuracy of the small (tenths of an inch) measured residual deflections, which presumed an initial vertical plane surface, could be legitimately questioned.

Acceleration records for the interior center surfaces of the walls were obtained for all tests except Test 9, but the record for Test 1 was totally unusable. For the remaining tests, the quality of the acceleration records varied widely, depending on the sampling rate of the digitizing process and the maximum value of the recorded data compared to the full-scale setting of the digitizing equipment. Extensive efforts were made to evaluate the responses of the walls by double integration of the acceleration records, but these efforts met with questionable success. These records, like most acceleration records, required some adjustment prior to integration if the integration was to produce reasonable results. Of the several adjustment methods tried, the most successful was a constant shift of the baseline sufficient to produce a final velocity of

zero, or in the case of an incomplete record, a final velocity that tended to zero. Such an adjustment seemed to produce reasonable results, because the maximum deflections that were computed by double integration of these adjusted records were in reasonable agreement with the measured deflections and with the deflections as estimated by other dynamic response computation methods.

C.   EVALUATION OF APPLICABILITY OF AVAILABLE SDOF COMPUTER PROGRAMS TO THE ANALYSIS OF IDF AND TYNDALL TYPE STRUCTURES

With varying degrees of success, each of the computer programs that were studied in this project was found to be useful in the study of the behavior of the IDF test structures and of the NATO-type structure that was tested at Tyndall Air Force Base. However, because each of those programs was developed independently and for a specific purpose, a comparison of their features and capabilities cannot be totally objective. Nevertheless, based on their experiences in the application of these programs to the IDF and the Tyndall tests, and with the objective of assisting future users of these programs in the selection of the program that would best serve their purposes, the authors have summarized below their assessment of the salient features, and the advantages and disadvantages, of each of the programs.

1.   The UofI Program
a.   General Characteristics:

This program is a basic, bare bones, undamped, SDOF response analysis program that requires the dynamic properties (natural period of vibration) of the system and its loading and resistance functions to be computed externally and provided as input to the program. It considers response only in the flexural mode, and provides output only in printed form and only out to the time of maximum deflection. It carries out the required numerical integration using the now widely accepted Beta Method.

b.   Advantages
(1)   Simplicity of operation
(2)   General purpose applicability
(3)   Requires only that the period of vibration of the system be given, and that the loading and resistance functions be generated externally and entered as input into the program as multilinear functions. Hence, it can be used for any system for which these functions can be found, not just for blast response analyses.
(4)   Because the period of vibration of the responding system is provided directly as program input, and because the loading and resistance functions are input in the same units, compatible load and mass factors are implicit in the program and need not be considered separately.

202

c. Disadvantages

(1) Has not been published and is not commercially available.

(2) Considers flexural response only.

(3) Requires the analyst to be sufficiently familiar with structural engineering and blast loading phenomenology to compute the natural period of vibration of the system and the loading and resistance functions that describe the system.

(4) Output is limited to a summary of the parameters that describe the SDOF system and a tabulation of the time-history of the response of that system up to the time of maximum response, or a summary of those data.

2. SASDE

a. General Characteristics

This program is designed specifically for the analysis of wall or roof elements of reinforced concrete box-type structures either above or below ground. It, too, is an SDOF program, and uses the same integration technique that is employed by UofI, but it considers response of the structural elements in both flexure and shear. It computes the dynamic properties and the resistance function of the element on the basis of structural geometry, edge restraint conditions, and material properties that are input by the analyst. It will accept a multilinear loading function that is input by the analyst, or it will generate its own loading function on the basis of a given explosive charge type, size, and location. It provides either graphical or tabulated response output for as long a period as the analyst desires.

b. Advantages

(1) Considers both flexural and shear behavior.

(2) Computes internally the dynamic properties and resistance function, including edge restraint and in-plane force effects, requiring as input only the structural geometry, support conditions, and material properties.

(3) Provides for consideration of both one-way and two-way slabs with a variety of support conditions.

(4) Permits consideration of either above or below ground structures.

(5) Accepts either externally generated loading functions or will generate loading functions internally from input explosive charge data.

(6) Considers viscous damping of any magnitude, if desired.

(7) Output complete and comprehensive, and available either in graphical or tabulated form.

c. Disadvantages

(1) Not very user friendly; user's manual difficult to understand and interpret.

203

(2)   Internal generation of resistance function presumes a specific reinforced concrete construction configuration, and requires compliance with support conditions and reinforcement patterns that are assumed by the program to exist.

(3)   Because of item 2, use of the program for slabs whose support conditions and/or reinforcement patterns differ from those assumed by the program requires the development by the analyst of an "equivalent" system that does conform to the constraints imposed by the program.

(4)   Users' Manual is not sufficiently detailed to permit the analyst to understand why the resistances computed by the program are sometimes significantly different from those that are computed by conventional structural theory using hand calculations.

(5)   Requires the analyst to provide the load and MF that are needed by the program to transform the real distributed mass system into an equivalent SDOF system.

3.   BIGGS
      a.   General Characteristics

BIGGS is a computerization of the SDOF structural analysis methods described in Reference 3, and is similar in many respects to other SDOF programs that have been discussed. Like UofI, both the loading and resistance functions must be computed externally and then be entered as multilinear functions for use by the program. Like SASDE, it considers both flexural and shear response of the element being studied, and permits the introduction of a damping factor. The output from the analyses is available in either graphical or tabular form.

      b.   Advantages

(1)   A versatile and user-friendly program; menu-driven, with a convenient, built-in editor.

(2)   Considers both flexural and shear behavior.

(3)   Permits the introduction of damping.

(4)   Output comprehensive and flexible.

(5)   Because loading and resistance functions are computed externally, the program can be used for any system for which these functions can be generated.

      c.   Disadvantages

(1)   Program constrained to use of a resistance function for which the final slope is zero, thereby negating its use for systems for which the resistance, having reached its maximum at some deflection, decays as deflection continues.

(2)   Requires the analyst to input load and MFs that convert the actual distributed mass system into an equivalent SDOF system.

(3) Requires access by the analyst to Reference 3 so that factors given in that reference that are descriptive of the dynamic reactions of the system may be entered as input into the program.

4. BLAST

a. General Characteristics

Fundamentally, BLAST is a SDOF analysis program that differs from the others only in detail. It was designed for use by nontechnical personnel to estimate the vulnerabilities of wall panels to damage from HE charges, rather than for detailed design analysis. The analyst specifies the type of wall to be studied, together with its external dimensions, and the type and location of the explosive charge. Using built-in default values for all other parameters that would be needed to define the elastic properties and the resistance function of the system, the program computes the deformation of the wall panel, considering both flexural and shear behavior. If more complete data regarding the nature of the panel and the properties of the materials of which it is made are available, the program permits the analyst to override the default values with those "better" data.

b. Advantages

(1) It can be used to obtain a quick and dirty estimate of the vulnerability of a wall panel to the blast effects of high explosives even if detailed data descriptive of the panel are limited.

(2) It enables the analyst to improve the quality of the vulnerability assessment by using actual panel thicknesses and material properties instead of the built-in default values of these quantities.

(3) It considers the possibility of failure in both flexure and shear.

(4) The load and MFs that are required to transform the actual system into an equivalent SDOF system are built into the program and need not be entered by the analyst.

(5) It permits the use of a wide variety of wall panel materials: reinforced concrete (with or without cut-outs), masonry (either infilled or bearing), and glass of numerous varieties.

(6) Output is provided in both graphical and printed form.

c. Disadvantages

(1) It presumes all wall panels to be completely symmetrical in every respect, and to be supported on all sides by nondeflecting non-moment resistant supports.

(2) Because its resistance functions are computed internally, it can be used for unsymmetrical panels only by formulating artificial symmetrical panels that have approximately the same dynamic and resistance characteristics that the actual panels have.

(3)   Because no provision is made for the introduction of an externally developed loading function, it can be used only to assess the vulnerability of a wall to the blast effects from conventional explosives.

D.   APPLICABILITY OF A GENERAL PURPOSE FINITE ELEMENT PROGRAM TO THE ANALYSIS AND DESIGN OF BLAST RESISTANT WALLS

The finite element analysis envisioned for this part of the project would carefully predict details of the behavior with the loading and resistance modeled as accurately as possible. This would require a model of the transient nature of the loading across the wall and the influence of concrete failure and reinforcement yielding on the resistance function. The purpose is to assess the use of a finite element program, and not to perform a specific study of the walls.

There are several finite element programs that have the necessary capabilities. ADINA was selected because of its use at other government laboratories and its suggested use by several experts in the field. The loading history and timing of the loading can be specified for each element, allowing the modeling of almost any loading history. A detailed concrete model is available that allows tensile cracking and compression crushing with the influence of stress in other directions on the cracking and crushing. There are several parameters that can be changed to adjust the concrete material model to fit the specific problem to some extent.

The authors had some experience with finite element programs at the start of the study, but had not worked with concrete material models extensively and had no familiarity with ADINA. The conclusions drawn from the authors' experience in using ADINA may not be typical of all finite element programs, as large general purpose systems each have their own characteristics; however, the experience will provide the nonexpert with some guidance in deciding whether such a program would be useful for his/her purpose, and in getting started with its use if the decision is to use one.

Several months of work with the program were required to become familiar with those aspects that were needed for the analysis of dynamically loaded concrete walls. It was necessary to learn to use the input processor and the output or plotting program, as well as the details of how the program performs the analysis. Toward the end of the study PATRAN was adopted for describing the geometry of some of the problems. This program is a geometric modeling system that is used to describe the nodes and elements, and there is a translator available from ADINA R&D, Inc. that converts the PATRAN file to the ADINA format. PATRAN greatly simplifies geometric modeling, which is especially significant for 3D models.

The procedure for obtaining a solution is first to prepare the input file that describes the geometry, loading, boundary conditions, and control parameters for the solution. In the input file the main program is told how often it should save solution information and what information to save. This file is processed

by the input processor, and then the main program is run using the file produced. The program creates several output files, one of which is used by the post processor to provide plots of any information desired that has been saved. The files created by the main program can be very large (e.g., 20 to 60 Mb in this study). There are many helpful commands that can be used in the input file that the preprocessor can use to make the description of the problem easier, such as generation of node geometry and grouping of elements that have the same properties.

Loading of the wall can be described by applying a pressure to any element, describing a normalized pressure-time function for the application of the pressure on each element, and then giving a delay time for the application of the pressure. Thus the loading can be applied uniformly over a surface or it can be applied as if it first reaches one edge and progressively engulfs the slab. It was found that the effects of the rapid loading in either of these ways can be modeled well by the program.

When the load was applied uniformly over the wall surface the initial deformations occurred only at the supports in shear while the center portion of the wall remained perfectly flat. The slab had not had time to respond in flexure, and if the pressure was sufficient to cause failure in direct shear at the supports then a shear failure occurred. When the pressure wave was allowed to start at one edge and move across the slab, a similar phenomenon occurred at the initially loaded edge. There was a shear response at the edge before the rest of the slab deflected, and this response moved across the slab in 2 to 3 ms before the flexural response had begun, because the peak flexural response required 9 to 12 ms. These initial deformations in shear were small, but in some cases were sufficient to cause shear failure.

The indication of a failure, whether shear or flexure, is difficult to interpret, because in general the program stops with an error message. It is then difficult to find where the problem that caused the error message occurred. It was generally from the material model. Then it is necessary to decide where in the slab model the material has failed. This may not be possible with great certainty, but it must be inferred from the deformed shape, the cracking pattern, and concrete stresses and strains; these must also be studied to determine whether the physical conditions would have actually resulted in a material failure. The source code for the program was not available for this academic version, so it was not possible to investigate the details of the concrete model and what caused the error message. With the availability of the source code in commercial versions of ADINA, experienced analysts might successfully pinpoint and correct problems that cause computational instabilities.

It was found, not surprisingly, that there is a significant difference between a uniform loading and a transient loading, particularly when the pressure is high enough to be near the failure pressure for the slab. In these studies the uniform pressure, based on that pressure measured at the wall midheight, gave a lower deflection than the transient pressure. It should be noted that the

207

deflections were small relative to those that might be allowed in design of a protective structure.

Investigation of the effect of tensile strength of the concrete with static loading indicated that there is a considerable influence of this parameter on the initial portion of the load-deflection curve, though the curves for different tensile strengths merged eventually. However, there are different areas under the load-deflection curves for the two cases, indicating a capacity to absorb more energy when the tensile strength is higher. This explains the difference in dynamic response, where it was found that the maximum deflections were lower as the tensile strength of the concrete increased.

It would be conservative to assume a very low concrete tensile strength, but in many cases this may be overly conservative. In studies like the present one in which the behaviors of test structures are to be predicted, it is difficult to determine what tensile strength should be used, particularly without tests on the specific materials used. The history of the structure must be considered, both relative to the environment and previous loading. In the case of the IDF structures the curing environment was probably harsh (dry desert) and led to shrinkage cracks that can act as initial stress concentrations. Also, these structures were subjected to repeated loadings; previous loads probably initiated some cracks, even if they were not visible, that caused additional cracking during the next loading at smaller stress. ADINA has the capability to restart a solution that would preserve the state of the model at the end of the last run. This would make it possible to reload the structure with the cracking and deflection preserved. In a dynamic solution it would be necessary to run the first solution until it has reached its final deformation state before starting the second solution, and for a complex model the run time for this may become very large.

Several input parameters influence the concrete material model. One of these is XSI, which governs the amount of tensile softening or slope of the tensile stress-strain curve after the tensile strength has been reached (see Section VIII-B-3). A larger value provides a flatter slope, and increases the residual stress across the crack after cracking begins. It was only after considerable work with the program that the importance of this parameter was realized. If the value is 8.0 as used in this study for a large number of solutions, then there is sufficient tensile stress in cracked regions to influence the moment after the reinforcement has yielded, and the pressure-deflection curve does not flatten but continues to climb. If the value is 1.0, there is a sudden drop in tensile stress across the crack. Though this is more realistic, it seems to make the numerical solution more unstable in some cases.

Smaller values of XSI, near 1.0, caused cracking to spread over the model more than the larger value of 8; however, the value of 8 caused an increase in the yield moment. Therefore, it appears that a larger value is desirable to promote localization of the cracking initially, but near yield of the reinforcement a smaller value is desirable. Localization of cracking affects the stress in the adjacent reinforcement, and thus the distribution of strain along

the reinforcing bars; the reinforcement strain in turn influences the slab deflection. The selection of XSI will therefore depend on the modeling objective, i.e., the macro vs micro behavior in the structure.

The element mesh used to describe the slab geometry can have a major influence on the analysis results, particularly if it is too coarse. Studies of three mesh configurations for the IDF slab indicated that a 10x6 element configuration using 2D elements was near optimum for deflection calculations because there was only 6 percent increase in dynamic maximum deflection when the number of elements in the longitudinal direction was doubled. The mesh can have an important influence on the solution in terms of CPU time required, as the time increases rapidly as the number of nodes increases. In this study several different models were constructed consisting of two dimensional and three dimensional elements and one way and two way slabs. Also, several different workstations were used. However, it was concluded that it was impractical to run any solutions on the workstations except the two dimensional element model of the one way slabs. The three dimensional model of the two way slab ran for 5 days on an HP/APOLLO Model 425 for an incomplete solution of less than 100 time steps.

The importance of in-plane forces resulting from the edge support resistance has been recognized for some time, and ADINA provides a means for investigating this effect. Springs can be added to the model that apply forces in the plane of the wall as in-plane deformations occur, and rotational springs can be used to simulate partial moment fixity. These springs can be given nonlinear properties, though only linear springs parallel to the plane of the wall were used in this study. It was found, as expected, that the linear springs resulted in little effect on the wall response until the primary reinforcement yielded, at which time the support edges moved outward and caused compression forces in the springs. Also, as expected, the effect increased with spring stiffness. The solutions could not be carried to displacements large enough to result in tension membrane forces in the walls.

There has been little work on the actual in-plane forces caused by the rest of the structure; this could be studied with ADINA by including in the wall model a significant part of the structure around the wall. This approach may make the numerical model so large that it is not practical to obtain a solution. However, a coarse mesh could be used to investigate the in-plane forces created, and then these forces applied to the wall model with a finer mesh through other means. Also, when the pressure wave reaches the roof of the structure the downward forces at its supports apply in-plane forces to the wall. In these studies the pressure wave reached the top of the wall in about 2 ms; after this time there is a time dependent reaction at the roof edges that act on the walls. This force on the wall may be more significant in the response than the force resulting from stiffness of the rest of the structure.

The compression stress-strain curve in the concrete material model is described by its initial modulus and the stress and strain at peak stress and at failure stress. There is evidence in the literature that the strain at these stresses is increased under dynamic conditions for unconfined uniaxial

conditions. Increasing the peak and failure strains was found to increase the dynamic response of the test wall model, but a thorough evaluation was not carried out. The topic requires further study before the effect on the wall response can be quantified.

There are several design details that can be investigated with the objective of improving the performance of walls. Some of these may require including a larger portion of the structure around the wall in the model. These include such questions as the following. Should primary reinforcement be of equal area on the inside and outside of the wall or would it be better to place more of the area on the inside? The orientation, type, and location of shear reinforcement can also be investigated.

Diagonal bars were placed at the top and bottom of the Tyndall structure walls that tied the wall to the adjoining roof and floor (see Figure 112 and 113). Detailed information was obtained for the stress in these bars when the wall was subjected to uniform static pressure to evaluate their effectiveness. For this model the bar stress was low because the outward movement of the support was of about the same magnitude as the downward movement of the top surface, resulting in very little change in length of the bars. Further study is needed before recommendations can be made about these bars as the dynamic loading of the wall and bending of the roof and floor slabs may change their stress completely. However, the effectiveness of these bars and other design details can be studied with the finite element program.

Prediction of the response of the IDF test walls with the finite element program was restricted to predicting the residual response after loading because that was the most reliable test data available. The predictions were fairly close to the measured residuals, when the residuals were accumulated, because each solution was obtained starting with zero initial deformation (see Figure 137). The material properties, loading and boundary conditions were all fairly uncertain for these tests, so the accuracy of the comparison is well within expected limits. Those parameters that define the resistance of the Tyndall structure walls were more reliable, but there was still some uncertainty about the loading. In these tests the maximum dynamic deflections were compared because they were measured with scratch gages and therefore considered to be accurate. The thin (south) wall deflected 2.5 inches and the thick (North) wall deflected 1.7 to 1.9 inches. The predicted values (Figure 138) were 2.1 and 1.5 inches, respectively.

In both cases the predicted response compares reasonably well with the measured values. The parameters defining the resistance and loading were the best-estimate values, and some of them could be changed to make the comparison better. However, the comparisons between predicted and measured response are not better than that provided by some of the SDOF programs discussed in Sections IV to VII. For design purposes it is generally adequate to know the maximum response of a wall and whether it fails under given loading conditions. Therefore, a SDOF program that adequately predicts deflection and whether failure occurs is sufficient. The program should be able to predict shear as well as

flexure failures. These programs require much less time and effort and can be applied without a knowledge of finite element theory, and therefore are generally more suitable for routine design.

The finite element solution can be useful in two ways. First, it can provide a better understanding of the behavior and thus help the designer consider the correct failure mechanisms and the potential trouble areas that might lead to failure. Second, it can be used to develop design guidelines that should be followed in those areas of design for which the SDOF solutions do not provide sufficient information. Some of these are as follows:

(1) Equivalent uniform loading to be used in the SDOF solution to provide the correct response when the actual loading is transient.

(2) Guidelines for the correct boundary conditions for the walls provided by the rest of the structure, both rotational and in-plane.

(3) The effect of in-plane time dependent forces caused by applied pressure on other parts of the structure such as the roof.

(4) Determine the optimum distribution of primary reinforcing bar areas between the inside and outside layers.

(5) Determine the optimum shear reinforcing type and distribution.

(6) Determine the effect of uncertainties in material properties, boundary conditions, and loading on the wall response.

APPENDIX A
RAW DATA FROM THE IDF TESTS

This appendix contains the unmodified data used in these studies. Other data were available but were not considered for reasons discussed in the report. The data were all provided on tape in digital form, and the pressures were also provided as plots. Summaries of the peak pressures, durations of pressure, peak accelerations, and information about the recording of the data were also provided. Only the data on the response of the two walls of Structure 1 that were tested were used and are shown here.

Figures A-1 to A-38 are the pressure plots provided by the IDF. Figures A-39 to A-50 are acceleration plots made from the digitized data. Only the acceleration records for the center of the wall (accelerometer 7) that the authors determined to be reasonable are shown. In some cases there are two plots for the same point. In these cases the same signal ranges are given for all the records in Table 6, and the gage locations are shown in Figure 5.

A code that was used to identify each measurement is shown on each record. This code, which is also shown on some of the data in the report, should be interpreted as follows:

First 2 digits	=	Test number
Second 2 digits	=	Gage location (see Figure 5)
Third 2 digits	=	Channel number used for recording.
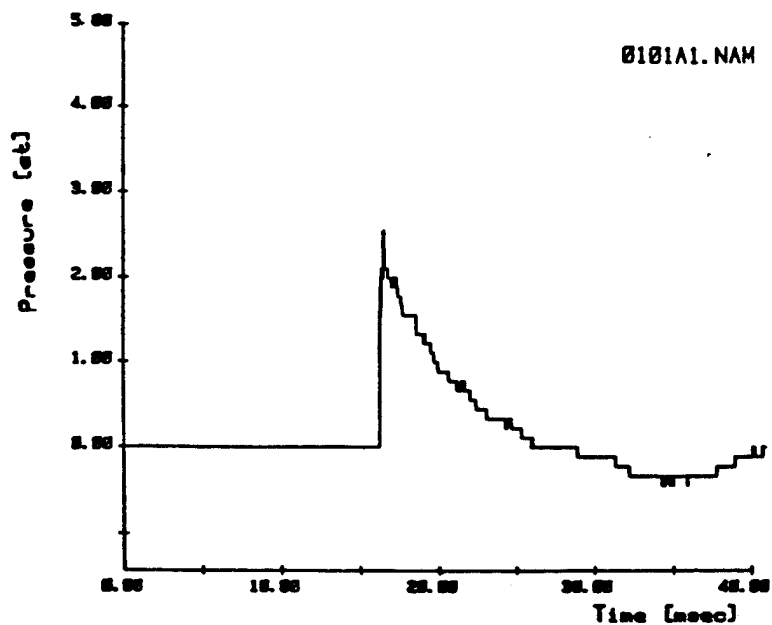
Figure A-1. Pressure for Test 1 at Point 1 on Channel A1.
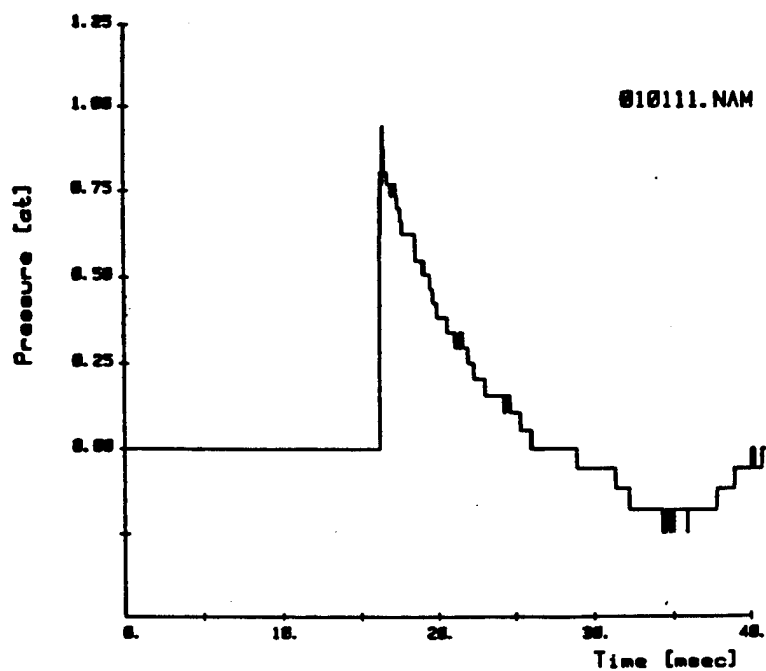
Figure A-2. Pressure for Test 1 at Point 1 on Channel 11.

213
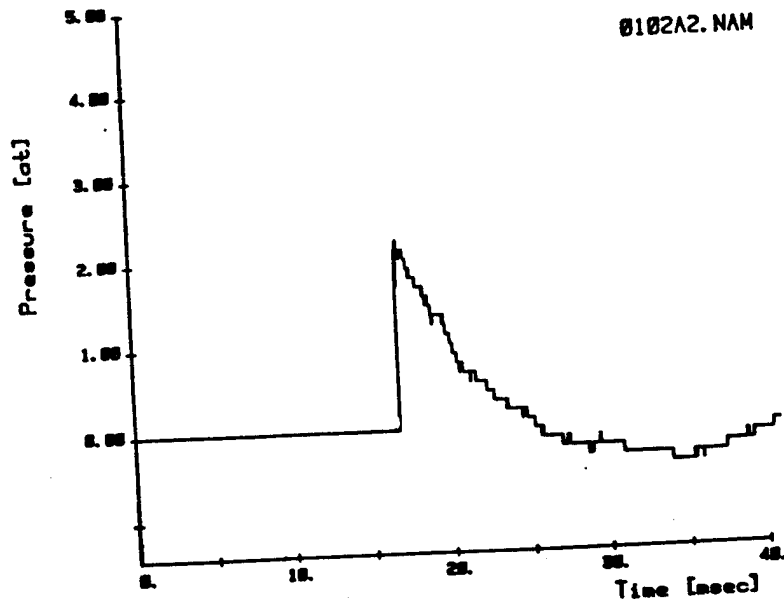
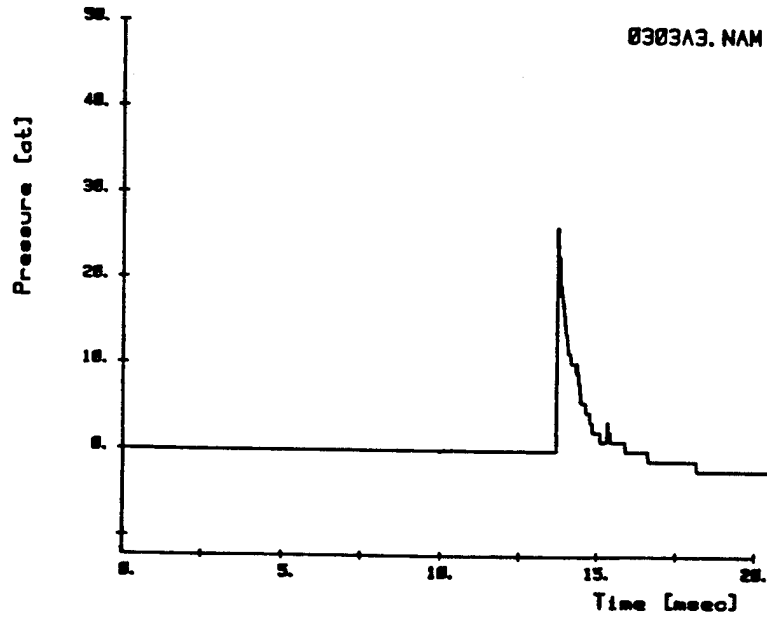Figure A-3.   Pressure for Test 1 at Point 2.
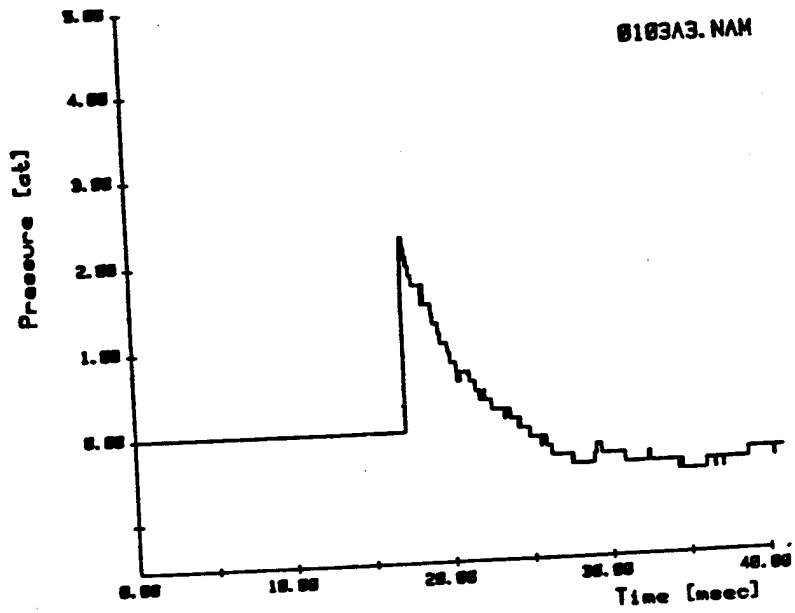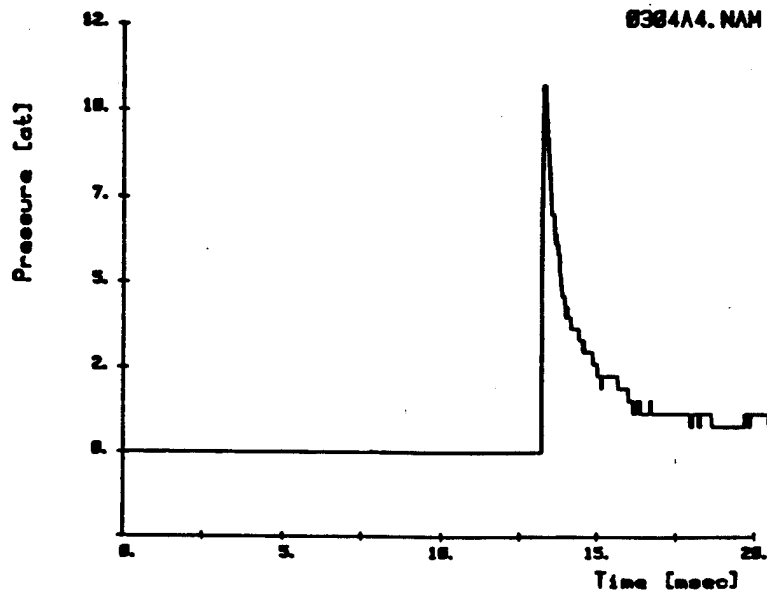

Figure A-4.   Pressure for Test 1 at Point 3.

214
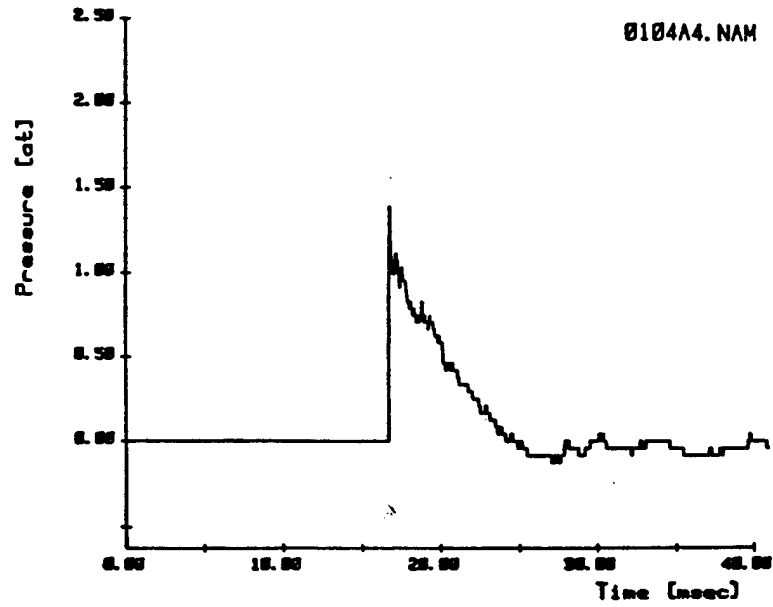
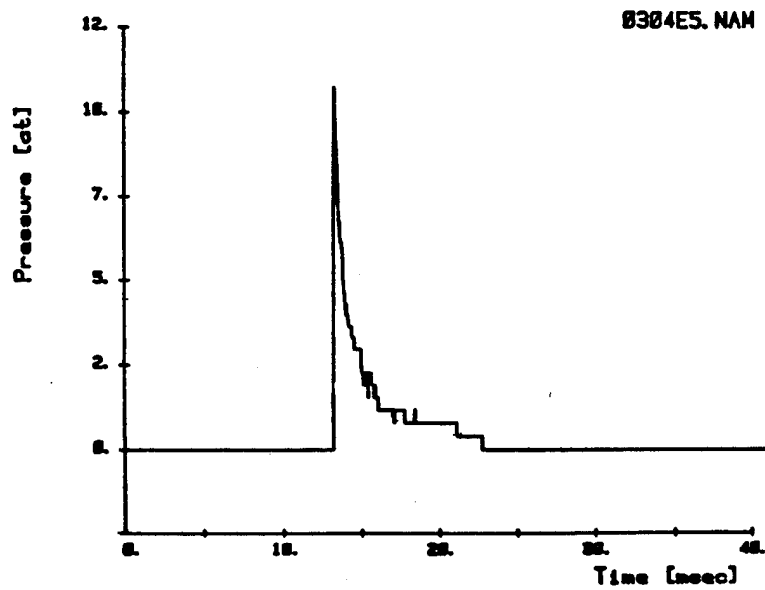Figure A-5.   Pressure for Test 1 at Point 4 on Channel A4.
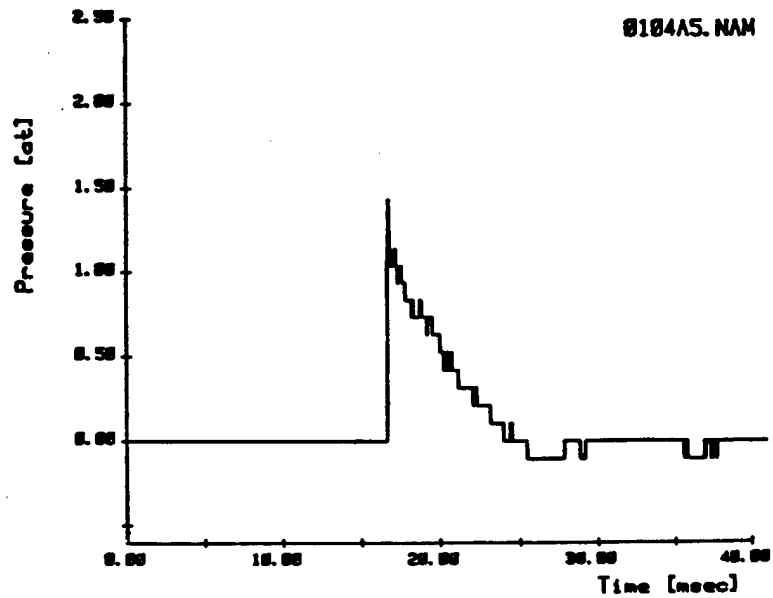
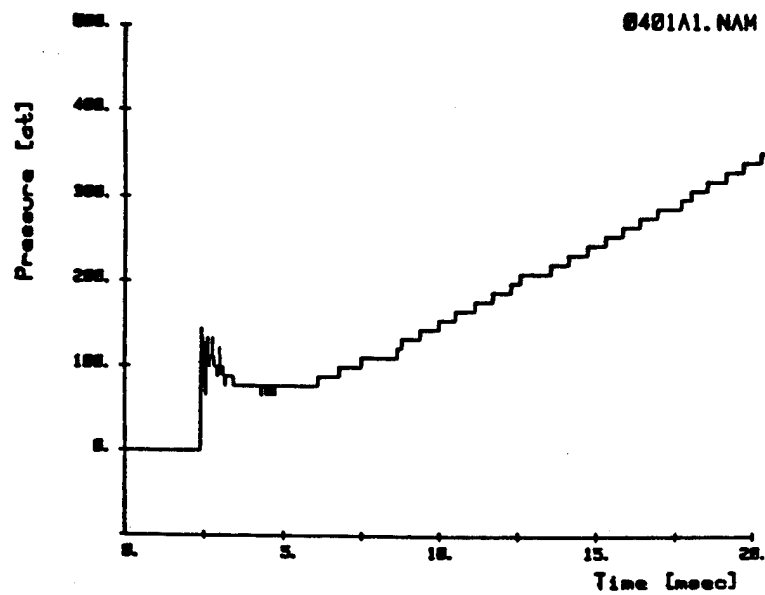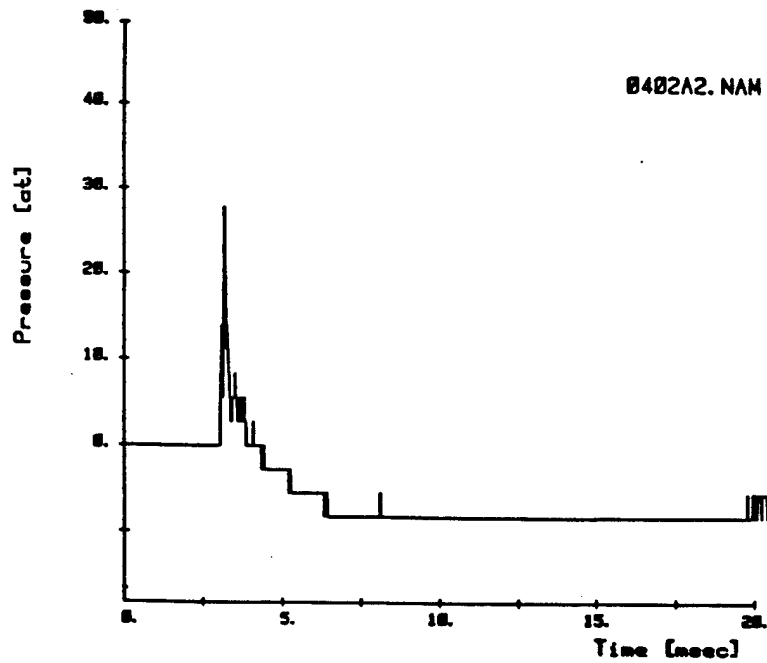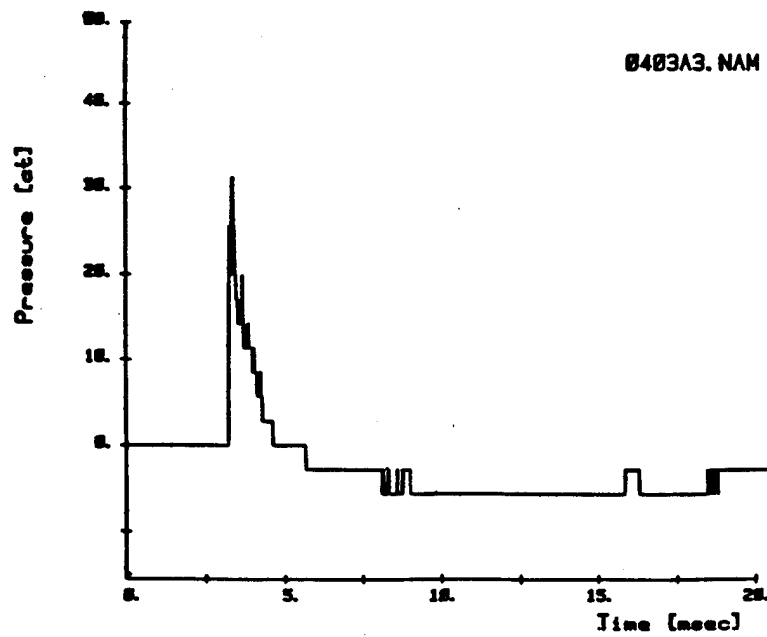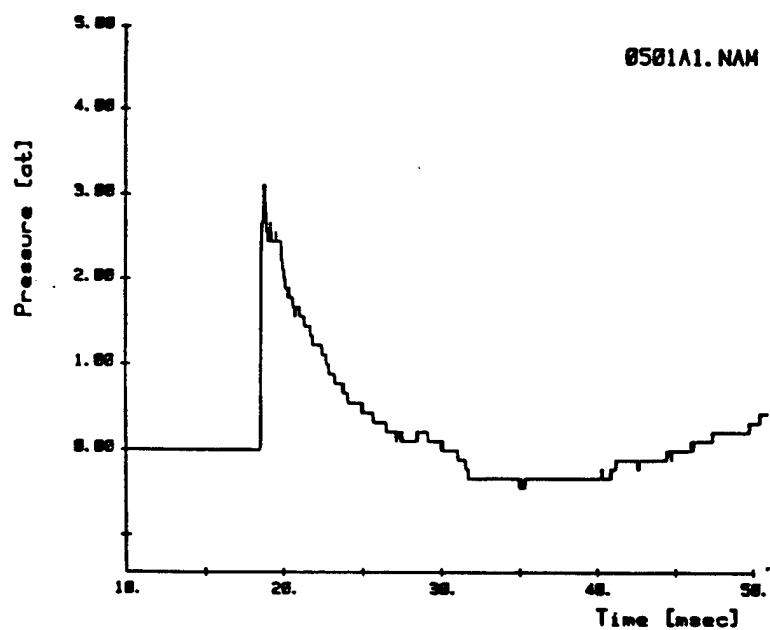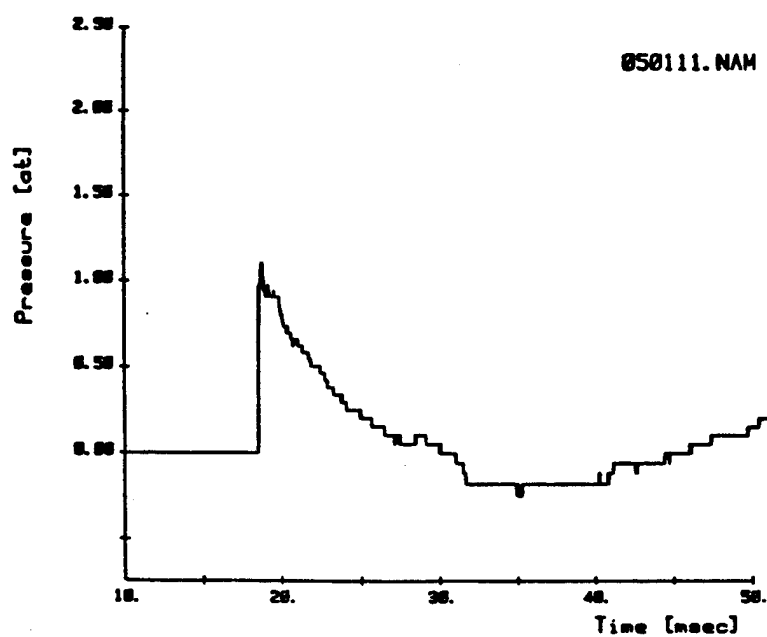

Figure A-6.   Pressure for Test 1 at Point 4 on Channel A5.
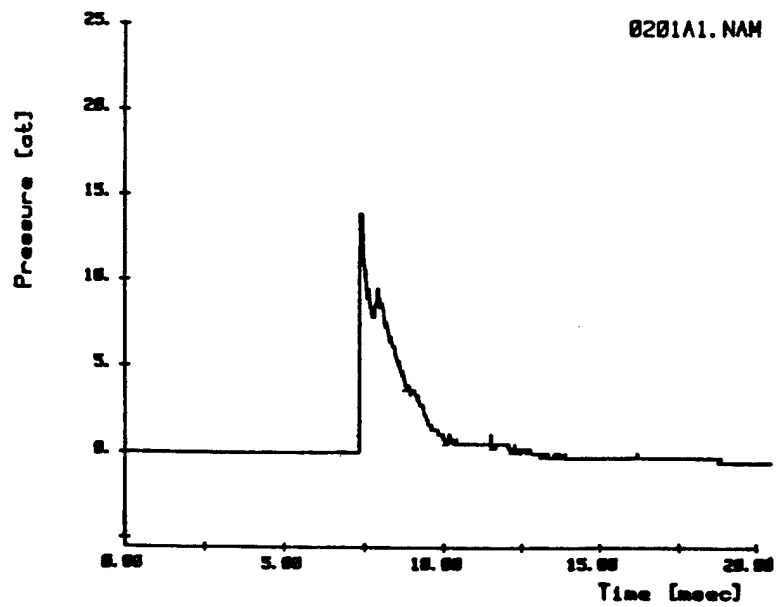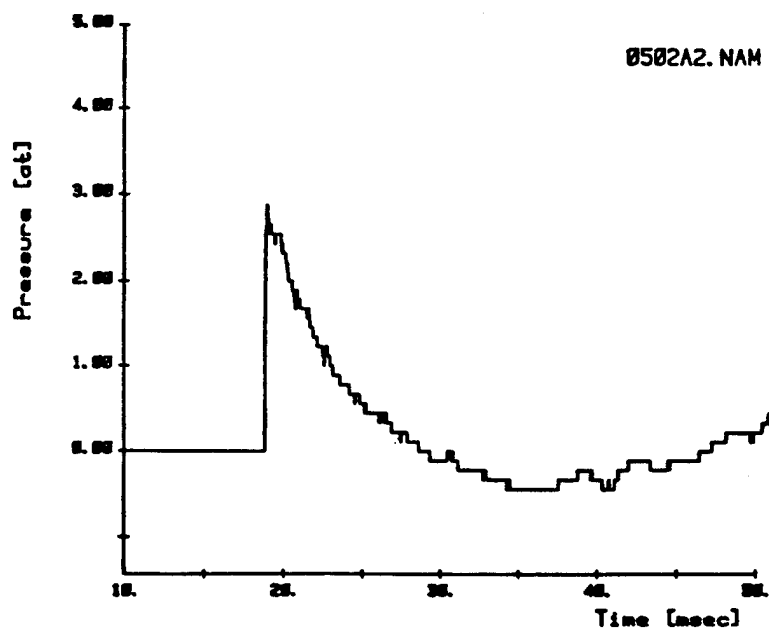
Figure A-7.   Pressure for Test 2 at Point 1 on Channel A1.
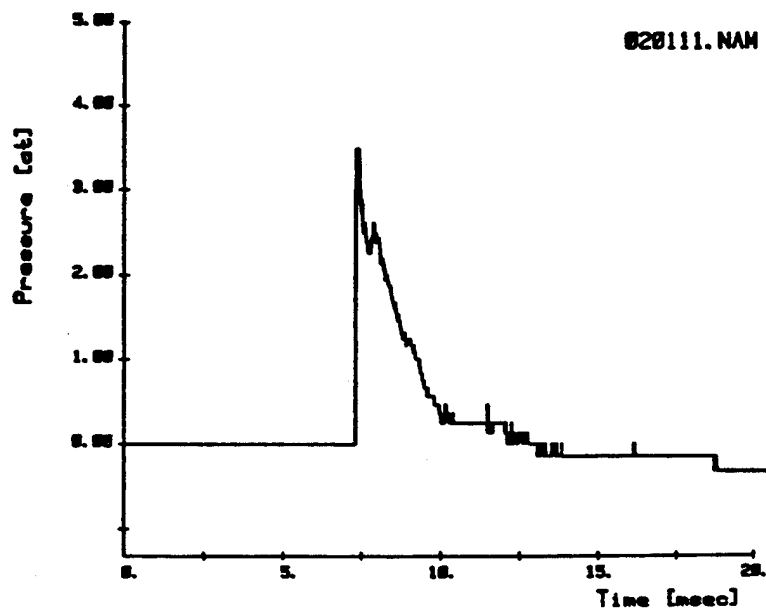
Figure A-8.   Pressure for Test 2 at Point 1 on Channel 11.
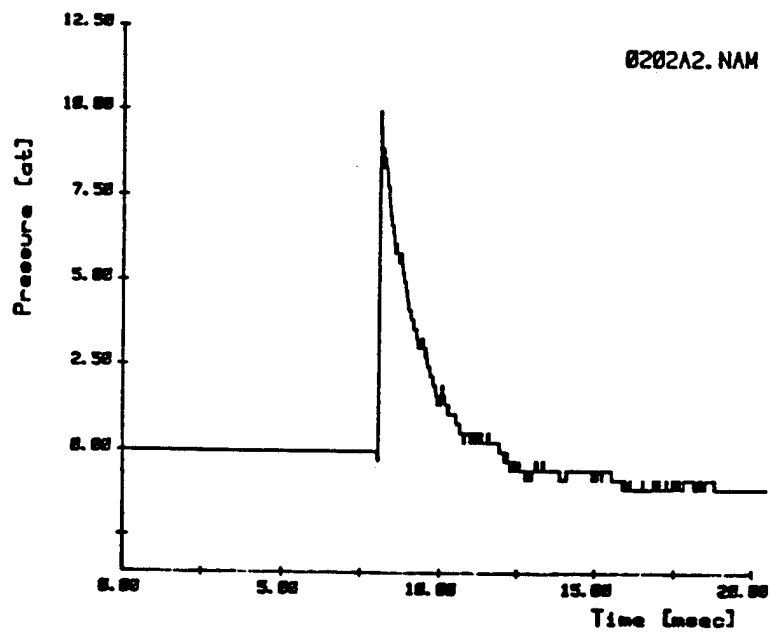
Figure A-9.   Pressure for Test 2 at Point 2.
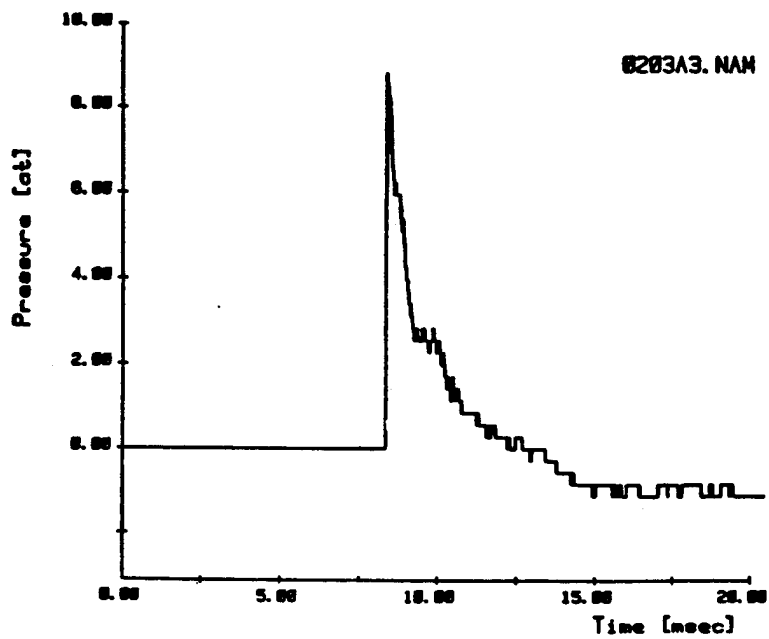
Figure A-10.   Pressure for Test 2 at Point 3.

217
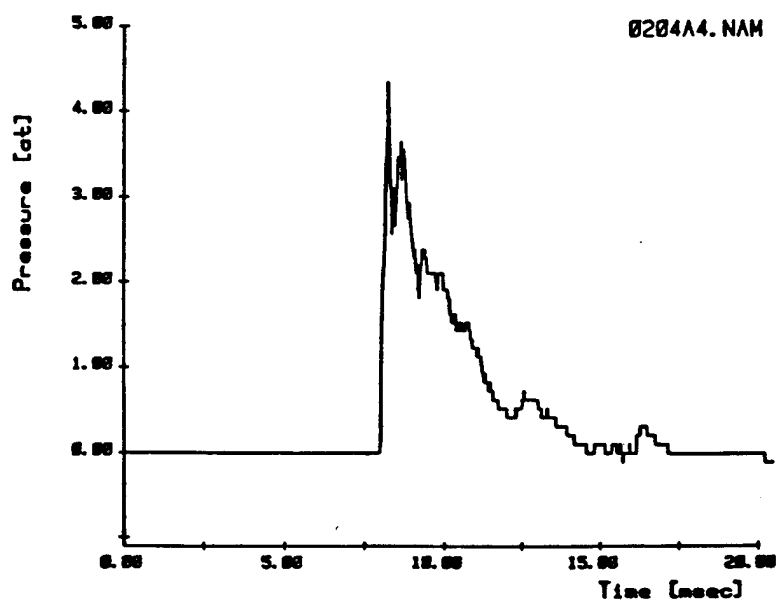
Figure A-11. Pressure for Test 2 at Point 4.
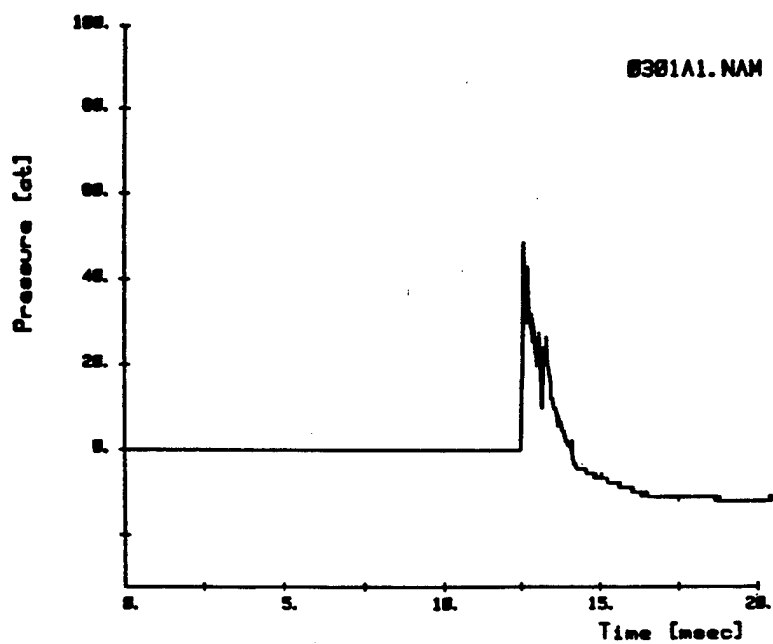
Figure A-12. Pressure for Test 3 at Point 1 on Channel A1.

218
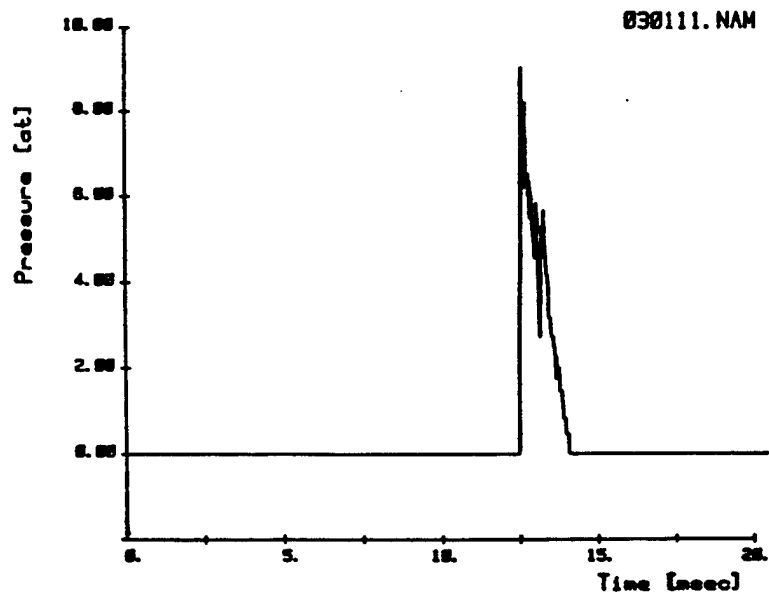
Figure A-13. Pressure for Test 3 at Point 1 on Channel 11.
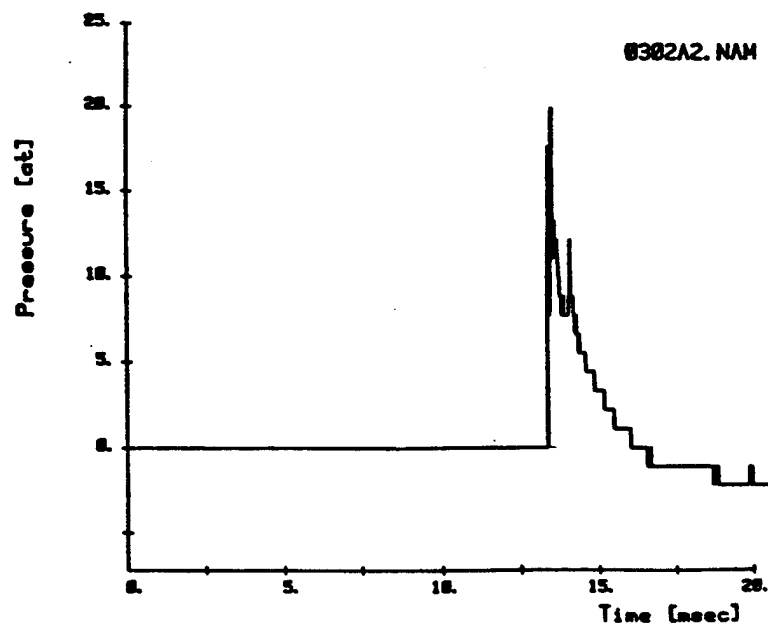
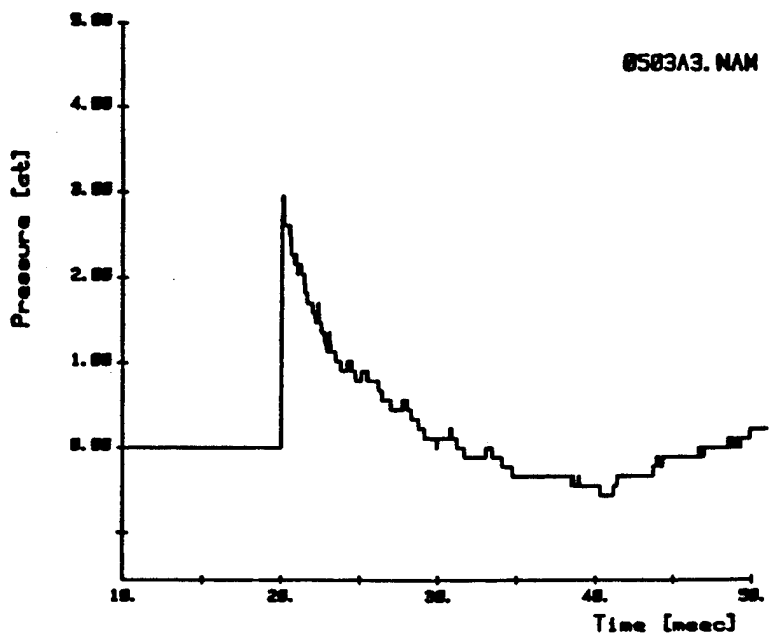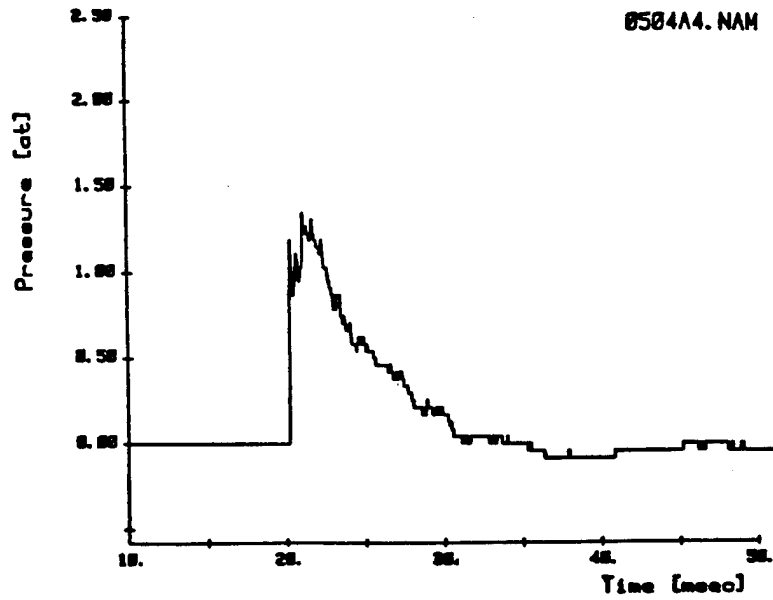Figure A-14. Pressure for Test 3 at Point 2.

219

Figure A-15.   Pressure for Test 3 at Point 3.

Figure A-16.   Pressure for Test 3 at Point 4 on Channel A4.

220

Figure A-17.   Pressure for Test 3 at Point 4 on Channel E5.

Figure A-18.   Pressure for Test 4 at Point 1.

221

Figure A-19.   Pressure for Test 4 at Point 2.

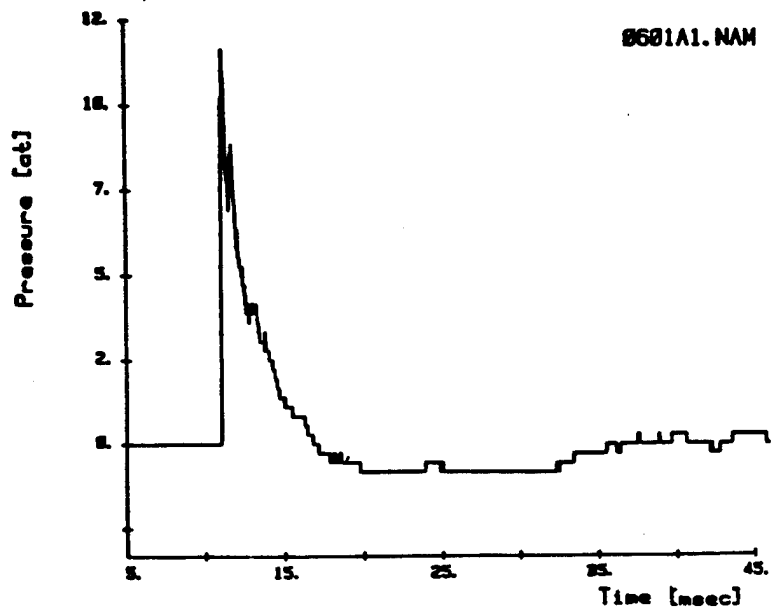Figure A-20.   Pressure for Test 4 at Point 3.

222

Figure A-21.   Pressure for Test 5 at Point 1 on Channel A1.

Figure A-22.   Pressure for Test 5 at Point 1 on Channel 11.

Figure A-23.   Pressure for Test 5 at Point 2.

Figure A-24.   Pressure for Test 5 at Point 3.

224

Figure A-25. Pressure for Test 5 at Point 4.

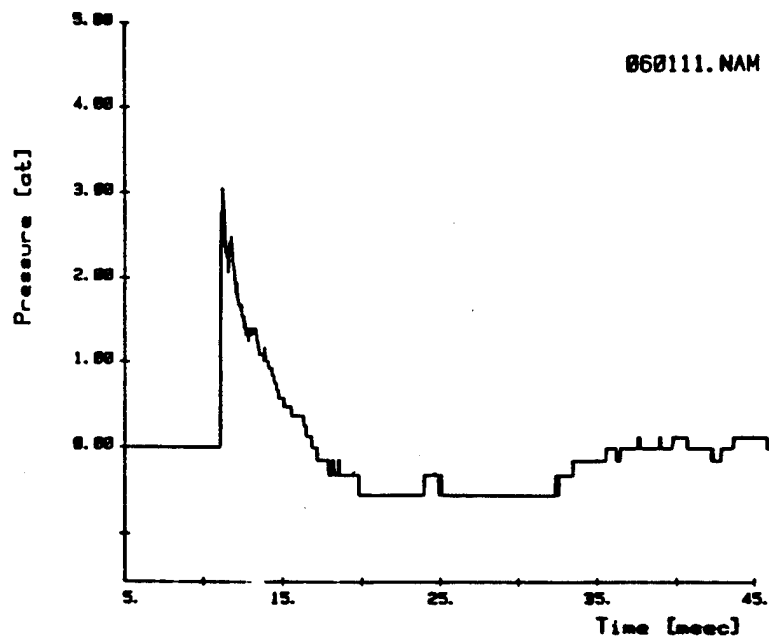Figure A-26. Pressure for Test 6 at Point 1 on Channel A1.

225

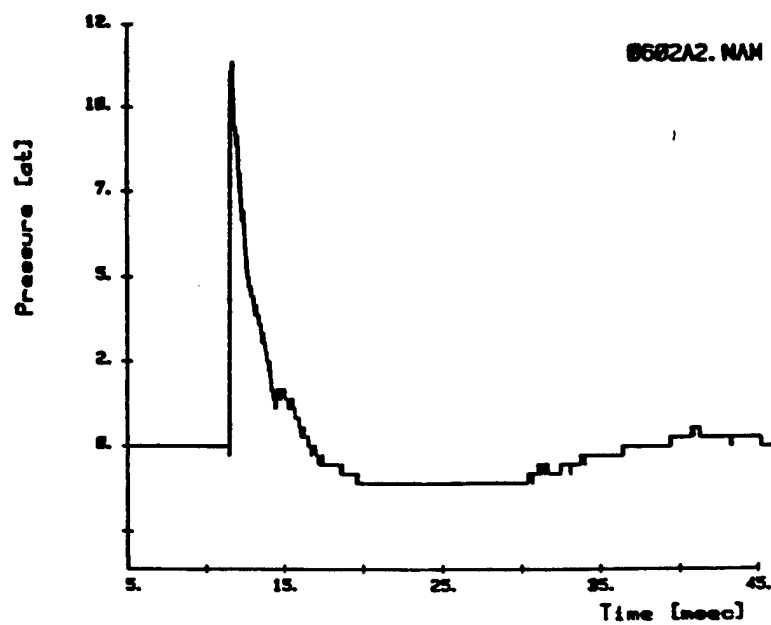Figure A-27.   Pressure for Test 6 at Point 1 on Channel 11.
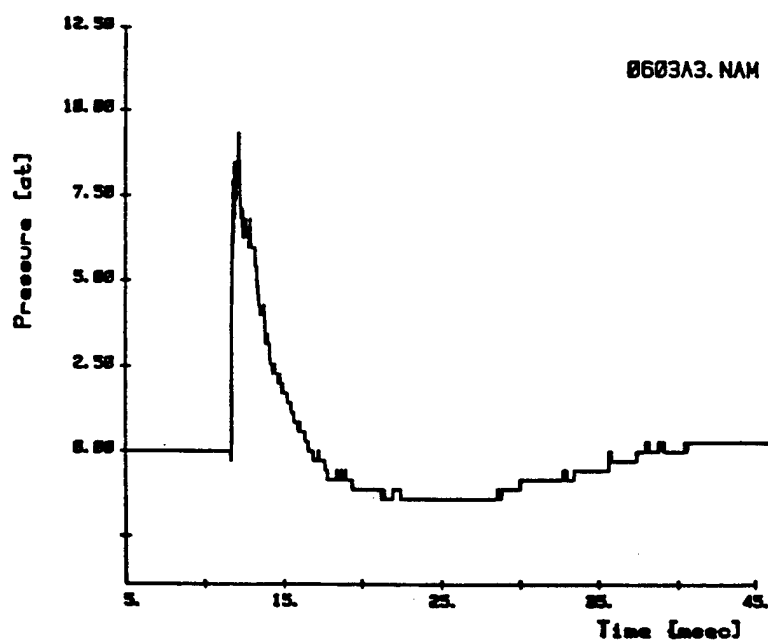

Figure A-28.   Pressure for Test 6 at Point 2.
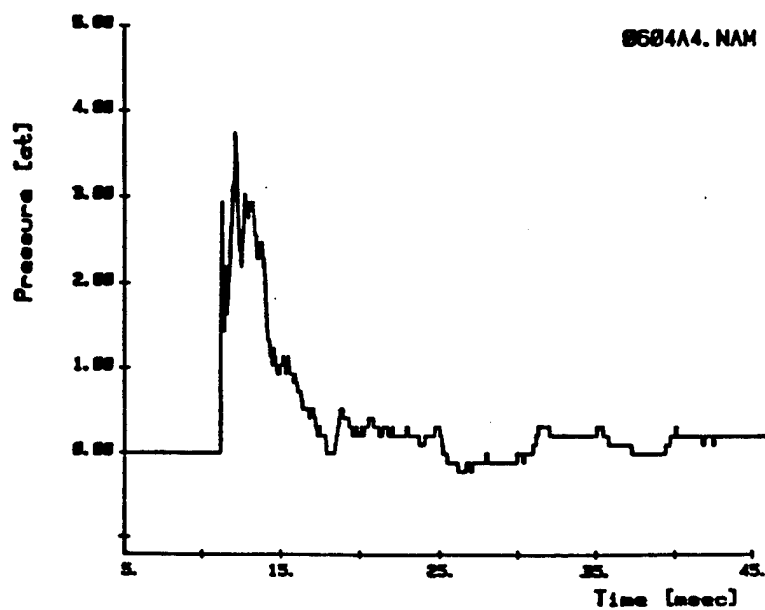
Figure A-29.   Pressure for Test 6 at Point 3.

Figure A-30.   Pressure for Test 6 at Point 4.
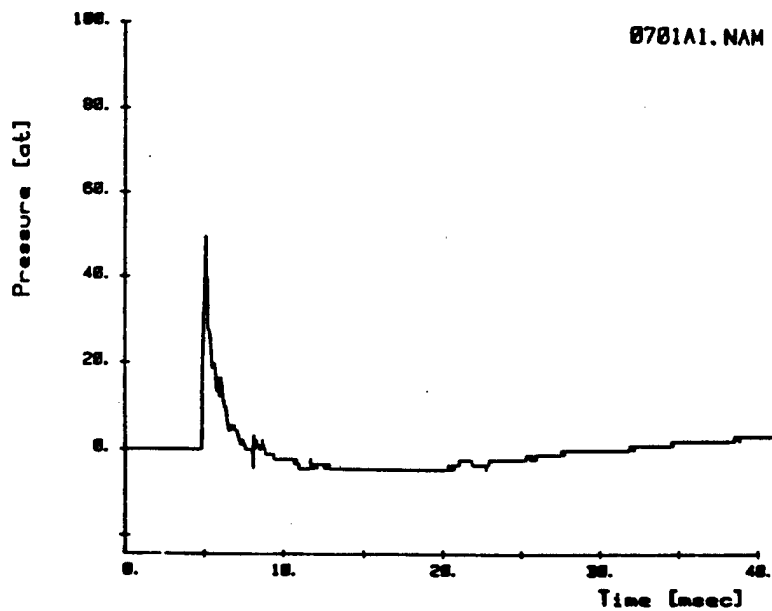
227

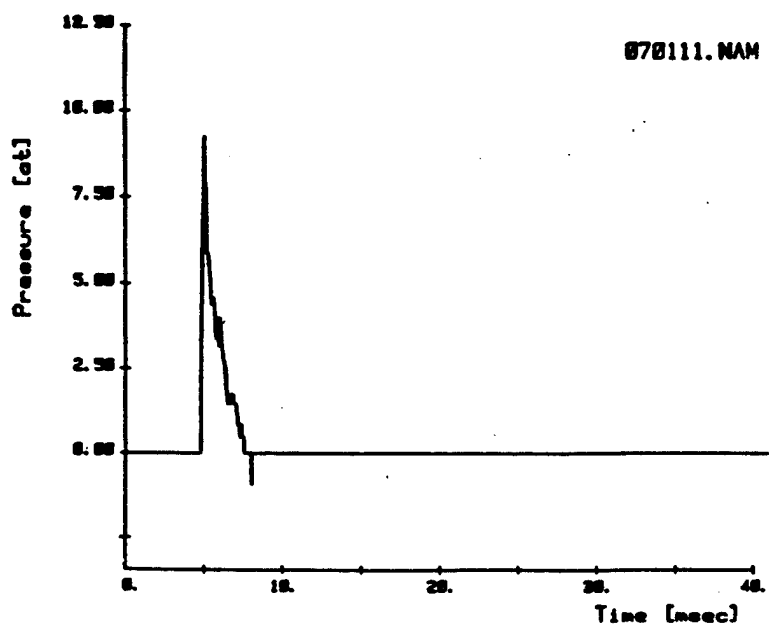Figure A-31.   Pressure for Test 7 at Point 1 on Channel A1.

Figure A-32.   Pressure for Test 7 at Point 1 on Channel 11.

228

Figure A-33. Pressure for Test 7 at Point 2.
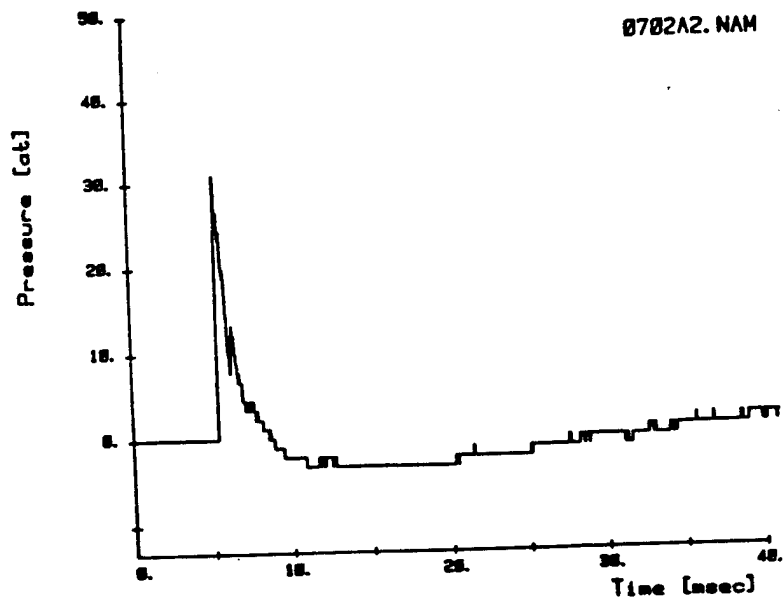

Figure A-34. Pressure for Test 7 at Point 3.

229
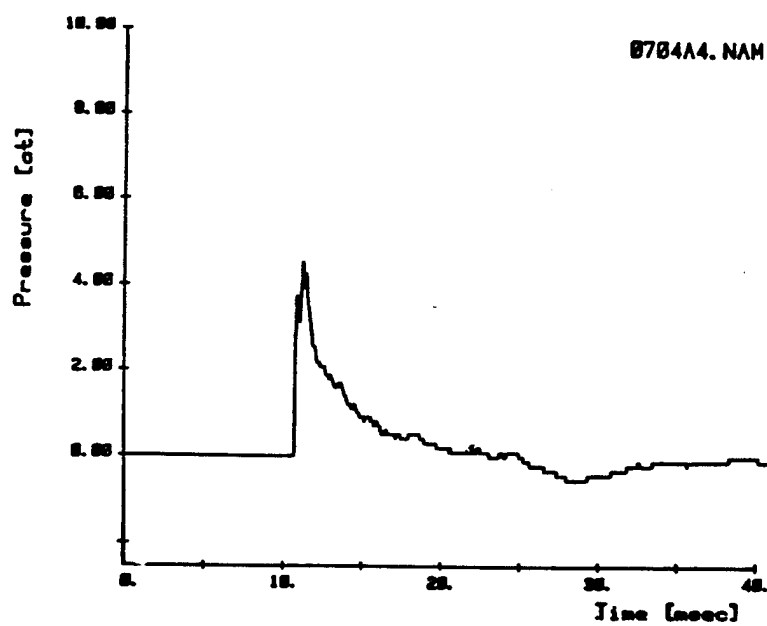
Figure A-35.   Pressure for Test 7 at Point 4.
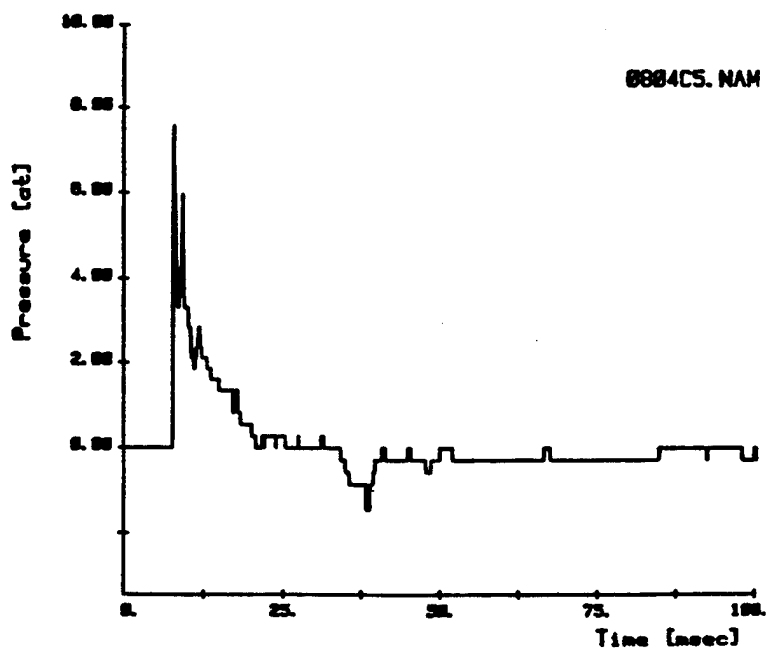
Figure A-36.   Pressure for Test 8 at Point 4.
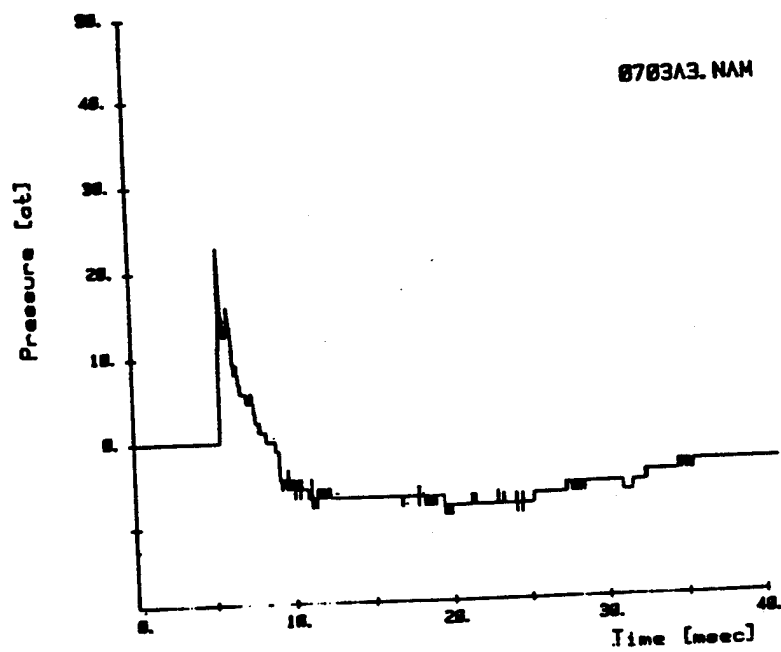
230
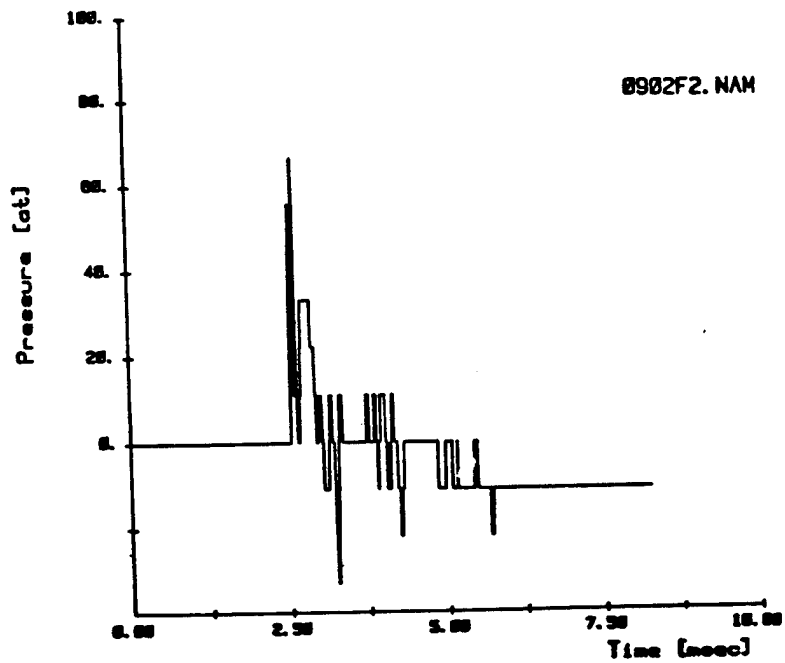
Figure A-37.   Pressure for Test 9 at Point 2.
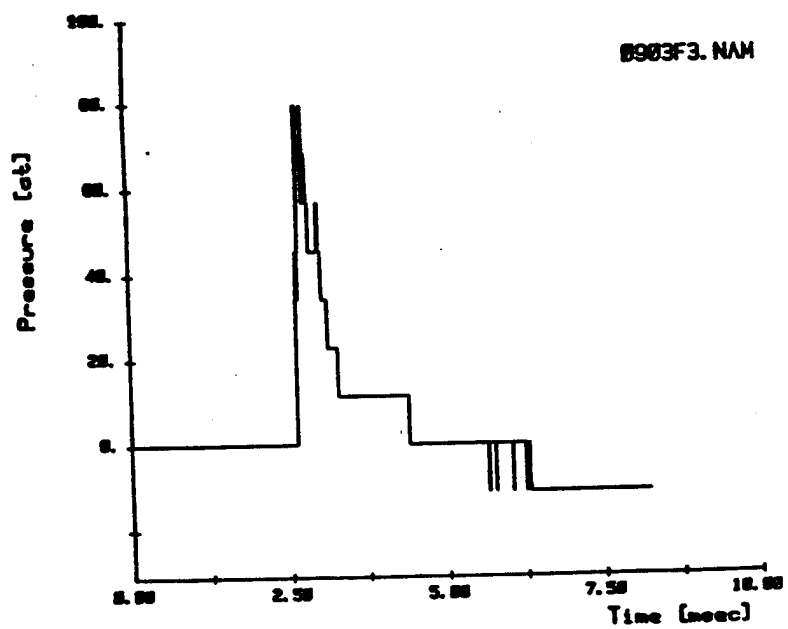
Figure A-38.   Pressure for Test 9 at Point 3.

231
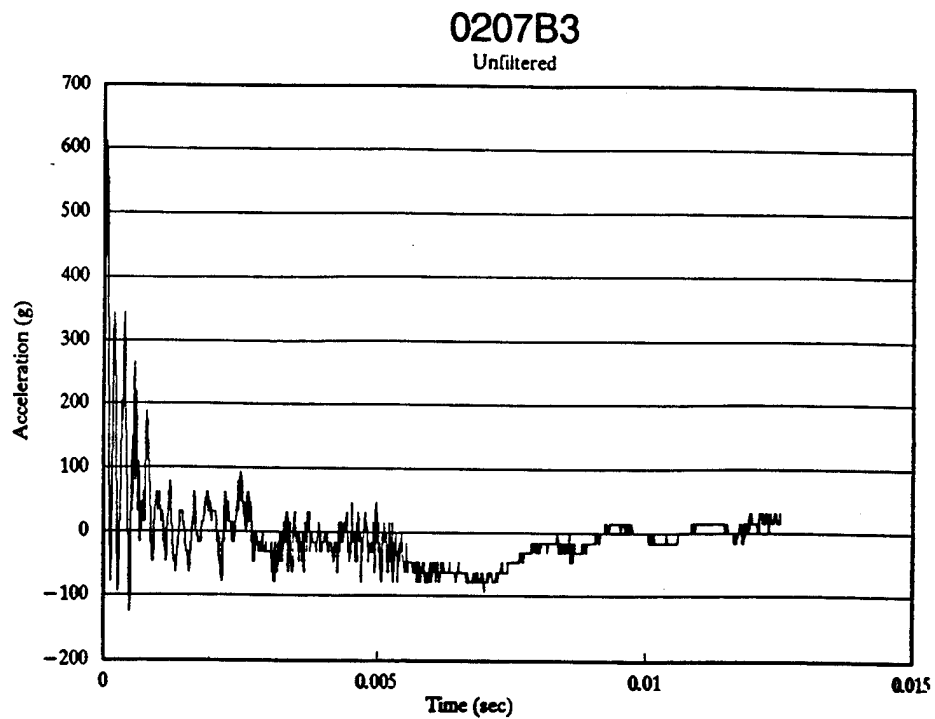
Figure A-39.   Pressure for Test 2 at Point 7 on Channel B3.
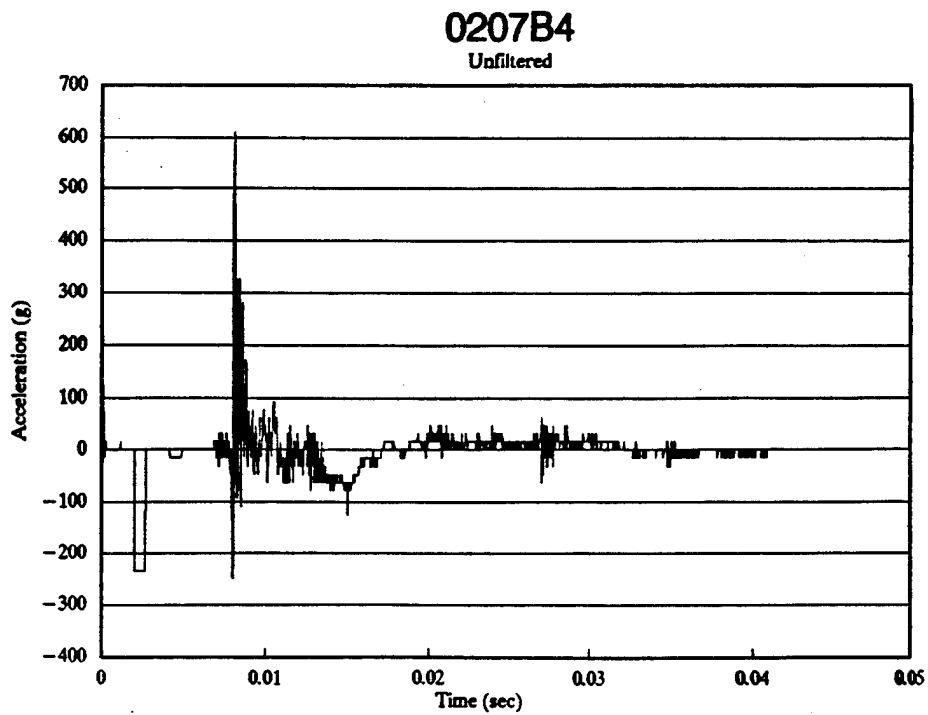
Figure A-40.   Pressure for Test 2 at Point 7 on Channel B4.

232

0307B4
Unfiltered
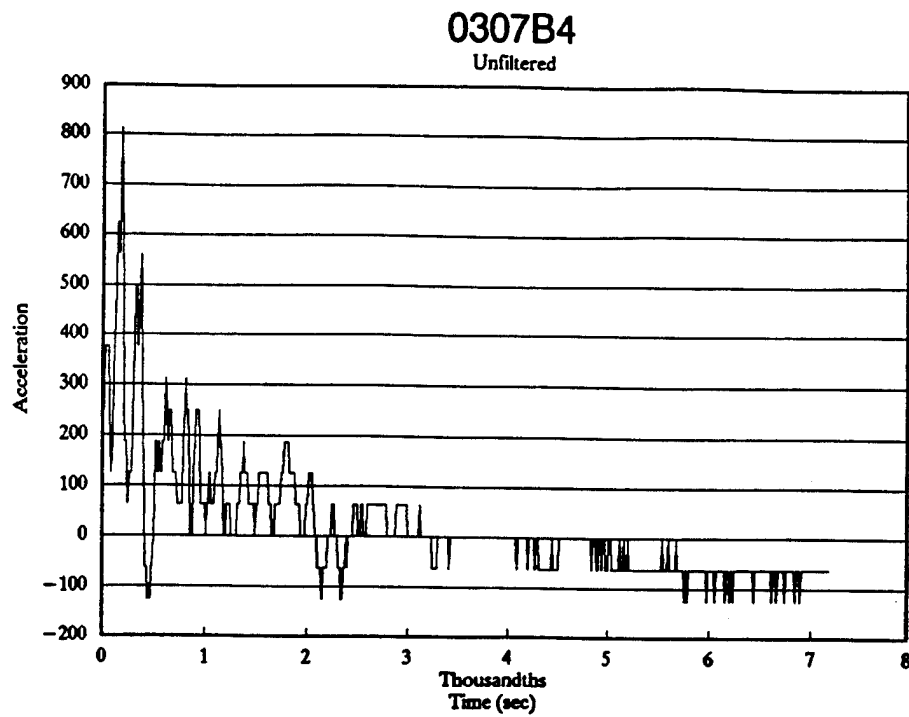
Figure A-41. Pressure for Test 3 at Point 7.

Gage 0407B3
Unfiltered
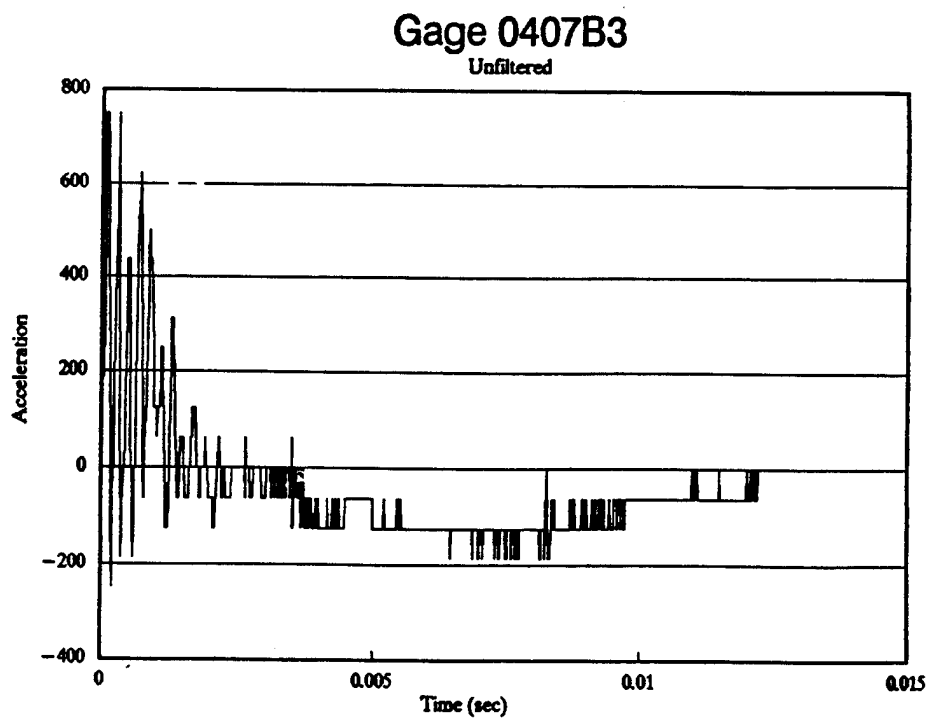
Figure A-42. Pressure for Test 4 at Point 7.

233

0507B3

Unfiltered
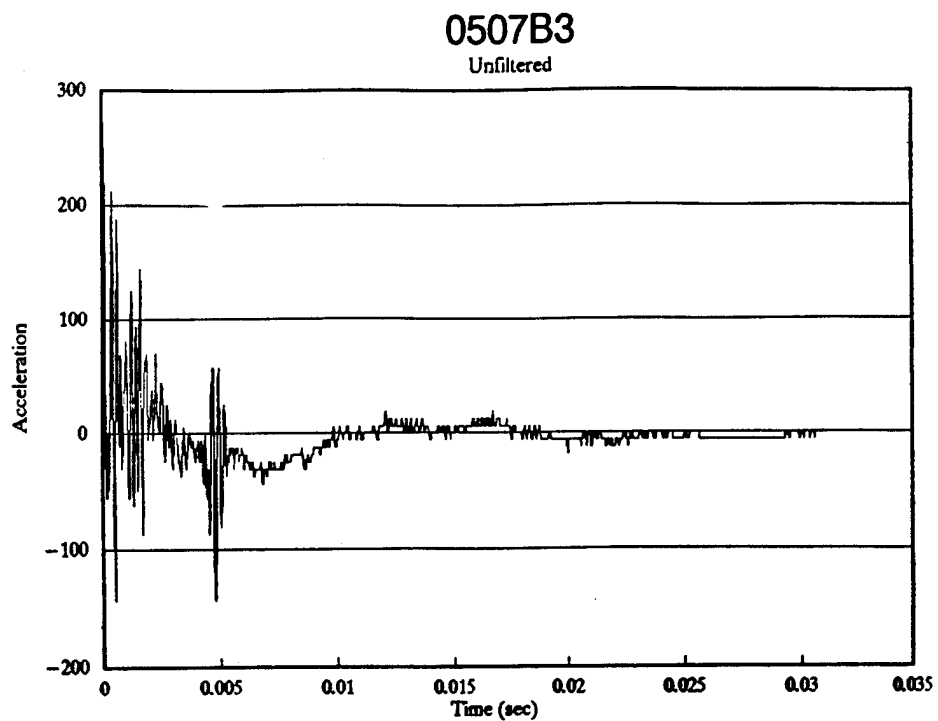
Figure A-43. Pressure for Test 5 at Point 7 on Channel B3.

0507B4

Unfiltered
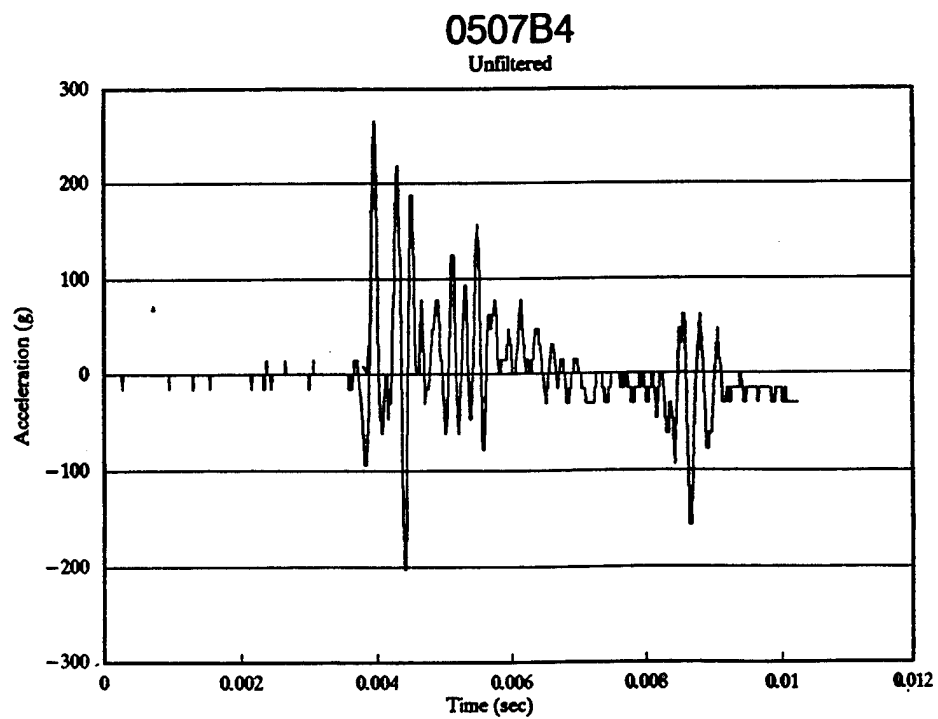
Figure A-44. Pressure for Test 5 at Point 7 on Channel B4.

234

Gage 0607B3

Unfiltered Data
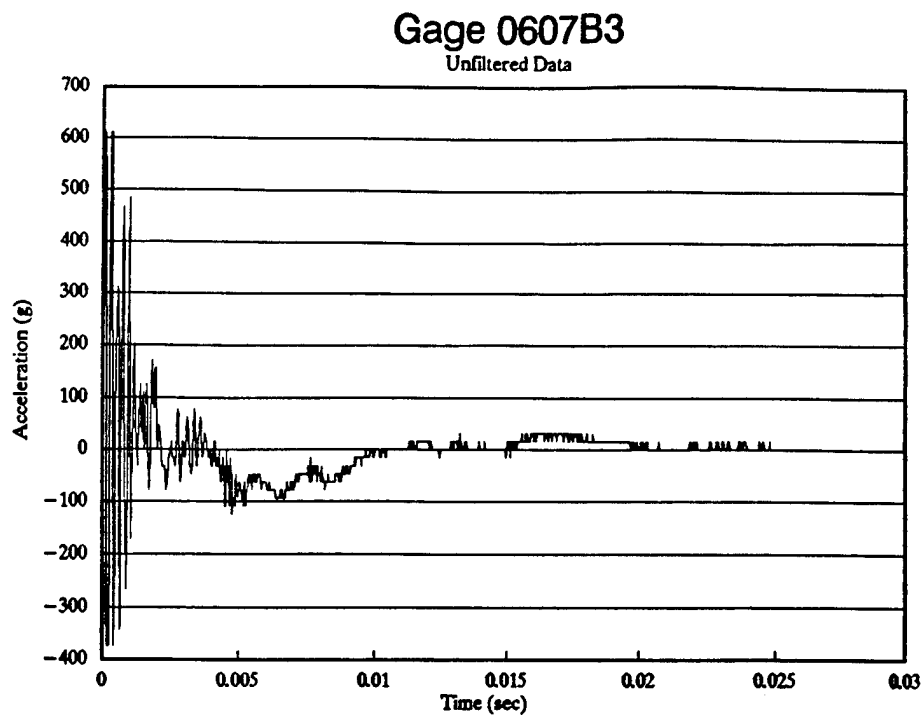
Figure A-45.   Pressure for Test 6 at Point 7.

0707B3

Unfiltered
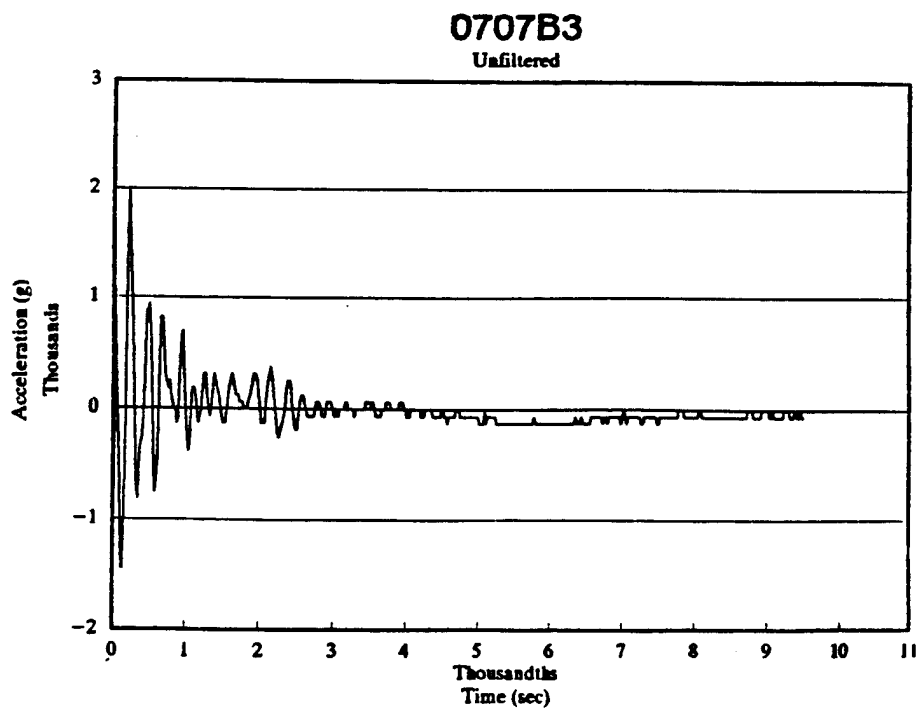
Figure A-46.   Pressure for Test 7 at Point 7 on Channel B3.

0707B4

Unfiltered
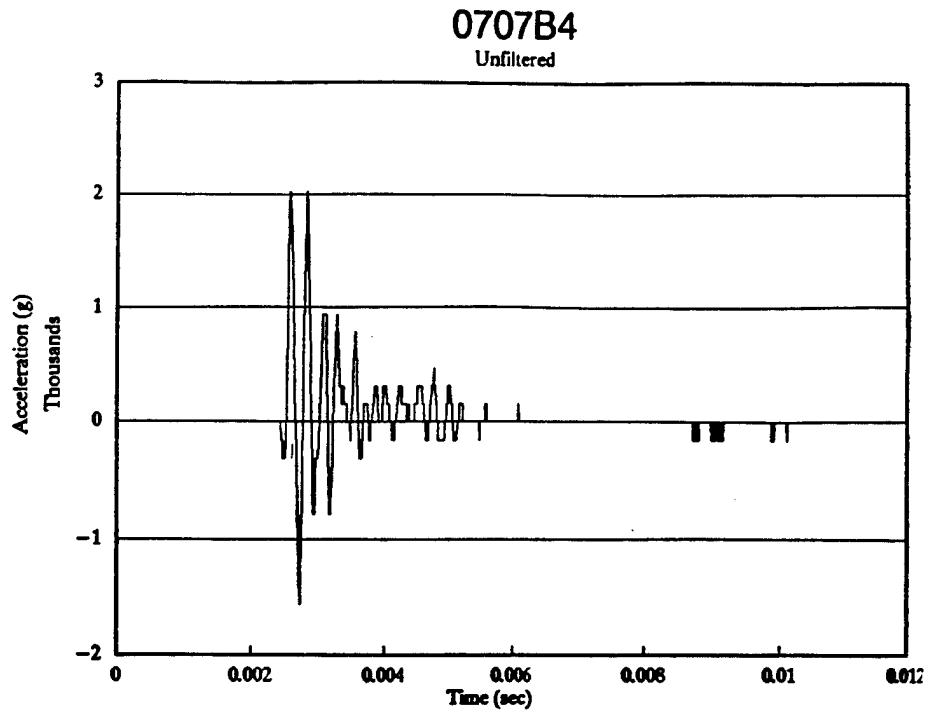
Figure A-47.   Pressure for Test 7 at Point 7 on Channel B4.

Gage 0707D5

Unfiltered
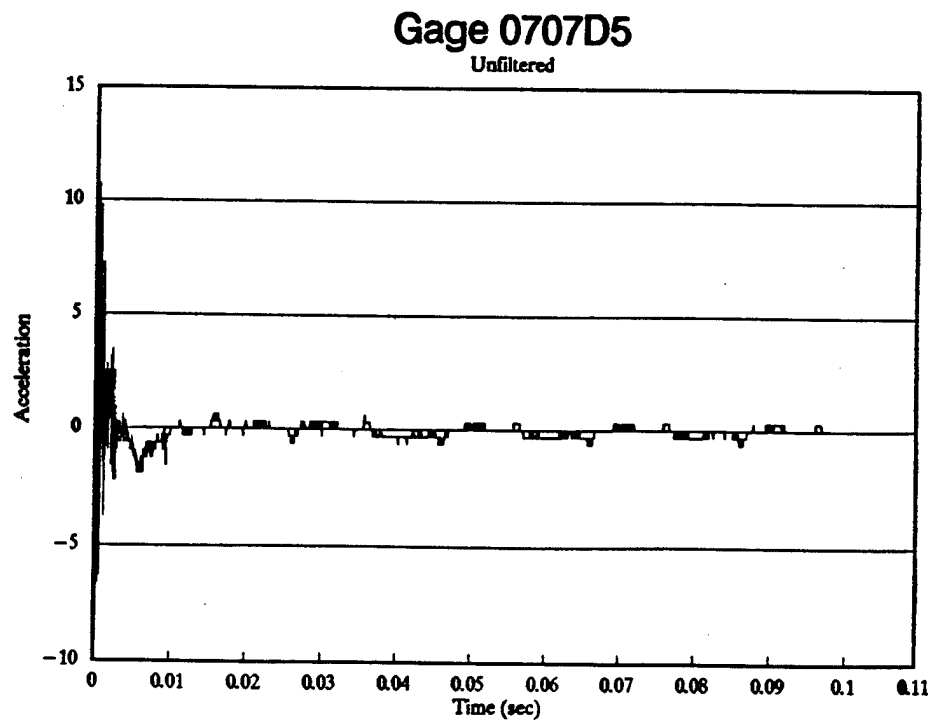
Figure A-48.   Pressure for Test 7 at Point 7 on Channel D5.

236

0807B3

Unfiltered
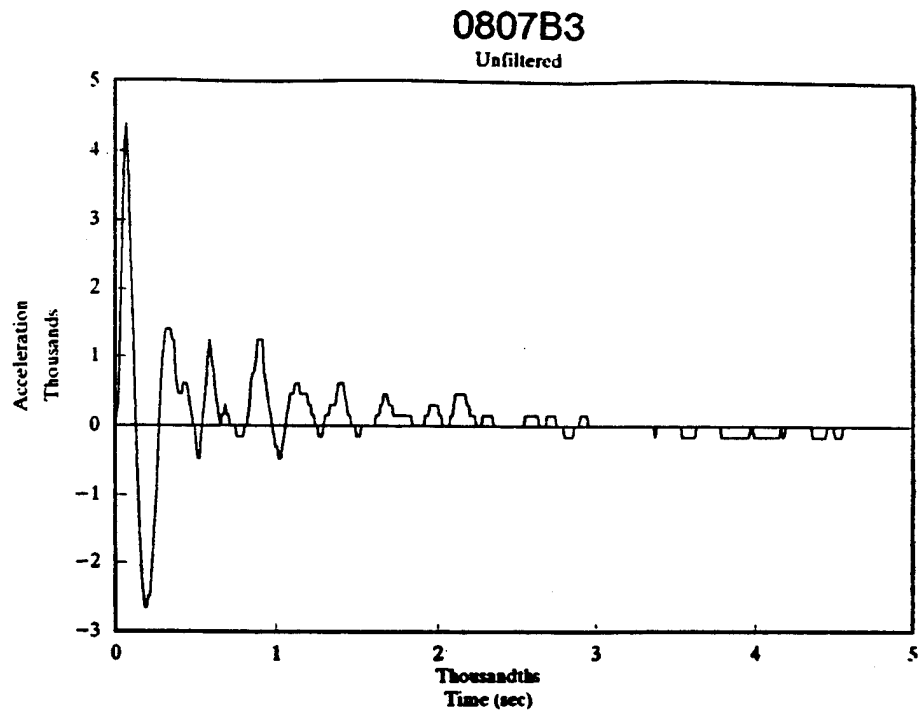
Figure A-49. Pressure for Test 8 at Point 7 on Channel B3.

0807B4

Unfiltered
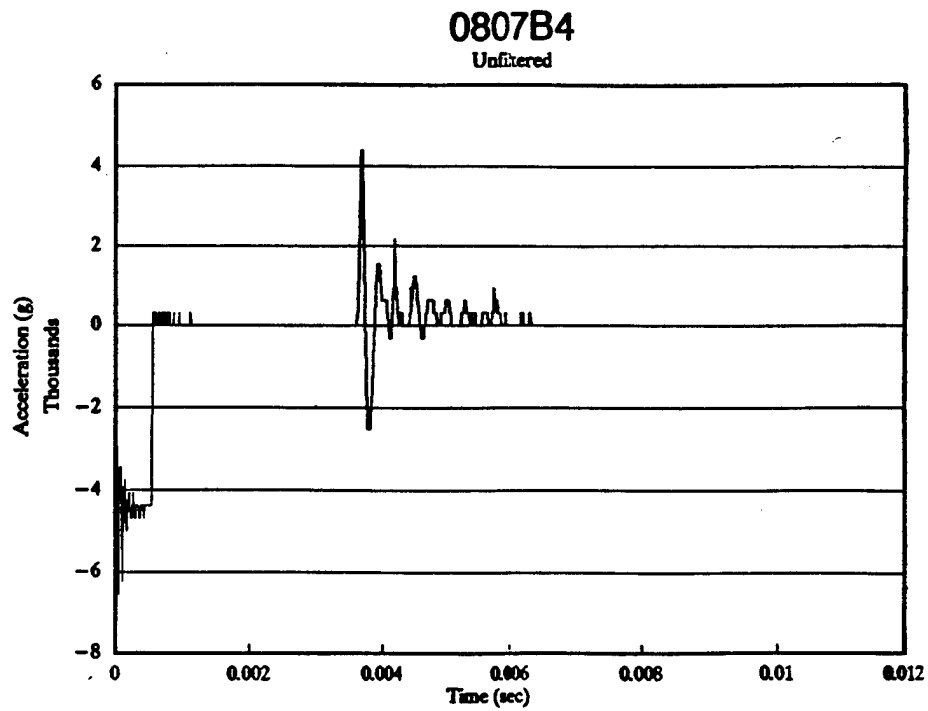
Figure A-50. Pressure for Test 8 at Point 7 on Channel B4.

237

APPENDIX B
COMPUTATION OF AIRBLAST LOADS FOR USE IN FINITE ELEMENT ANALYSES

A. INTRODUCTION

The accuracy of any structural analysis is directly affected by the validity of the loading function for the model structure. A major shortcoming of the SDOF models reported previously is the approximate nature of the airblast loading functions used in their application. Typically, loading is based on spherical or hemispherical explosive shapes, and loading is applied uniformly over the structure surface. In both the IDF and the Tyndall test series, the explosive charges were cylindrically shaped and were placed at the ground level. The loads created by the explosives' detonation were therefore nonuniform, both spatially and temporally.

While a detailed study of airblast load characterization techniques was beyond the scope of the project, the authors devoted some effort to developing load functions for the finite element analyses that more closely resembled test records and computations that can be made using procedures reported in the literature. This appendix briefly outlines these efforts.

B. GENERAL

The basis for the majority of the airblast calculations used here is the Modified Friedlander Equation for approximating the positive phase portion of the airblast pressure-time history. This exponential decay function is typically expressed as:

$$P(t) = P_p \left[1 - \left(\frac{t - t_a}{t_o}\right)\right] e^{-\left(\frac{t - t_a}{\theta}\right)}, \quad t \geq t_a \tag{A-1}$$

where, P_p = Peak pressure

t = Elapsed time after detonation

t_a = Blast wave arrival time at structure

t_o = Positive pressure phase duration time

θ = Time constant

When the airblast strikes a rigid surface, such as a wall, it is reflected. The magnitude of the reflected pressure is largely a function of the incident pressure magnitude, the angle of incidence of a radial line from the source to the reflecting surface, and interactions with the ground and other surrounding objects. Algorithms are available to compute the reflected pressure magnitude as a function of incident pressure magnitude and angle of incidence.

In this study, for both planar and three-dimensional models, the subject wall surface in each test was divided into a grid of one foot square areas. The

reflected pressure-time history for the center of each one foot square grid was then computed. The modified Friedlander equation was essentially developed for the reflected pressure on each grid area. To develop the equation, the amount, type, and location of the explosive were used; each case assumed a surface detonation of a hemispherical charge. This procedure was handled very easily by a microcomputer program known as WALLPLOT, Reference B1, which was developed and is distributed by the Protective Design Center of the Omaha District of the U.S. Army Corps of Engineers. WALLPLOT computes reflected pressure-time histories for a gridded wall area; it is convenient and easy to use. In the WALLPLOT version used by the authors, it was necessary to compute the "TNT equivalence" of the explosive before running the program (it only computes pressure-time histories for TNT charges). This was also done by microcomputer, using a program known as "ConWep," Reference B2, which was developed and is distributed by the U.S. Army Waterways Experiment Station.

A sample WALLPLOT printout for one grid area is shown in Figure B-1. ADINA does not readily permit the use of a continuous nonlinear load function such as that shown. Rather, it accepts linear definitions of pressure-time histories; it will accept any number of defined pressure-time coordinates and then interpolate linearly between the defined points to determine pressure magnitudes at computation time steps. A separate definition of load magnitude, duration, and arrival time can be made for every element in a structure. To translate the exponential function generated in WALLPLOT into a linear one, the authors manually overlaid each exponential plot with a series of straight line approximations that closely fit the exponential decay function. Figure B-2 provides a sample of this procedure and is typical of all basic pressure-time histories that were developed for this study. Note that pressure durations used in these approximations did not include the relatively long periods of low pressure in the exponential decay functions. Shorter duration times were used in the linear approximations, in which the total impulse (area under pressure-time curve) was maintained.

While this general procedure results in good approximations to the theoretical loads from hemispherical charge surface bursts at the proper standoff distances, a number of other factors entered into modeling each test series.

C.   IDF STRUCTURE

The finite element analyses concentrated on Tests 1-4 of the IDF series. The four tests were conducted opposite one wall of the test structure. Successive detonations of uncased cylinders, with a length to diameter (l/d) ratio of 1.0, of Composite-B explosive occurred at distances of 49.2 feet, 32.8 feet, 23.0 feet, and 16.4 feet from the structure. The detonations were labelled Tests 1-4, respectively. Each cylinder weighed 181 pounds. CONWEP yielded a TNT equivalence of 189 pounds for the charge weight; this was used in all IDF analyses.

As reported in Section II, the IDF tests included collecting actual airblast data at a limited number of locations on the test walls. Peak reflected

REFLECTED PRESSURE HISTORY FOR SUB-PANEL 101

IDF TEST 4

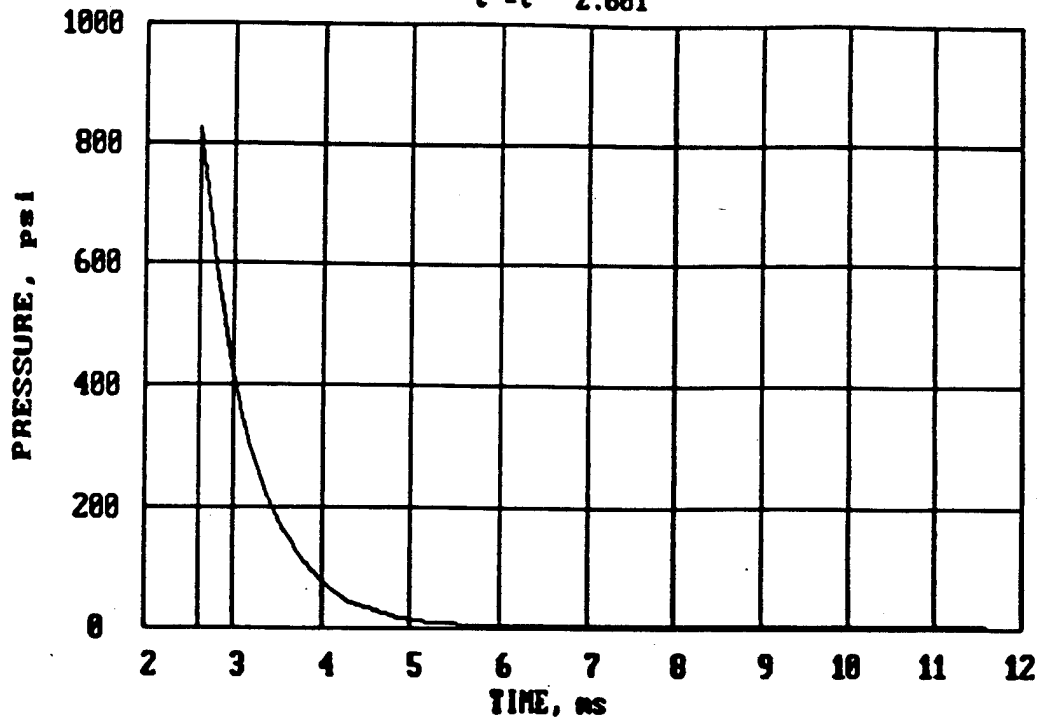P(t)=(823.9)*(1.-(t'/ 9.281)*exp(-15.010*t'/ 9.281)

t'=t- 2.601

Figure B-1. Sample WALLPLOT Printout.

REFLECTED PRESSURE HISTORY FOR SUB-PANEL 101

IDF TEST 4

P(t)=(823.9)*(1.-(t'/ 9.281)*exp(-15.010*t'/ 9.281)
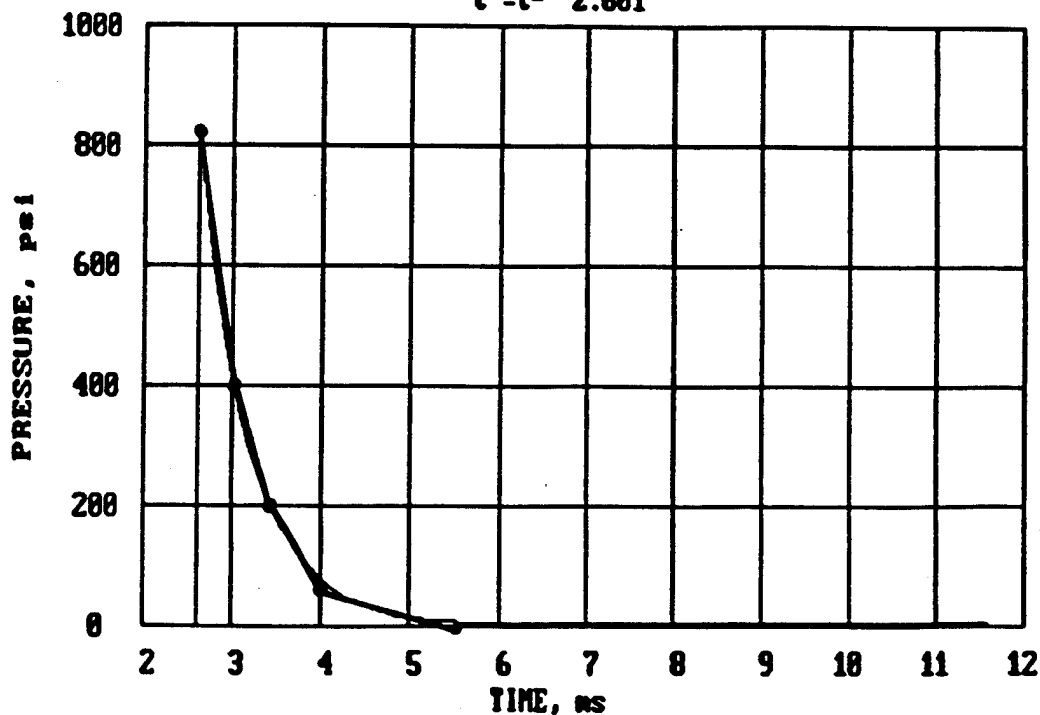
t'=t- 2.601

Figure B-2. Multilinear Approximation to WALLPLOT Printout.

240

pressures at wall midheight for Tests 1-4 are reported in Table 5 of this report. The authors used those peaks as benchmarks for the theoretical calculations and adjusted the peak pressures used as loadings accordingly. These adjustments are described below.

The cylindrical charge shape was a factor requiring consideration in all four IDF tests. Would the cylindrical shape create reflected pressure patterns significantly different from those predicted using WALLPLOT, which is predicated on a hemispherical shape? In general, the smaller the standoff distance, the more significance the charge shape assumes. To gain some insight, the authors referred to Figure 4.23 of Reference B3. The figure provides empirically-based ratios of equivalent spherical mass to cylindrical mass for various scaled charge standoff distances. For Tests 1 and 2, the ratios were 0.85 and 1.20, respectively. Recalling that the predicted peak pressure is a function of the cube root of the charge mass or weight, the authors concluded the charge shape effects would not be significant. For Tests 3 and 4, the ratios were 1.40 and 1.80, respectively; the authors deemed these differences to be large enough to warrant considering their effects in the analyses.

In Test 1, the detonation occurred at considerable distance from the structure. The shock wave was almost planar when it arrived at the structure. There also was very little difference between the theoretical peak pressure based on a hemispherical charge and the measured peak pressure from the cylindrical charge. The peak theoretical reflected pressure at wall midheight was 34 psi, while the peak measured pressure was about 31 psi. WALLPLOT calculations showed minimal differences in times of arrival and duration over the wall height. Therefore, a uniform load was applied over the height of the wall slab in the ADINA analyses. The load had a peak of 34 psi and decayed to zero in 12.1 msec.

The slightly closer charge placement in Test 2 resulted in a less uniform loading than that of Test 1. For the ADINA analyses, the arrival and duration times were distributed in accordance with the WALLPLOT values. WALLPLOT calculations showed that shock wave arrival times were slightly later, about 0.5 msec, at the top of the wall than at the base, and that duration times were slightly longer at the base. Duration times averaged 8.0 msec over the wall height. Peak pressures were difficult to resolve for this test. While information on the effects on the nonhemispherical charge shape is limited, the authors judged that Test 2 had a sufficiently large charge standoff distance to avoid correction of computed pressure parameters. WALLPLOT indicated a peak midheight pressure of 100 psi, while the field data showed a peak of 142 psi. None of the IDF data yielded an explanation for the high pressure measurement. Without any refuting data, the authors felt that the reported IDF value had to be accepted. Therefore, the midheight peak reflected pressure was adjusted upward to 142 psi. All other calculated pressures were also adjusted upward by 42 percent. At the wall base, the peak was therefore 148 psi; at the roof line, the peak was 129 psi.

WALLPLOT calculations for Test 3 provided a variation in pressure peaks and shock wave arrival and duration times along the wall height. Peak reflected pressures calculated using WALLPLOT varied from 304 psi at the wall base to 227 psi at the roof line. Arrival times at the roof line were about 0.7 msec later than at the base. Duration times varied from 5.1 msec at the base to 7.4 msec at the roof line. WALLPLOT indicated a peak midheight pressure of 288 psi, while the IDF data indicated 282 psi. Because of this close agreement, the WALLPLOT values were used without adjustment.

Test 4 had the smallest charge standoff distance in the series; it was thus the most demanding of Tests 1-4. The authors judged that charge shape effects were more likely to be influential in Test 4 than in Tests 1-3. The WALLPLOT calculations showed wide peak pressure variation, from 882 psi at the base to 480 psi at the roof line, indicating that the hemispherical charge shape assumed in WALLPLOT significantly affects the shock wave characteristics. There was also a large discrepancy between the measured midheight peak pressure, 443 psi, and the WALLPLOT value of 715 psi. In the absence of refuting information, the authors once again accepted the measured peak pressure. Figure 29 in Reference B4 provided some illuminating information for a cylindrical charge. It shows that, for close charge standoffs, peak reflected pressures on a wall over a height from its base equal to the height of a cylindrical charge are likely to exceed those predicted using a hemispherical charge, while, above the charge height, the opposite is likely to be the case. Because of the anticipated load variations, alternate load functions were developed. For the first function, the theoretical peak values were all scaled down linearly by the same factor that was required to reduce midheight pressure from 715 psi to 443 psi. This resulted in a peak pressure distribution ranging from 546 psi at the base to 298 psi at the roof line. As an alternative to this function, an "enhanced" load function used the computed WALLPLOT peak pressures for the bottom 2 feet of the wall. This was an attempt to check the sensitivity of the ADINA models to the charge shape effects portrayed in References B3 and B4. A third variant of Test 4 involved using the midheight pressure-time history (peak of 443 psi) on all elements uniformly. This was run to analyze the differences between structural responses using a realistic transient loading and the uniform type of loading so frequently applied in SDOF models. For the two transient load functions, arrival and duration times computed using WALLPLOT were used. Arrival times varied by 0.8 msec from base to roof line; duration times varied from 2.4 msec at the base to 3.1 msec at the roof line.

D.   TYNDALL AFB STRUCTURE

While the analyses of the Tyndall AFB Structure cover two different tests, the explosive charge characteristics were the same for both. It was therefore desirable to develop a reflected pressure-time history that could be used to replicate either test. The Tyndall test environment was significantly different from the IDF tests, so that procedures developed for the IDF analyses could not automatically be assumed to be applicable in the Tyndall tests. The explosive

charge used in the Tyndall tests was significantly larger than the charge in the IDF tests, and the charge standoff distance was much smaller in the Tyndall tests. Further, the charge in the Tyndall tests had a more slender cylindrical shape, with an l/d ratio of approximately 4; this configuration was much less like a hemisphere than that of the IDF tests. Finally, the charge was lightly cased. Note that actual charge characteristics for the Tyndall AFB tests are prohibited from publication in this unclassified report.

The authors set out to compare calculated structural responses using several definitions of the reflected pressure-time histories along the wall height. Because of the highly variable nature of the reflected pressure, both spatially and temporally, no effort was made to develop a uniform load function for the wall.

The first, load function, referred to as "T-1" in Section VIII, was based directly on WALLPLOT calculations using the procedures already described for the IDF structure analyses. Peak pressures ranged from almost 6,000 psi at the wall base to approximately 1,500 psi at the roof line. Duration times ranged from 1.7 msec at the base to 4.7 msec at the roof line. At the roof line, the shock wave arrived about 1.0 msec after it arrived at the base.

The second load function was based directly on the first; it is referred to as "T-2" in Section VIII. The only difference was that the pressure-time history for each loaded element was assumed to have a triangular, rather than exponential, decay function. This is often assumed in analysis. New duration times were computed for each pressure-time history, assuming that total impulse (area under the pressure-time history curve) remained the same as found for the exponential decay function. Peak pressures and arrival times were those originally computed using WALLPLOT.

The third load function, labelled "T-3" in Section VIII, again used the original WALLPLOT calculations as a point of departure. Peak pressures were adjusted downward, based on pressure data from the Tyndall tests. Tests 6 and 10, while not in total agreement, indicate peak pressures in the sub-3,000 psi range in the zone below the wall midheight. The data also show reasonably uniform peak pressure distributions over the height of the explosive charge. The third load function therefore reduces basic pressure peaks on all elements by approximately 50 percent from those computed in WALLPLOT, and it maintains a uniform pressure distribution over the lower half of the wall, with a peak of 2900 psi.

For the fourth load function, labelled "T-4" in Section VIII, both the charge slenderness and the casing effects were considered. Southwest Research Institute (SwRI), as reported in Reference B5, performed cased cylindrical charge calculations to support the project. With the appropriate charge size, standoff, and slenderness ratio, SwRI first calculated peak reflected pressures and impulses on the same one foot square grid described earlier, based on empirical equations developed at SwRI, for the uncased explosive. Significantly, the data on which the empirical relationships are based are very limited for small charge standoff distances. The values provided by SwRI were based on extrapolations of

curves for very small standoff regions from data of larger standoff distances. Next, SwRI computed the anticipated added impulse on the wall grid areas due to casing fragment impacts. Using assumed triangular pressure-time history functions, the peak reflected pressure and total impulse (from reflected airblast pressure and fragment impacts) for each grid area were used to calculate duration times. Using these techniques, peak reflected pressures ranged from over 48,000 psi at the wall base to slightly under 500 psi at the roof line. Duration times ranged from 0.28 msec at the base to 0.55 msec at the roof line. Arrival times were kept the same as those in the third WALLPLOT-based function. In the course of the ADINA analyses, the authors found that the numerical procedures in ADINA would not accommodate such ultra-high pressures, because concrete compressive stresses exceeded the bounds of the defined compression failure envelope (see Section VIII for discussion of failure envelopes), causing premature program execution termination. Subsequent analyses halved the peak reflected pressures in the wall base region and raised the concrete f'_c to permit execution. This introduced another artificiality into the model. See Section VIII for discussion.

REFERENCES FOR APPENDIX B

B1. WALLPLOT, MSDOS Computer Program, Protective Design Center, Omaha District, U.S. Army Corps of Engineers, undated.

B2. Hyde, D, ConWep, Microcomputer Applications of TM 5-855-1, Fundamentals of Protective Design for Conventional Weapons, MSDOS Computer Program, U.S. Army Waterways Experiment Station, undated.

B3. A Manual for the Prediction of Blast and Fragment Loadings on Structures, U.S. Department of Energy Report DOE/TIC-11268, November 1980.

B4. Coltharp, D, Vitayaudom, K, and Kiger, S; Semihardened Facility Design Criteria Improvement, Air Force Engineering and Services Center Technical Report ESL-TR-85-32, September 1985.

B5. Esparza, E, Bielefeld, W, and Marchand, K; Reflected Airblast Pressure and Impulse on a Vertical Wall from a Cased Cylindrical Charge Detonated Vertically on the Ground, Southwest Research Institute Letter Report, 14 July 1992.

REFERENCES

1. Unpublished original test data provided by the Israeli Defense Forces.

2. Hyde, D., "NATO Semihardened Facility Test," HQ Air Force Engineering and Services Center, Engineering and Services Laboratory, HQ AFESC/RDCS, Tyndall AFB, FL, 32403-6001, ESL-TR-89-06, Final Report, June 1989.

3. Biggs, J.M., <u>Introduction to Structural Dynamics</u>, New York, NY, McGraw-Hill, 1964.

4. Mindess, S. and J.F. Young. <u>Concrete</u>. Englewood Cliffs, NJ: Prentice-Hall, 1981.

5. "Fundamentals of Protective Design for Conventional Weapons." (TM 5-855-1, Department of the Army), November 3, 1986.

6. WALLPLOT, MSDOS Computer Program, Protective Design Center, Omaha District, U.S. Army Corps of Engineers, undated.

7. Mayor, R.P. and R. Flanders, "Users Manual, Simplified Computer Model of Air Blast Effects on Building Walls," U.S. Department of Transportation, Research and Special Programs Administration, Transportation Systems Center, for U.S. Department of State, Office of Diplomatic Security, June 1990.

8. Hyde, D.W. and J.H. Weatherby, "Data Package for NATO Semihardened Design Criteria Full-Scale Tests, Volumes 2 and 3," Structural Mechanics Division, Structures Laboratory, USAE Waterways Experiment Station, Vicksburg, Miss., for Air Force Engineering and Services Center, Tyndall AFB, FL, October 1987

9. Newmark, N.M., "A Method of Computation of Structural Dynamics." <u>Journal of the Engineering Mechanics Division, ASCE</u>, Vol 127, 1962.

10. Haltiwanger, J.D., "An Exploratory Study of the Effects of Revised Definitions of the Free-Field Pressure Environment on the Isodamage Curves for Typical Urban-Industrial Targets," H&H Consultants, Inc., P.O. Box 2219, Station A, Champaign, IL 61820, DNA-tr-88-13, February 1990.

11. ASCE Manual of Engineering Practice No. 42, <u>Design of Structures to Resist Nuclear Weapons Effects</u>, American Society of Civil Engineers, 345 East 47th St., New York, NY, Revised 1985.

12. Kiger, S.A., T.R. Slawson, and D.W. Hyde, "Vulnerability of Shallow-Buried Flat-Roof Structures, Report 6, Final Report: A Computational Procedure," Department of the Army, Waterways Experiment Station, September 1984.

13. "Protective Construction Design Manual," ESL-TR-87-57, Sections I through XIII, AFESC, Tyndall AFB, FL, November 1989.

14. Unpublished construction material properties report for the investigation reported in Reference 2.

15. Krauthammer, T., "Structural Analysis for Severe Dynamic Environments," User's Manual for computer program Version 1.4, November 1988.

16. Krauthammer, T., N. Bazeos, and T.J. Holmquist, "Modified SDOF Analysis of RC Box-Type Structures," <u>Journal of the Structural Division, ASCE,</u> Vol 112, No. 4, April 1986.

REFERENCES
(Continued)

17. Krauthammer, T., "Shallow-Buried RC Box-Type Structures," _Journal of the Structural Division, ASCE,_ Vol 110, No. 3, March 1984.

18. Keenan, W. A., "Shear Stresses in One-Way Slabs Subjected to Blast Load," Technical Memorandum No. M-51-77-10, U.S. Naval Civil Engineering Laboratory, Port Hueneme, CA, August 1977.

19. Park, R. and T. Paulay, _Reinforced Concrete Structures_, John Wiley & Sons, Inc., NY, pp 195-269, 1975.

20. Park, R. and W.L. Gamble, _Reinforced Concrete Slabs_. Wiley-Interscience, 1980.

21. Keenan, W.A., "Shear Stress in One-Way Slabs Subjected to Blast Load," 17th Explosive Safety Seminar, Denver, CO, September 1976.

22. Murtha, R.N. and T.J. Holland, "Analysis of WES FY82 Dynamic Shear Test Structures," Naval Civil Engineering Laboratory, Technical Memorandum No. 51-83-02, December 1982.

23. Newmark, N.M., "Design of Structures for Dynamic Loads Including the Effects of Vibration and Ground Shock," _Symposium on Scientific Problems of Protective Construction_, Zurich, July 1963.

24. Criswell, M.E., "Strength and Behavior of Reinforced Concrete Slab-Column Connections Subjected to Static and Dynamic Loadings," Technical Report N-70-1, U.S. Army Engineer Waterways Experiment Station, Vicksburg, MI, December 1970.

25. Furlong, R.W., J.N. Thompson, N.H. Burns, and E.S. Perry, "Shear and Bond Strength of High-Strength Reinforced Concrete Beams Under Impact Loads-First Phase," Technical Report AFWL-TR-67-113, Air Force Weapons Laboratory, May 1968.

26. Seabold, R.H., "Dynamic Shear Strength of Reinforced Concrete Beams-Part III," Technical Report R695, Naval Civil Engineering Laboratory, September 1970.

27. Soroushian, P., and K. Obaseki, "Strain Rate-Dependent Interaction Diagrams for Reinforced Concrete Section," _ACI Journal_, Vol 83, No. 1, January-February 1986.

28. Soroushian, P., K.B. Choi, and A. Alhamad, "Dynamic Constitutive Behavior of Concrete," _ACI Journal_, Vol 83, No. 2, March-April 1986.

29. Soroushian, P., and K. B. Choi, "Steel Mechanical Properties at Different Strain Rates," _ASCE Journal of the Structural Division_, Vol 113, No. 4, April 1987.

30. "BIGGS, Version 2.0 Users Manual", Wilfred Baker Engineering Inc., P.O. Box 6477, San Antonio, TX 78209, July 1990.

31. Mayor, R.P. and R. Flanders, "Users Manual, Simplified Computer Model of Air Blast Effects on Building Walls," U.S. Department of Transportation, Research and Special Programs Administration, Transportation Systems Center, for U.S. Department of State, Office of Diplomatic Security, June 1990.

REFERENCES
(Continued)

32. Mayor, R.P. and R. Flanders, "Technical Manual, Simplified Computer Model of Air Blast Effects on Building Walls," U.S. Department of Transportation, Research and Special Programs Administration, Transportation Systems Center, for U.S. Department of State, Office of Diplomatic Security, June 1990.

33. Moor, D.M., "Proposed Method for Determining the Thickness of Glass in Solar Collector Panels," Jet Propulsion Laboratory, Pasadena, Calif., JPL Publications 80-34.

34. Meyers G.E., "User Data Package for Blast Resistant Windows," Naval Facilities Engineering Command, Alexandria, VA, Technical Memo 51-86-13, June 1986,

35. McDowell, E., K. McKee, and E.J. Sevin, "Arching Action Theory of Masonry Walls," ASCE, Structural Division, V82, No. ST2, March 1956, pp 915/1-8.

36. ADINA Theory and Modeling Guide, Report ARD 87-8, ADINA R&D, Incorporated, December 1987.

37. Bathe, K.J., J. Walczak, A. Welch, and N. Mistry, "Nonlinear Analysis of Concrete Structures," Computers and Structures, Vol 32, No. 3/4, 1989, pp. 563-599.

38. Meyer, C., and K.J. Bathe, "Nonlinear Analysis of R/C Structures in Practice," Proceedings, ASCE, Vol 108, No. ST7, July 1982, pp. 1605-1622.

39. Bathe, K.J., and J. Walczak, A. Welch, N. Mistry, "Nonlinear Analysis of Concrete Structures," J. Computers & Structures, Vol. 32, No. 3/4, pp 563-590, 1989.

40. Bathe, K.J., and A.P. Cimento, "Some Practical Procedures for the Solution of Nonlinear Finite Element Equations," Computer Methods in Applied Mechanics and Engineering, Vol 22, 1980, pp. 59-85.

41. Balakrishnan, S., and D.W. Murray, "Concrete Constitutive Model for NLFE Analysis of Structures," ASCE Journal of Structural Engineering, Vol 114, No. 7, July 1988, pp. 1449-1467.

42. Balakrishnan, S., A.E. Elwi, and D.W. Murray, "Effect of Modeling on NLFE Analysis of Concrete Structures," ASCE Journal of Structural Engineering, Vol 114, No. 7, July 1988, pp. 1467-1487.

43. Suaris, W., and S.P. Shah, "Constitutive Model for Dynamic Loading of Concrete," ASCE Journal of Structural Engineering, Vol 111, No. 3, March 1985, pp. 563-576.

44. Ghaboussi, J., W.A. Millavec, and J. Isenberg, "R/C Structures Under Impulsive Loading," ASCE Journal of Structural Engineering, Vol 110, No. 3, March 1984, pp. 505-522.

45. Khan, M.H., and B. Saugy, "Evaluation of the Influence of Some Concrete Characteristics on Nonlinear Behavior of a Prestressed Concrete Reactor Vessel," Concrete for Nuclear Reactors, American Concrete Institute Special Publication SP-34, 1972, pp. 159-179.

248

REFERENCES
(Concluded)

46. Kupfer, H., H.K. Hilsdorf, and H. Ruesch, "Behavior of Concrete Under Biaxial Stresses," _Journal of the American Concrete Institute_, Vol 66, No. 8, August 1969, pp. 656-666.

47. _Finite Element Analysis of Reinforced Concrete Structures_, State-of-the-Art Report, Task Committee on Finite Element Analysis of Reinforced Concrete Structures, ASCE Special Publication, 1982.

48. Riad, H.L., _Finite Element Analysis of Reinforced Concrete Structures Under Impact Loading_, Doctoral dissertation, Pennsylvania State University, May 1991.

49. Bathe, K.J., _Finite Element Procedures in Engineering Analysis_, Prentice-Hall, 1982.

50. Cook, R.D., D.S. Malkus, and M.E. Plesha, _Concepts and Applications of Finite Element Analysis_, Third Edition, John Wiley & Sons, 1989.

51. Liebengood, L., D. Darwin, and R.H. Dodds, "Parameters Affecting FE Analysis of Concrete Structures," _ASCE Journal of Structural Engineering_, Vol 112, No. 2, February 1986, pp. 326-341.

52. Barzegar-Jamshidi, F., and W.C. Schnobrich, _Nonlinear Finite Element Analysis of Reinforced Concrete Under Short Term Monotonic Loading_, Civil Engineering Studies, Structural Research Series No. 530, UILU-ENG-86-2012, University of Illinois at Urbana-Champaign, November 1986.

53. Hughes, T.J.R., _An Assessment of Modeling Techniques for the Finite Element Analysis of Reinforced Concrete Plate and Shell Structures_, Navy Civil Engineering Laboratory Contract Report CR-88.008, January 1988.

54. Shugar, T.A., T.J. Holland, and L.J. Malvar, _Advanced Finite Element Analysis of Drydocks and Waterfront Facilities-A Technology Assessment_, Navy Civil Engineering Laboratory Technical Note N-1835, October 1991.

55. Ghaboussi, J., W.A. Millavec, and J. Isenberg, _Finite Element Analysis of Shallow-Buried Protective Structures_, Defense Nuclear Agency Technical Report DNA-TR-84-215, 1 October 1981.

56. Coltharp, D.R., Vitayaudom, K.P., Kiger, S.A., "Semihardened Facility Design Criteria Improvement," U.S. Army Engineer Waterways Experimental Station, Final Report ESL-TR-86-32, October 1981-December 1984.

57. Kiger, S.A. and Getchell, J.V., "Vulnerability of Shallow-Buried Flat-Roof Structures," Technical Report S1-80-7, Report 1, USAEWES, September 1980.